Many Faces of Young Neutron Stars

Thesis by
Gautam Vasisht

In Partial Fulfillment of the Requirements
for the Degree of
Doctor of Philosophy

California Institute of Technology
Pasadena, California

1996
(Submitted April, 8 1996)

Acknowledgments

I first thought about astronomy as a freshman in college. As a science, it offers something that has greater significance for my world view. The reason I chose it as a profession is now so complicated that every time I tell it, I contradict myself and whenever I get it right, I am misquoted. One night I lay thinking— I would build a telescope so powerful, that it could study photons that once escaped Earth and got bounced-off shiny things in Andromeda. I could then study the Australopithecines, my first love. Having had this thought, I promptly fell asleep and forgot about it. Clearly, I had not yet mastered the black Cafe'-art of the "back of the envelope" calculation, and was too lazy to do a simulation. Four years later, I graduated as an electrical engineer. And now, almost six years later I'll be a certified astronomer.

This thesis is largely an anthology of information gathered by my colleagues and I during my years at the California Institute of Technology and based on stories proferred by countless other astronomers, spread throughout scientific literature. Many people have contributed to this thesis in more ways than I can remember. To those I may forget in this time of distress, confusion and urgency to finish, please forgive my sluggish memory and accept my heartfelt apologies.

I cannot thank enough my advisor Shri Kulkarni for all the impetus for this project. I have been very fortunate to work with him and learn from him. Shri provided me techno-refuge for applying my engineering skills to astronomy when I first came to Caltech. He let me loose on the FFB project during my first year and I've stayed with him to complete graduate school. I confess jealous admiration for Shri's enthusiasm and energy, abundance of irresistible ideas and the gall to execute those ideas. I'm most grateful for his constant support and sound advice, sometimes good-humored and sometimes not.

I have benefited greatly from the suggestions and help of colleagues who have participated in the work of this thesis. I owe a special debt of gratitude to Dale Frail of NRAO for scientific collaborations and generous contributions of time

and advice. Steve Thorsett, then at Caltech and now at Princeton University for diversely stimulating discussions. I thank Simon Johnston, Andrew Lyne and Dick Manchester for orientation at Parkes Observatory and in Sydney; Daniel Altschuler, Alex Wolszczan, Norberto Despiau and Willy Portalatin at Arecibo Observatory; Ger de Bruyn, Lodie Voûte and Han Weggemans at the Netherlands Foundation for Radio Astronomy. I must thank Don Backer and Dan Wertheimer of UC Berkeley for useful initial discussions on the FFB. Harry Hardeback, Mark Hodges and Russ Keeney for FFB related assistance at the Owens Valley Radio Observatory. I'll forever remember the two grueling months spent erecting the FFB with John Yamasaki of the subterranean Miracle Laboratories. He poured his heart and soul into it.

For loads of local help, I'm grateful to Helen Knudsen, Ann Snyder, Candi Lewis, Sandy Lester, Diane Fujitani and Gita Patel.

The company of my D-officemates Ben Oppenheimer and Erik Leitch was a pleasure during the months of writing. So were the late night visits by Martin Shepherd. I'm grateful, for a variety of reasons to past and present members of the shr-intelligentsia: Will Deich, Tom Hamilton, Helen Johnston, Vicky Kaspi, Marten van Kerkwijk, Tadashi Nakajima and Jose′ Navarro. I apologize that I cannot devote enough words for my friends. They best understand my need to finish quickly. At Robinson, I thank: Lin Yan, Angela Putney, Donna Womble, Todd Small, John Gizis, Rudi Danner, Glen Soberman, Jagmit Sandhu, Chris Fassnacht, Brian Kern and Peter Bryant. Away from the tedium of academics were the influences of: Tracy Katz, Laura Adams, Colette Brown, Kiriaki Xilouris, Vassily Hatzimanikatis, Nikos Bekiaris and Niel Brown. Sophia Kyriazopoulou is a vast and wonderful influence on my life.

This thesis would not have been possible without the years of selfless and endless support and encouragement of my terrific family: my father Sham, my mother Pramod and my brother Aney.

Lastly and firstly, I might say, I want to thank friends and colleagues for their knowledge of syntax and editorial enthusiasm. Without their help this manuscript would never be a book. I am most appreciative, indeed, to Dale Frail, Shri Kulkarni, Ben Oppenheimer, Erik Leitch, Glen Soberman and John Yamasaki for criticisms on one or more chapters. I owe an immense debt of gratitude to the diligence of Andrea Dzurik and Lori Silverman for belaboring through the monotonous astronomical jargon of "The Many Faces of Young Neutron Stars". Despite vague attempts on my part, the text was never really tailored for architects. Miraculously, however, they got the gist of it and remarked, "*Are you guys really sure of anything you do!*"

Its overwhelming to have met Lori Silverman. I cannot thank her enough for too many things: but if I may, thank-you for all the music, and for bolstering me during the months of writing this graduate school "swan song".

I thank Bacardi for making my rum and Burton for making my snow-board. I dedicate this thesis to the memory of my beautiful ancestor Sumitra Devi Moudgil.

ABSTRACT

The hardware aspect of this thesis consists in the design, fabrication and assembly of twin analog Flexible Filter Banks at Caltech. These are user-friendly, workhorse, radio-pulsar search and timing instruments. Novel features include the flexibility in configuring channel center-frequencies and widths, the rapid sampling down to 25 μs and a total instrument bandwidth ranging from a narrow 0.2 MHz to a mammoth 100 MHz. Frequency synthesis is used to downconvert, detect and sample the telescope receiver bandpass as 32 separate time-series in each polarization. The collected data are later subjected to standard pulsar search and timing algorithms in software.

The vital scientific issue addressed here is the nature of young neutron stars. In the standard picture, young neutron stars are rapidly spinning radio-luminous pulsars, which may also display pulsed emission at high X-ray and γ-ray energies. However there is no evidence that all neutron stars are born according to this standard picture. We present radio or X-ray investigations of steady nebular emission produced by three clearly non-standard and ill-understood objects. In all likelihood, these are young neutron stars, a notion upheld by their association with young Galactic supernova remnants.

Based on its display of high energy transients, the soft γ-ray repeater SGR 1806$-$20 is posited to be a seismically active "magnetar", i.e., a neutron star with a super-strong magnetic field (10^{15} G) nearly three orders of magnitude greater than pulsar dipolar fields. Our VLA observations of fleeting small-scale structure around SGR 1806$-$20 provide intriguing, although preliminary, support for the magnetar model. In time, similar observations could unravel the riddle of soft γ-ray repeaters and possibly establish the reality of magnetars.

X-ray observations of the remnant of the historical supernova of 386 A.D., SNR G 11.2$-$0.3 are presented. The nature of an embedded underlumnious plerion discovered in these observations argues for a central neutron star very different from the prototypical Crab pulsar. The urgency to undertake a large scale study

of young and hollow Galactic shells in broadband X-rays with fine spatial resolution is elucidated.

X-ray spectroscopy of the object 1E 1207.4−5209 at the core of the large remnant PKS 1209−51/52 has revealed a non-thermal source with a very steep spectrum. After considering various scenarios for 1E 1207.4−5209, we conclude that its spectral signature, its lack of optical emission and its position at the center of a supernova remnant make it a source similar to the mysterious anomalous X-ray pulsars.

A large and sensitive search for radio pulsar companions of massive stars was undertaken. Primary motivation stems from the recent discovery of binary radio pulsar B 1259−63 as the first member of such a population and a "missing link" in the current models of evolution. Prevalent expectations, based on binary evolution scenarios, suggested that many more such systems should exist and would be uncovered in sensitive targeted searches. Together with other smaller searches, this survey uncovered no pulsars orbiting early-type stars. We conclude that such binary systems must be rare.

Contents

List of Tables

List of Figures

CHAPTER 1: PROLOGUE

1.1 – A BRIEF HISTORY

In 1934 Baade and Zwicky proposed the idea of neutron stars, pointing out that they would be at very high material density and of small radius. They also made the remarkably prescient suggestion that neutron stars would be formed in supernova explosions. At that time there was no advance knowledge of, and much pessimism about, whether such objects would ever be revealed to us.

The discovery of cosmic, non-solar X-ray source Sco X-1 by Giacconi et al. in 1962 revitalized interest in neutron stars. A large number of the theorists independently speculated that the X-ray telescope was observing young, hot neutron stars, and a devoted effort to compute neutron star cooling curves began. The identification of the first "quasi-stellar object" (QSO or quasar) by Schmidt at Palomar in 1963 triggered further interest in neutron stars, except that later it became apparent that the greatest QSO redshifts were already beyond the maximum gravitational redshifts possible from a neutron star surface thus immediately dispelling the connection between neutron stars and QSOs (Salpeter 1965).

During these years much scientific literature was generated on the equilibrium properties of compact bodies and on stellar collapse. In spite of this theoretical effort, a large body of the astronomical community did not take the idea of extremely compact objects such as neutron stars and black holes very seriously. All this changed when pulsars were discovered in late 1967 (Hewish et al. 1968). Gold (1968) argued that they were rotating magnetized neutron stars and this idea is almost axiomatic today.

Since then, there has been much experimental and theoretical work on the properties of neutron stars. This has been further stimulated by the discovery with the Uhuru satellite of pulsating, compact X-ray sources since 1971. These are believed to be neutron stars in close binary systems that are accreting gas from their normal companions. Although the idea of accreting binary systems had been proposed long before, the first evidence of binarity through periodicities was found in the sources Cen X-3 and Her X-1 (Schreier et al 1972, Tannenbaum et al. 1972).

The near simultaneous discoveries of the Vela and Crab pulsars in the late Fall of 1968, both of which were located inside of supernova remnants, provided the first evidence for the formation of neutron stars in supernova explosions (Large et al. 1968, Richards and Comella 1968). The Crab nebula for example is the remnant of the supernova explosion documented by the Chinese astronomers in 1054 A.D.. The Vela pulsar and supernova remnant are estimated to be about $20,000$ yr old.

Today over 700 pulsars are known. A vast majority are isolated neutron stars, having pulse periods typically in the range $0.001 - 5$ s and surface dipole magnetic field strengths in the range of $1 \times 10^8 - 3 \times 10^{13}$ G. During the last fifteen years a new class of pulsars have emerged, with ages comparable to the age of the universe. These are the overlapping sets of binary, millisecond (Backer et al. 1982) and globular cluster pulsars (Backer and Kulkarni 1990, Phinney and Kulkarni 1994) whose discovery revived pulsar astronomy. Soon, some millisecond pulsars were discovered to orbit low mass companions. The relatively small number of binary pulsars have, however, made an unusually large contribution to our understanding of the evolution of neutron stars and their magnetic fields in the course of billions of years, and of the formation and evolution of other types of binary neutron stars such as the X-ray binaries (Bhattacharya & van den Heuvel 1991). In addition to their obvious interests to astronomers, such pulsars are intriguing objects for diverse kinds of physics experiments. They have been used to test aspects of general relativity and cosmology, and they may eventually

provide for improved time standards on Earth. Significant among pulsars that have contributed to development of evolutionary scenarios are PSR B 1913+16 (the Hulse-Taylor relativistic binary; Hulse & Taylor 1975), the eclipsing binary pulsar PSR B 1957+20 (Fruchter et al. 1988) and the pulsar with planets PSR B 1257+12 (Wolszczan & Frail 1992).

Since two decades ago, neutron stars have been discussed in the context of sources showing even higher energy emissions such as the soft gamma-ray repeaters (SGRs) and the gamma-ray bursters (GRBs). The former are a truly rare class of objects with two known Galactic SGRs and one in the LMC (Norris et al. 1991). Counterparts to SGRs at other wavelengths were not known until this thesis was well underway. GRBs on the other hand, are isotropically distributed and are representative of a symmetrically distributed population either in a large Galactic halo or in the universe at large. Counterparts at other wavelengths for GRBs are yet not discovered, leaving their nature shrouded in mystery and presenting one of the more outstanding astrophysical puzzles.

1.2 – YOUNG PULSARS AND SUPERNOVA REMNANTS

Neutron star - supernova associations are potentially valuable for understanding the fate of big stars, the birth and evolution of neutron stars and supernova remnants (SNRs). Establishing that a neutron star is part of an SNR is important in classifying the remnant in terms of one type of explosion (Type II or Type Ib, Ic). Furthermore, associations with pulsars can provide independent estimates of some crucial properties such as age and distance and clarification of unusual morphology as is sometimes observed in SNR (Becker & Helfand 1985, Shull et al. 1989, Frail & Kulkarni 1991).

There is independent strong motivation for the search of very young pulsars. With their higher spin-down luminosities, young pulsars are more likely to be detected at higher X-ray and γ-ray energies, providing an important observational

for testing cooling models of neutron stars, which are intimately linked to the solid state physics of the neutron star. Young pulsars often show rotation glitches (McKenna & Lyne 1990) that have been used as diagnostics of the interiors of neutron stars. Young pulsars also show marked random rotational irregularities that are ill-understood (Johnston et al. 1995). Their rapid spin-down sometimes allows the measurement of nature of the electro-magnetic torques that are responsible for pulsar death (Lyne et al. 1988, Kaspi et al. 1994). A small sample of young pulsars will do for all the above investigations. However, study of the genesis of neutron stars and subsequent evolution need a large sample since there appears to be considerable diversity (as this thesis study will demonstrate).

Young pulsars, it is stressed, provide crucial diagnostics for pulsar and neutron star physics. They also provide us with estimates of the *initial birth and period distribution of newborn neutron stars.* These two parameters essentially determine further evolution of the star. A number of factors, however, barricade rapid progress in this quest for an evolutionary picture. First, we know of only few confirmed pulsar-supernova associations. We also lack a coherent construct in our knowledge of neutron star birth brought forth by important examples. For instance, even some of the youngest nearby supernova remnants that we know of do not contain observed pulsars. Prominent among them being the 300 yr old SNR Cassiopeia A, and the recent LMC supernova SN 1987A. Much is therefore incomplete and murky in our understanding of this subject. This subject is clearly in the need of more empirical data.

1.3 – FORMATION OF NEUTRON STARS IN SUPERNOVAE

Observational evidence shows that ~ 85 % of supernovae are of Type Ibc or II (Evans et al. 1989; Muller et al. 1992) which are commonly thought to have evolved from massive progenitors, and are hence likely to have formed compact objects. This is consistent with the rough agreement between the occurrence rate of supernovae (and the birth-rate of remnants) with the estimated neutron star

of supernovae (and the birth-rate of remnants) with the estimated neutron star birth-rate (Helfand & Becker 1984; Weiler & Sramek 1988). This is not, however, consistent with the observation that the Galaxy is largely impregnated with shell-type remnants.

The pulsar birth rate is uncertain (Narayan & Ostriker 1990; Lorimer et al. 1993), and the fraction of black holes formed (Bethe & Brown 1995) at the time of supernovae is unknown. Critical masses of black holes range between $18M_{\odot}$ (Bethe & Brown 1995) to 50 $M_{\odot}$. This uncertainty is unlikely to explain the lack of NS in SNR though. Requiring only a small fraction of supernovae to produce neutron-star remnants would be difficult to reconcile with most of the available evidence. *Could a substantial fraction of supernovae result in objects that cannot be radio pulsars of the sort we know (e.g. the Crab pulsar)?* There is to-date no direct evidence for this. But the birth of black-holes, exotic compact stars and non-pulsar (weak or short-lived pulsars) neutron stars in supernova explosions is observationally not ruled out.

1.4 – USING WIND NEBULAE

Whether neutron stars form a homogeneous class of objects at birth is not known, although that is indeed a pleasant albeit mundane hypothesis. In the standard picture, pulsars are born as rapid rotators ($P \lesssim 0.1$ s) with magnetic field strengths of $B \sim 10^{12}$ G. There could, in principle, exist a class of neutron stars that are not born with the standard birth parameters, or parameters that are familiar to us from years of studies of radio pulsars, e.g., exotic neutron stars that are born with extremely large magnetic fields ($\gtrsim 10^{14}$ G) or neutron stars with extremely low magnetic fields ($\lesssim 10^{8}$ G). These could either not display pulsar action at all or be visible as pulsed emitters for extremely short time-scales, such that the chance of observing them as radio or X-ray pulsars (the standard way) is vanishingly small. Forces that curtail the radio pulsar lifetime could be internal

to neutron star, or external, such as accretion. In what way can we then infer the presence of such exotic objects?

Synchrotron nebulae present a way out of this dilemma (Pacholczyk 1970). A lot is to be said about the utility of synchrotron nebulae in astrophysical systems. For the longest time, synchrotron light has been an indispensable tool in probing the physics of energetic phenomena in the universe. It helped unravel exciting phenomena with jets and giant lobes in active galactic nuclei, quasars and galactic black hole binaries (Begelman et al. 1984); and furthered the understanding of supernova remnants and supernovae (Weiler & Sramek 1988). It has been used in investigation of pulsar winds, a field still in its infancy, by detailed modeling of the Crab nebula (Kennel & Coroniti 1984, Gallant & Arons 1994). Emission from pulsar bow-shocks is also used to study the relativistic winds of high-velocity and binary pulsars (Frail et al. 1996, Kulkarni et al. 1992). In this dissertation, inquiries of synchrotron nebulae around the enigmatic soft-gamma ray repeaters and in plerions are presented. Lastly, it is probable that radio synchrotron observations will solve the great γ-ray burst puzzle.

The motivation for this thesis stems from the lack of neutron stars in supernova remnants. We approached this problem in two ways. The first approach would be to detect neutron stars that have unusual parameters (i.e., unlike the Crab pulsar). In addition, we suspected that this problem could be partially solved if a fair fraction of neutron stars were born is binary systems. It is thought that most neutron star progenitors are in massive binaries. This dissertation presents empirical studies targeted towards unusual supernova remnants and early type stars in hopes of detecting active neutron stars through their synchrotron nebulae, and then, using these nebulae to infer some properties of the neutron star. A summary of all included studies is given:

1. Chapter 2 describes the construction of twin analog Flexible Filter Banks (FFBs). These are pulsar search and timing instruments, that have the novel feature of tunable channel widths in a large frequency range. The FFB can

be adapted to suit a large variety of pulsar observations. One FFB is installed as an observatory backend at the Westerbork Synthesis Radio Telescope (WSRT). We are using the WSRT FFB in a program to search for young pulsars towards their birth places, i.e., the OB-associations.

2. Chapter 3 presents the study of the enigmatic soft γ-ray repeaters. These are thought to be young neutron stars that were first detected as burst sources at $\sim$ 50 kilo-volt energies almost two decades ago (Norris et al. 1991). Burst properties motivated Thompson and Duncan (1995) to suggest that the central neutron star must be highly magnetized (10^{15} G), i.e., a *magnetar* with magnetic flux densities 10^3 times higher than those occurring on radio pulsars. Our radio investigations of small-scale radio structure in the vicinity of SGR 1806−20 have generated support for this hypothesis.

3. Chapter 4 presents X-ray observations of the so-called "plerionic" emission. Plerions are powered by neutron star energy losses. Armed with a better understanding of the pulsar wind and with good models, we can use plerions to better study a wider range of neutron star properties than are possible with radio pulsars. We present ASCA observations of two interesting plerionic X-ray sources in SNR. Based on our observations, we hypothesize that the historical SNR G 11.2−0.3 could have an associated magnetar-like object. The source 1E1207.4−5209, centrally located in SNR G 296.5+10.0 is discussed in the context of the anomalous X-ray pulsars.

4. Chapter 5 describes a large unsuccessful search for pulsars in binary systems. Most massive stars are born in binary systems. Yet the known pulsar/SNR associations involve single pulsars and not pulsars in binary systems. This motivated us to conduct a search for binary pulsars towards Be-stars. During the course of this study, the pulsar B 1259−63 was discovered orbiting a Be-star (Johnston et al. 1992) in an untargeted search, validating our original idea. We had a two pronged approach. We searched for direct pulsed emission and shock emission that could arise from interaction of an energetic

wind from a pulsar with the wind from its companion. This can create an observable radio nebula in the vicinity of the searched star. Mostly Be-stars were targeted, however, no pulsars were discovered. Our results suggest that visible pulsars around such stars, contrary to original expectations are quite rare, and that less than 8 % Be-stars have observable pulsar companions.

REFERENCES

Baade, W. & Zwicky, F. 1934, Phys. Rev., 45, 138

Backer, D. C, Kulkarni, S. R., Heiles, C., Davis, M. M. & Goss, W. M. 1982, Nature, 300, 615

Backer, D. C. & Kulkarni, S. R. 1990, Physics Today, 43(3), 26

Becker, R. H. & Helfand, D. J. 1985, Nature, 313, 115

Begelman, M. C., Blandford, R. D. & Rees, M. J. 1984, Rev. Mod. Phy., 52, 255

Bethe, H. A. & Brown, G. E. 1995, ApJ, 445, L129

Bhattacharya, D. & van den Heuvel, E. P. J. 1991, Phys Report, 203, 1

Evans, R., van den Bergh, S. & McClure, R. D. 1989, ApJ, 345, 752

Frail, D. A. & Kulkarni, S. R. 1991, Nature, 352, 785

Fruchter, A. S., Stinebring, D. R. & Taylor, J. H. 1988, Nature, 333, 237

Gallant, Y. A. & Arons, J. 1994, ApJ, 435, 230

Giacconi, R., Gursky, H., Paolini, F. R. & Rossi, B. B. 1962. Phys. Rev. Lett., 9, 439

Gold, T. 1968, Nature, 218, 731

Hewish, A., Bell, S. J., Pilkington J. D. H., Scott, P. F. & Collins, R. A., 1968, Nature, 217, 709

Helfand, D. J. & Becker, R. H. 1984, Nature, 307, 215

Hulse, R. A. & Taylor, J. H. 1975, ApJ, 195, L51

Johnston, S., Manchester, R. N., Lyne, A. G., Bailes, M., Kaspi, V. M. & Qiao, G. J. 1992, ApJ, 387, L37

Johnston, S., Manchester, R. N., Lyne, A. G., Kaspi, V. M. & D' Amico, N. 1995, A&A, 293, 795

Kaspi, V. M., Manchester, R. N., Siegman, B., Johnston. S. & Lyne, A. G. 1994, ApJ, 422, L83

Kennel, C. F. & Coroniti, F. V. 1984, ApJ, 283, 694

Kulkarni, S. R., Phinney, E. S., Evans, C. R. & Hasinger, G. 1992, Nature, 359, 300

Large, M. I., Vaughan, A. E. & Mills, B. Y. 1968, Nature, 220, 340

Lorimer et al. 1993, MNRAS, 263, 403

Lyne, A. G., Pritchard, R. S. & Smith, F. G. 1988, MNRAS, 233, 667

McKenna, J. & Lyne, A. G. 1990, Nature, 343, 349

Muller, R. A., Newberg, H. J. M., Pennypacker, C., Perlmutter, S., Sasseen, T. P. & Smith, T. K. 1992, ApJ, 349, L9

Narayan, R. & Ostriker, J. P., 1990, ApJ, 352, 222

Norris, J. P., Hertz, P., Wood, K. S. & Kouveliotou 1991, ApJ, 266, 240

Pacholczyk, A. G. 1970, Radio Astrophysics, Chap. 7, San Francisco: Freeman

Phinney, E. S. & Kulkarni, S. R. 1994, ARAA, 32, 591

Richards, D. W. & Comella, J. W. 1969, Nature, 222, 551

Salpeter, E. E. 1965, in Quasi Stellar Sources and Gravitational Collapse, eds. I. Robinson, A. Schild & E. L. Schucking, Univ. of Chicago Press, Illinois.

Schreier, E. et al. 1972, ApJ, 172, L79

Shull, J. M., Fesen, R. A. & Saken, J. M. 1989, ApJ, 346, 860

Tannenbaum, A. et al. 1972, ApJ, 174, L143

Thompson, C. & Duncan, R. C. 1993, ApJ, 408, 194

Weiler, K. W. & Sramek, R. A. 1988, ARA&A, 26, 295

Wolszczan, A. & Frail, D. A. 1992, Nature, 355, 145

CHAPTER 2: THE FLEXIBLE FILTER BANK

G. Vasisht, M. W. Hodges, D. Kornreich, S. R. Kulkarni, J. Navarro, P. S. Ray, S. E. Thorsett & J. K. Yamasaki

Radio Astronomy Laboratory, Caltech, MS 105-24, Pasadena, California 91125

ABSTRACT: In this chapter we describe an analog filter bank system for pulsar observations. Analog design keeps the system increasingly cost and time effective when weighed against an equivalent digital system, such as an autocorrelator or a digital filter bank, although, this is usually obtained at the compromise of flexibility available with digital systems. Traditionally, filter banks in astronomy employ contiguous bandpass filters each with a separate fixed response, making the instrumentation rather rigid and suitable only for very specific applications. Herein we describe the flexible filter bank (FFB) which uses novel digitally tunable analog low-pass filters. All processing is at baseband, so that the bank of filters is realized by down-converting the appropriate sky frequencies. Individual channel widths over four decades of frequency can be realized adaptively to suit the type of observation. A version of the FFB is now operational at the Westerbork Synthesis Radio Telescope (WSRT) and a duplicate will be installed in the near future at the Very Large Array.

2.1 – SCIENTIFIC ASPECTS

Pulsars are rapidly rotating neutron stars emitting radiation in hollow cones that appear to be rigidly coupled to the star (Manchester & Taylor 1977). They are a unique astrophysical laboratory as a consequence of this emission, whereby, we probe fundamental physics and astronomy under extreme conditions. Pulsar astronomy has drawn from and contributed to a range of subjects covering Newtonian dynamics, magnetohydrodynamics, solid state physics, optics, plasma physics and general relativity (Blandford 1992). Pulsars act as excellent probes of physical processes as a result of the precision measurements of the spin period that are feasible with the technique of pulsar timing (Backer & Hellings 1986).

Listed are the reasons to build better instrumentation and continue searching for pulsars:

1. Pulsar observing has evolved into an increasingly sophisticated technique from its early days. However, the future of this branch of astronomy lies in a concerted observational effort into the thus far unexplored pulsar parameter space, which relies on better instrumentation and more sensitive searches. The discovery of even one pulsar spinning at sub-millisecond periods would by far be the most exciting. The fastest to-date is 1.6 ms. Past searches have not been sensitive to such rapidly spinning objects. Discovery of these would help address highly fundamental issues, such as the nuclear physics governing matter at supra-nuclear densities.

2. During the span of 27 years since their discovery, the number of ordinary pulsars has risen to more than 700. Practically all of them are observed at radio wavelengths with a peak of emission lying around 100 MHz. Statistical estimates suggest that less than a percent of the Galactic population has so far been revealed. A significant increase in the number of detected pulsars would greatly improve our view of demography of pulsars. This provides an impetus for continued pulsar searches.

3. Roughly, the faster a pulsar rotates, the more rich the physical characteristics associated with it, and the more precise is its timing. In this context, millisecond pulsars (MSPs) form a very interesting class, owing to their rich evolutionary history (Phinney & Kulkarni 1994). The expected steady state number of these objects in the Galaxy is estimated to be similar to that of the ordinary pulsars ($\sim 10^5$) with roughly $\sim$ 10,000 bright (> 10 mJy-kpc^2) sources (Lorimer 1994), but only a few dozens have so far been found. Exotic MSPs, in various evolutionary stages, such as a black-widow pulsar which evaporates its companion by impinging energetic particles and radiation on it, and a pulsar with planets, have been revealed as the body of known MSPs grows.

Pulsars emit in the radio as broadband bursts of radiation which are brightest at meter-wave and fade rapidly at higher frequency ($S_\nu \propto \nu^{-\alpha}$ where $\alpha \sim 1$ to 3). Various selection effects play a major role in restricting their observability. At low frequencies where the emission is the strongest, the Galactic background radiation limits sensitivity. Dispersion and scattering in the interstellar medium broaden the pulse and thereby limit the distance out to which pulsars can be detected, while also putting limits on the lowest detectable periods (P_m, see section 2.2). Plasma dispersion manifests itself as a frequency dependent refractive index. The group velocity v_g for an electromagnetic wave in a plasma is given as

$$v_g = c(1 - \frac{\omega_p^2}{\omega^2})^{1/2} \qquad (2.1),$$

where ω is the frequency propagation and ω_p is the plasma frequency below which propagation of rays cuts off. Pulses of radiation arrive at low frequencies later than at high frequencies over a finite observing bandwidth, resulting in smearing of the broadband pulse. Proper observations of these objects require restricted bandwidths so that the dispersion within such a band is typically not large enough to destroy the pulse structure, that is, dispersion smearing $\Delta t_{smear} \ll w$ the width of the pulse (see equation 2.2). This restriction makes viewing already faint signals even more difficult. Searches for new pulsars overcome this restriction by

recording signals from many narrow adjacent frequency bands, as in an analog filter bank. The resultant two-dimensional time series (or dynamic spectrum) can be searched off-line with the aid of large computers for pulsars of unknown period and unknown dispersion. When digital autocorrelators are used instead, autocorrelation functions are recorded at each time-step. These autocorrelations are then Fourier transformed to synthesize a dynamic power spectrum.

Pulsar observatories have two primary requirements that can be very challenging at most times. First, one needs a wide bandwidth and long integrations to obtain a good signal to noise ratio from these typically faint sources (the median flux density at 400 MHz is 15 mJy; 1 Jansky (Jy) = 10^{-23} erg cm^{-2} s^{-1} Hz^{-1}). However, besides increasing telescope usage, long integrations does not necessarily result in increased sensitivity. To appreciate this point, consider the observation of a very rapid rotation pulsar in a tight binary orbit, i.e. a MSP or a sub-MSP, where the pulse coherence is Doppler smeared during the course of a few minute observation. Second, the system needs good spectral resolution to deal with the dispersion of pulses due to propagation in the ISM.

Analog filter banks have been used in radio astronomy for spectroscopy, pulsar searching and timing. Over the last decade, digital correlators have taken the place of filter banks for spectroscopic applications. Analog filter-banks do not possess the channel-to-channel gain stability over large time-scales that is essential for sensitive spectroscopy. Secondly, correlators are cheaper to manufacture if a very large number of channels is required as in interferometry. This is because the high quality factor (large $f_c/\Delta f$ with f_c centered at intermediate frequencies) filters used in filter bank applications can be prohibitively expensive. On the other hand, filter banks have been the principle workhorses in pulsar radio astronomy for at least two good reasons. First, the demand for channel stability is not such a major issue (except in sensitive timing) where the signal is switched on time-scales of the pulse period, usually $P \sim 1 - 1000$ ms. Second, filter banks with modest numbers of channels are easy to assemble and usually do not require the five year development time-scale required of a correlator system.

2.2 – DESIGN CONSIDERATIONS

Pulsar signals are usually buried in noise contributed to by the Galactic plane and the receiver system of the telescope. Deep surveys for weak pulsars, therefore, require high-sensitivity receivers. Searches for short period pulsars (the most interesting class of very young and very old pulsars) requires high time resolution. Presently known pulsars fall in the period range of well over three decades in range from about 1.5 ms to over 5 s, and pulse duty cycles that are typically of the order of a few percent. The observed duty cycle is usually higher due to previously discussed propagation effects in the intervening medium and the limited bandwidth of the receiver. As searching constitutes obtaining an n-channel power spectrum spanning a bandwidth B at a certain sampling rate f_s, and then de-dispersing the channel timeseries to recover the original pulse train from the pulsar, an understanding of the time constants involved is necessary so that sensitivity to a pulsar of period P can be appreciated (e.g., Kulkarni 1992).

The spectrum sampling interval is $\Delta t = f_s^{-1}$. The smearing of signal within one channel due to dispersion is approximated as

$$\Delta t_{smear} = 8.3\ \mu\text{s}\ \ b\ (\text{MHz})\ \nu^{-3}\ (\text{GHz})\ DM\ (\text{cm}^{-3}\text{pc}) \tag{2.2}$$

where b is the channel width, ν is the frequency of observation and DM is the dispersion measure of the pulsar ($DM = \int n_e dl$, the electron column density along the line-of-sight). The rise time of a channel is $\Delta t_f = 1/b$ and, therefore, intensity fluctuations on time-scale $\lesssim \Delta t_f$ are suppressed by the instrument. Multi-path propagation results in an effective time constant,

$$\Delta t_{ISS} \propto \nu^{-4} DM^3 \tag{2.3}$$

where the two exponents are approximate. The effective temporal resolution of the dedispersed timeseries is

$$\Delta t_e = \sqrt{(}\Delta t^2 + \Delta t_s^2 + \Delta t_f^2 + \Delta t_{ISS}^2) \tag{2.4}.$$

A pulsar survey is sensitive to pulsars with $P \gtrsim P_m \sim \beta \Delta t_e$. Normally, $\beta = 2$ is sufficient to detect one harmonic. Due to radio frequency interference effects, it is important to detect many harmonics and, therefore, $\beta \gtrsim 8$ is a good empirical choice.

Techniques for reducing dispersion smearing are of the coherent and incoherent types. Coherent de-dispersion requires predetection deconvolution, where, the response function of the interstellar medium is deconvolved from the front-end signal to recover the electric field fluctuations as due to the pulsar (Hankins & Rickett 1986). Incoherent de-dispersion employed in all filterbanks is more suitable to blind pulsar searches in which a search for unknown pulsars in DM-space is required. The total bandwidth of observation is subdivided into a large number of narrow channels, the outputs from which are detected and then combined (usually in software) after appropriate dispersion delay corrections. An optimal choice for channel bandwidth is given by the expression

$$\Delta f \text{ (MHz)} = 1.2 \times 10^2 \tau_f \text{ (ms)} \; \nu^3 \text{ (GHz)} \; DM^{-1} \text{ (cm}^{-3}\text{pc)} \qquad (2.5)$$

where $2\pi\tau_f/P$ (ms) is the allowed phase smearing of a pulsar of period P, ν is the frequency of observation and DM is the dispersion measure of the pulsar in cm^{-3}pc.

Search observations of high time resolution (as in the case of millisecond pulsars) result in very high data rates and consume massive data storage. Considerable reduction in the effective data rate and size is possible by quantizing the data into a smaller number of bits (1 or 2) per sample. The degradation of sensitivity of 0.8 and 0.9 respectively for the two types of sampling can be overcome with longer integration times which do not offset the advantage achieved in reduced data collection rates. For instance, the FFB employs two bit sampling of the channel data. With typical sampling rates of 100 μs per channel, this results in cumulative data rates of 160-kb/s filling a mass storage 2-Gb tape in 3.5 hr.

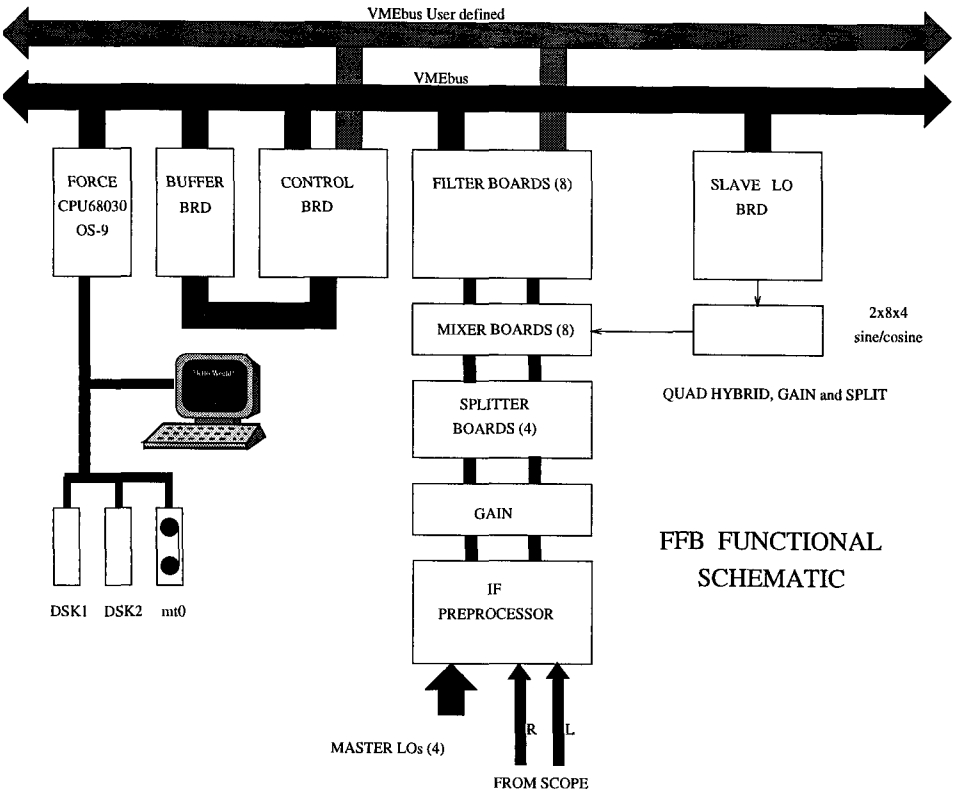

Figure 2.1: A simplified flow schematic of the FFB displaying the signal flow. Each set of boards are discussed in this chapter and hardware details are in appendix 1. Refer to section 2.3 for detailed explanation. The signal enters the FFB at the IF-preprocessor (or IF-chassis) stage and is thereafter systematically down-converted to a set of baseband signals using two local oscillator stages. The baseband signals are converted into the filterbank format in the Filter boards. Sampled data is transmitted from the Filter boards to the Buffer board via the Control board. The computer then makes data transfers from the Buffer board to mass storage media.

2.3 – FFB HARDWARE

We provide a general overview of the FFB hardware (see figure 2.1 for a simple conceptual schematic). The design philosophy adopted in this analog processor was aimed at reducing the size while retaining flexibility and simplicity of operation. A secondary goal was to achieve independence from any observatory setup. Only an IF-Preprocessor, which converts the observatory IF to a set of baseband signals, is required to be matched to the observatory's specifications. The Preprocessor has a set of appropriately tuned local oscillators (LOs). The FFB design has been made as modular as possible to facilitate quick developments in the field or for enhancing the present capability of the system. The processor lends itself nicely into functional subdivisions which are implemented on separate printed circuit boards (pcbs).

The FFB is equipped with the hardware capability to generate 32 complex spectral channels in either polarization. In principle, channel bandwidths (b) can be varied to accept a cumulative double sided signal bandwidth ($B = 32b$) ranging between 0.2-100 MHz. This flexibility in bandwidth control is achieved with a novel set of digitally programmable low-pass filters and tunable local oscillators. Since a channel coverage is $f_s \pm b/2$ (f_s being the sky frequency) mixed down to baseband, double sideband detection becomes necessary to recover full signal-to-noise ratio. This is achieved by complex down-conversion of the signal with both sine and cosine mixing with tunable local oscillators. Total power is detected in each channel and smoothed to time-scales ($\ll P$, P being the pulsar period) of interest. Thereafter, the signal is two-bit sampled, packed and recorded onto a high density storage medium which is either a hard disk or a tape drive. The parameters related to each of these functions are software controlled to suit the observing strategy. To facilitate data I/O, the sampled data is buffered into memory blocks before being written onto the recording medium (§ 2.3.2). Data acquisition and machine control is by a FORCE 68030-CPU computer running

OS9, a flexible multi-tasking real time operating system and communication with peripheral memory is via standard VMEbus (Section 2.4).

The FFB rests in a $6' \times 3'$ crate which houses the entire machine (Fig 2.4; see appendix 1 Fig A.3). The lower-most section of the crate contains the power supplies. Just above this rests the entire IF section of the machine. On top of the IF section is a custom designed VME Card Cage, with 6 6U slots and 15 9U slots (1U equals 1.75 inches). The 6U section contains the computer card, a hard drive and the data acquisition card (the buffer board). The 9U section houses the filter boards, the local oscillator card and the master control board (see description of the individual cards below). An additional hard drive and an 8-mm EXABYTE tape drive are provided via a SCSI connection with the computer. All in all, the machine dissipates about 0.5 kW of power in full operation, mainly in the VME cage. Two fan trays for continuous heat dissipation from the VME enclosure have been provided.

2.3.1 - IF Circuitry

The dual polarization front end signal is fed into the IF section of the FFB. Since the channels are constructed at baseband, 32 independent sky frequencies must be down-converted to baseband. Two stages of mixing are employed for this purpose. First, a set of four master local oscillators mix chosen sections of the IF band, each 50 MHz wide, to baseband and then a secondary set of eight slave oscillators further down-convert selected frequencies. Thus, up to 32 independent sky frequencies are mixed down to dc. The slave oscillators are tunable in extremely fine steps between 10 MHz and 32 MHz resulting in almost continuous frequency coverage of the IFs. This is necessary to complement the near continuous frequency resolution available with the channel filters. All oscillators are phase locked to the master PLL (phase locked loop) which outputs stable sinusoids at 10 and 80 MHz. The master PLL itself is locked to the observatory hydrogen maser or some other frequency standard.

The four master oscillators reside in an "IF-chassis", the interface between the telescope and the FFB and the only observatory specific module in the entire machine. If the machine is moved to new location, the IF chassis can be removed as a single unit and replaced with one that is designed specifically for IF requirements for the latter location. These LOs require an operating range that is compatible with the front end IF which is down-converted to baseband and low-pass filtered for image rejection with a 50 MHz cutoff. Each signal is now split 16 ways and disseminated into a set of eight Mixer boards along with sine and cosine outputs of slave oscillator system. Each of eight Mixer boards houses 16 mixers operable in the LO range 0.1-400 MHz with outputs in the dc-400 MHz range. They combine to generate 128 independent outputs of 32 complex and dual polarization signals that are low-pass filtered, amplified with a resident video amplifier and ac-coupled. These outputs are then fed via coaxial cables to the eight Filter boards. The smallest industry standard connectors, the SMBs, are used everywhere to prevent board dimensions from being determined by the connector dimension.

A few words about the generation of the slave oscillators. The slave oscillators are synthesized on the Local Oscillator pcb (section A.4.3). This pcb can output up to 16 independent pure tone signals with the help of 8 dual NCO STEL 1378A DDS (direct digital synthesis) mother boards, which are mounted on the pcb along-with support circuitry (section A.4.3). All LOs are generated from the 80 MHz reference signal which is phase locked to the observatory maser for phase stability. At present only four STELS are in use to generate eight slave oscillators spanning the range 12 MHz to 32 MHz. The STEL 1378A has 32 bits of frequency resolution (19 milli-Hz @ 80 MHz). Amplitude bits, generated every reference clock cycle, are fed into a fast digital to analog converter. The spectral purity of an NCO-DAC combination depends upon variables such as phase and amplitude quantization, ratio of reference clock to output frequency and the dynamic characteristics of the final DAC. STEL 1378A generates 13-bits of phase resolution and 12-bits of amplitude resolution resulting in theoretical spurious levels that are at least 75 dB down from the main signal level. All spurious sidebands as well as the reflection

spur at $80 - f$ MHz, f being the LO rate, are filtered with a sharp passive low-pass with cutoff to 32 MHz. Each of the eight slave LO signals are fed into 4 LO-Splitter boards for further massaging. Here the signal is amplified, split and quadrature phase shifted to create a sine and cosine which is routed with cables to the mixer boards for the second mixing stage.

The secondary frequency standards or local machine standards are generated in a synthesizer box producing two reference sinusoids at 80 MHz and 10 MHz (section A.3.1). As mentioned above, this is locked to the observatory maser generated 5 MHz reference signal. All frequency generation is via custom-built ultra-stable oscillators which permit highly precise and accurate clocks to be developed.

2.3.2 – The Master Control and Buffer Boards

A Master Control board (MCb) oversees the sampling of the family of Filter boards and transfers the sampled data stream to two large memory banks on the Buffer board for later rapid DMA transfer to the storage medium (section A.4.2). The system sample clock is generated on the MCb. At each rising edge of the sample clock, the filter boards are sequentially addressed in burst mode spaced within a small fraction (2 μs) of the clock cycle, τ_s (typically 100 μs). The hardware upper limit to the clock circuitry is $\tau_s \sim 0.1$ μs, but at present a much lower limit of $\tau_s \sim 25$ μs is set by sustainable data transfer rates to mass storage media. The address generation is achieved via a simple state machine that is triggered with every rising clock edge. Each addressed filter board responds by transparently latching a 2-byte sample (2-bits times 8 channels) onto user defined sections of the VMEbus. All data samples are picked up by the MCb and driven along with a data strobe to the appropriate memory (see below) on the Buffer board via a 40 pin ribbon cable. Sampling starts when an arming command is issued to the MCb circuitry by the data-taking program. When the exact startup time is an issue, as in timing applications, an external pulsed signal (such as a one pulse per second IPP) generated by the observatory maser can be used in conjunction with the arming signal as a trigger for data-taking.

Besides the sample clock, the control board also generates two other T^2L clocks which reach the filter boards via dedicated VMEbus lines and distribution circuitry. These clock the control circuitry on the switched capacitor AUDIO and smoothing filters, thereby determining their passband cutoff frequencies (see the section on the Filter boards). All three clocks are synthesized using a dedicated direct digital synthesis NCO STEL 1173A. The required frequency is translated into a 4-byte word and loaded onto an on-chip register through a parallel interface, providing 32 bits of frequency resolution. All NCOs are referenced to the FFB 10 MHz standard. For timing applications, the sample clock can by dynamically adjusted to apply a pseudo-acceleration in sampling a pulsar period to help counter-adjust for secular changes in the pulsar period. These could be due to intrinsic spin-down, Doppler modulations in a binary orbit or the orbit of the Earth.

The Buffer board is a 6U VMEboard which the FFB uses to store samples before they are finally read by the computer onto an intermediate buffer on the system hard disk. From the disk, the data is dumped to a sequential storage medium, in this case, an 8-mm tape drive. Input data to the board can be 1, 2 or 4-bytes wide. The MCb directs samples from each filter board as parallel 16 bit words into the Buffer board, along with a data strobe. The input data is automatically written to one of two large resident memories, each 256-kb large. The standard double buffering scheme is employed. When one memory is full, an VMEbus interrupt is issued to the computer and the incoming data stream is routed to the other memory bank. The memory not is use is then read by the computer asynchronously. All DMA transfers are long words, i.e., 32-bits wide, allowing for least overhead on the CPU. Sustained rates of 1.5-2.0 Mb s^{-1} have been achieved with large disk drives.

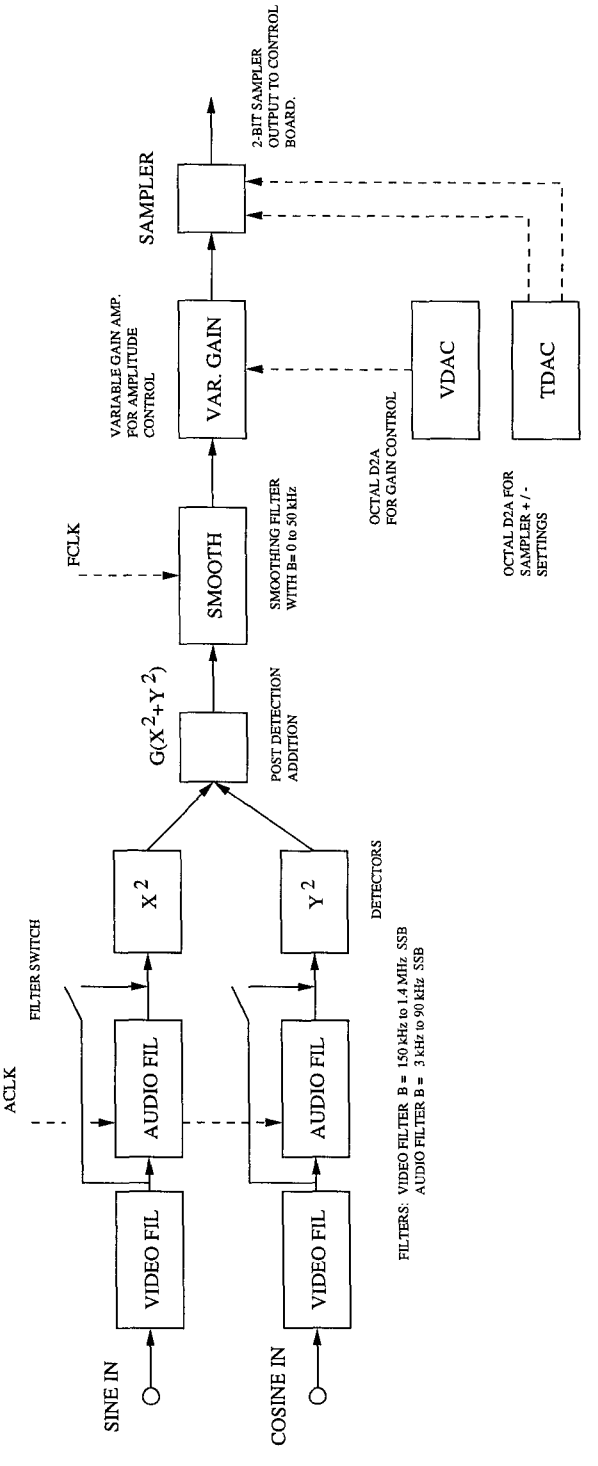

FIG. 2.2 SCHEMATIC OF A SINGLE FILTER BOARD CHANNEL

2.3.3 – The Filter Boards

A component side view of a Filter board is displayed as figure 2.5. The simple functional block diagram is shown as figure 2.2. The 32 independent complex baseband signals are fed frontally to a family of eight Filter boards. These are standard 9U VME boards occupying eight of the fifteen such available slots. The channel capacity of the machine is easily expanded by an additional six Filter boards to the VMEcage, resulting in a 56 channel machine. Each complex input signal (each defining a separate sky frequency) is filtered to the programmed 3 dB cutoff, thus defining the bank of filters. Each component of the complex signal is then linear envelope detected and the powers are then summed. The detected signal in each frequency channel is 2-bit sampled and buffered for output to the VMEbus at the arrival of the sample clock. Data in each polarization is recorded separately. Each filter board, therefore, has eight identical signal channels (4×2 polarizations) which cumulatively define the analog muscle of the board. A digital section controls manipulation of various analog subsystems and data I/O to the board. The standard VMEbus interface is used to address all resident peripheral memory and data registers whereas a special J2 VME interface using user defined pins communicates the sampled data to the Master Control board.

Channel filtering is done in either of two parallely available active filters which offer different ranges of cutoff frequencies. The appropriate filter is selected by opening or cutting off either of two analog switches controlling the signal flow path. Single sideband cutoffs of $f_{3dB} = 3 - 100$ kHz are available on the so called AUDIO filter and $f_{3dB} = 140 - 1500$ kHz are available on the VIDEO filter. The filters are dubbed in a way as to appropriately describe their range of operation. The VIDEO filter (SSI 32F8131) is a 7-pole programmable low-pass video filter with 0.15 MHz $\lesssim f_{3dB} \lesssim$ 1.5 MHz under SSB operation. The SSI 32F8131 bandwidth and boost (gain) operations are controlled by two on-chip 7-bit current DACs that are programmed via a 3-line serial interface. The boost is programmable between 0-10 dB and, as this is implemented as two zeroes on the real axis of

the complex response, with opposing signs, the flat group delay characteristics of the filter are not affected by boost programming. The AUDIO filter is a clock sweepable Cauer switched-capacitor 8-pole low pass (pno. LTC 1064-4; 14 pin DIP). An external T^2L clock (ACLK) (see section on the master control board) determines the AUDIO filter passband cutoff at f_3dB ($f_3dB = f_{ACLK}/50$). The filter response, along-with the provided compensation, has a passband ripple of ± 0.1 dB and a stopband attenuation of 80 dB at $2f_c$. Cutoff frequencies of up to 100 kHz can be achieved. Input to the AUDIO filter is always pre-filtered with the VIDEO filter in order to limit its passband. This is required to get around the annoying characteristic of switched filters of aliasing back any input around multiples of the clock frequency (ACLK) into the primary filter passband.

Linear envelope detection of the filtered complex components in each channel is done with a multiplier IC set up in squaring mode to give a response of $0.5V_{in}^2$ accurately with input bandwidths of up to 2.5 MHz. The four quadrant multiplication IC provides good operation over the range of channel bandwidths with multiplication errors of typically a percent or less. After detection, the two signals are added and smoothed to a programmable time constant using an audio filter chip. For millisecond pulsar searches, a time constant of 0.2 ms suffices. Because of the large range of channel bandwidths available, amplitude control of channel voltages before they are sampled is essential to maintain appropriate voltage levels. We provide two levels of control for this as a variable gain amplifier and variable sampler thresholds. The variable gain is provided by a multiplier sandwiched between two cascaded inverting amplifiers. The variable gain is generated by multiplying the signal with a DAC generated dc voltage. An octal DAC provides independent gain control for all channels on each board. The sampling circuitry consists of three comparators which determine the sign and magnitude bits of the voltage. The sign bit is determined by comparison of the signal to ground. The magnitude bits are determined by comparison with positive and negative thresholds which are output by independent programmable DACs. Sixteen bits per sample are generated, two per channel. The T^2L bits are routed to a

tristate buffer which is connected to user selected VMEbus lines. Every time the Filter board is addressed by the Master Control board the data is routed onto these lines and transfered to the MCb.

2.4 – THE FFB COMPUTER AND SOFTWARE

The Motorola 68030, with its 32-bit address and data paths resides on the SYS68K/CPU-30 pcb (see Fig 2.1). The FORCE SYS68K/CPU-30 based CPU board has an enhanced 68882 floating point CO-processor and 16 Mbyte of shared memory. A full 32-bit DMA controller, supporting data transfers to/from VMEbus memory as well as to/from local RAM, is provided in a 281 pin FORCE Gate Array. Mass memory control is provided through a SCSI controller and a floppy controller. Both are connected to the 32-bit DMA controller providing rapid data throughput to collected mass memory devices. Serial communication with a terminal, for example, is provided through four fully independent multi-protocol channels. A LAN controller with its own data buffer allows interconnection of the CPU board with a standard Ethernet controller mounted on the front panel of the board. Mass storage media in use include two disk drives including a 2.5 G-byte drive, an 8-mm tape drive and a floppy drive connecting the CPU board via the SCSI controller.

The host computer for the FFB system runs under the Microware OS9 operating system, with real-time and multi-tasking capability. Most of the code is written in Microware's ULTRA C and MC68030 assembly language and linked with other compiled object modules to produce one major data-taking executable file, and a host of other control and debugging software. The data-taking program performs various tasks. It sets up the initial configuration of the numerous settings on the machine which include all clock and local oscillator frequencies, channel filter widths, channel gains and sampling thresholds. It also reprogrammes the channel gains and sample thresholds in real time by collecting a few buffers worth of the 2-bit sampled data. The frequency of occurrence of the four signal levels in this

data is compared with expectations from Gaussian statistics. This procedure is iteratively repeated until the proper gains and sampling levels are achieved.

The data collection procedure first sets up the record header for the observation it is about to perform. The header data structure, placed in the beginning of each data record, contains mainly important bits of information about the observation such as time, observed coordinates, FFB setup and the record number. Each data record is equivalent to the memory capacity of the Buffer board. Once the record header is set up, two temporary disk files are created to act as buffers for the incoming data blocks from the Buffer board before these are written onto tape drive. The data-taking program forks the Tape I/O program into the background. This program performs actual writes to takes, allowing the main program to proceed with data collection. After initializations are complete, the control board is armed and set into sampling mode and the buffer board is reset and then waits for interrupts generated by the buffer board. Each time a Buffer board interrupt is intercepted, the interrupt servicing routine reads the appropriate Buffer board memory and appends the data to the temporary disk file. When the temp disk file is full, a signal is sent to the Tape I/O program instructing it to write that file to tape. This process continues, toggling between temp files, until the end-of-data command is issued. Data taking stops and the last of the data is written to tape. Automatic observing is possible by launching a command file that contains all observing details that the program is to follow. A location dependent communication socket to the telescope control computer is required.

2.5 – APPLICATIONS AND SUMMARY

The Flexible Filter Bank system is duplicable for a total cost of about $100 K in materials, is transported with relative ease and is usable with a wide variety of telescope hardware. A partial version of the machine was first tested in June 1993 with the Owens Valley Radio Observatory 40-m telescope. A complete version of the machine is now installed at Westerbork Synthesis Array (WSRT), where in mid

1995 it has started observing pulsars on a regular basis as a standard observatory backend. One of the principle projects to be undertaken with the FFB at WSRT (FFB-I) would be to observe a complete flux limited sample of steep spectrum point sources that would emerge from the data analyses of the Westerbork Northern Sky Survey (WENSS). Other important projects will include searches for globular cluster millisecond pulsars, pulsar timing and polarization studies (section A.1).

A second filter bank (FFB-II) will be used as part of an enhanced system for recording direct baseband signal (or electric field) with the processor acting as an intermediate between the telescope and a set of fast ADC cards (Fig 2.3). Predetected signal from each FFB-II channel is made available to a fast programmable ADC. All 32 digitized channel data streams are then bit-packed and written to fast tape drives, such as the soon to be commercially available Mammoth Exabyte drives, which when used in parallel can be written to at data-rates of up to 8 Mb/s (Fig 2.3).

Searches for millisecond pulsars are best performed at meter wavelengths where the environments of most observatories suffer from man-made interference. Often this interference (RFI) manifests itself as narrow band spikes in the observing band. The FFB can be used adaptively to tune in and out of zones of the observing band that are plagued by transient interference (on timescales of minutes). This is achieved by monitoring the power in each channel at optimally chosen and regular intervals in time. Channels in which interference is detected can be switched to another sky-frequency by simply reprogramming the settable slave oscillators, thus quickly moving a loaded channel to a relatively quiet part of the band.

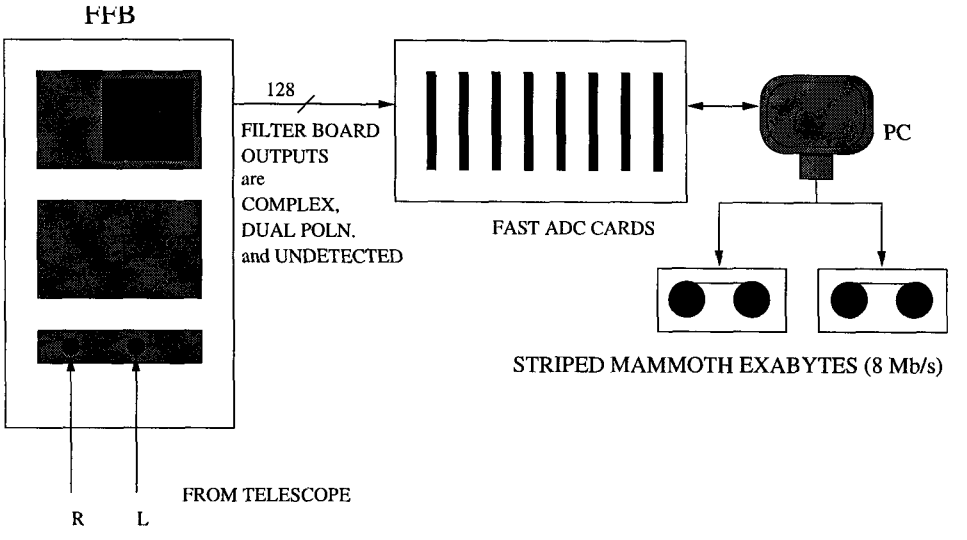

Figure 2.3: A possible Direct Baseband Recorder. The telescope IF is fed into the FFB where selected sky-frequencies are converted to a filter-bank format and channels are realized at baseband. The 128 baseband outputs are available to the analog to digital converter cards which hold one fast 8-bit ADC for every FFB channel. The undetected 8-bit digitized data stream is written to fast tape drives. A PC controls all ADC and tape drive operations.

2.6 – INITIATION OF OB-CLUSTER SEARCHES

Both neutron stars and black holes are formed from massive stars. There is general consensus that the threshold in the stellar mass spectrum for formation of NS is $M_i > 8M_\odot$ (Bhattacharya & van den Heuvel 1992). A similar number for black holes is not well known and the figure ranges between 25 to 50 $M_\odot$ (Kulkarni et al. 1993). OB-associations are the stellar factories of compact objects because most of the presumed and shortlived progenitor stars are born here. However, no pulsars have yet been clearly associated with OB-associations. The payoffs for targeted searches towards OB clusters, which have never been done before are

potentially high (Blaauw 1986). It could result in the discovery of a rich variety of pulsars, especially young pulsars associated with supernova remnants. The pulsar-MS star systems which have been mentioned in chapter 5 should also be concentrated towards such star clusters. Finally, black hole/pulsar systems should be concentrated towards clusters (Narayan et al. 1991). Since black holes form out of MS stars with extremely short lifetimes a psr-bh system, a holy grail of pulsar astronomy, should also lie in such regions. At the very least, a lower threshold to the mass limit for black hole formation could be determined.

We have initiated a search for young pulsars in the nearby rich Galactic OB-clusters with the WSRT. The strategy is simple and is performed in two steps: (i) The first part consists of making mosaicked wide field images of OB associations with the array P-band receiver system (340 MHz) which has 40 MHz of imagable bandwith in which eight sub-bands of 5 MHz each are tunable over a range of 80 MHz to avoid zones of intereference (Reference: The WSRT User Documentation). All observations are performed at night so that interference levels are at a minimum. Large scale radio emissions maps of the vicinity of the rich associations consisting of emission from the Galaxy, bright supernova remnants and H-II regions are synthesised. The background noise in these maps is usually source confusion limited in the Galactic plane and is near thermal off the plane. (ii) The maps will be subject to a point source search. Point sources with steep spectral indices and high polarization content would be the best targets for further follow-up with a pulsed search using the FFB-I.

An interferometric map of size 10 deg. $\times$ 15 deg. of the Cygnus OB-associations was made with the WSRT during November 1994 (Fig 2.6). The limiting noise in the map is approximately 3 mJy in the plane and somewhat better at higher latitudes making us sensitive to point sources $\sim$ 20 mJy in strength. Numerous point sources are visible in the final map (Fig 2.6) and others will be discovered in a software point-source search. Observations of six Perseus OB-clusters have been completed in November 1995.

ACKNOWLEDGEMENTS

We thank D. C. Backer and D. Wertheimer for discussions during the initial phase of the project. We are indebted to the staff at Owens Valley Radio Observatory for all help during the initial testing of the FFB there, and especially to H. Harteback and R. Keeney. We thank J. S. Sandhu for his NCO simulations and A. Hubbard for important tech work. Finally, we would like to thank the staff at NFRA, especially L. Voûte, W. T. S. Deich and A. Boonstra for their very important debugging and modifications to the machine to make it a much better working instrument.

REFERENCES

Backer, D. C. & Hellings, R. W. 1986, ARAA, 26, 574

Bhattacharya, D. & van den Heuvel, E. P. J. 203 Phys Rep , 1

Blaauw, A. in "Birth and Evolution of Massive Stars and Stellar Groups", Eds. W. Boland and H. van Woerden, Reidel Publishing Company, 211 (1986)

Blandford, R. D. 1992, Phil. Trans. R. Soc. Lond. A., 341, 177

Hankins, T. H. & Rickett, B. J. 1986, ApJ, 311, 684

Kolkman, O. F. 1993, The Westerbork Synthesis Radio Telescope User Documentation: Version 1.0.0

Kulkarni, S. R. 1992, Phil. Trans. R. Soc. Lond. A., 341, 77

Kulkarni, S. R., Hut P. & McMillan, S. 1993, Nature, 364, 421

Lorimer, D. R. 1994, MNRAS, 274, 300

Manchester, R. N. & Taylor, J. H. 1977, in Pulsars, W. H. Freeman and Co.

Narayan, R., Piran, T. & Shemi, A. 1991, ApJ, 379, L17

Phinney, E. S. & Kulkarni, S. R. 1994, ARAA, 32, 591

Ray, P. S. & Kornreich, D. 1993, "The FFB Software Manual", Version 1.2

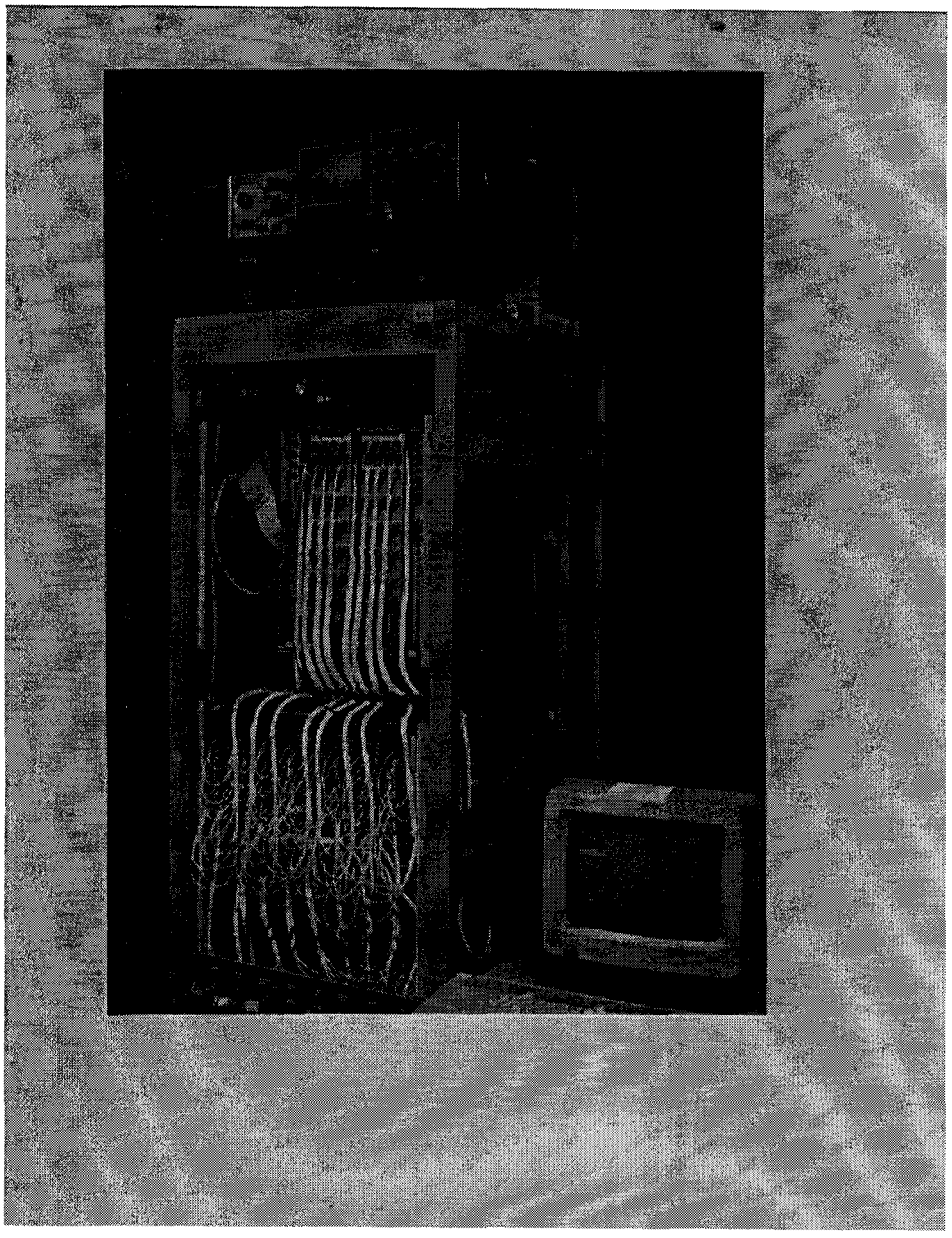

Figure 2.4: The Flexible Filter Bank (FFB) at Westerbork Observatory. The FFB has been part of the standard observatory instruments at WSRT since August 1995.

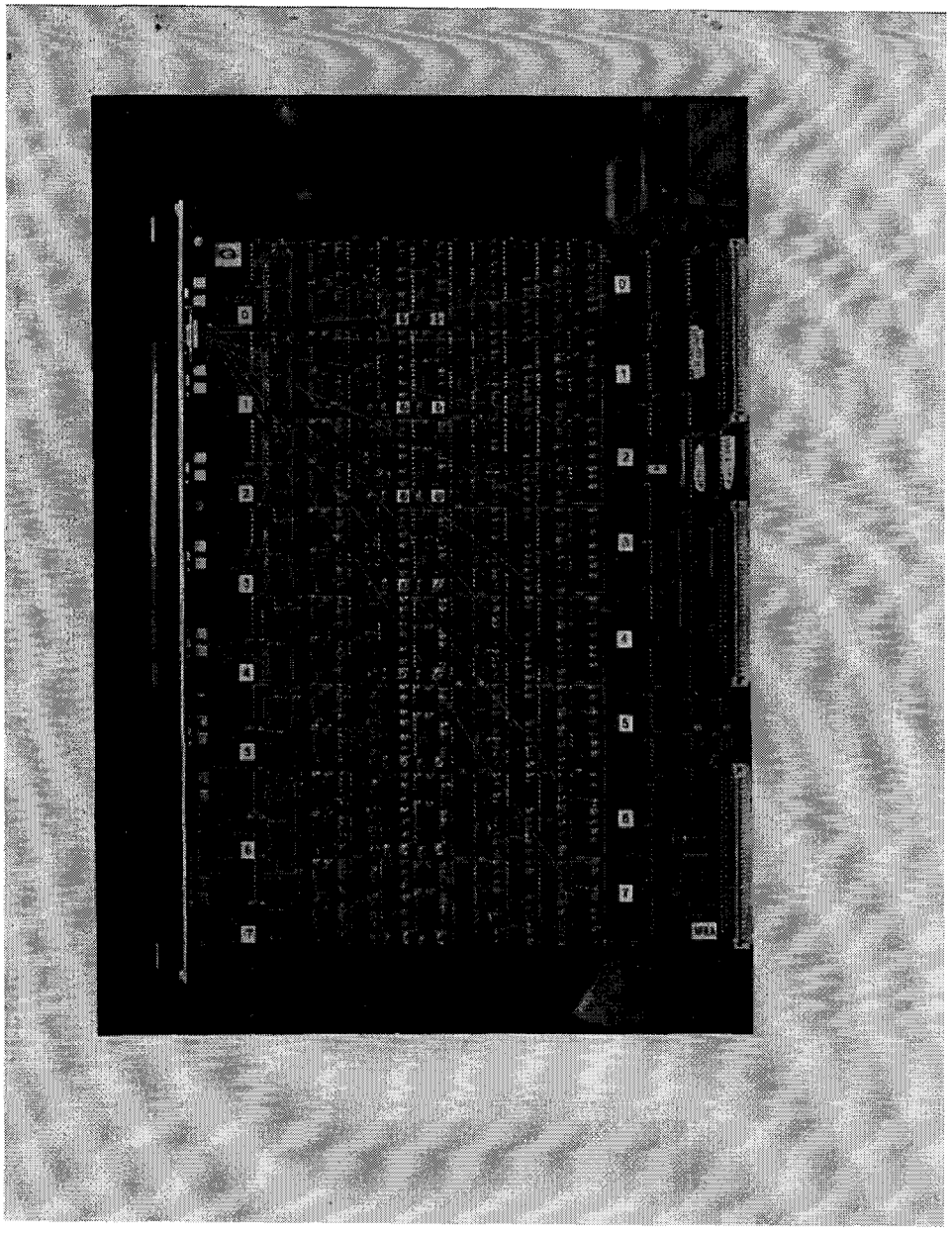

Figure 2.5: A component side view of a FFB filter board which is composed of eight separate complex filter channels.

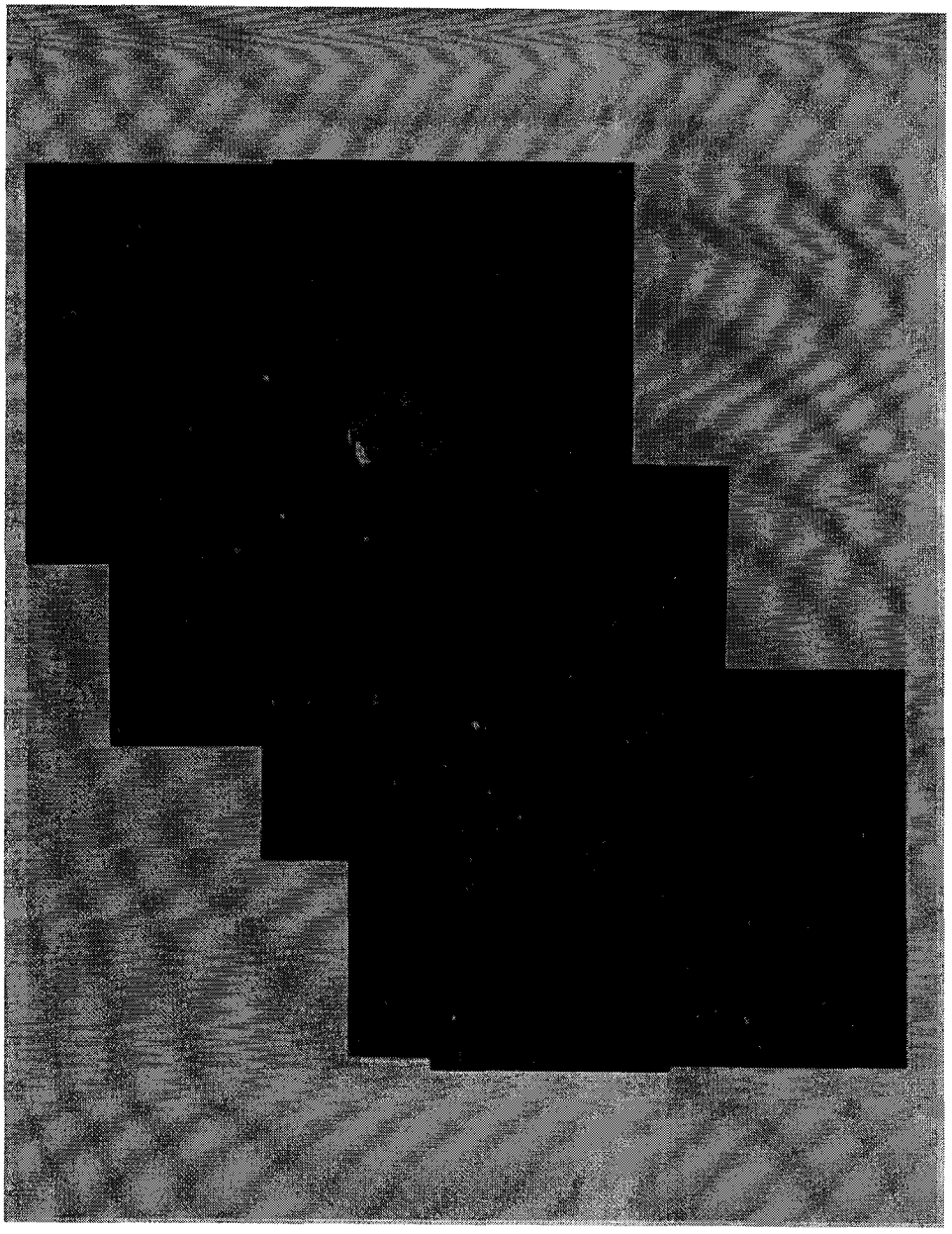

Figure 2.6: A WSRT P-band mosaicked image (200 sq. degree) of the Cygnus-X star forming region made as part of a project of search for young pulsars.

CHAPTER 3: SOFT GAMMA RAY REPEATERS AS HIGHLY MAGNETIZED NEUTRON STARS

3.1 INTRODUCTION

3.1.1 – GENERAL CHARACTER OF SOFT REPEATERS

The soft gamma repeaters (SGRs) are a set of rare high energy transients with three known members (Norris et al. 1991). They are widely believed to be neutron stars (NS) based on the possible coincidence of all three repeaters with young ($t \sim 10^4$ yr) supernova remnants (Cline et al. 1982, Kulkarni et al. 1994a, Murakami et al. 1994, Vasisht et al. 1994), as well as by the detection of persistent X-ray emission from at least two sources, SGRs 0526−66 and 1806−20 (Rothschild et al. 1993, Rothschild, Kulkarni and Lingenfelter 1994, Murakami et al. 1994, Sonobe et al. 1995) and the detection of a ROSAT all sky survey X-ray source within the recently revised error box of the third repeater, SGR 1900+14 (Vasisht et al. 1994, Hurley et al. 1994, Vrba et al. 1995).

The well known γ-ray superburst of March 5, 1979, is ascribed to the source SGR 0526−66 and came from the direction of the supernova remnant N49 in the Large Magellanic Cloud. This burst lasted a thousand times longer than the typical SGR burst, had a time profile consisting of a hard ($\sim$ 0.5 MeV) peak followed by an exponentially decaying soft-tail ($\sim$ 30 keV) and released 10^4 times more energy than the 16 other recorded repeat events from this source, or the hundred odd events recorded over the past two decades from the other two SGRs, 1806−20 and

1900+14. The March 5 event, as has become apparent, constitutes a more powerful and much more rare class of bursts from such sources. No events displaying such energetics have been observed from known or previously undiscovered SGRs (Kouveliotou 1996, Hurley et al. 1994b, Kouveliotou et al. 1994). Therefore, any theoretical model for SGRs must try to account for the vast differences displayed in the March 5 event and other seemingly standard bursts from SGRs, and the rarity and energetics of events of the superburst type (Thompson & Duncan 1995 and references therein).

3.1.1.1 – Comparison with other Transients

SGR bursts are much more luminous than the common X-ray bursts of Types I and II ($L \sim 10^3 - 10^4\ L_{Edd}$ for a 1.4 $M_\odot$ NS as compared to $L \sim L_{Edd}$) and have much harder spectra (a black body temperature of ~ 30 keV for the bursts of SGR 1806−20). In addition SGR bursts display weak spectral evolution during single events (Kouveliotou et al. 1987; Golenetskii et al. 1987), but bursts of widely differing fluences from the same SGR have remarkably similar spectra (Fenimore et al. 1994). For example, the similarity between the soft tail of the March 5 event and the ensuing short soft bursts is impressive given that factor of $\sim 10^4$ difference in the total burst luminosities. Unlike the Type I and II X-ray bursts, SGR bursts show no correlation between the burst energy and the time until the next burst (Laros et al. 1987).

X-ray bursters exhibit transient activity falling into two categories: (i) The Type-I bursts invoking thermonuclear flashes in the surface layer of an accreting neutron star, and (ii) Type II bursts as shown by the Rapid Burster believed to involve instabilities in the accretion flow (Lewin et al. 1992, Kouveliotou et al. 1996). The absence of X-ray pulsations and eclipses from the bursting sources casts some doubt on the identification of bursters as accreting neutron stars. Pulsations are expected from such objects provided that they possess magnetic fields strong enough to funnel the accretion flow and misaligned with the rotation axis, as in the case of the binary X-ray pulsars that are associated with the population I objects.

It is therefore thought that the bursters are older neutron stars whose magnetic fields have either decayed away or have aligned themselves with the rotation axis. It is also possible that the channeling of gas by the strong magnetic fields in the young neutron stars suppresses the thermonuclear flash phenomenon. This would explain why binary X-ray pulsars are not bursters.

In contrast, the physical mechanism responsible for soft γ-ray repeaters are very likely different from that of the other X-ray transients. SGR youth as inferred from SNR associations, their possibly large inferred velocities ($\sim 10^3$ km s^{-1}) and clear differences in bursting properties compared to accretion powered sources, cumulatively suggest that SGR bursts are triggered not by accretion, but by some other mechanism.

The key to understanding SGR sources is to address their remarkable luminosities. In order to create a hyper-Eddington burst some strong confinement mechanism for the radiating plasma is required. An optically thick radiating plasma around a neutron star will be driven as a strong wind due to photon pressure so that the emergent radiation is maintained near Eddington rates and showing strong spectral evolution. Thompson and Duncan (1995; TD95 hereafter), theorize that strong magnetic fields can provide the necessary confinement. The weakening of the Thompson cross-section in high magnetic fields allows much more luminous outbursts. The plasma confinement schemes are therefore in accord with the relatively weak spectral evolution of the bursts.

Other, more direct evidence that SGR bursts are internally generated comes from the March 5 burst (Thompson & Duncan 1995). The hard initial transient phase of this burst contained an energy $\sim 1 \times 10^{44}$ erg (assuming that it radiated isotropically) and had a harder spectrum than the remainder of the burst (Fenimore et al. 1981). The mechanism that triggered this event must have released the large amount of energy outside of the neutron star in a plasma consisting almost entirely of photons and e^+e^- pairs. Any small contamination by ions and electrons would provide a large enough scattering depth to soften the observed

photon spectrum (via adiabatic work done on the baryons) to energies well below the electron rest mass (the temperature of the hard front). Thus, accretion seems not to be the driving mechanism for powering the March 5 event, and one is limited to an energy source intrinsic to the star. A magnetic field is the cleanest plausible source for such a plasma, i.e., one which is not contaminated by baryonic matter. We discuss such a model later (the "magnetar" model) in section 3.1.4.

3.1.2 – CONTENTS OF THIS CHAPTER

Three separate studies of soft γ-ray repeaters are included in this dissertation in sections 3.2, 3.3 and 3.4. They are as follows:

1. In section 3.2 we describe a detailed search for the counterpart of SGR 1900+14, the SGR about which least is known. Motivated by the association of the other two repeaters with young supernova remnants, we have carried out radio, optical and X-ray studies of two cataloged SNRs in the large Konus error box ($11^\circ \times 8'$) of SGR 1900+14. Two SNR were found to intersect the elongated error box for which sensitive VLA images were made. At that time Hurley et al. (1994) reported a new, very small error box close to G 42.8+0.6. There is no radio feature within, or close to, the error box. However, a ROSAT source is found just outside this localization. We speculate that this is the quiescent X-ray counterpart of SGR 1900+14. We suggest that SGR 1900+14 is a neutron star that was born with high speed which has now overtaken the expanding shell of SNR G 42.8+0.6. Owing to the low confining pressure, there has been no development of a synchrotron bubble which explains the absence of the radio plerion. In our picture, SGR 1900+14 is the oldest known SGR.

2. Section 3.3 describes a detailed VLA monitoring experiment for variations of core flux in G 10.0−0.3, the nebula surrounding SGR 1806−20, during its three month long reactivation in late 1993. This was the first observed reactivation of this SGR after almost a decade. Ten epochs of VLA observations were accumulated during this time and tested for flux changes. The "core" flux was observed to remain constant to a level of a few milli-Jansky, consistent with no change at all. Also reported is the first high angular resolution observation at 3.6-cm of the core region (epoch 1). This resulted in the first ever sub-arcsecond localization of a γ-ray transient and the subsequent discovery of a remarkable infra-red star at this position (Kulkarni et al. 1995). Also discovered was a core-jet appearance of the SGR at an arcsecond scale.

We suggest that the jet is due to an outflow of plasma from the central source (the seat of the SGR) and is possibly related to single bursts. Powering the large scale structure of G 10.0−0.3 by SGR outbursts is also considered (Fig 3.4).

3. Section 3.4 discusses the second epoch of high angular resolution VLA observations conducted a year after the first epoch. Surprisingly, there is an angular displacement of the jet-like extension (Figs 3.5, 3.6 & 3.8) by almost 45°. We argue that the new feature is physically unrelated to the one seen in the data of the first epoch (Fig 3.6). It is most likely a new extension possibly created simultaneously with an unobserved γ-ray burst. We argue that the SGR is a slowly rotating neutron star on the grounds that these observed features are not rotationally smeared. Energetics in the radiating plasma are discussed. These observations are compared to, and lend support to, the magnetar model of TD95. Another nine epochs of data has been accumulated and reduced after the report of another BATSE burst on 30th September 1995. These data were collected in B-array and displayed in figure 3.11. Lacking the resolution of the A-array we are unable to make definitive statements about structural changes, however, "bubbling" in the radio maps is undoubtedly seen.

3.1.3 – CRITICISMS FOR AN ACCRETION BASED MODEL

Accretion of matter onto a compact object is always a viable and efficient source of energy conversion, necessary in an SGR model. However, accretion scenarios have a hard time explaining the observed properties of SGRs, especially the superburst of March 5, 1979. There is indeed supporting evidence for accretion, especially since the discovery of a remarkable infrared counterpart to SGR 1806−20 (Kulkarni et al. 1995, van Kerkwijk et al. 1995). Only a vanishing probability exists of chance positional coincidence of two such rare classes of objects, i.e., SGRs and luminous blue variable (LBV) type stars. Let us say that the IR-star is

a companion the compact star which is the soft γ-ray repeater. So far the evidence for accretion is meager. I list below the arguments that are both for and against accretion based scenarios.

For accretion:

1. Discovery of a LBV type star at the position of SGR 1806−20 (Kulkarni et al. 1995; van Kerkwijk et al. 1995) is the strongest argument for accretion power. Estimated extinction to the star, $A_v \sim 30$ mag., is quite similar to that inferred from the hydrogen column density, $N_H = 6 \times 10^{22}$ cm^{-2}, to the persistent X-ray counterpart to the SGR (Murakami et al. 1994), putting both objects at similar distances. If the SGR and the optical star are associated (say companions in a binary system), then with the revised distance to the SGR of ~ 15 kpc (Corbel et al. 1996; placing the source on the far side of the Galactic center), the star would be among the few brightest in the Galaxy.

2. The quiescent X-ray emission in SGR 0526−66 of $L_X \sim 7 \times 10^{35}$ erg s^{-1} (Rothschild et al. 1994) implies an accretion rate $\dot{M} \sim 10^{-10}\ M_\odot$ yr^{-1}. This implies an equilibrium spin period for the neutron star of

$$P_{eq} = 8 \text{ s}\left(\frac{B_{dipole}}{1 \times 10^{12} \text{ G}}\right)^{6/7}\left(\frac{\dot{M}}{1.4 \times 10^{-2}\dot{M}_{Edd}}\right)^{-3/7}$$

which for a $B = 10^{12}$ G neutron star, is the period of the observed modulation during the decay of the March 5 event from SGR 0526−66. Here, $\dot{M}$ is the accretion rate and $\dot{M}_{Edd} \sim 2 \times 10^{-8}\ M_\odot$ yr^{-1} is the Eddington accretion rate.

Against accretion:

1. Neither SGR 0526−66 nor SGR 1900+14 have ultra-luminous stars as companions. In fact, deep searches for an optical counterpart to SGR 0526−66 have established a firm optical limit of $m_v \gtrsim 23$ (Fishman et al. 1981), which at the distance of the LMC corresponds to a dwarf fainter than the Sun. In case accretion does actually power SGR 0526−66, the neutron star would

have to be quite ordinary in its magnetic field strength. On the other hand, it would be extraordinary in that it is actively accreting while still residing in a young SNR, a short time for accretion to develop into an energy liberating device.

2. The inferred velocities of SGRs from their displacement from the centers of the host SNR imply large space motions, $v \sim 10^3$ km s^{-1}. Even the tightest of binaries would be disrupted with such large space motions.

3. The quiescent X-ray luminosity, $L_X \sim 3 \times 10^{35} d_{15}^2$ in SGR 1806−20, is low. This is suggestive of accretion from a wind rather than Roche lobe overflow. It is hard to imagine how accretion of a steady wind could power the sharp super-Eddington bursts displayed by this source. More importantly, the required mass accretion rate of $\dot{M} \sim 10^{-11}$ M$_\odot$ yr^{-1} that is required to power the observed X-rays is two orders of magnitude too small in comparison to for the outward flow of energy from the central source (see Section 3.4.3.3; the outward flow of energy is $\gtrsim 10^{37}$ erg s^{-1}). Furthermore, any accretion flow would be easily halted by the outward pressure of the particles required to power the nebula, unless ad-hoc geometries are considered.

4. The constancy of the X-ray and radio fluxes from SGR 1806−20 during the 1993 phase of bursting for SGR 1806−20 argue against accretion. Binaries known to be accreting show large flaring in radio and stochastic flickering of X-ray fluxes during episodic accretion events (Vasisht et al. 1995; Sonobe et al. 1995).

5. Accretion models cannot sidestep the problem of baryon contamination. The hard initial transient of the March 5 burst could not arise directly from the hot accreted material, since the baryon density in the material would be high enough to cause adiabatic dilution of photons in the expanding fireball to energies well below the hard X-ray and γ-ray range.

6. Sudden accretion scenarios have great trouble accounting for the $\sim 3 \times 10^{24}$ g (which is 0.1 M_{moon} and also equal to the entire mass of the asteroid belt)

of material required to account for the luminosity of the March 5 event. A detailed criticism is given in TD95.

3.1.4 – THE MAGNETAR MODEL

Confinement of the plasma that radiated the soft tail of the March 5 event requires a large surface dipolar field. Direct comparison of the magnetic pressure with the overpressure generated by the energy in the soft-tail of the burst requires a magnetic field B satisfying the condition of equivalence of magnetic pressure in the near magnetosphere to the pressure in the radiating plasma

$$\frac{B^2(R_{NS}+\delta R)}{8\pi} \gtrsim \frac{E_{tail}}{3\ \delta R^3}$$

where δR is the outer radius of the field loops, E_{tail} is the energy in the tail of the event $\sim 4\times10^{44}$ erg and R_{NS} is the stellar radius. For a dipole field geometry $B(R) = B_{NS}(R/R_{NS})^{-3}$, which is an approximation for $\delta R \gtrsim R_{NS}$, a polar field strength of

$$B_{NS} > 4\times10^{14}\ \mathrm{G}\ (\frac{\delta R}{10\ \mathrm{km}})^{-3/2}$$

is implied (Thompson & Duncan 1995). Even though this is a rough estimate of the field strength of such a neutron star, the important conclusion is that in order to hold in the energy radiated in the tail of the March 5th event, the surface magnetic field strength of the SGR neutron star must exceed that of a typical radio pulsar by a factor $\gtrsim 10^{2-3}$. Such an object is termed a "magnetar" (Thompson & Duncan 1992).

Once the neutron star magnetic field is estimated from considerations of plasma confinement, the magnetar hypothesis lends itself to self-consistent explanations for other SGR properties (Thompson & Duncan 1993 and 1995). Like a radio pulsar, a magnetar spins down by the usual mechanism of a magnetized, relativistic wind, albeit in a very short time. As a result, rotation plays little role in this model of the SGRs. The essential physical difference between pulsars ($B_{NS} \sim 10^{12} - 10^{13}$ G) and magnetars ($B_{NS} \sim 10^{14} - 10^{15}$ G) is that in the

latter, due to large spin-down torques, the (external) magnetic energy begins to dominate the rotational energy at a very early age. The following observations of SGRs are explained with large surface field neutron stars:

1. A dipole field $B_{NS} \sim 6 \times 10^{14}$ G is required to spin down an isolated neutron star to the observed period of 8.0 seconds with the $\sim 10^4$ yr age of the surrounding supernova remnant N49. There is also weak evidence that SGR 1806−20 is a 2.8 s rotator (Ulmer et al. 1993). In section 3.4, we show additional evidence for slow rotation. In short, the magnetic breaking torques on the neutron star are large enough so that all the spin-down energy is radiated away in a very short time. In contrast, all radio pulsars of equivalent ages spin rapidly at ~ 100 ms periods.

2. If the March 5 event was powered by a decaying magnetic field, then its total energy, $E_{tot} \sim 5 \times 10^{44}$ ergs, must be no more than a fraction of the available magnetic free energy. Approximating the external field as a dipole with polar strength B_{NS}, this suggests $\frac{1}{6} B_{NS}^2 R_{NS}^3 >> E_{tot}$, or equivalently, $B_{NS} >> 10^{14}$ G. Typical bursts, however, have energies $\sim 10^{41}$ ergs. In this model, they result from the cracking of the neutron star crust by enormous and growing stresses due to the embedded B-field. This action requires that

$$B_{crust} \sim 10^{15} \left(\frac{E_{SGR}}{10^{41} \text{ erg}}\right)^{-1/2} \left(\frac{l}{1 \text{ km}}\right) \left(\frac{\theta_{max}}{10^{-3}}\right) \quad \text{G}$$

   (Thompson & Duncan 1995) where l is the length of the fracture and $\theta_{max} \sim 10^{-3}$ is the limiting strain angle.

3. SGR sources are associated with young ($t \sim 10^4$ yr) neutron stars. The decaying magnetic field must be capable of triggering SGR activity on this time-scale. Diffusion of magnetic field lines through the crust by Hall drift, and through the core by ambipolar diffusion (Goldreich and Reisenegger 1992), both occur on this time-scale if $B \gtrsim 3 \times 10^{15} G$ where $t_{Hall} = 5 \times 10^8 B_{12}^{-1}$ yr and $t_{diff} \sim 3 \times 10^9 B_{12}^{-2}$ yr.

4. A very strong magnetic field suppresses the electron scattering cross section of one polarization state, by a factor $\sigma_{es}/\sigma_T \sim 4\times10^{-4}(\omega/\ 10\ \mathrm{keV})^2(B/B_{cr})^{-2}$. The flux density $B_{cr} = m_e^2c^3/e\hbar \sim 4\times10^{13}$ G is where the electron cyclotron energy becomes comparable to the electron rest mass. With increased magnetic field strengths, it becomes harder for electrons and positrons to oscillate perpendicular to the direction of the local magnetic field under the influence of the scattered photon, resulting in the reduced electron scattering opacity. The consequent decrease in the scattering opacity allows a much higher radiative flux to escape from a magnetically confined photon-pair plasma. This can lead to photon luminosities much higher than the standard Eddington values, $L_{SGR} \sim 10^4 L_{Edd}$, as observed in SGRs, but only if these neutron stars have surface magnetic fields $B_* > 3\times10^{14}$ G (Paczynski 1992; TD95).

5. Persistent X-ray emission from SGR 0526−66 has been detected by both Einstein (Rothschild et al. 1993) and ROSAT (Rothschild et al. 1994). This persistent emission could be powered by continuous decay of crustal magnetic field. The minimum magnetic energy in the crust required to power this $L_X \sim 7\times10^{35}$ erg s^{-1} of X-ray emission is

$$(B_{crust}^2/8\pi)4\pi R_{NS}^2\Delta R_{cr} \gtrsim L_X t_{SGR},$$

where ΔR_{cr} now is the depth of the crust ~ 1 km. and $t_{SGR} \sim 0.5\times10^4$ yr is the age of the neutron star (inferred from SNR N49; Vancura et al. 1992). This implies that $B_{crust} \gtrsim 1\times10^{15}$ G.

6. The initial hard spike of the March 5 event had a duration of about 0.15 s (Mazets et al. 1979; Cline et al. 1982). This is comparable to the crossing time of an Alfv́en wave inside the star (or, equivalently, the growth time of an internal hydromagnetic instability) if

$$B \sim 7\times10^{14}\left(\frac{\rho}{10^{15}\ \mathrm{g\ cm^{-3}}}\right)^{1/2}\left(\frac{l}{10\ \mathrm{km}}\right)\ \mathrm{G}.$$

3.1.4.1 – Formation of Magnetars and High Velocities

How is a magnetar formed? A hot newborn neutron star can undergo vigorous convection with an overturn time of $\sim$ 1 ms (Burrows and Lattimer 1988; Duncan and Thompson 1992). This happens as soon as the energy outflow settles down to a quasi-steady state in the outermost layers of the proto neutron star. As a result of this, a very strong magnetic field is generated by efficient dynamo action if the initial spin is in the millisecond range. Since the dynamo rapidly cuts off at longer birth periods, this mechanism can operate only in a very narrow range of initial conditions. Thus a bimodal distribution of magnetic fields is expected in this scenario and neutron stars born with such high fields could be very rare since the core needs to be spinning very rapidly.

There exist strong selection effects against observing strong B_{dipole} neutron stars as radio pulsars, both because they spin-down rapidly and because their birth rate is low. By the same token, only those neutron stars with the strongest magnetic fields are detectable as sources of SGR bursts, since otherwise the diffusing field cannot generate sufficient stresses to crack the neutron star crust (which is the favorable mechanism for triggering SGR bursts), and since the bursts emitted by neutron stars with dipole fields of intermediate strengths generate sub-luminous bursts (Thompson & Duncan 1995). A millisecond spin period is the natural outcome of accretion induced collapse of a white dwarf (Narayan and Popham 1989).

Although the strongest white dwarf magnetic fields, $B \sim 5 \times 10^8$ G (Schmidt 1988), correspond to a neutron star magnetic field of order 10^{14} G upon compression to nuclear matter density, stronger magnetic fields can be generated in a rapidly rotating, newborn neutron star. The ratio of the convective kinetic energy to the gravitational binding energy is larger during the short phase of diffusive neutrino cooling than during any previous convective phases that are driven by nuclear burning. As a result the magnetic field generated by dynamo action in a newborn neutron star will be higher in strength than any inherited field from previous phases of stellar evolution.

There is some evidence that SGRs are high-velocity neutron stars. The identification of SGR 0526−66 with a quiescent X-ray source (Rothschild et al. 1993; Rothschild et al. 1994) has revealed that the star is displaced 25″ from the SNR center. The age of the SNR is $t \sim 5.1 \times 10^3 (E_{51}/n)^{-1/2}$ yr, where $n \sim 0.9$ cm^{-2} is the ambient hydrogen density inferred from shocked X-ray emission and E_{51} is the energy of the explosion in units of 10^{51} erg (Vancura et al. 1992). The transverse velocity therefore is $V = 1200 \pm 300$ km s^{-1}. The position of SGR 1806−20 in the SNR G10.0−0.3 also suggests a high transverse velocity, $V \gtrsim 500$ km s^{-1}, although in this case the uncertainty is larger because of the more irregular shape of the SNR. Finally, there is some tentative evidence that SGR 1900+14 has $V \gtrsim 10^3$ km s^{-1}, based on the displacement of the SGR error box (Hurley et al. 1994) from the center of the SNR G 42.8+0.6 (Vasisht et al. 1994). If this SNR is truly the birth place of SGR 1900+14, then the SGR acquired sufficient recoil velocity to escape from the remnant.

Large proper motions are not so uncommon in the isolated radio pulsars: from recent interferometric measurements, 10% of the neutron stars had $V > 800$ km s^{-1} (Lyne & Lorimer 1994). Although none of the pulsars with high proper motion seem to have particularly strong magnetic fields, the inferred proper motion of SGR 0526−66 is at the high end tail of the pulsar velocity distribution. A significant fraction of the proper motion of SGR 0526−66 may well be be a byproduct of the mechanism that generated the strong magnetic field. For example, a strong field in a newborn neutron star can suppress convection and impart an anisotropy to the escaping neutrino radiation. This mechanism clearly predicts a positive correlation between B_{dipole} and V, but it should be emphasized that the required strong field may sometimes be internal to the star.

After outlining SGR properties and theoretical models, we describe three observational projects in the following sections of this chapter.

REFERENCES

Burrows, A., & Lattimer, J. M., 1988, Phys. Rep., 163, 51

Cline, T. L. et al. 1982, ApJ, 255, L45

Corbel, S. et al. 1996, preprint

Duncan, R. C. & Thompson, C. 1992, ApJ, 392, L9

Fenimore, E. E. et al. 1981, Nature, 289, 42

Fenimore, E. E., Laros, J. G. & Ulmer, A. 1994, ApJ, 432, 742

Fishman, G. J., Duthie, J. G. & Dufour, R. J. 1981, Ap. Sp. Sci., 75, 135

Goldreich, P. & Reisenegger, A. 1992, ApJ, 395, 250

Golenetskii, S. V. et al., 1988, Sov. Astron. Lett., 13, 166

Hurley, K. et al. 1994, ApJ, 431, L31

Hurley, K. et al. 1994, ApJ, 423, 709

Kouveliotou, C. 1996, IAU Symposia, 165, 477

Kouveliotou, C. et al. 1987, ApJ, 322, L21

Kouveliotou, C. et al. 1996, Nature, 379, 799

Kulkarni, S. R. & Frail, D. A. 1993, Nature, 365, 33

Kulkarni, S. R., Frail, D. A., Kassim, N. E., Murakami, T. & Vasisht, G., 1994, Nature, 368, 129

Laros, J. G. et al. 1987, ApJ, 320, L111

Lewin, W. H. G., van Paradijs, J., and Taam, R. E., 1992/3, Space Sci. Rev., 62, 223

Lyne, A. G. & Lorimer, D. R. 1994, Nature, 369, 127

Margon, B. 1984, Annu. Rev. A&A, 22, 507

Mazet, E. P. et al. 1979, Nature, 282, 587

Mazets, E. P. & Golenskii, S. V. 1981, Astrophys. Space Sci, 75, 47

Murakami, T. et al. 1994, Nature, 368, 127

Narayan, R. & Popham, R. 1989, ApJ, 346, L25

Norris, J. P., Hertz, P., Wood, K. S. & Kouveliotou, C. 1991, ApJ, 366, 240

Rothschild et al. 1993, in Friedlander M., Gehrels, N., Macomb, R. J., eds., Compton Gamma Ray Observatory, Am. Ins. Phys., New York, 808

Rothschild, R. E., Kulkarni, S. R. & Lingenfelter, R. E. 1994, Nature, 368, 432

Schmidt G. D. 1989, in IAU Colloquium 95: Faint Blue Stars, eds: A. G. D. Davies-Phillips et al., V. L. Davis press, Schenectady, N. Y., 377

Sonobe, T., Murakami, T., Kulkarni, S. R., Aoki, T. & Yoshida, A. 1994, ApJ, (in press)

Stewart, R. T., Caswell, J. L., Haynes, R. F. & Nelson, G. J. 1993, MNRAS, 261, 593

Thompson, C. & Duncan, R. C. 1993, ApJ, 408, 194

Thompson, C. & Duncan, R. C. 1995, MNRAS, 275, 255 (TD95)

Ulmer, A., Fenimore, E. E., Epstein, R. I., Ho, C. & Klebesadel, R. W. 1993, ApJ, 418, 395

Vancura, O., Blair, W. P., Long, K. S. & Raymond, J. C., 1992, ApJ, 394, 158

van Kerkwijk, M. H., Kulkarni, S. R., Matthews, K. & Neugebauer, G. 1995, ApJ, 444, L33

Vasisht, G., Kulkarni, S. R., Frail, D. A. & Griener, J. 1994, ApJ, 431, L35

Vrba, F. J. et al. 1995, Astro. Sp. Sc., 231, 85

3.2 SUPERNOVA REMNANT CANDIDATES FOR THE SOFT GAMMA-RAY REPEATER 1900+14†

G. Vasisht & S. R. Kulkarni

California Institute of Technology 105-24, Pasadena, CA 91125

D. A. Frail

National Radio Astronomy Observatory, Socorro, NM 87801

J. Greiner

Max Planck Institut für extraterrestrische Physik

D-85740 Garching bei München, Germany

ABSTRACT: Motivated by the association of two soft γ-ray repeaters (SGR) with supernova remnants (SNR) we have carried out radio, optical and X-ray studies of two cataloged SNRs in the large Konus error box ($11^\circ \times 8'$) of SGR 1900+14. Our VLA observations of SNR G 43.9+1.6 do not reveal any obvious plerionic component. A radio flat spectrum source, close to, but outside the error box was found. We suggest this to be a distant HII region foreground to the SNR. A sensitive VLA image at meter wavelengths show that the other SNR, G 42.8+0.6, is an ordinary typical SNR with a shell morphology with no peculiarities such as a plerionic component. No ROSAT source with an apparent flux $\gtrsim 10^{-13}$ erg cm^{-2} s^{-1} is found within the two SNRs. Recently, Hurley et al. have reported a new very small error box close to G 42.8+0.6. There is no radio feature within or close to the error box. However, a ROSAT source is found just outside this localization. We speculate that this is the quiescent X-ray counterpart of SGR 1900+14. We suggest that SGR 1900+14 is a neutron star that was born with high speed which has now overtaken the expanding shell of SNR G 42.8+0.6. Owing to the low confining pressure, there has been no development of a synchrotron bubble which explains the absence of the radio plerion. In our picture, SGR 1900+14 is the oldest known SGR.

† Published in the Astrophysical Journal, 431, L35

3.2.1 – INTRODUCTION

Soft γ-ray repeaters are a subset of the high energy transients and have distinctive spectral and temporal properties compared to the γ-ray bursters (GRB; see Cline 1990 for a review). Unlike the GRBs, SGRs repeat, hence the name. There are three known SGRs: 0526−66, 1806−20 and 1900+14. SGR 0526−66 apparently lies in the SNR N49 (Cline et al. 1982) and SGR 1806−20 has been associated with the SNR G10.0−0.3 (Kulkarni & Frail 1993, Murakami et al. 1994, Kulkarni et al. 1994). A steady X-ray counterpart coinciding with the peak of central radio emission has been detected by ROSAT (Cooke 1993) and ASCA (Murakami et al. 1994).

SNR G10.0−0.3 is a radio "plerion", a non-thermal nebula with emission from the center. In contrast, a majority of SNRs have edge brightened emission or a shell morphology. Plerions are powered by a central source of relativistic wind (particles and magnetic fields) usually from the spin-down of a pulsar. Mathewson et al. (1983) detected excess emission in N49 close to the error box of SGR 0526−66, but its possible relation to the SGR appears not to have been appreciated. The newer ROSAT data (Rothschild, Kulkarni & Lingenfelter 1994) shows clearly the excess emission to be a point source which has been interpreted as synchrotron nebula powered by a young pulsar (i.e., SGR 0526−66). Logically, the next step is to investigate whether SGR 1900+14 (Mazets et al. 1979) is also associated with a SNR. Such an investigation is very timely since this repeater is now active again after more than a decade of quiescence (Kouveliotou et al. 1993).

Discovery of such plerions is very important for further understanding of the nature of SGRs. The plerion acts as a convenient calorimeter and allows us to observationally infer the time integrated and instantaneous energetics of the SGR. The plerion constrains the age of the SGR and the spatial offset of the SGR from the centroid of the plerion yields an upper limit on the velocity of the SGR. Driven by the unique and fundamental diagnostics offered by plerions, we investigated the Konus error box (Mazets et al. 1979). We have found two

cataloged SNRs, G 43.9+1.6 and G 42.8+0.6. This coincidence was independently noted by Kouveliotou et al. (1994) and in the companion paper by Hurley et al. (1994). Here we present detailed investigations at radio, optical and X-ray wavelengths.

3.2.2 – THE ERROR BOX OF SGR 1900+14

The 2σ error box for SGR 1900+14 (Figure 3.1) was generated with the help of position errors for the three March 1979 events for this source, from detectors aboard the Venera space probes, kindly provided to us by Dr. Mazets. Two cataloged SNRs, G 43.9+1.6 and G 42.8+0.6, fall within this error box, the details of which can be found in Green 1991. We investigated the confines of this error box using the 21-cm (Reich et al. 1990a), 11-cm (Reich et al. 1990b) and 11-cm linear polarization (Junkes et al. 1987) maps obtained at the 100-m Effelsberg telescope. Using the Effelsberg maps, we independently searched for SNR candidates and failed to find any more SNRs other than the two discovered by Reich and coworkers. We also note that search of the Princeton pulsar data base showed that there is no known pulsar within the Konus localization.

3.2.3 – G 43.9+1.6

G 43.9+1.6 is a large ($35' \times 50'$), poorly defined, faint source which Green (1991) has classified as "F?" i.e. a possibly center-filled morphology. The plerion classification is exciting for the diagnostic reasons listed above. Additionally, since only 10% of the SNRs are plerions, the coincidence becomes statistically more meaningful. We estimate the 21-cm and 11-cm fluxes from the survey contour maps (Reich et al. 1990a, Reich et al. 1990b) to be 10 Jy and 9 Jy respectively. From our estimated measurement error of $\sim 20\%$ we obtain a spectral index α of 0.16 ± 0.5, where $S_\nu = S_\circ \nu^{-\alpha}$. The spectrum seems to be flat like that of plerion. However, this is inconclusive due to the large error in α.

VLA observations towards G 43.9+1.6 were conducted on 18 and 26 November 1993 at a central frequency of 327 MHz. We obtained 50 minutes of useful data out of a total of 1.5 hours of observations. The mode of observations and data reduction procedure were identical to that described in Frail, Kassim and Weiler (1994). Due to the incomplete sampling of the u-v plane (spatial frequency plane), much of the extended flux that is apparent in the Effelsberg survey maps is missing (see Figure 3.3). The poor uv coverage and the presence of bright radio sources in the primary beam, prevented us from cleaning the map to below 12 mJy/beam, which is 4 times worse than the expected theoretical value. Much of the emission we see in this image is the western limb of the SNR. We see some features in the intersection between the Konus error box and the SNR limb. Most likely these are associated with the SNR limb. It is fair to say that we see no source similar to G10.0−0.3 in this portion of the error box.

The most interesting radio object closest to the 2σ error box, but perhaps within the 3σ error box, is a bright compact radio source protruding to the east. This source has an estimated flux of $\sim$ 1 Jy at 90-cm (VLA data), 21-cm (Reich et al. 1990a) and 11-cm (Reich et al. 1990b). However, it is unpolarized (Junkes et al. 1987), leading us to believe that it may be a foreground HII region. Nonetheless it is intriguing to note that high resolution ("HIRES") maps of the region in all the four IRAS bands do not show any infra-red counterpart. We observed this source at the Palomar 60-inch telescope with a re-imaging camera (field of view, 8 square arcmin) and a CCD detector with narrow Hα (20Å) and [SII] (20Å) filters and suitable wide-band off-line filters for a total integration time of 1 hour each. We derive an upper limit of 24 mag/arcsec^2 at the location of this source, in each band. Thus if this source is an HII region it must be suffering from extinction. Parenthetically we note that there is a point source at α=19:02:45 and δ=10:30 (equinox 1950) which lies outside the SGR 1900+14 error box but close to the center of the SNR.

Crucial to further discussion is the distance to the SNR and to the SGR. The Σ-D relation (radio surface brightness-diameter; Milne, 1979) puts G 43.9+1.6 at

4 kpc. However, in our opinion, these estimates are unreliable because the basis of this relation, homogeneity in SNe explosions and properties of the ambient media, are clearly not satisfied. Assuming that the luminosity of primary bursts is the same for all repeaters, and that SGR 0526−66 is located in the LMC, Norris et al. (1991) argue $d_{10} \sim 1$ for SGR 1900+14. However, there is no compelling reason to believe that SGR bursts are standard candles.

The radio luminosity of G 43.9+1.6 is $L_R \sim 10^{35} d_{10}^2$ ergs s^{-1}, where d_{10} is the distance to the remnant in units of 10 kpc; here we assume a high frequency cutoff at 100 GHz. A minimum energy calculation (Pacholcyzk, 1970) shows that the energy in particles and magnetic field is $E_{min} = 4 \times 10^{50} d_{10}^{17/7}$ ergs. We stress this point because if SGR 1900+14 and G 43.9+1.6 are associated then the system must be much closer, probably at a distance of $\lesssim 5$ kpc; otherwise the energetics and linear size are unprecedented and the transverse velocity implied by the spatial offset of SGR 1900+14 from the center is an impressive $\gtrsim 2.5 \times 10^3 d_{10} t_4^{-1}$ km s^{-1}. Here the age of the remnant is $10^4 t_4$ yr.

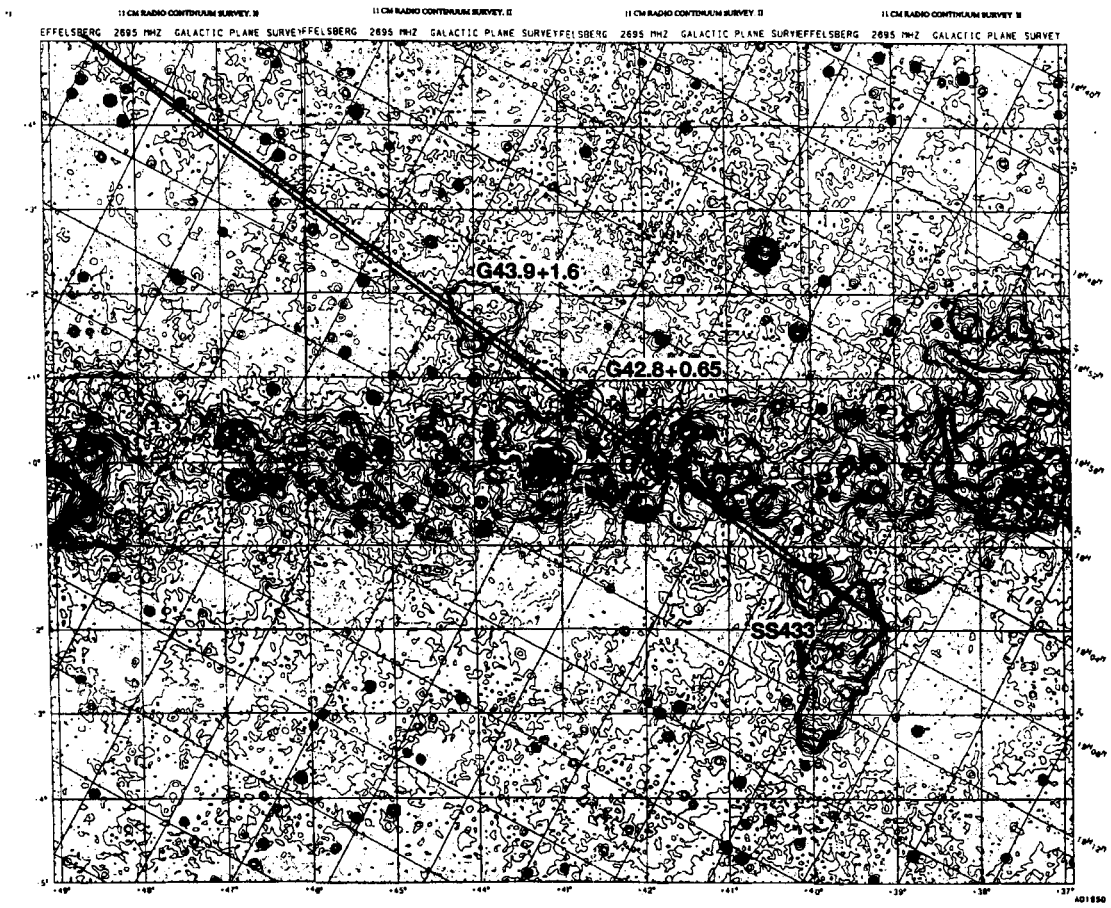

Figure 3.1: 11-cm map of the Galactic plane in the area of the SGR 1900+14 error box. The map was made from a survey of the plane from the Effelsberg 100m telescope (Reich et al. 1990a). The error box and the intersecting SNRs are clearly marked. Vertices of the Konus error trapezium are $(\alpha, \delta)_{1950}$ $(284^{\circ}.885, 16^{\circ}.147), (285^{\circ}.178, 14^{\circ}.698), (286^{\circ}.635, 6^{\circ}.120), (286^{\circ}.808, 4^{\circ}.442)$.

3.2.4 – G 42.8+0.6 AND THE NEW NETWORK LOCALIZATION

The second remnant in the error box is G 42.8+0.6, a faint SNR shell (Fürst et. at. 1987). Its spectral index α of 0.5 seems to confirm its classification as a shell SNR but its high linear polarization of 22% (at 4750 MHz) is more commonly seen for plerions (Reynolds 1988). Interest in this otherwise ordinary SNR is heightened by the fact that the recent interplanetary network (IPN) localization, reported by Hurley et al. in a companion paper is less than 15 arcmin from this SNR. Observations were conducted at P-band (327 MHz) with the VLA in the D-array and spectral line mode on 7 February 1994. The total integration time was 2 hours spread over 4 hours which enable reasonable spatial frequency coverage. The data reduction procedure was similar to that employed for G 43.9+1.6.

G 42.8+0.6 is seen as a typical shell in the new VLA image. There is no indication of any sort of plerionic component close to the eastern limb where the Konus error box intersects nor is there is evidence for a radio plerion at the IPN position (Figure 3.2). Parenthetically we note that there is a flat-spectrum, polarized point source at the edge of the remnant (at α= 19:07:42, δ=09:06, equinox J2000; see also Fürst et al. 1987) that could be related in some way to the remnant. However it does not lie within the error box of SGR 1900+14.

The Σ-D distance to G 42.8+0.6 is $\sim$ 5 kpc. As above, if the SNR is associated with SGR 1900+14 then its distance can be as large as 10 kpc and much of the above discussion i.e. the energetics and the size are also applicable to this SNR. It is interesting to note that the Konus error box does not pass through the center of the SNR and the velocity of SGR (assuming an association) is 10^3 km s^{-1} for an assumed remnant age of 10^4 yr.

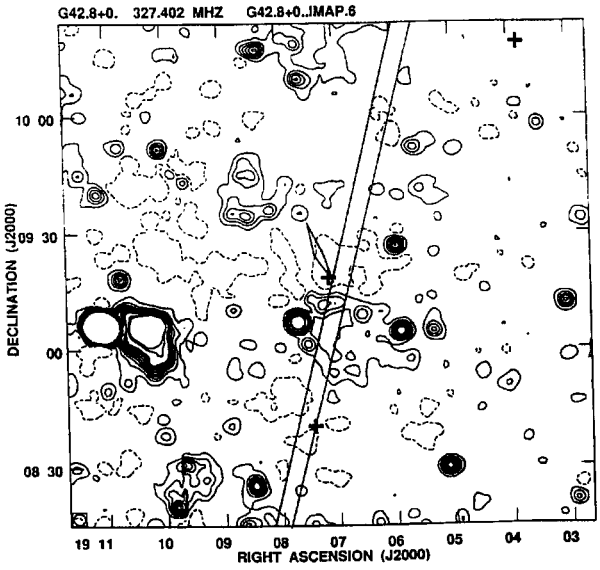

Figure 3.2: P-band (327 MHz) VLA image of G 42.8+0.6 and its vicinity. See caption for figure 3.2 for approximate beam size. Noise level in the image is at 7 mJy/beam with contours at −3, 3, 8, 13, 18, 23, 28, 33, 38, 43, 75, 100 times the noise. The parallel lines enclose the Konus localization box. The diamond to the North of G 42.8+0.6 is the IPN localization of Hurley et al. (1994). Rosat sky survey sources in the field are indicated by crosses with RX J190717+0919.3 marked close to the IPN and Konus error boxes. We speculate this is the quiescent X-ray counterpart of SGR 1900+14. RX J190724+0843.4 which lies close to the Konus localization is identified as possible coronal emission from the star HD 178215 (ref. Table 3.2). All coordinates are J2000.

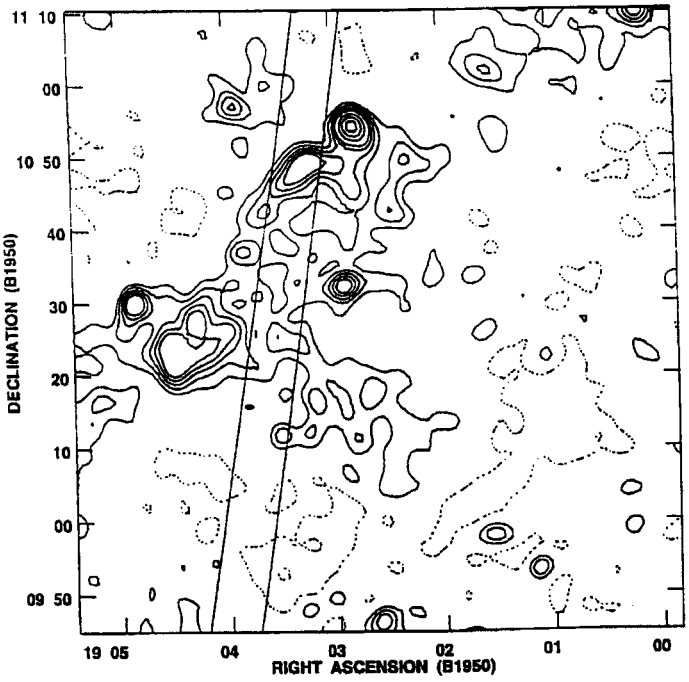

Figure 3.3: P-band (327 MHz) image of the remnant G 43.9+1.6 from observations at the Very Large Array in D configuration. The integration time on the source is 16 minutes. The synthesized beam size is 202×193 arcsec^2. Noise level is at 12 mJy/beam with contours at -3, 2, 4, 6, 8, 10, 15, 20, 25 times the noise level. The position of the Konus error box is superimposed, as lying between the vertically running parallel lines. All coordinates are B1950.

3.2.5 – ROSAT SKY SURVEY OBSERVATIONS

The identification of a quiescent counterpart to SGR 1806−20 (Murakami et al. 1994) and SGR 0526−66 (Rothschild et al. 1994) prompted us to look for a similar quiescent source in the general vicinity of the two SNRs in the ROSAT All Sky Survey (Trümper 1983). This survey scanned the sky in the range between 0.1–2.4 keV. The area of SGR 1900+14 was scanned by ROSAT between September 22 and October 9, 1990 for a mean total observing time per location of about 500–630 s.

We find no hint of X-ray emission from these SNRs and the mean point source 3-σ upper limit is 0.006 counts s^{-1}. A number of sources in the general vicinity of the SNR were found (Table 3.1), some of which we identify with coronal emission of bright stars. Our upper limit is a factor of 4 higher than the detection counting rate of RX J180840−2024.5, the quiescent ROSAT source of SGR 1806−20 (Cooke 1993). However, if the SGR is located at a distance between 5 to 10 kpc then the quiescent X-ray source would be heavily absorbed (cf. the counterpart of SGR 1806−20; Murakami et al. 1994) and our upper limits are not inconsistent with the possible presence of a source similar to the counterparts of SGR 1806−20 and SGR 0526−66.

3.2.6 – DISCUSSION

We have investigated the two cataloged SNRs G 43.9+1.6 and G 42.8+0.6 that lie in the Konus error box. To this end we conducted observations at the VLA and Palomar 60-inch telescope and analyzed the ROSAT sky survey in this region of the sky. We come to the following conclusions:

(1) Although G 43.9+1.6 has been classified to be a possibly center-filled SNR (Green 1991), we find the motivating evidence, neither the center-filled morphology nor the apparent flat spectral index, not compelling. G 43.9+1.6 appears to be an ordinary evolved shell. A flat spectrum component has

been found close to but outside the intersection region. We believe that this is a distant HII region.

(2) Our new high quality images of G 42.8+0.6 and its vicinity (which includes the new IPN position of Hurley et al. 1994) show that this SNR is an ordinary shell with no plerionic component either at the center or intersecting the Konus error box.

(3) No radio plerion similar G10.0-0.3 is seen at the new IPN diamond.

(4) No ROSAT source is seen within the intersection of the error box with either of the two SNRs to a limiting apparent flux sensitivity in the ROSAT band of $\sim 6 \times 10^{-14}$ erg cm^{-2} s^{-1}; the unabsorbed flux, assuming a Crab-like spectrum and $N_H \sim 10^{22}$ cm^{-2} is a factor of 10 higher. However, one of the X-ray sources from Table 3.1, RX J190717+0919.3, is located only 1.5 arcmin from the IPN diamond (Figure 3.2). A check of the X-ray position on the Palomar Observatory Sky Survey plate reveals no optical object brighter than 17th mag. Thus, the lower limit of the ratio of the X-ray to the optical luminosity of RX J190717+0919.3 excludes stellar coronal emission of late-type stars, WDs, CVs, etc., but not LMXBs, AGNs or SNRs (though there are no hints for the X-ray source to be extended).

RX J190717+0919.3 is tantalizingly close to the IPN diamond. It is possible this is the quiescent X-ray source of SGR 1900+14. We propose that SGR 1900+14 is a highly evolved version of SGR 0526−66. As with SGR 0526−66, we propose that the neutron star SGR 1900+14 was born with a large velocity, $\sim 10^3$ km s^{-1} but in the latter case, it eventually overtook the rapidly slowing down SNR blast wave and is now outside its parent SNR. Indeed, this phenomenon is quite commonly seen in many SNRs associated with pulsars (Kulkarni et al. 1988, Shull et al. 1989). Owing to the low confining pressure, the SGR 1900+14 does not develop any substantial radio plerion.

We thank Dr. E. Mazets for communicating to us the coordinates of the Konus error box; the staff at the Infrared Processing and Analysis Center (IPAC)

for help with the analysis of the IRAS data. We appreciate the free discussion and exchange of data sets with Dr. K. Hurley. SRK's research is supported by the US NSF, NASA and the Packard Foundation. Optical observations were made at the Palomar 60-inch telescope which is jointly owned by the California Institute of Technology and the Carnegie Institute of Washington.

REFERENCES

Cline, T. L. 1990, Proc. 21st Intl. Cosmic Ray Conference 12, 19

Cline, T. L. et al. 1982, ApJ, 255, L45

Cooke, B. A. 1993, Nature, 366, 413

Frail, D. A., Kassim, N. E., & Weiler K.W. 1994, AJ, 107(3), 1120

Fürst, E., Handa, T., Reich, W., & Reich, P. 1987, A& ASS, 69, 403

Green, D.A. 1991, PASJ, 103, 209

Hurley, K., Sommer, M., Kouveliotou, C., Fishman, G., Meegan, C., Cline, T., Boer, M. & Niel, M. 1994, ApJ (submitted)

Junkes, N., Fürst, F. & Reich, W. 1987, A&ASS, 69, 451

Kouveliotou, C., et al. 1993, Nature, 362, 728

Kouveliotou, C., et al. 1994, Nature, 368, 125

Kouveliotou, C., et al. 1992, ApJ, 392, 179

Kulkarni, S. R. et al. 1988 Nature 331, 50

Kulkarni, S. R. & Frail, D. A. 1993, Nature, 365, 33

Kulkarni, S.R., Frail, D.A., Kassim, N.E., Murakami, T., & Vasisht, G. 1994, Nature, 368, 129

Mathewson, D. S. et al. 1983, ApJ Supp. 51, 345

Mazets, E. P. et al. 1979, Sov. Astron. Lett. 5(6), 343

Milne, D.K. 1979, Aust. J. Phys., 32, 83

Murakami, T., Tanaka, Y., Kulkarni, S. R., Ogasaka, Y., Sonobe, T., Ogawara, Y., Aoki, T. & Yoshida, A. 1994, Nature, 368, 127

Norris, J. P., Hertz, P., Wood, K. S. & Kouveliotou, C. 1991, ApJ, 366, 240

Pacholczyk, A. G. 1970, Radio Astrophysics, Chap. 7, San Francisco: Freeman

Reich W., Fürst E., Reich P. & Reif K. 1990b, A&ASS, 85, 633

Reich, W., Reich, P. & Fürst, E. 1990a, A&ASS, 83, 539

Reynolds, S. P. 1988, ApJ, 327, 853

Rothschild, R. E., Kulkarni, S. R. & Lingenfelter, R. E. 1994, Nature 368, 432

Shull, J. M., Fesen, R. A., & Saken, J. M. 1989, ApJ 346, 860

Taylor, A. R., Wallace, B.J., & Goss, W. M. 1992, AJ, 103, 931

Trümper, J. 1983, Adv. Space Res. 2, 241

3.3 RADIO MONITORING AND HIGH RESOLUTION IMAGING OF THE SOFT GAMMA REPEATER 1806−20†

G. Vasisht

California Institute of Technology, MS 105-24, Pasadena, CA 91125

D. A. Frail

National Radio Astronomy Observatory, P.O. Box 0, Socorro, NM 87801

and

S. R. Kulkarni

California Institute of Technology, MS 105-24, Pasadena, CA 91125

ABSTRACT: We report the results of radio flux-monitoring and high resolution observations at 3.6-cm with the VLA, of the central condensation in G 10.0−0.3, the radio nebula surrounding the soft gamma ray repeater (SGR) 1806−20. The quiescent X–ray source AX 1805.7−2025 is coincident with the radio core suggesting that G 10.0−0.3 is a plerionic supernova remnant. The monitoring experiment was performed in 10 epochs spread over five months, starting just before the latest reactivation of SGR 1806−20 in γ-rays. There is no apparent increase in the radio flux density from the central region of G 10.0−0.3 on time-scales of days to months following the γ-ray bursts. At a resolution of 1 arcsec, the peak region of G 10.0−0.3 is seen to consist of a compact source with diffuse, one-sided emission, reminiscent of core-jet geometry seen in AGNs and some accreting Galactic binaries. By analogy with these latter sources, we argue that the SGR 1806−20 is coincident with the core component. If so, this is the first arcsecond localization of a high energy transient. The lack of radio variability and the low brightness temperature of the central component distinguish SGR 1806−20 from other accreting binaries. The structure of the high resolution radio image also does not particularly resemble that seen in the vicinity of young pulsars. Thus there is no compelling observational evidence for either of the two models discussed for SGRs, the pulsar model or the accreting binary model.

---

† Published in the Astrophysical Journal, 440, L65

3.3.1 – INTRODUCTION

Since soft gamma ray repeaters were first recognized as a separate class of the gamma ray burster population with distinct temporal, spectral and recurrence signatures (Mazets & Golenskii 1981, Atteia et al. 1987, Kouveliotou et al. 1987, Larson et al. 1987), attempts to understand their nature have concentrated primarily on their high energy emissions (Norris et al. 1991). The recent suggestion by Kulkarni and Frail (1993) that SGR 1806−20 was associated with the radio supernova remnant (SNR) G 10.0−0.3, and the subsequent confirmation by the ASCA X-ray satellite (Murakami et al. 1994) and the BATSE experiment (Kouveliotou et al. 1994) on board the Compton Gamma Ray Observatory (CGRO), has underscored the importance of multi-frequency observations for these objects. Since then, a number of observations have been reported including X-ray observations of SGR 0526−66 and its SNR N49 (Rothschild et al. 1994), further detailed observations of SGR 1806−20 (Sonobe et al. 1995) and SNR G 10.0−0.3 (Kulkarni et al. 1994a), and searches for the SNR counterpart to SGR 1900+14 (Kouveliotou et al. 1994a, Hurley et al. 1994a, Vasisht et al. 1994).

No model proposed thus far is commensurate with all the observations, but a general picture is starting to emerge from the various studies. SGRs are young ($\lesssim 10^4$ yrs), energetic neutron stars. The rarity of SGRs (Kouveliotou et al. 1994, Hurley et al. 1994b) means that either the SGR phase is short-lived phase that all neutron stars undergo or that a small subset of the neutron star population with some distinguishing characteristic evolve to SGRs (e.g., large B-fields, high velocities, a special type of binary system, etc.).

Specifically for SGR 1806−20, two models explaining observations of nebula G 10.0−0.3 and the X-ray source AX 1805.7−2025 have been proposed (Kulkarni et al. 1994a).

(1) A radio pulsar whose spin-down luminosity powers a synchrotron nebula or a "plerion" e.g. the Crab Nebula or 3C58.

(2) An accreting binary neutron star system with a radio nebula such as the one associated with the X-ray binary Cir X-1 (Stewart et al. 1993) or perhaps even SS 433 (Margon 1984).

Radio and X–ray observations offer the possibility of distinguishing between these alternatives. In particular, the central sources in Cir X-1 and SS 433 are easily detectable bright radio sources which undergo dramatic changes in their flux density, both in radio and X–ray bands. In contrast, most pulsars are faint radio sources with little changes in their flux density, especially at high frequencies.

SGR 1806−20 is the most prolific of the three known SGRs, with greater than 10^2 burst events detected in several different instruments by the late 1970's and early 1980's (Ulmer et al. 1993, Laros et al. 1987). Recently SGR 1806−20 became active in γ-rays again after being quiescent for nearly a decade (Kouveliotou et al. 1987). A total of six new bursts were detected, including three on 29 Sept. 1993 and one each on 5 Oct., 9 Oct. and 10 Nov. 1993. Fortunately, motivated by our earlier paper (Kulkarni & Frail 1993) we had begun and carried out extensive radio observations of G 10.0−0.3, two weeks prior to the first BATSE burst (Kulkarni et al. 1994a). Following the announcement of the 29 Sept. event we initiated a radio monitoring program with the Very Large Array (VLA) to search for variable radio emission from the radio counterpart of SGR 1806−20. We also carried out high resolution imaging of the central core of G 10.0−0.3 in an effort to accurately localize the stellar counterpart of SGR 1806−20. In this *Letter* we report on both these observations.

3.3.2 – OBSERVATIONS AND RESULTS

The observations were obtained at 3.6-cm with the VLA in its so-called "D" configuration (the most compact configuration). In all there are ten epochs of observations spanning nearly five months during which there were a total of six γ-ray bursts (Table 3.2). The pre-reactivation radio observation on 13 Sept. 1993 was obtained in the "DnC" configuration, not too dissimilar to the remaining

observations. As this observation was just prior to the initial burst, it provides a useful dataset against which to search for changes in the radio emission from the source.

During each observation two separate IF bands, each measuring both hands of circular polarization and each with a bandwidth of 50 MHz, were used at 8.415 GHz and 8.465 GHz (the 3.6-cm or X band). Calibration of the data and reduction was done using the AIPS package. The total integration time of the source depended on the epoch of observation, and varied between 0.2 hrs and 1 hr.

The data from each epoch were added to form a single image, and this is shown in Figure 3.4. This image is similar but considerably deeper than the image from Kulkarni et al. (1994). A point-like "core" sits near the center of a 1 arcmin nebulosity with extensions leading off to the North and Southwest. Since the aim of the experiment was to measure flux variations across the source, especially in the core, images from the various epochs were convolved to the same beam. These core fluxes and total fluxes are shown in Table 3.2. Shown also is the time interval between the epoch of each radio observation and the last γ-ray outburst from SGR 1806−20 (see section 1; Kouveliotou et al. 1994).

We saw no significant variability for any of the components of G 10.0−0.3 during the 5 month interval in which we monitored this source. There are apparent variations at the 25% level. These could arise from a number of reasons. Most importantly, observations of a complex source such as G 10.0−0.3 in the "snapshot" (short-integration) mode are sensitive to the actual spatial frequency (u-v) coverage. For example, the observations of 22 November 1993 suffered from a shortage of low spatial frequency data points resulting in an underestimation of the total flux. We conclude that the source is essentially constant at a level of 25%.

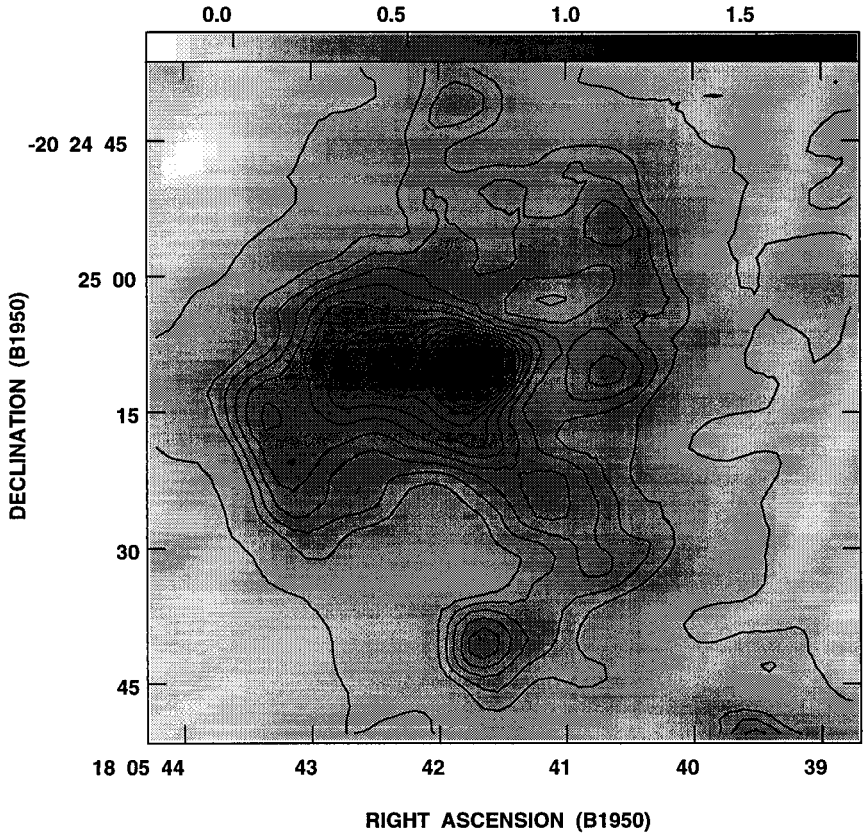

Figure 3.4: A 3.6-cm radio continuum image of a one arcmin region around the central core of G 10.0−0.3. The image was made using co-added datasets from the various monitoring epochs. Extensions are seen prominently to the east and also the North and Southwest to a lesser extent. Contours are at 90, 360, 450, 540, 630, 720, 810, 900, 990, 1080, 1170, 1260, 1350, 1440, 1530, 1620, 1710 and 1800 μJy. The rms noise is 40 μJy/beam and the peak flux is 1.8 mJy. The synthesized beam is 6.6 arcsec by 4.9 arcsec at a position angle of −86 degrees (measured counter-clockwise).

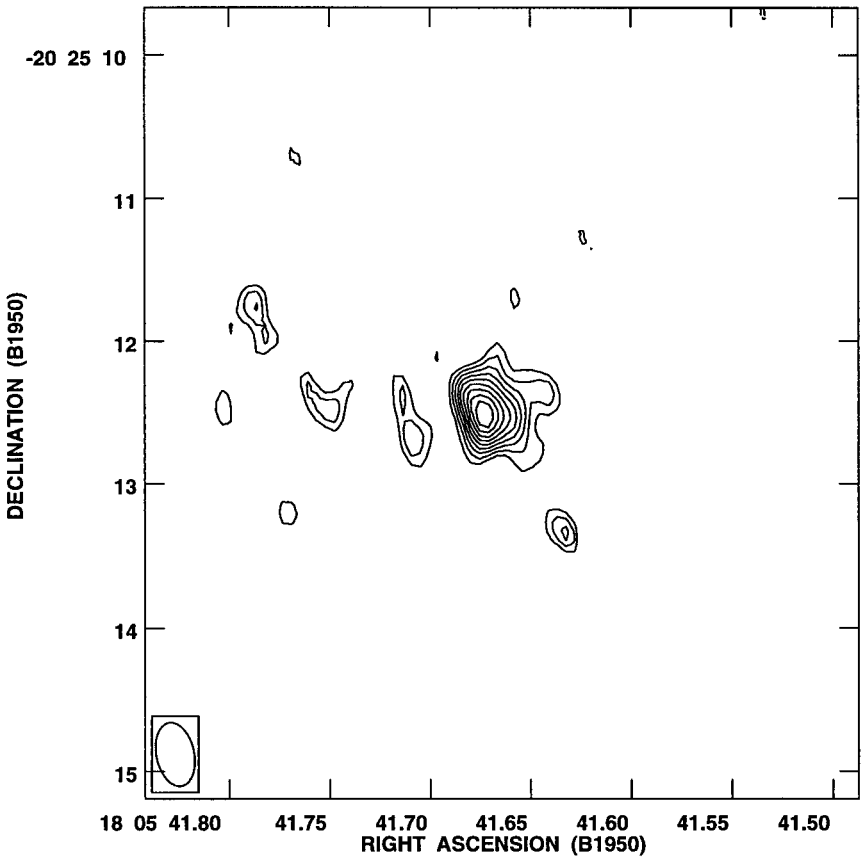

Figure 3.5: A 3.6-cm radio continuum image of the radio "core" of G 10.0−0.3, revealing the arcsecond core which we postulate is the seat of the SGR (α= 18^h 05^m 41.675^s ($\pm$0.005), $-20°$ $25'$ $12.5''$ ($\pm$0.1) (B1950)). Faint structure is seen to the East of the central source. The image was made with natural weighting, producing a synthesized beam of 0.45 arcsec by 0.26 arcsec and position angle (measured counter-clockwise) of 12 degrees. Contours are −60, 70, 80, 90, 100, 110, 120, 130, 140 and 150 μJy/beam. The rms noise is 20 μJy/beam and the peak flux density is 0.15 mJy.

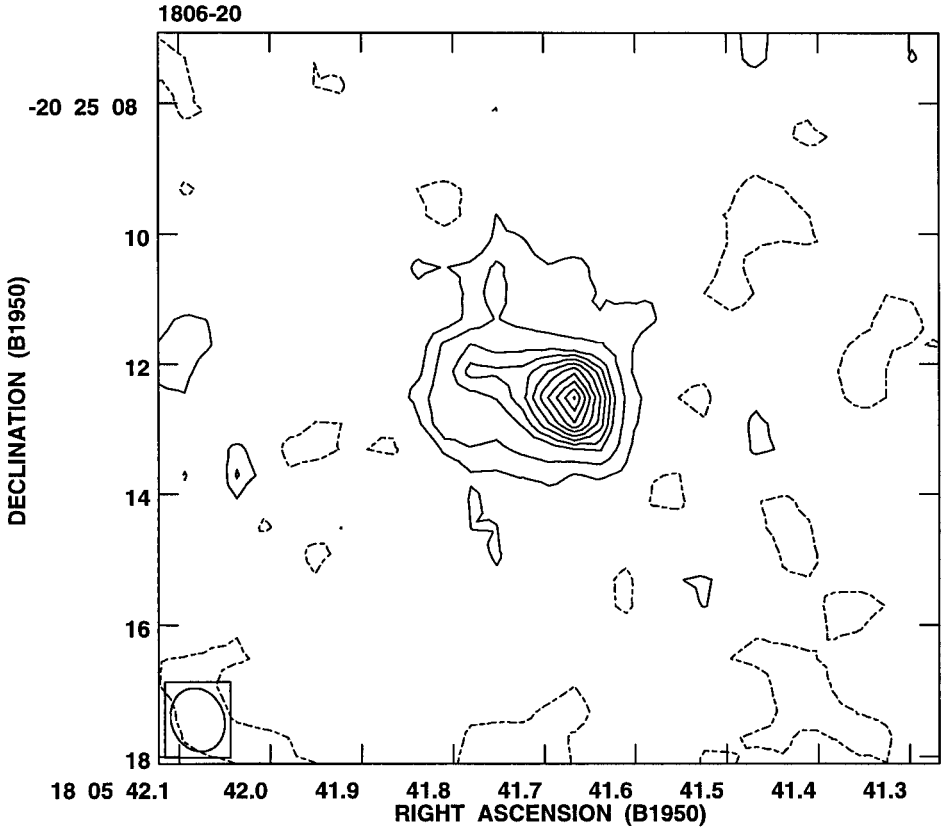

Figure 3.6: A 3.6-cm radio continuum image of radio "core" of G 10.0−0.3, suggesting a collimated flow to the East of the central source, on scales of 2 arcsec. The image was made by uniform weighting of the data, along with a taper which resulted in a synthesized beam of 0.9 arcsec by 0.8 arcsec. This procedure is sensitive to picking up extended flux. Contours are at −90, 90, 150, 210, 240, 270, 300, 330 μJy. The rms noise is 30 μJy/beam and the peak flux density is 0.3 mJy.

All the previous observations of this source were obtained with the VLA in compact configurations. In order to better localize the seat of SGR 1806−20 as well as to study the source structure of the peak region, we observed the source at 3.6-cm, on 7 March 1994, with the VLA in its most extended configuration, the "A" array. At the highest angular resolution (0.2 arcsec), the compact source is resolved (Figure 3.5), giving a source dimension of $4 \times 10^{16} d_{10}$ cm where the distance to SGR 1806−20 is $10 d_{10}$ kpc. In order to improve our surface brightness sensitivity, we tapered the data in the u-v domain. The resulting picture has a lower angular resolution and is shown in Figure 3.6. The source appears to be quite asymmetric with extended emission to the east. This picture of a core-jet geometry is not too dissimilar to that seen in AGNs, especially weak AGNs. If the analogy is correct, then the eastern extended feature probably represents the outflow of material from the compact core.

We now review the observational facts with a view towards establishing the seat of SGR 1806−20. We proceed by a series of steps from γ-rays to radio wavelengths. First, the quiescent X–ray source AX 1805.7−2025 detected by Murakami et al. (1994) was localized to G 10.0−0.3 and is coincident with the radio peak. This morphology is characteristic of plerions, and for this reason it is well accepted that AX 1805.7−2025 represents the compact source which powers G 10.0−0.3 and is also the X–ray counterpart of SGR 1806−20. The best localization of AX 1805.7−2025 is by ROSAT (Cooke 1993) and this coincides with the radio peak within the 90% error radius of 11-arcsec. Second, the sequence of Figures 3.4, 3.5 and 3.6 strongly suggest that this compact source is located at the peak in Figure 3.5. By analogy to AGN we interpret the core-jet appearance in terms of an outflow of particles from the compact source. If this chain of reasoning is correct, then the compact radio source is the seat of SGR 1806−20.

In view of the complexity of the radio peak region, the localization of the core is best done in the image with the highest angular resolution, Figure 3.5. This peak encompasses an integrated flux density of 0.6 mJy and is centered at $\alpha=$ $18^h\ 05^m\ 41.675^s$ (± 0.005), $-20^\circ\ 25'\ 12.5''$ (± 0.1) (B1950). We henceforth refer to

this component as the compact component, "C". Subject to the caveats discussed above, this localization is the first subarcsecond localization of a high energy transient. More importantly, it allows deep searches to be made at optical and infrared wavelengths, and preliminary observations are reported in the companion paper (Kulkarni et al. 1993b, Kulkarni et al. 1994b).

Parenthetically, we note that Kulkarni et al., 1994a, using low resolution data similar to Figure 3.4, reported a position for SGR 1806−20 which is offset from that of "C" in Figure 3.5. by 1.3 arcsec. The origin of the offset is clearly due to the asymmetric nature of the source, not fully resolved in the low resolution image reported in Kulkarni et al. 1994a.

3.3.3 – DISCUSSION

Despite an extensive monitoring campaign of G 10.0−0.3 with post-burst time-scales ranging from as little as two days after a γ-ray burst to three months after the bursting finally ceased, we detected no radio variability above the 25% level. Variability at this level can be reasonably attributed to uncertainties due to calibration and varying spatial frequency coverage (section 2). Thus for all practical purpose, the radio counterpart of SGR 1806−20 is constant. Indeed, the constancy of both the radio and X-ray flux (Sonobe et al. 1994) seems to be one of the defining characteristics of the emission surrounding SGR 1806−20, punctuated only by brief (0.1 sec), intense ($\sim 10^{41}$ erg s^{-1}) γ-ray bursts.

Dramatic radio flaring is often seen in Galactic binaries such as Cyg X-3, Cir X-1 and SS 433, which are correlated with episodes of X-ray activity in these sources (Seaquist 1994, Hjellming 1988). VLBI and VLA studies of these sources (Cir X-1, Preston et al. 1983; Cyg X-3, Geldzahler et al. 1983; SS 433, Hjellming & Johnston 1981) reveal bright ($\sim$ Jy or greater), highly variable compact component (sizes typically in the range of a milli-arcsec to tens of milli-arcsecs) coincident with the stellar binary source. Most likely a fraction of the gravitational potential energy of the accreted material is harnessed to accelerate particles to relativistic

energies primarily during episodes of super-Eddington accretion (Inoue 1989). The implied brightness temperatures are in excess of 10^6 K at centimeter wavelengths. In contrast, component "C" in SGR 1806−20 is dim, only about 0.6 mJy (section 2) and is resolved by a beam of 0.2 arcsec. Here we make the reasonable assumption that, given the high frequency of the observations, the observed size is intrinsic and not a result of broadening by interstellar scattering.

Thus the compact component in SGR 1806−20 differs from the radio counterpart of accreting neutron star systems associated with radio nebulae in two substantial ways: (*i*) no dramatic variation in the total flux has been seen and (*ii*) the brightness temperature is small, about 100 K. We mention a caveat with reference to (*i*) above. The peak flux values in Table 3.2 refer to the entire core region, of which 70% is due to the extended emission in Figure 3.6. Since the total flux density of the core region did not change significantly ($<S_p>\sim 4.8\pm1.0$ mJy) either before, during or after the γ-ray bursts, it seems that the one-sided outflow, if it originated from during the last bursting phase of SGR 1806−20, did not produce dramatic synchrotron flaring. However, for variations in the integrated flux in "C" to have been discerned above the extended emission from the core, it would had to increase in flux density by more than a factor of 10. Thus we cannot rule out variability in "C" at the factor of 10 level. Nevertheless, this is in marked contrast to other radio variables including Cyg X-3 and LSI+61° 303 whose flux densities during the flaring phase rise to $10^2 - 10^4$ of their quiescent values (Hjellming 1988).

We note that the size of "C" which, as argued above, appears to be quiescent is not very different from that in Cir X-1 (0.2 arcsec; Preston et al. 1983) and GRS 1915+10 (0.1 arcsec; Mirabel & Rodriguez 1994). The implied size, 4×10^{16} cm, is much larger than any binary orbit. Thus, as in other radio emitting neutron star binaries, the energetic particles are injected on scales much larger than either the neutron star or any potential binary orbit.

In what way do the new observations constrain possible models for SGRs? The constancy of the radio and X–ray emission are in accord with the pulsar model. Structure in radio emission is often seen around energetic pulsars and usually interpreted to be the working surface of the pulsar relativistic wind as it shocks the nebular gas, e.g., the wisps in the Crab nebula or the bow shock seen around several pulsars. However, it is fair to say that the one-sided structure seen in Figure 3.5 is quite unusual for a pulsar powered plerion.

Some authors have suggested a connection between fast moving neutron stars and SGRs, both to explain the rarity of SGRs and the greatly offset position of SGR 0526−66 from the center of the SNR N49 (Cline et al. 1982). If so, the asymmetric structure seen in Figures 3.5 or 3.6 can be interpreted as a bow shock of a rapidly moving pulsar. However, we consider the bow shock hypothesis to be unlikely. Specifically, we draw the reader's attention to the fact that the east-west asymmetry is seen on angular scales ranging from 1-arcmin (Figure 3.4) to 1-arcsec (Figure 3.6). If this is the wake of an ejected pulsar, then the wake should be directed radially outwards with respect to the center which is not the case because the SGR is offset to the NE with respect to the center of G 10.0−0.3. We suggest instead that there has been a one-sided outflow from this object for quite some time. This hypothesis (see below) satisfactorily explains the observations that the east-west asymmetry is seen on large and small scales.

The lack of radio flaring, the low brightness temperature and the lack of a marked flow geometry make the central compact component quite unlike the radio counterparts of accreting neutron star binaries. Other difficulties with the binary model have been raised by Sonobe et al. (1994), including the constancy of the quiescent X-ray emission and its low luminosity ($L_x \simeq 10^{35}$ erg s^{-1}). While we cannot rule out the binary model due to our limited number of radio observations, it is reasonable to conclude that the existing data do not necessarily favor a binary model.

Finally, we come to the important issue of the role played by the outbursts in powering the plerion. Kulkarni et al. (1994) have suggested that the γ-ray outbursts are accompanied by an energetic (but an otherwise invisible) particle outburst and these outbursts cumulatively power the nebula. Our observations allow us to derive an upper limit to the ratio of the particle luminosity to photon luminosity, β. The 2-arcsec feature in Figure 3.6 corresponds to $4d_{10}$ light months, comparable to the duration of our radio monitoring. We apply the standard synchrotron model (Pacholczyk 1970) to this feature to deduce E_{min}, the minimum energy in particles and magnetic fields. Assuming low and high cutoffs of 10 MHz and 100 GHz for radio luminosity, we can make an estimate of the minimum energy in particles and magnetic fields. Owing to the lack of direct spectral information we assume that these structures have a spectral index same as that of the entire nebula ($\alpha \sim -0.6$). We estimate $E_{min} \sim 1 \times 10^{45} d_{10}^{17/7}$ ergs. Over this period, a total of six bursts with a mean fluence of 10^{-7} erg cm^{-2} have been detected by BATSE (Kouveliotou et al. 1994). Thus the total photon burst energy is $10^{40} d_{10}^2$ erg.

The fact that we see no change in the radio emission of the central region sets an upper bound to the particle energy to be less than $\sim 10\, E_{min}$ (see above). Thus $\beta \lesssim 10^6$, roughly independent of distance. This is a true upper limit since we have assumed the propagation speed for particles to be equal to the speed of light. Unfortunately, this limit is not very interesting since one naively expects β to be around unity rather than such a high number. However, this simple exercise demonstrates that, in principle, β can be constrained by observations alone. Clearly, it is of great value to continue high angular resolutions of the compact core.

We conclude that, with the available data, it is not possible to assert whether the bursts power the nebula. Regardless of this we note that the same east-west asymmetry exists on scales of arcseconds to arcminutes which suggests that the on-going energy injection, impulsive or steady, has been occurring over a long time scale.

Acknowledgements: We thank M. Rupen for his assistance with the October observations and DAF acknowledges useful discussions with R. Hjellming. The VLA is is operated by Associated Universities Inc. under cooperative agreement with the US National Science Foundation.

REFERENCES

Atteia, J. L. et al. 1987, ApJ, 320, L105 (1987)

Cline, T. L. et al. 1982, ApJ, 255, L45

Cooke, B. A. 1993, Nature, 366, 413

Hjellming, R. M. & Johnston, K. J. 1981, Nature, 290, 100

Hjellming, R. M. 1988, in Galactic and Extragalactic Radio Astronomy, 2nd Edition, Eds. G. L. Verschuur and K. I. Kellermann (Springer-Verlag: New York), p 381

Hurley, K., Atteia, J. L, Jourdain, E., Barat, C., Niel, M., Vedrenne, G., Sunyaev, R., Kuznetsov, A. and Terekhov, O. 1994, ApJ, 423, 709

Hurley, K., Sommer, M., Kouveliotou, C., Fishman, G., Meegan, C., Cline, T., Boer, M. & Niel, M. 1994, ApJ, 431, L31

Geldzahler, B. J. et al. 1983, ApJ, 273, L65

Inoue, H. 1989, Proc. 23rd ESLAB Symp. on Two-Topics in X-ray Astronomy, ESA SP-296, 109

Kouvelioutou, C. et al. 1994, Nature, 38, 125

Kouvelioutou, C. et al. 1987, ApJ, 322, L21

Kulkarni, S. R. & Frail, D. A. 1993, Nature, 365, 33

Kulkarni, S. R., Frail, D. A., Kassim, N. E., Murakami, T. & Vasisht, G. 1994, Nature, 368, 129

Kulkarni, S. R., Matthews, K., Neugebauer, G., Reid, N., Soifer, T. & Vasisht, G. 1993, IAU Circ. 5883

Kulkarni, S. R., Matthews, K., Neugebauer, G., Reid, N., van Kerkwijk, M. H. & Vasisht, G. 1994, ApJ, 440, L61

Laros, J. G. et al. 1987, ApJ, 320, L111

Margon, B. 1984, Annu. Rev. A&A, 22, 507

Mazets, E. P. & Golenskii, S. V. 1981, Astrophys. Space Sci, 75, 47

Mirabel, I. F. & Rodŕiguez, L. F. 1994, Nature, 371, 46

Murakami, T. et al. 1994, Nature, 368. 127

Norris, J. P., Hertz, P., Wood, K. S. & Kouvelioutou, C. 1991, ApJ, 366, 240

Pacholczyk, A. G. 1970, Radio Astrophysics, Chap. 7, San Fransisco: Freeman

Preston, R. A. et al. 1983, ApJ, 268, L23

Rothschild, R. E., Kulkarni, S. R., & Lingenfelter, R. E. 1994, Nature, 368, 432

Seaquist E. 1994, Rep. Prog. Phys., 56, 1145

Sonobe, T., Murakami, T., Kulkarni, S. R., Aoki, T. & Yoshida, A. 1994, ApJ, (in press)

Stewart, R. T., Caswell, J. L., Haynes, R. F. & Nelson, G. J. 1993, MNRAS, 261, 593

Ulmer, A., Fenimore, E. E., Epstein, R. I., Ho, C. & Klebesadel, R. W. 1993, ApJ, 418, 395

Vasisht, G., Kulkarni, S. R., Frail, D. A. & Greiner, J. 1994, ApJ, 431, L35

3.4 CHANGING STRUCTURE IN THE VICINITY OF SGR 1806–20

3.4.1 – RADIO STRUCTURE AROUND SGR 1806–20

High resolution radio observations (0.3″) of the core of G 10.0−0.3 have revealed a compact core about 0.4″ across, along with a collimated extention to the East extending radially to $\sim 2''$ (Vasisht et al. 1995; section 3.3). The simplest interpretation of this structure invokes the compact core as the seat of the soft repeater SGR 1806−20, and the eastward limb as emission from a plasma outflow that accompanies γ-ray burst acitivity which is the defining characteristic of this class of sources. The first observations were made at 3.6-cm (see §3.2), with the VLA in A-array, on March 7, 1994, a little more than half a year after the SGR started a new series of bursts after almost a decade of quiescence (Kouveliotou et al. 1994).

After seeing the radio maps of this source (figs. 3.4 and 3.5, for example), it is tempting to compare this Eastern feature with collimated jets associated with other Galactic compact sources such as GRS 1915+105 ((Mirabel & Rodriguez 1994) and GRO J1655−40 (Hjellming & Rupen 1995; Harmon et al. 1995). The inferred brightness temperature (T_b) of the SGR jet is in striking contrast to temperatures observed in jets in Galactic accreting binaries. These demonstrate large, or even superlumninal bulk velocities and high brightness temperatures ($T_b \gtrsim 10^6$ K) in the ejecta, which shoot outward along a preferred direction, presumably the spin axis of the compact star (Mirabel & Rodregues 1994; Hjellming & Rupen 1995). The brightness temperature in SGR 1806−20 is ~ 500 K and the elongated dimension of the radio collimation is $\sim 0.1 d_{15}$ pc. In conjunction with the associated development timescale of 0.5 yr, bulk transverse speeds of around $\beta_j \sim 0.6 d_{15}$ are inferred, where the distance is $15 d_{15}$ kpc.

The low brightness temperature, $T_b \sim 500$ K, suggests that the flow mechanics and the driving mechanism must be different from that seen the the accreting

black-hole binaries or QSOs. High T_b in the latter is thought to be due to powerful synchrotron emission from local shocks associated with relativistic bulk motion of the ejected plasma. The strength of this shock emission depends on the composition of the injected plasma (predominantly electron or predominantly ion): we conjecture that the outbursts of SGR 1806−20 are primarily $e^+ - e^-$ plasma and furthermore the ambient density must be low. The surrounding medium could have been swept away by episodic ejection events creating an evacuated channel. Such a channel can be associated with a tubular radio emitting zone in the wide field image of G 10.0−0.3 (see Fig 2.2.1). The low T_b is in accord with the absence of radio flaring during burst periods.

3.4.2 – MONITORING OBSERVATIONS

We are presently undertaking a second multi-epoch monitoring program of the core of G 10.0−0.3. We hope to monitor the activity of SGR 1806−20 on small angular scales (1″) over an extended period of time. All observations are carried out with the 3.6-cm receiver at the VLA in the available array configuration. The first epoch of observations was on March 7, 1994. The results of this observation, as elaborated in section 3.3, were instrumental in gearing us up for the monitoring experiment. The second A-array epoch is on August 1, 1995 with observations at 3.6-cm and 6-cm (Table 3.3). Note that the time elapsed between the first and the second epochs is approximately 1.3 yr.

All 3.6-cm observations are in the continuum mode. During the observation two separate IF bands, each measuring both hands of circular polarization and each with a bandwidth of 50 MHz, were used at 8.415 GHz and 8.465 GHz. Calibration of the data and reduction was done using the AIPS software package. Details of all the observations including epoch, observing band and integration times are listed in Table 3.3. A single epoch of 6-cm observations were accumulated in the spectral line mode in order to facilitate polarization mapping. Large distance estimates to the SGR (6-15 kpc) and its location near the Galactic center guarantee smearing

of polarization information within the large 50 MHz continuum bandpass. Instead we obtain spectral line data in the 1-IF mode at an edge frequency of 4.702 GHz with four contiguous channels, each 3.125 MHz in bandwidth.

On 30 September, 1995, the BATSE team (Kouveliotou et al. 1995) announced the detection of a single γ-ray burst localized to lie in the direction of 1806−20. The burst lasted for a duration of 60 ms and had an upper energy cutoff of ~ 100 keV, i.e., a typical SGR burst (Kouveliotou et al. 1996). This presented an opportune moment to carry out observations at the VLA on October 5 and October 10, 1995. Since then, the source has been observed repeatedly due to hints of changing structure in its vicinity. All post-burst observations, have been carried out in the B configuration at 3.6-cm, in the VLA continuum mode. The resulting maps (shown in Fig 3.11), unfortunately, have reduced structural detail (resolution $\gtrsim 1''$) because of a larger synthesized beam.

3.4.3 – CHANGING STRUCTURE

3.4.3.1 – Structural Changes at 3.6-cm

Total intensity 3.6-cm maps from the data collected on August 1, 1995, are displayed in figure 3.7 (at full resolution) and figure 3.8 (tapered to display extended flux). In figure 3.8 the data have been "uniform weighted" and tapered to produce a beam roughly $1''$ in extent. There is clear and surprising contrast between this map and those generated previously (figures 3.5 and 3.6). The Eastward feature seen during the previous epoch (March 7, 1994) is now indistiguishable from the background noise in the map. Instead, a separate collimated feature not unlike the original eastward jet is now observed towards the *NorthEast* with a clockwise angular displacement of $\sim 45°$. The new feature is of similar length $l \sim 4 \times 10^{17} d_{15}$ cm. The peak contour flux of 0.33 mJy in the core is unchanged within the uncertainties. A cumulative flux of 1.3 mJy (at 3.6-cm) is observed from the vicinity of SGR 1806−20.

A simple argument illustrates that the feature to the northeast must be independent of the old eastward arm (figure 3.6), and must have developed during the period March 1994 to August 1995. Rotation of the old feature is unlikely because of near radial appearance of the ridges of peak emission in either feature (lack of rotational shear). The only way to maintain rigid rotation is via large curvature magnetic field lines that are coupled to the central neutron star. This requires a light cylinder radius of the neutron star of $\sim 10^{17} d_{15}$ cm which is highly unlikely. The definitive conclusion is that the shifted jet is brand new and not just an angular displacement of the previous one. Given this, one automatically infers a jet speed $v \gtrsim 0.3 d_{15}$c. *We hypothesize that the creation of jet-like entities is impulsive and episodic and takes place in different directions, like a rotating canon that fires randomly.* This conjecture, of course, will be tested over the next few years.

If the bursts are powered by the sudden dumping of energy into a neutron star magnetosphere, then part of this energy will be deposited into a plasma that escapes along the open magnetic field lines (Fig 3.10). An optically thick plasma wind ensures that the particles will be released on a timescale similar to the average observed duration of bursts in γ-rays, ~ 0.1 s. In order to prevent shearing of the ejected plasma by the rotation of the rigid magnetosphere spin period $P \gg 0.1$ s. Weak evidence does exist for a 2.8-s periodicity in the summed spectra of the 20 brightest bursts from SGR 1806−20 (Ulmer et al. 1993). Strong evidence for an 8-s periodicity was seen in the soft-tail of the March 5 burst from SGR 0526−66.

In the accretion model, angular momentum arguments would require the mass ejection to occur along the spin axis of the neutron star. Precession of the neutron star spin axis would then explain the moving jet. Precession of a jet's axis has been observed in the Galactic binary SS433 (V1343 Aql) which contains a compact object in the form of either a neutron star or a black hole. The precession angle of the jet axis is about 20° with a precession period of 162 d. Continuous ejection of matter along the jets, driven by accretion and coupled with the precessional motion, results in a superimposed "corkscrew pattern" on

the jet. In SGR 1806−20, no such smearing in the jet structure is seen. The low signal-to-noise ratio in our data cannot, at the moment, rule out steady accretion powered outflow, but there is indeed strong evidence that ejection of the material entrained in the jet is not continuous, and occurs in separate implulsive episodes during large γ-ray events.

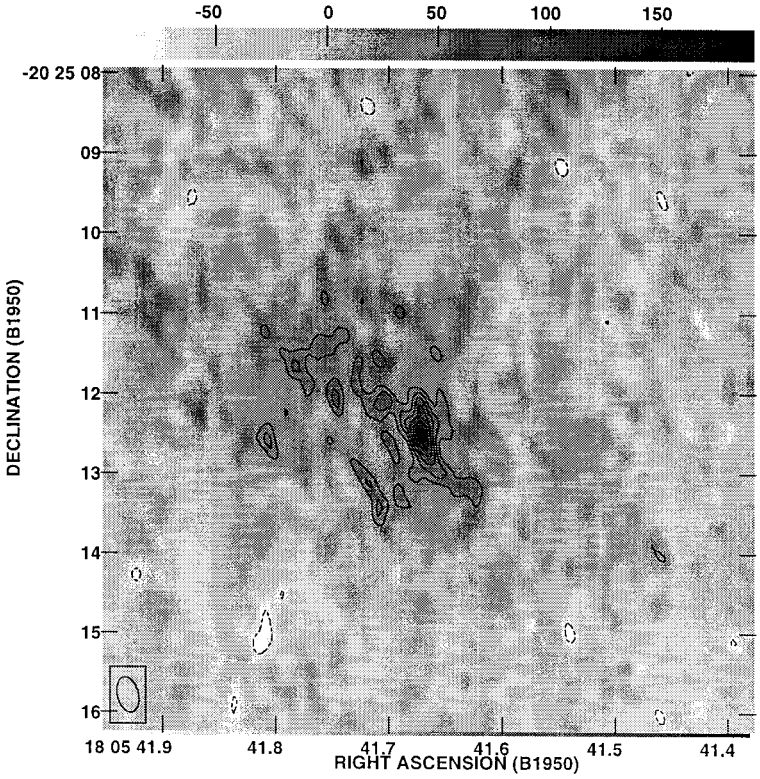

Figure 3.7: A 3.6-cm VLA radio continuum image around the central core of the radio nebula G 10.0−0.3 (observation epoch is August 1, 1995). The size of the synthesized beam is $0.45'' \times 0.26''$ with a position angle of 13.51°. The u-v data were natural weighted. Peak contour flux is 190 μJy/beam and the thermal

of the map is 22 μJy. Contours are in multiple steps of the thermal noise of -3, 3, 5, 7, 8, 9, 10. All coordinates are B1950.

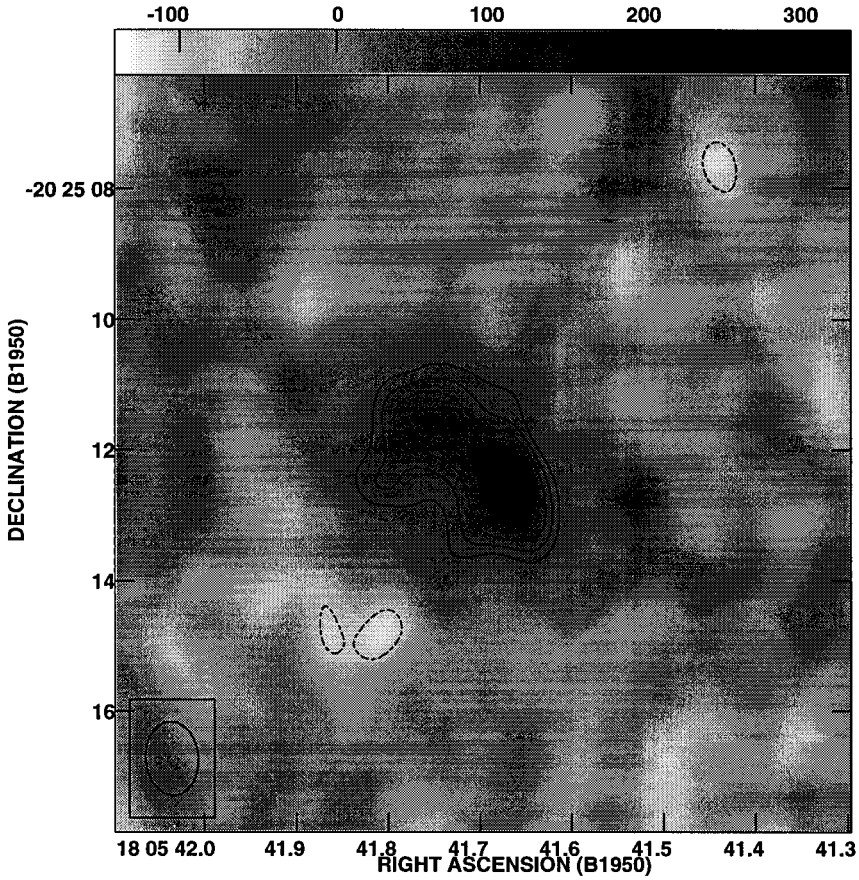

Figure 3.8: A 3.6-cm radio continuum image of the radio "core" of G 10.0−0.3, suggesting a collimated outflow towards the northeast of the central source, on a scale of $\sim 2''$. The image is natural weighted, with a taper to produce a $1.1'' \times 0.81''$ beam with a position angle of 4.8°. This procedure picks up extended flux around the source. The peak contour flux is 302 μJy and the noise is 32μJy. Contour multiples are in steps -3, 3, 5, 7, 8, 9, 10. All coordinates are B1950

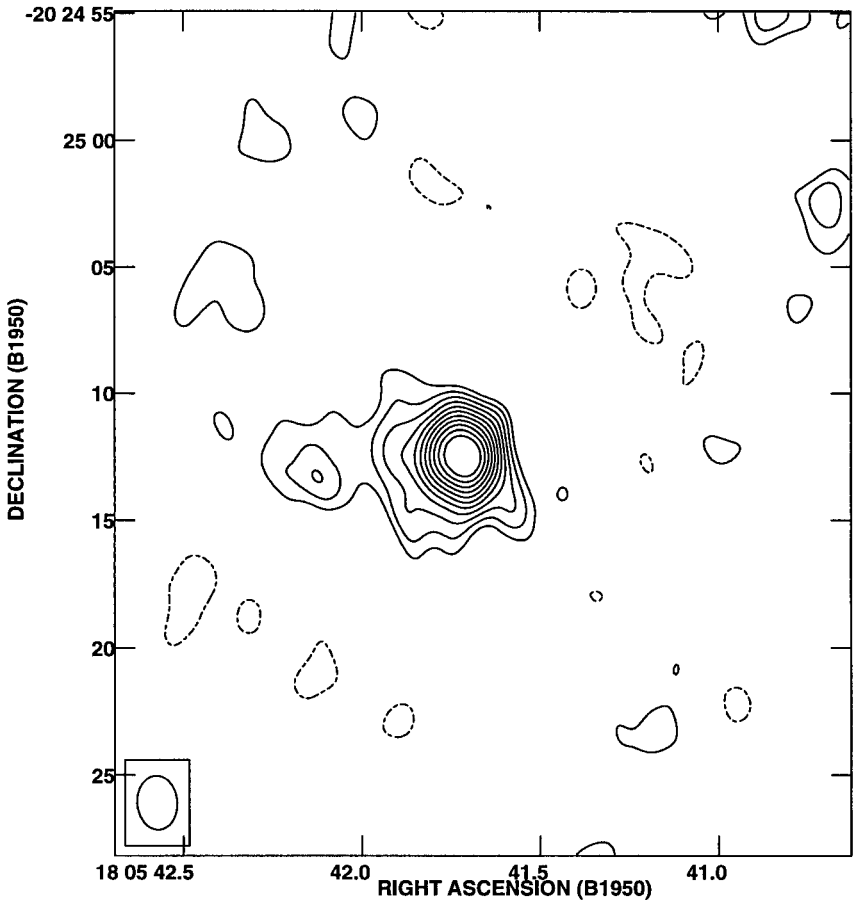

Figure 3.9: A 6-cm radio image of the radio "core" of G 10.0−0.3, suggesting a collimated outflow towards the east of the central source, on a scale of $\sim 6''$. The extended emission to the east is possibly a leftover from the emission seen in the earlier epoch of observation. The image is natural weighted, with a taper to produce a $2.12'' \times 1.57''$ beam with a position angle of 4.2°. This procedure picks up extended flux around the source. The peak contour flux is 820 μJy and the noise is 60 μJy. Contour multiples are -3, 2, 3, 4, 5, 6, 7, 8, 9. All coordinates are B1950.

3.4.3.2 - Morphology at 6-cm: Observing Intermediate Scales

Figure 3.9 displays a 6-cm spectral line map in total power after stacking all four frequency channels. The peak flux density of the core is 0.8 mJy beam^{-1} with a synthesized beam of $2'' \times 1.8''$. The cumulative flux is ~ 5 mJy corrosponding to a luminosity $L_R \sim 2.5 \times 10^{30} d_{10}^2$ erg s^{-1}. The small features visible at 3.6-cm (figure 3.8) close to the core are now unresolved. However, the map displays intermediate scale ($10''$) diffuse emission, mostly concentrated in the core but extending out to the east and southwest. This intermediate scale structure is beautifully reproduced at even larger scale (1 arcmin) in the VLA D-array map (Fig 3.4); providing an undisputable connection between morphology on the smallest (1 arcsec) and largest scales (1 arcmin) seen in G 10.0−0.3. A natural extension to this line of thought is as follows: If bursts accompany the ejection of particles seen on arcsecond scales, then all the emitting particles in the large nebula G 10.0−0.3 could have been deposted by the mechanism that powers the γ-ray bursts.

3.4.3.3 - Energetics of G 10.0−0.3

We apply the standard synchrotron model to G 10.0−0.3 (Pacholczyk 1970) in order to compute the quantity E_{min}, the energy in a synchrotron emitting plasma and associated magnetic fields assuming equipartition. Using low and high frequency cutoffs of 100 MHz and 100 GHz, $E_{min} \sim 10^{48}(1+k)^{4/7} d_{15}^{17/7}$ erg for G 10.0−0.3. Parameter $k = m_i/m_e$ parameterizes the nature of the plasma. Here m_e is the electron mass and m_i is the mass of the positively charged species.

For an $e^- - p^+$ plasma, $k \approx 2000$ and $E_{min} \sim 5 \times 10^{49} d_{15}^{17/7}$ erg. In a magnetar model with decaying magnetic fields powering the nebula, simple energy equivalence requires that the neutron star magnetic field B_{init} must be greater than 2×10^{16} G ($E_{min} \approx B^2 R_{NS}^3/6$). We note, however, that dipole fields with $B \gtrsim 6 \times 10^{15}$ G would suppress surface seismic activity due to continuous plastic deformation of the crust and therefore cannot power impulsive bursts (Thompson

& Duncan 1995). The magnetar burst model requires sudden movement of the neutron star crust to be associated with the bursts.

Alternatively, in a radiating e^+e^--plasma (as required in magnetar powered bursts) the minimum energy is $E_{min} \sim 10^{48} d_{15}^{17/7}$, requiring $B_{init} \sim 3 \times 10^{15}$ G. The activity of such a highly magnetized neutron star takes place on timescales of $10^4 - 10^5$ yr (Thompson & Duncan 1995). It is quite likely that G 10.0−0.3 is $\sim 10^5$ yr in age due to the absence of a pronounced shell of radio emission from a possible host supernova remnant (SNR lifetimes are $\sim 5 \times 10^4$ yr). The required energy injection rate in radio emitting particles during outbursts is therefore $E_B \sim 10^{43} d_{15}^2$ erg yr^{-1}. Our observations indicate $E_{min} \sim 5 \times 10^{42}$ erg in each individual feature associated with the small scale structure around the SGR certainly demonstrates that the required energy input could be satisfied by bursts alone. Using the 6-cm and 3.6-cm fluxes, we determine the spectral index of the core to be $\alpha \sim 0.6$ where $S_\nu \propto \nu^{-\alpha}$. We estimate an $E_{min} \lesssim 10^{43} d_{15}^{17/7}$ ergs alongwith an equipartition field strength of $B \sim 0.5$ milli-G.

The observed photon-to-particle energy ratio in a burst, E_γ / E_p, is of order 0.1 to 0.01 in SGR 1806−20. Using the same ratio, approximately 10^{46-47} erg could deposited in particles as an aftermath of the March 5 event due to SGR 0526−66. As a crucial test of our model, an "afterglow" of the March 5, 1979 event should be observable as a synchrotron nebula in the vicinity of that SGR.

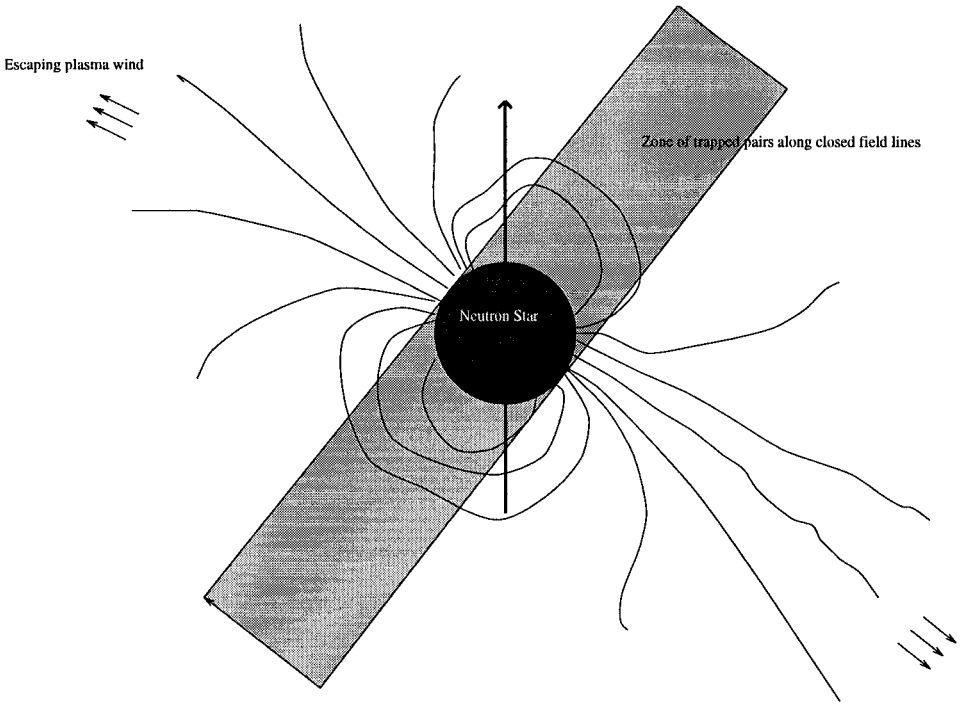

Figure 3.10: Deposition of $\gtrsim 10^{40-41}$ erg in the magnetosphere is sufficient to generate an optically thick photon-electron-positron plasma. The surface of the plasma lies along the magnetic field lines. The surface layers lose heat by radiative diffusion. Not all the energy released in a burst can be contained in the magnetosphere. The pressure of the photon-pair plasma drives a wind from the surface of the neutron star. This wind could possibly be observed as jet-like extentions in our radio data.

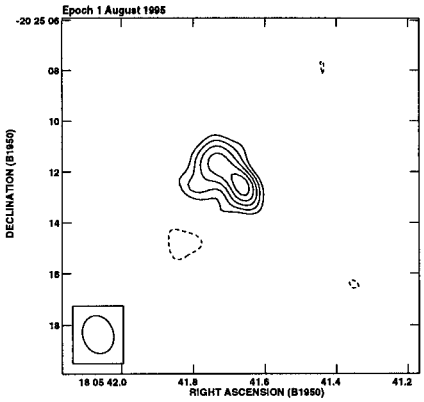
Epoch 1 August 1995
-20 25 06
08
10
12
14
16
18
DECLINATION (B1950)
18 05 42.0
41.8
41.6
41.4
41.2
RIGHT ASCENSION (B1950)

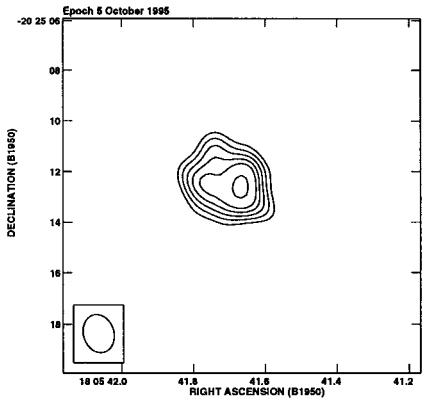
Epoch 5 October 1995
-20 25 06
08
10
12
14
16
18
DECLINATION (B1950)
18 05 42.0
41.8
41.6
41.4
41.2
RIGHT ASCENSION (B1950)

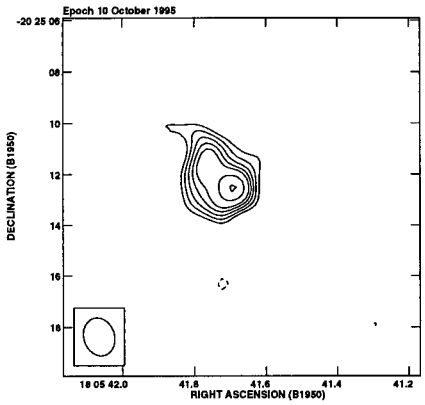
Epoch 10 October 1995
-20 25 06
08
10
12
14
16
18
DECLINATION (B1950)
18 05 42.0
41.8
41.6
41.4
41.2
RIGHT ASCENSION (B1950)

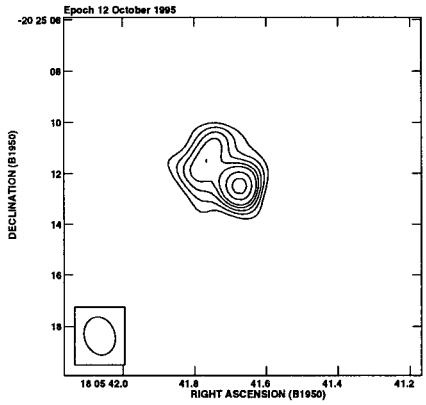
Epoch 12 October 1995
-20 25 06
08
10
12
14
16
18
DECLINATION (B1950)
18 05 42.0
41.8
41.6
41.4
41.2
RIGHT ASCENSION (B1950)

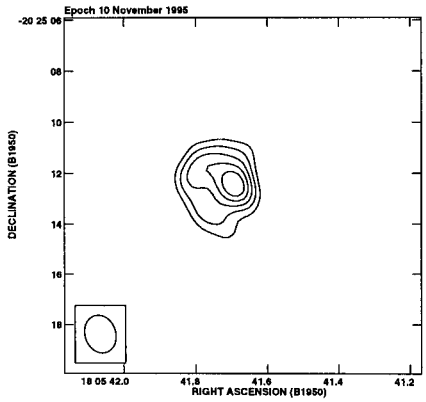
Epoch 10 November 1995
-20 25 06
08
10
12
14
16
18
DECLINATION (B1950)
18 05 42.0
41.8
41.6
41.4
41.2
RIGHT ASCENSION (B1950)

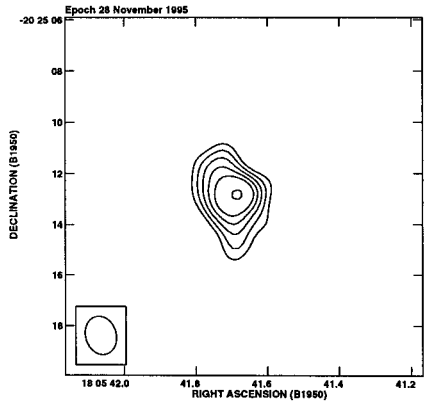
Epoch 28 November 1995
-20 25 06
08
10
12
14
16
18
DECLINATION (B1950)
18 05 42.0
41.8
41.6
41.4
41.2
RIGHT ASCENSION (B1950)

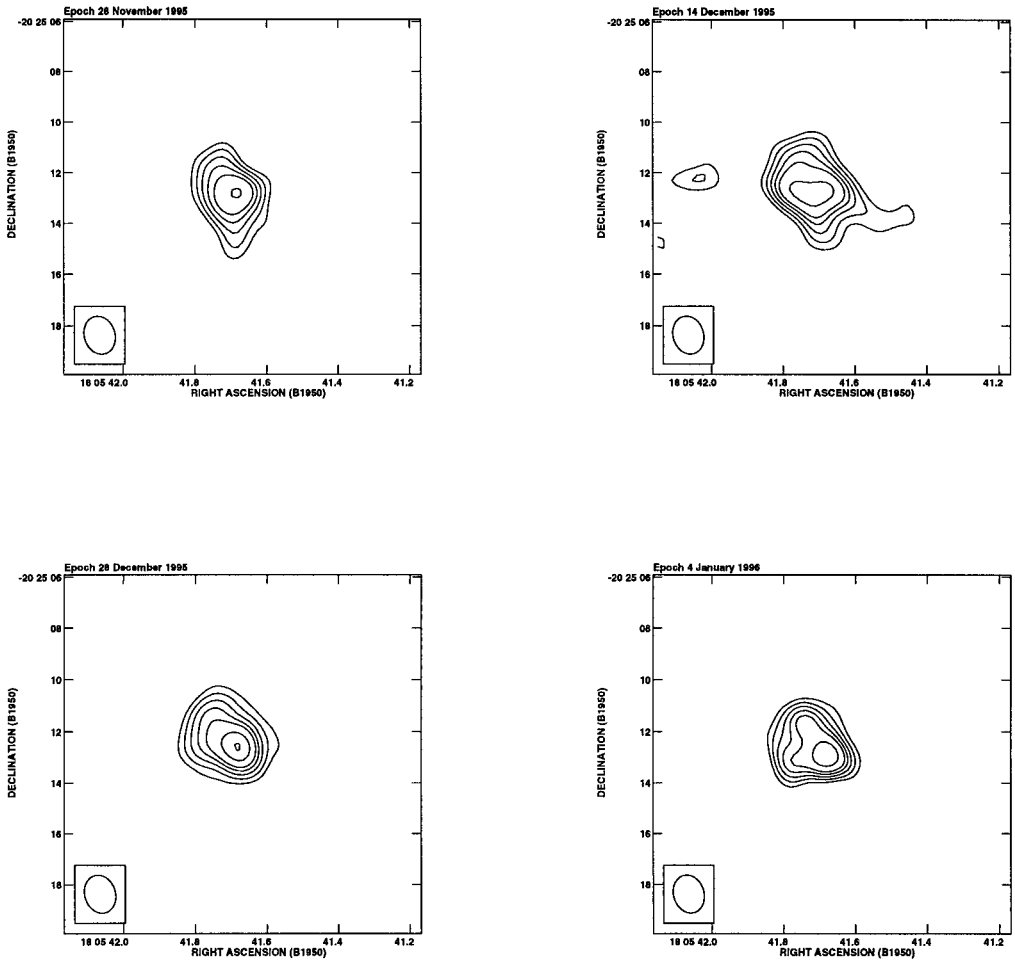

Figure 3.11: Multi-epoch X-band VLA B-array maps (except panel-1, which is an A-array map) of the central core of G 10.0−0.3 before and after the September 30, 1995, γ-ray burst. Details of the these observations are provided in Table 3.3. There is clear evidence for structural bubbling around the central peak. Contour levels are at -3, 3, 4, 5, 6, 7, 9, 11 times 45 μJy beam^{-1}. All coordinates are B1950.

REFERENCES

Harmon B. A. et al. 1995, Nature, 374, 703

Hjellming, R. M. & Rupen, M. P. 1995, Nature, 375, 464

Kouveliotou, C. et al. 1994, Nature, 368, 125

Kouveliotou, C. et al. 1995, I.A.U.C., 6242

Mirabel, I. F. & Rodriguez, L. F. 1994, Nature, 371, 46

Pacholczyk, A. G. 1970, Radio Astrophysics, Chap. 7, San Francisco: Freeman

Thompson, C. & Duncan, R. C. 1995, MNRAS, 275, 255 (TD95)

Ulmer, A., Fenimore, E. E., Epstein, R. I., Ho, C. & Klebesadel, R. W. 1993, ApJ, 418, 395

Vasisht, G., Frail, D. A. & Kulkarni S. R. 1995, ApJ, 440, L65

Table 3.1: ROSAT X-ray sources near the two SNRs*

Name	countrate cts/sec	brightness mag.	optical position (2000.0)
RX J190333+1043.9	0.072	10.1	19 03 33.7 +10 44 00
RX J190350+1039.1	0.013	11.1	19 03 48.5 +10 39 36
RX J190448+1025.8	0.008	-	
RX J190354+1018.1	0.010	-	
RX J190724+0843.4	0.015	10.1	19 07 23.4 +08 43 32
RX J190935+0845.2	0.009	-	
RX J190717+0919.3	0.011	-	

* X-ray position error is 30 arcsec in each co-ordinate

The first two X-ray sources have GSC counterparts. The source RX J190724+0843.4 is identified with star HD 178215.

Table 3.2: Monitoring history of G10.0−0.3

Epoch	τ_{int} (min)	"Core" flux (mJy)	Flux in nebula (mJy)	Elapsed time (days)
13^{th}Sep. 1993	33	4.78	38.1	-
2^{nd}Oct. 1993	22	4.24	32.0	3
6^{th}Nov. 1993	16	4.37	35.0	28
8^{th}Nov. 1993	10	3.91	32.0	30
22^{nd}Nov. 1993	19	3.73*	30.0	12
29^{th}Nov. 1993	27	6.32	48.1	19
6^{th}Dec. 1993	30	5.59	45.2	26
13^{th}Dec. 1993	49	5.38	40.5	33
7^{th}Jan. 1994	66	5.03	36.5	58
24^{th}Jan. 1994	50	5.22	39.9	75

Elapsed time is with respect to the last γ-ray burst.

All fluxes are in mJy; convolved beam 20×10 arcsec^2.

Epoch 1 in CnD array; rest in D array.

* Substantial number of short baselines missing during this epoch.

Table 3.4: Monitoring history of the G10.0−0.3 Core

Epoch	VLA array	τ_{int} (hr)	Peak Core Flux (mJy)	Elapsed time (days)
7^{th}Mar. 1994	A	1.1	0.35	-
1^{st}Aug. 1995	A	1.1	0.36	-
5^{th}Oct. 1995	B	0.5	0.44	5
10^{th}Oct. 1995*	B	0.8	0.51	10
12^{th}Oct. 1995	B	0.9	0.54	12
10^{th}Nov. 1995	B	0.6	0.37	41
28^{th}Nov. 1995	B	0.8	0.41	59
14^{th}Ded. 1995	B	0.5	0.45	75
28^{th}Dec. 1995	B	1.0	0.50	89
4^{th}Jan. 1996	B	2.0	0.49	95

Elapsed time is with respect the γ-ray burst on Sept 30, 1995.

All fluxes are in mJy; convolved beam 2×1.5 arcsec^2.

Epoch 6 is repeated twice in Fig 3.10 for continuity.

* Substantial number of short baselines missing during this epoch.

CHAPTER 4: X-RAY OBSERVATIONS OF PULSAR PLERIONS

4.1 OVERVIEW

4.1.1 – YOUNG NEUTRON STARS

An interesting astrophysical problem is the determination of birth magnetic fields and spin period distribution of neutron stars. In the so-called "vacuum models" for pulsars these two parameters determine the fate of the newborn neutron star. For this, young pulsars are useful as their surface dipole fields are easily inferred and thought not to undergo decay at least on timescales of $\lesssim 10^5$ yr (Bhattacharya et al. 1992, Wakatsuki et al. 1992). If their true ages are known from historical records, as in the Crab pulsar, or from diagnostics of the surrounding supernova remnant (Draine & Mckee 1993), the initial spin period can be determined using a standard spin-down law (Manchester & Taylor 1977). Let us, however, address the two caveats at hand here:

i) Just two historical radio pulsars the Crab (Clark & Stephenson 1977) and PSR B 1509−58 (Thorsett 1992; Chin & Huang 1994) are known and five others have reliable supernova remnant associations (Kaspi 1996). Most young galactic remnants have a shell morphology, i.e., are hollow (Weiler & Sramek 1988, Blandford et al. 1983). The sample of stars from which initial pulsars parameters can be determined is, therefore, rather small. Unfortunately, in spite of the relatively nearby SN 1987A, we have so far been unable to detect

the neutron star, let alone measure its parameters (recent searches are by Manchester & Peterson 1996, Percival et al. 1995).

ii) Neutron stars may have a large spread in the B and P_{init} phase space, whereby, some may never turn on as pulsars; others could have a short-lived or underluminous pulsar phase (Radhakrishnan & Srinivasan 1983, Narayan 1987). It is of utmost importance, therefore, to gather evidence to such alternative scenarios of pulsar birth. Evidence for "magnetars" may already be mounting (see Chapter 3; Vasisht et al. 1995, Thompson & Duncan 1995). Neutron stars that do become radio pulsars could have a restricted range in spin period and magnetic field distribution at birth. The observed sample of the youngest pulsars has rather uniform characteristics: magnetic field strengths, $B \sim 10^{12.5}$ G and inferred initial periods of less than 100 ms, and almost all are associated with an SNR (Frail et al. 1994). The converse is certainly not true, and many young remnants are seemingly pulsar-less (prominent among them is Cas A; Holt et al. 1994). At least one statistical study of pulsar populations has claimed that a large fraction of all pulsars must be born spinning slowly with periods $P_i \gtrsim 0.5$ s (Narayan 1987). This so called "injection hypothesis" is controversial, as other pulsar population analyses also do not find injection compelling (Lorimer et al. 1993). Energy content in relativistic particles of observed plerions argue for rapid spin periods of pulsars at birth (Helfand & Becker 1987).

The largest fraction ($\gtrsim 0.90$) of pulsar spin-down losses are dominated by torques from a relativistic wind (Goldreich & Julian 1969, Rees & Gunn 1974, Kennel & Coroniti 1984). This wind is shocked at a certain distance from the pulsar to create a synchrotron nebula, termed as a "plerion". In the absence of direct observations of a pulsar, plerions provide the best diagnostic tool to measure the characteristics of the neutron star (see Section 4.1.5) as well as for the study of the composition of the pulsar wind. Both of these are poorly understood. Plerions emit isotropically, unlike the pulsars powering them. Modern X-ray and

radio observatories with high sensitivity and spectral coverage could detect enough plerions to permit a comprehensive study of the variations in the "central engine".

4.1.1.1 – Associations of Pulsars with Supernova Remnants

Most neutron stars are thought to have their origin in type II or Ibc supernova explosions associated with comparatively young, high mass stars (Arnett 1978 and 1979). When the central pressure support of the star fails, the core implodes and the surrounding envelope undergoes a radial inflow, followed by bounce and then outward ejection. If the newborn neutron star can initiate pair cascades (Sturrock 1970, Manchester & Taylor 1977) then it should be visible as a radio luminous pulsar within an expanding supernova remnant (SNR).

Statistical studies of the Galactic pulsar population have established that their birthplace is the OB-associations and denser gas in the spiral arms from which massive stars arise. The evidence includes the Galactic pulsar distribution (Lyne, Manchester & Taylor 1985), their kinematics (Lyne, Anderson and Salter 1982), and their birthplaces (Narayan & Ostriker 1990). However despite the insight gained from these indirect methods, statistical analysis is no substitute for direct observational proof. Lacking any recent supernovae nearby, we turn to young pulsars and their associated supernova remnants. There exist ~ 25 proposed associations between radio pulsars and supernova remnants (Frail et al. 1994; Kaspi 1996) to date, amongst ~ 700 pulsars (Taylor et al. 1993; Princeton pulsar database at `http://pulsar.princeton.edu/`) and nearly 300 SNR (Green 1991, Green Catalogue at `http://www.phy.cam.ac.uk/www/research/ra/SNRs/`). Only seven (Kaspi 1996) of these are compelling. Several others could be mere chance positional coincidences. Intriguingly though, all but three of the youngest radio pulsars have host supernova remnants (The characteristic ages of young pulsars are $\tau \lesssim 6 \times 10^4$ yr; the rationale we use for the definition of "young" is the typical radio lifetime of a SNR (Frail et al. 1994)).

4.1.1.2 – Types of Supernova Remnants

Detailed radio and X-ray observations have established that there are three distinct types of supernova remnants. The vast majority have the appearance of shells with little or no central emission (the Tycho and Kepler SNR, SNR 1006 etc.). Another class are centrally filled which have no limb brightening (e.g., the Crab and 3C58). The third category of remnants are of a hybrid nature and are called "Composite" SNR – they possess a shell surrounding a centrally condensed nebula. The relative numbers of these three classes are in the ratio 10:1:1 (Weiler & Sramek 1988, Green 1991).

The reasons for the occurrence of these three types of remnants is well understood. It is widely accepted that the filled-center SNR are powered by the spin-down luminosity of an energetic central pulsar, although in many cases the pulsar may not be beamed in our direction. Pronounced shell emission is the result of interaction of the supernova ejecta with the surrounding interstellar medium. The hybrid remnants, by extension, are the result of an active pulsar at the site of the supernova explosion (Bhattacharya 1990).

It is not well understood, why the majority of SNR have hollow interiors. The explanation most often invoked is that shells and plerions are the result of different types of supernovae. Although it is reasonable to associate plerions with supernovae that left behind an active pulsar, it is not at obvious that the hollow shells do not harbor active pulsars. The identification of the majority of shells with Type Ia supernovae is difficult for the following reason: recent studies of supernova statistics indicate that Galactic statistics of supernovae of Type Ia, Type Ib and Type II are in the ratio 3:4:11 (van den Bergh et al. 1987). If the progenitors of the Type Ibc supernovae are also massive, but binary, stars (van den Bergh 1988), then they too might leave behind neutron stars. Thus the hollow appearance of most SNRs cannot, in most cases, be attributed to the absence of central pulsars.

The surface brightnesses of the shell and plerionic components will determine the morphology of the supernova remnant, i.e. $\Sigma_{shell}/\Sigma_{plerion}$. These are independently determined by the following items:

i) Dependence of the morphology on the pulsar parameters. The plerionic surface brightness is a function of the initial spin and magnetic field of the pulsar (Bhattacharya 1990). Pulsars like the Crab can produce bright long-lived plerions; very rapidly spinning pulsars ($\sim$ 5 ms) produce only very short lived, but brilliant plerions whereas slow pulsars are expected to power faint, low surface brightness plerions.

ii) Mechanical energy in the supernova ejecta. Weak supernova ($_{\circ} \sim 10^{49}$ erg) dynamics can be altered by a central pulsar. Crab and 3C58 like SNR that display no limb brightening (Frail et al. 1995) could be the consequence of such weak explosions ($E_{\circ} \sim 10^{49}$ erg).

iii) Variations in the ISM density. Due to the evacuation of a bubble by the pre-supernova stellar wind or due to the vagaries of the ISM, the ambient density around the expanding supernova could vary between 0.001 cm^{-3} to 10 cm^{-3}. The surface brightness of the supernova shell is a function of this ambient density. Shells expanding into low density medium are fainter than those expanding into dense interstellar matter.

When all these effects are taken into consideration, it is apparent that bright plerions can occur only under certain special conditions. The observed excess of shell-type remnants may be artifact of these effects. It is important to realize that in the future more shells could be reclassified as composite remnants when the dynamic ranges of radio and X-ray observations of SNR improve.

4.1.2 – PULSAR PLERIONS

The simplified picture of a non-Type-Ia SNR is described below. In a supernova, a blast wave moves out initially at $\sim$ 5000 kms^{-1}. The blast wave shocks the

interstellar medium, radiates non-thermally in the radio, thermally in the X-rays and is visible as an expanding shell. After an initial free expansion phase (when $M_{swept} \gg M_{ejecta}$ the blast's development is governed by the Sedov solution (McCray 1987):

$$R_s(t) \approx 10 \text{ pc } (\frac{E_o}{10^{51} \text{ erg}})^{0.2} (\frac{n_o}{1 \text{ cm}^{-3}})^{-0.2} (\frac{t}{5 \times 10^3 \text{ yr}})^{0.4} \tag{4.1}$$

where $R_s(t)$ is the shell radius, E_o, the mechanical energy in the ejecta, n_o, the ambient particle density of the ISM and t, the time since explosion. Meanwhile, the nascent pulsar creates an expanding bubble of magnetic fields and relativistic particles which radiate via synchrotron mechanism from radio to X-ray wavelengths. The time dependence of the pulsar energy input $\dot{E}$ into the bubble is given by

$$\dot{E} = \frac{\dot{E}_\circ}{(1 + t/\tau_\circ)^p} \tag{4.2}$$

where $p = (n+1)/(n-1)$, with n the standard braking index, $n \equiv \Omega\ddot{\Omega}/\dot{\Omega}^2$ (Ω is the pulsar angular speed). So p is expected to be in the range 1.8-2.7, or roughly 2 (for the Crab, $p = 2.3$: Groth 1975). This corresponds to a theoretically reasonable range of n between 2 and 5 (Manchester & Taylor 1977). For a pure dipole rotator, $p = 2$. Here t is the time since the supernova and $\tau_\circ$ is a characteristic slowing-down time; generally $\tau_\circ \sim 300$ to 700 yr. The injected particles are visible as a central non-thermal nebula i.e. a "plerion". The plerionic shock radius R_p, the point at which the pulsar wind is thermalized, is easily determined by equating the momentum-flux of the pulsar wind: $P_p \sim \dot{E}/4\pi R_p^2 c$, to the pressure of the isothermal gas in the shell interior: $P_s \sim E_o/2\pi R_s^3$. We obtain

$$R_p \sim 0.1 \text{ pc } (\frac{\dot{E}}{10^{38} \text{ erg s}^{-1}})^{0.5} (\frac{t}{\tau_0})^{-0.5p} (\frac{E_o}{10^{51} \text{ erg}})^{-0.2} (\frac{n_o}{1 \text{ cm}^{-3}})^{-0.3} (\frac{t}{5 \times 10^3 \text{ yr}})^{0.6} \tag{4.3}$$

Here n_o is the particle density of the pre-shocked gas. Most young (t $< 10^4$ yr) non-Type-Ia shells should then harbor neutron stars and possess a compact filled center component which would be seen in X-rays via synchrotron emission (Weiler and Panagia, 1980; Becker et al. 1982). Such a center filled remnant

is known as a "Composite". The lifetime of a typical plerion is $\sim 10^4$ yr and depends upon the pulsar power and the synchrotron cooling rate of the pulsar wind (Bhattacharya 1990). We have stressed before that the minimum size (eqn. 4.3) and the luminosity of a plerion are governed by a large set of free parameters. These possess large intrinsic variations, e.g., n_o can vary from 0.001 to 10 cm^{-3}. As another example, extreme variations in E_o as in weak supernovae (small E_o) can give rise to pure plerions if the pulsar's initial rotational energy is comparable to E_o (usually negligible; < 1 %) as in the Crab nebula (Bhattacharya 1990).

In order to predict the synchrotron luminosity and spectrum of the bubble, a detailed calculation of the spectrum of the injected relativistic particles in energy and time is required (Reynolds & Chevalier 1984). Evolutionary effects, chiefly synchrotron and adiabatic losses, will cause the bubble's particle distribution to differ from the injected spectrum, say $N(E) \propto E^{-s}$. Synchrotron losses will affect the shape of this spectrum of the continuously injected particles in a standard way (see, e.g. Pacholczyk 1970): Above some break energy E_b, the spectrum steepens by one power of the energy, with E_b the energy at which the synchrotron loss time-scale equals the dynamical timescale $\tau_{dyn} \approx \dot{R}_p/R_p$, where R_p is the plerion radius. E_b is found by the relation,

$$\tau_{dyn} = \frac{6\pi}{\sigma_T c} \frac{(m_e c^2)^2}{B^2 E_b} \qquad (4.4).$$

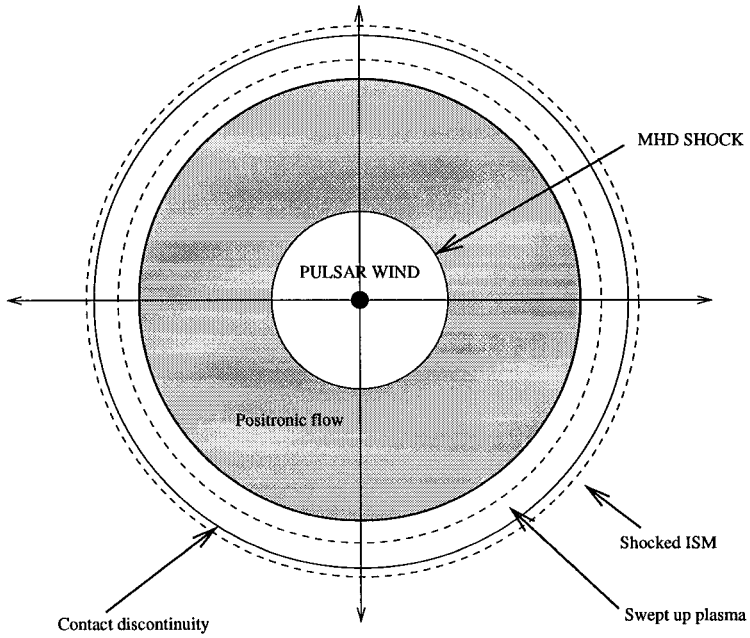

Schematic relation between a Plerion and Supernova Remnant

Figure 4.1: Schematic relation between a plerion and an expanding supernova remnant: This figure represents an idealized model of a plerion (e.g. the Crab Nebula). The dot in the center represents the pulsar with its magnetosphere where a relativistic positronic plasma is created. The plasma organizes itself into a reasonable spherically symmetric wind which is contained within the innermost circle of the figure. The wind zone is bounded by a strong relativistic MHD shock (this zone has a radial extent of ~ 0.1 pc in the Crab). The plerion is the zone of decelerated positronic flow between the shock and the inner edge of the supernova remnant. The inner shock forms as a result of the ram pressure of the relativistic pulsar flow. Adapted from Kennel & Coroniti (1984a).

At the very earliest times, the plerion expands freely and the magnetic energy density is large and the newly injected particles loose energy rapidly via both synchrotron radiation and adiabatic expansion. The initial spectrum of radiating particles is given by $\propto E^{-s-1}$ ($E_b < m_e c^2$) for an injected particle spectrum, $N(E) \propto E^{-s}$. At later times, as the plerion expands, E_b the spectral break propagates to higher energies with a value determined by particles whose synchrotron cooling times are equal to τ_{dyn} of the plerion. We mention that the break energy increases with time because of the rapid fall in B as the plerion expands.

Plerions are observed to fall into this framework but with some important differences. In the Crab the spectral break is at $\approx 10^4$ GHz with a spectral change of 0.5 (Marsden et al. 1984). However reported breaks in spectra of other filled center remnants, most of which are thought to be older than the Crab are at frequencies between $\approx$ 10 to 100 GHz (Reich, Fürst & Sofue 1984, Morsi & Reich 1987, Salter et al. 1989). For example 3C58 has a distinctly low break near 50 GHz. It is similar to Crab in both distance and age but has twice the diameter and is much fainter at all wavelengths (Green 1986). It pointed out by Green and Scheuer (1992) it is possibly very significant that the Crab has a central pulsar, but not 3C58, G21.9-0.9 and G74.9+1.2 for which there is evidence for cm-wave break frequencies.

4.1.2.1 – Plerion Search Strategy

Supernova remnants have classically been studied well at the low frequency radio ($\nu_R \sim 1$ GHz) and in soft X-rays. Viewed in this manner, there are clear drawbacks to finding plerionic emission. The surface brightness of shell emission usually dominates X-ray emission in the soft X-ray band of 0.1-2 keV and in the radio at low frequencies. A better recipe for searching for plerions is to obtain:

i) High radio frequency mapping of SNR. Shells have steep synchrotron spectral index of 0.7 ($S_\nu \propto \nu^{-\alpha}$). Plerionic emission in the radio is flat spectrum, with $\alpha \sim 0.2$. Plerions should, therefore, become more dominant at higher

radio frequencies. An interferometric survey of Galactic SNR at 10-100 GHz frequencies would be most interesting.

ii) Broadband X-ray imaging and spectroscopy. Supernova shocks produce thermal bremsstrahlung at $kT \lesssim 1$ keV; much of the energy appears at $h\nu \sim 4kT$. Plerions, on the other hand, are expected to show harder non-thermal tails that can be mapped with X-ray observatories having detectors with good hard X-ray coverage (5 to 10 keV) or better still, a good broadband response (0.1 to 10 keV).

4.1.2.2 – Using Plerions as Calorimeters

Plerions can be used as crude calorimeters to measure the host pulsar energetics in the absence of directly observed pulsed emission. The total energy of radio emitting particles, inferred from the plerion radio spectrum, is a fossil record for the initial state of the pulsar with $E_{min} \sim 1/2I\Omega_i^2$ (Helfand & Becker 1987). This minimum energy estimate based on the radio spectrum should give a reasonable value for the total energy in the nebula. This is because radio emitting particles of Lorentz factors $\gamma \sim 10^2$ have radiative lifetimes much larger than the age of the nebula (the time taken for a particle to radiate half its energy is $t_{1/2} \sim 5 \times 10^8/\gamma B^2$ s). The X-ray luminosity reflects the present day $\dot{E}$ because of short radiative times ($\sim$ years) of X-ray emitting particles ($\gamma \gtrsim 10^6$). A small fraction ~ 5 % of the spindown luminosity is channeled into the X-ray luminosity.

The shape of the radio to X-ray spectrum of the plerion is extremely informative. For instance the location of the synchrotron burn-off break frequency $\nu_b \propto B_n^{-3}\tau^{-2}$ in the spectrum, resulting from aging of high energy particles, can be used to estimate the age (τ) or ambient magnetic field (B_n). The spectral shape also puts constraints of the injected particle spectrum and the wind constituents (Kennel & Coroniti 1984; Gallant & Arons 1994). Constructing a detailed MHD model of a pulsar wind has been possible only for the Crab nebula as it has been studied in great detail (Kennel & Coroniti 1984). Although other plerions have

poorly determined spectra, there is clear evidence that they can be quite different from the Crab's (Green & Scheuer 1992; Vasisht et al. 1995). Measurements leading to classification of various types of plerions are therefore of utmost importance.

4.1.3 – PLERION SEARCHES WITH ASCA

In our estimation, a complete census and study of plerionic SNR is essential before one can start tackling questions about neutron star birth from an empirical standpoint. This chapter discusses our ongoing program to search and study plerionic emission with the Advanced Satellite for Cosmology and Astrophysics (ASCA). As part of this program, we have first observed the historical supernova remnant G 11.2−0.3 (see Section 4.2). Also observed, is the intriguing central source in the SNR PKS 1209−58 (Section 4.3). Sensitive observations of three other SNR showing marked signature of plerionic activity have recently been accumulated. These are Kes 73, MSH 11−62 and G 327.1−1.1 (Seward 1990)

Sensitive observations of other remnants using ASCA are being undertaken by several other groups. However, the main thrust of many of these investigations is to study the emission from the shock heated shell region. Eventually, supernova remnants in these datasets should be thoroughly examined for residual harder emission and should result in a plerion database of unprecedented quality.

ASCA's wide band response (0.5-10 keV) is optimal for the study of supernova remnants (Tanaka et al. 1994). Its good sensitivity at higher energies makes it attractive for searching for residual non-thermal emission from plerions over and above the confusing thermal shock emission. Along with Solid State Imaging Spectrometer (SIS) imaging and spectral analysis, Gas Scintillation Imaging Spectrometer (GIS) time tagged photons can be utilized to do a time series analysis in search of a pulsed component to the X-ray emission (SIS and GIS are ASCA detectors; see §2.2 for details of ASCA detectors and Tanaka et al. 1994).

In conjunction with studies of the plerion, thermal X-ray studies of the blast wave (shell component) are equally necessary to establish a complete picture of

the SNR, as the shell is what the plerion expands into. Accurate post-shock temperature estimates are necessary for a complete Sedov solution of the supernova blast. Spectral line information coupled with sophisticated NEI modeling gives good constraints for the age of the remnant (Draine & Mckee 1993). Elemental abundances derived from line emission (such as K-α emission from various metal species) give clues as to the nature of the original supernova (Aoki 1995; Vasisht et al. 1995). Hughes et al. (1995) have recently demonstrated classification of six young LMC remnants based on an abundance analysis of ASCA spectra alone and claimed a higher incidence rate of Type Ia supernovae than expected.

4.1.3.1 – Lessons learnt from G11.2-0.3

ASCA observations of the young shell SNR G 11.2−0.3 have been of pedagogical value in many regards (Section 4.2 for details). This SNR has proven the validity of the strategy outlined in §4.1.2.1. In-spite its importance as the only candidate for historical supernova of AD 386, the nature and classification of G 11.2−0.3 has certainly been a confused issue. The SNR has been classified as Type II based on the structure of its radio shell (Green 1988) and flattening of the spectral index at the high radio frequencies (Morsi & Reich 1988); and as Type Ia based on soft X-ray ROSAT PSPC observations (Reynolds et al. 1994). Our ASCA observations (described in detail in section 4.2), support the suspected historical nature of the remnant and have detected a centrally concentrated hard X-ray plerion. However, the youth of G 11.2−0.3 inferred from its bright radio shell is not in congruence with its underluminous plerion. Though G 11.2−0.3 shares with the Crab SNR, a young age, its plerion vastly differs in character, implying a central energy source very different from the Crab pulsar. In addition, these observations strongly suggest that the preponderance of shells in the Galaxy must be an artifact of the lack of high enough dynamic range observations of its SNR (Bhattacharya 1990).

We summarize some important properties of the plerion. For G 11.2−0.3 the X-ray spectrum is $S_\nu \approx 1\mu\text{Jy}(\nu/2.5\times10^{18}\text{ Hz})^{-0.8}$ at 5 keV. Using radio measurements (Morsi & Reich 1987) we infer a break in the spectrum $\nu_b \lesssim 32$ GHz. Equating the dynamic age to the synchrotron cooling age, $\nu_b \approx 4\times10^{23}B^{-3}\tau^{-2}$ Hz; and using the G 11.2−0.3 parameters, $\tau \sim 1600$ yr and $\nu_b \lesssim 32$ GHz we infer a huge nebular magnetic field $B_n \gtrsim 2$ mG; more than an order of magnitude larger than the ambient field in the Crab nebula. B_n can be also be derived under the condition that the shell interior and plerion are in close pressure equilibrium. The shell is isobaric with interior pressure $P \approx E_\circ/2\pi R_s^3$; where $E_\circ$ is the supernova energy and R_s is the shell radius (G 11.2−0.3 characteristics are deduced in Section 4.2.3). The inferred pressure $P \sim 3\times10^{-7}$ dynes cm^{-2} is identical to the plerion pressure $B_n^2/8\pi$, if only as above $B_n \sim 2.5$ mG. The nebular field derived from equipartition assumptions, however, is an order of magnitude too low. We can compute a minimum energy in the radio synchrotron particles assuming equipartition. From radio emission (see Fig 4.3), the minimum energy in the radio nebula is $E_{min} \sim 10^{47}d_5^{17/7}$ erg and the equipartition field strength is $B_e \sim 0.1$ milli-G; distance is $5d_5$ kpc (Pacholczyk 1970). Using the equipartition field strength in conjunction with the break frequency ($\nu_b \sim 30$ GHz) we infer a nebular age of 9×10^4 yr. This age (10^5 yr) is much larger than the actual age of plerion ($\sim 2\times10^3$ yr). We regard the equipartition assumption as incorrect and conclude that most of the nebular energy is free magnetic energy and not in radiating particles, making the source underluminous and far from equipartition.

With a plerion extent of $\gtrsim 1d_5$ pc, the minimum energy in magnetic fields in the G 11.2−0.3 core is simply $W_p \gtrsim 2\times10^{49}d_5^3$. The minimum size of 1 pc is deduced from the angular extent of the core X-rays in the EINSTEIN HRI image (Fig 4.2). Its actual size may be greater than $1d_5$ pc as X-ray radiating particles are short-lived and may under-fill the plerion. The maximal plerion would completely fill the shell interior, implying that $R_p < 3.1d_5$ pc and $W_p < 6\times10^{50}d_5^3$ erg (section 4.2.3). Since neutron star spin-down energizes the nebula, it follows that the birth period must fall in the range 4 ms $< P_{init} \lesssim 30$ ms. Also, the central pulsar has

to be born powerful, requiring an average power input of $\dot{E} = W_B/\tau \gtrsim 5 \times 10^{38}$ erg s^{-1} to be pumped into the plerion within the last two millennia. This is more than an order of magnitude greater than the present day $\dot{E} = 10^{36.9}$ erg s^{-1} as inferred from L_X (Section 4.2.3).

Even though they are contemporaries, the plerion in G 11.2−0.3 differs from the Crab nebula in striking ways: the former seems to be dominated by magnetic energy and is underluminous from radio to X-rays and does not seem in equipartition. Qualitatively, we can say that the central pulsars could be very different in energetics and in composition of the wind. If, unlike the Crab, the pulsar wind in G 11.2−0.3 is dominated by outflow of magnetic fields, the magnetic field strength would diminishes as r^{-3} within the pulsar light cylinder and as r^{-1} in the radiation zone. For a magnetic field profile in the Crab nebula refer to Kennel & Coroniti (1984). A backward extrapolation of B_n to the core of G 11.2−0.3 requires that the *surface field of the neutron star must be enormous*, at least a factor $\gtrsim 10$ higher than the $B_{dipolar} \approx 4 \times 10^{12}$ inferred in PSR B 0531+21.

REFERENCES

Aoki, T. 1995, PhD Thesis, Gakushuin University

Arnett, W. D. 1978, ApJ, 219, 1008

Arnett, W. D. 1979, "Gravitational Collapse of Evolved Stars as a Problem in Physics," ApJ, ed. L. L. Smarr, Cambridge University Press, Cambridge, England.

Becker, R. H., Helfand, D. J. & Szymkowiak, A. E. 1982, ApJ, 255, 557

Bhattacharya, D. 1990, JAA, 11, 125

Bhattacharya, D., Wijers, R. A. M. J., Hartmann, J. W. & Verbunt, F. 1992, A&A, 254, 1992

Blandford, R. D., Applegate, J. H. & Hernquist, L. 1983, MNRAS, 204, 1025

Chin, Y. N. & Huang, Y. L. 1994, Nature, 371, 398

Clark, D. H. & Stephenson, F. R. 1977, in The Historical Supernovae (Oxford: Pergamon)

Draine, B. T. & McKee, C. F. 1993, ARA&A, 31, 373

Frail, D. A., Goss, W. M. & Whiteoak, J. B. Z. 1994, ApJ, 437, 781

Frail, D. A., Kassim N. E., Cornwell T. J. & Goss, W. M. 1995, ApJ, 454, L129

Gallant, Y. A. & Arons, J. 1994, ApJ, 435, 230

Goldreich, P. & Julian, W. H. 1969, ApJ, 157, 869

Green, D. A. 1986, MNRAS, 218, 533

Green, D. A. 1991, PASP, 103, 209

Green, D. A. & Scheuer, 1992, MNRAS, 258, 833

Groth, E. J. 1975, ApJS, 29, 453

Helfand, D. J. & Becker, R. H. 1987, ApJ, 314, 203

Holt, S. S., Gotthelf, E. V., Tsunemi H. & Negoro, H. 1994, PASJ, 46, L151

Hughes, J. P. et al. 1995, ApJ, 444, L81

Kaspi, V. M. 1996, to appear in IAUC 165, PASP, eds. S. Johnston, M. Bailes and M. Walker

Kennel, C. F. & Coroniti, F. V. 1984, ApJ, 283, 694

Lorimer, D. R., Bailes, M., Dewey, R. J., Harrison, P. A. 1993, MNRAS, 263, 403

Lyne, A. G., Anderson, B., Salter, M. J. 1982, MNRAS, 201, 503

Lyne, A. G., Manchester, R. N. & Taylor, J. H. 1985, MNRAS, 213, 613

Manchester, R. N. & Peterson, B. A. 1996, ApJ, 456, L107

Manchester, R. N. & Taylor, J. H. 1977, "Pulsars", W. H. Freeman & Co.

Marsden, P. L. et al. 1984, ApJ, 278, L29

McCray, R. 1987 in Spectroscopy of Astrophysical Plasmas, Eds. A. Dalgarno & D. Layzer, Cambridge Univ. Press, 255

Morsi, H. W. & Reich, W. 1987, A&ASS, 71, 189

Narayan, R. 1987, ApJ, 319, 162

Narayan, R. & Ostriker, J. P. 1990, ApJ, 352, 222

Pacholczyk, A. G. 1970, Radio Astrophysics, Chap. 7, San Francisco: Freeman

Percival, J. W. et al. 1995, ApJ, 446, 832

Radhakrishnan, V. & Srinivasan, G. 1983, in IAU Symposium 101: Supernova Remnants and their X-ray Emission, eds. J. Danziger & P. Gorenstein, D. Reidel, Dordrecht, 421 pp.

Rees, M. J. & Gunn, J. E. 1974, MNRAS, 167, 1

Reich, W., Fürst, E. & Sofue, Y. 1984, A&A, 133, L4

Reynolds, S. P. & Chevalier 1984, ApJ , 278, 630

Reynolds, S. P., Lyutikov, M., Blandford, R. D. & Seward, F. D. 1994, MNRAS, 271, L1

Salter, C. J., Reynolds, S. P., Hogg, D. E., Payne, J. M. & Rhodes, P. J. 1989, ApJ, 338, 171

Seward, F. D. 1990, ApJS 73, 781

Shapiro, S. L. & Teukolsky, S. A. 1983 in Black Holes, White Dwarfs and Neutron Stars, A Wiley-Interscience publication

Sturrock, P. A. 1970, Nature, 227, 465

Tanaka, Y., Inoue, H. & Holt, S. S. 1994, PASJ, 46(3), L37

Taylor, J. H., Manchester, R. N. & Lyne, A. G. 1993, ApJS, 88, 529

Thompson, C. & Duncan, R. C. 1993, ApJ, 408, 194

Thorsett, S. E. 1992, Nature, 356, 690

van den Bergh, S. 1988, ApJ, 327, 156

van den Bergh, S., McClure, R. D. & Evans, R. 1987, ApJ, 323, 44

van den Bergh, S. & Tammann, G. 1991, ARA&A, 29, 363

Vasisht, G., Aoki, T., Dotani, T., Kulkarni, S. R. & Nagase, F. 1995, ApJ, 456, L59

Wakatsuki, S., Hikita, A., Sato, N. & Itoh, N. 1992, ApJ, 392, 628

Weiler, K. W. & Panagia, N. 1980, A&A, 90, 269

Weiler, K. W. & Sramek, R. A. 1988, ARAA, 26, 295

4.2 DETECTION OF A HARD X-RAY PLERION IN THE CANDIDATE HISTORICAL REMNANT G 11.2–0.3†

G. Vasisht

California Institute of Technology, MS 105-24, Pasadena, CA 91125

T. Aoki

Institute of Space and Astronautical Science, 3-1-1

Yashinodai, 3-Chome, Sagamihara, Kanagawa 299, Japan

T. Dotani

Institute of Space and Astronautical Science, 3-1-1

Yashinodai, 3-Chome, Sagamihara, Kanagawa 299, Japan

S. R. Kulkarni

California Institute of Technology, MS 105-24, Pasadena, CA 91125

and

F. Nagase

Institute of Space and Astronautical Science, 3-1-1

Yashinodai, 3-Chome, Sagamihara, Kanagawa 299, Japan

ABSTRACT: We present the results of a 32-ks ASCA observation of G 11.2−0.3, by far the strongest candidate for the remnant of the historical supernova SN 386AD. A center brightened, hard, non-thermal X-ray source was found within the remnant which we interpret to be plerionic emission due to an embedded pulsar. Our observations indicate that the remnant is a member of the class of "composite" remnants, as was hinted by previous observations. The central emission is not pulsed down to a detection limit of $\sim 10^{33}$ erg s^{-1}. It could be that the putative pulsar is not beamed in our direction. We also argue that the distance and surface brightness of G 11.2−0.3 imply that the remnant is young and very likely to be the counterpart of the supernova observed by the Chinese in AD 386 making it the youngest known Galactic composite. The possible similarity between the spectra of G 11.2−0.3 and 3C58, two of the youngest plerions, is brought out. These

† Published in the Astrophysical Journal, 456, L59

spectra are observed to be quite different from that of the Crab, which is very similar in age. Lastly we remark that only after a sustained observational effort spanning two decades by various groups is the true nature of G 11.2−0.3 at last clear. To us this has been a valuable lesson highlighting that proper classification of remnants requires a detailed multiwavelength effort, with emphasis on high frequency radio and X-ray spectral observations. The overabundance of pure shell remnants must be an artifact of lack of such observations and the selection effects that work against the discovery of plerions.

4.2.1 – INTRODUCTION

G 11.2−0.3 is proposed (Clark & Stephenson, 1977) to be the counterpart of the historical supernova (SN) of AD 386, one of the 8 historical supernovae recorded over the last two millenia. The high surface brightness of the remnant both in the radio and X-rays is consistent with a young age. Radio observations made with the VLA at 20-cm with angular resolution of $\sim 20''$, show emission along a circular shell (Downes 1984; see also Becker et al. 1985). Green et al. (1988) observed G 11.2−0.3 with the VLA at 20-cm and 6-cm. At an angular resolution of $3''$ the maps reveal a clumpy nature. The lack of a sharp defining boundary for the shock is dissimilar to that seen in other young remnants such as Tycho and Kepler which are thought to be Type Ia remnants. Infact the shell morphology is reminiscent of the young Type-II SNR, Cassiopeia A. The inferred radio spectral index of the shell is $\alpha \sim 0.56$, where $S_\nu \propto \nu^{-\alpha}$. The highest frequency observations of this source were made at 32 GHz by Morsi and Reich (1987) with the 100-m Effelsberg telescope. Their image, made with a $35''$ beam shows evidence for a central flat spectrum component to the SNR, suggesting G 11.2−0.3 to be a class "C" or composite remnant i.e. a shell with central emission powered by a compact source, a pulsar. A lower estimate for the distance $\sim$ 5 kpc was derived from HI observation (Radhakrishnan et al. 1972). ROSAT PSPC observation put the remnant at a distance of 9 kpc (Reynolds et al. 1994). At a distance of 5 kpc, G 11.2−0.3 has a diameter of 3.3 pc.

In X-rays, G 11.2−0.3 was observed with both the IPC and the HRI aboard the X-ray satellite EINSTEIN (Becker et al. 1985). A total of 800 photons were collected with the IPC and this meager data was fitted to a thermal spectrum $0.2 < kT < 2$ keV. The MPC observations suggested higher temperatures of $2 < kT < 5.7$ keV. EXOSAT observations were fitted with a much hotter plasma of $kT \sim 6$ keV (Smith 1988). The HRI observations also revealed a bright (10 % of the total flux) and resolved ($1'$) central source. ROSAT PSPC observations show the detailed X-ray morphology (Reynolds et al. 1994). Spectral fits suggest a $kT = 2.4$ keV and a column density $N_H = 1.3 \times 10^{22}$ cm^{-2}. The small spectral bandwidths and energy resolution of EINSTEIN IPC (1 to 4 keV; $E/\delta E \gtrsim 1$) and ROSAT PSPC (0.1 to 2.5 keV; $E/\delta E \sim 2$ at 1 keV) contribute to uncertainty is deducing the post-shock temperature. In case of G 11.2−0.3 the fits would be inaccurate due to significant contributions from unresolved spectral lines (Mg, Si & S) and a non-thermal component (see Section 3).

The radio shell morphology, the high surface brightness and possible plerionic components in both radio and X-ray are consistent with a young age for the remnant. X-ray plerions fade rapidly due to pulsar spindown and short synchrotron lifetimes of X-ray emitting particles. Hence the association of G 11.2−0.3 with the SN of AD 386 is quite likely.

In this paper, we present the results of an ASCA observation of G 11.2−0.3, designed to infer the presence of a young pulsar within the confines of the SNR. An equally important goal was to infer the shock speed which can be used in conjunction with the Sedov solution to constrain the age of the SNR. ASCA is well suited for both these goals. It's high sensitivity at hard X-rays ($\gtrsim$ 5 keV) allows us to separate the thermal (shock) emission from the pulsar powered nebular emission (plerionic emission). Its wide spectral response (0.5 to 10 keV) coupled with a high spectral resolution resolves line emission which helps in better determining the temperature of the post-shocked gas.

4.2.2 – OBSERVATIONS AND RESULTS

G 11.2−0.3 was observed with the X-ray satellite ASCA on 1994 April 10, 03:00 UT through April 11, 04:40 UT, achieving $\sim 3.2\times10^4$ s of net exposure with both the Solid State Imaging Spectrometer (SIS) and the Gas Scintillation Imaging Spectrometer (GIS). The SIS are based on CCDs and have a high energy resolving power of about 100 eV (FWHM) at 5.9 keV (see Tanaka et al. 1994 for instrumental aspects). The GIS on the other hand have a higher detector efficiency at the upper end of the observing band. The SIS are read slowly, every 4 seconds whereas in the GIS, photons can be time tagged to several tens of microseconds to milliseconds. We used the PH mode for the GIS and 1 CCD faint mode for the the SIS. X-ray photons of about 0.61 ± 0.03 counts s^{-1} in the 0.6 - 10.0 keV range were detected by each SIS detector and of 0.76 ± 0.04 counts s^{-1} by each GIS detector.

Figure 4.2 (Plate) shows SIS images of G 11.2−0.3 after deconvolution using Lucy's (1974) algorithm, in three energy bands. The point spread function (PSF) of ASCA is $3'$ but sources $1'$ apart can be resolved because the PSF has a sharp core. Energy selected hard emission [$>$ 3.3 keV, Fig 4.2b] is clearly concentrated towards the center of the remnant with an angular extent $\sim 1'$. The obtained celestial position of this central component is $\alpha_{(2000)} = 18^h11^m33^s$, $\delta_{(2000)} = -19^o26'$ with an error radius of $1'$. This coincides with the centroid of the flat-spectrum radio emission component discovered by Morsi and Reich (1987) in their 32 GHz map of the remnant. This component is clearly seen in the EINSTEIN HRI observations (Becker et al. 1985; Fig. 4.2d). It is observed with reduced response in the ROSAT PSPC (Reynolds et al. 1994). Because of ROSAT's softer response (0.1 – 2.5 keV) the shell component is much more dominant. The hot spots in the shell coincide with increased surface brightness features seen in the radio images.

The focus of this paper is a study of a possible plerion in G 11.2−0.3. Elsewhere we present a detailed analysis of the thermal spectrum of the shell (Aoki 1995). For the sake of completeness, we summarize the results of that analysis. The SIS spectra from the remnant as a whole and from the central region are

quite distinguishable. The final values of the fits for the various parameters are strongly dependent on the assumed model, since the thermal component and the non-thermal component are strongly coupled. The simplest model for composite SNRs consisting of a single temperature bremsstrahlung and a power-law, along-with Gaussian fits for emission lines of Mg, Si, S, Ar and Ca resulted in a reduced χ^2 value of 1.14. The resultant parameter values are a postshock temperature $kT = 0.73^{+0.11}_{-0.08}$ keV, an absorbing column density $N_H = 1.38^{+0.08}_{-0.09} \times 10^{22}$ cm^{-2}, and a photon index Γ of $1.4^{+0.54}_{-0.68}$. An independent estimate of the temperature is obtained by the line intensity ratios of the $K - \alpha$ He-like and H-like lines of the elements S and Si. Values ranging between 0.81−0.97 keV and 0.66−0.98 keV were derived for Si and S respectively. A non-equilibrium ionization model (NEI) fit (Masai 1994), appropriate for young remnants resulted in $kT = 0.80^{+0.04}_{-0.06}$ keV, a photon index α of $1.80^{+0.28}_{-0.54}$ and a higher absorbing column density $N_H = 2.19^{+0.14}_{-0.16} \times 10^{22}$ cm^{-2} ($\chi^2 = 1.2$) (see figure 4.3). An approximate upper bound on the age is obtained by NEI modeling of the spectrum which results in a ionization time of $\sim$ 2000 yr. The ionization time is thought to be greater than the age of the remnant (Draine & McKee, 1993), in good agreement with the assumption that G 11.2−0.3 is the remnant of the supernova of AD 386. In addition the spectrum shows a strong Mg feature comparable in strength to the Si line. This is further evidence that the supernova of G 11.2−0.3 was of the non-Type Ia.

We test the hard source [3.3−10 keV] for aperiodic variability. The GIS light curves were binned with the satellite orbital period ($\sim$ 96 min) to remove the effect of the observing window. The data were also binned on shorter timescales of 10 minutes. In each case the obtained light curves are χ^2 tested against a constant model of the mean count rate. Reduced χ^2 values of 1.22 and 0.96 were obtained in each case. The estimated count rate in the hard band is 0.0768±0.002. We conclude that there is no significant variation in the central hard source on timescales varying from a few minutes to a few hours.

Two separate time series of GIS photons were constructed with the following criteria: photons [0.5-10 keV] from the entire remnant and hard photons [3.3-10 keV] from the entire remnant. Photons chiefly from the central region could not be selected because GIS spatial resolution was compromised for better time resolution for a given telemetry rate. All photon times of arrival were translated to the barycentric frame. The barycentered data were then binned with time steps of 0.488 ms and 7.8 ms into two separate time series. The barycentering and binning procedure was then tested on a series of test data of the Crab pulsar, PSR 0540−69 and PSR 1509−58. We had calibration data worth several minutes on the Crab pulsar, and about 35 ks each on latter two. The time series data is Fourier transformed and interesting periodicities are harmonically summed and later folded at the period of interest. The predicted periods and pulse fractions of the test pulsars from known parameters such as the period and the period derivative were verified to the precision of our frequency resolution. The FFT analysis for G 11.2−0.3 showed no obvious peak in the range 1 msec to several seconds. An acceleration search was performed, where the the time-series was re-sampled in accordance with a test acceleration which simulates pulsar spindown. The searched $\dot{p}/p$ range was 0 - 9.9×10^{-12} s s^{-1}, where the upper value corresponds to the smallest characteristic age used in the analysis, assuming the pulsar was born in AD 386. Again no significant excess power was found in any frequency bin. We estimate that there is no pulsed emission in G 11.2−0.3, $L_P \lesssim 10^{33} d_5^2$ erg s^{-1}.

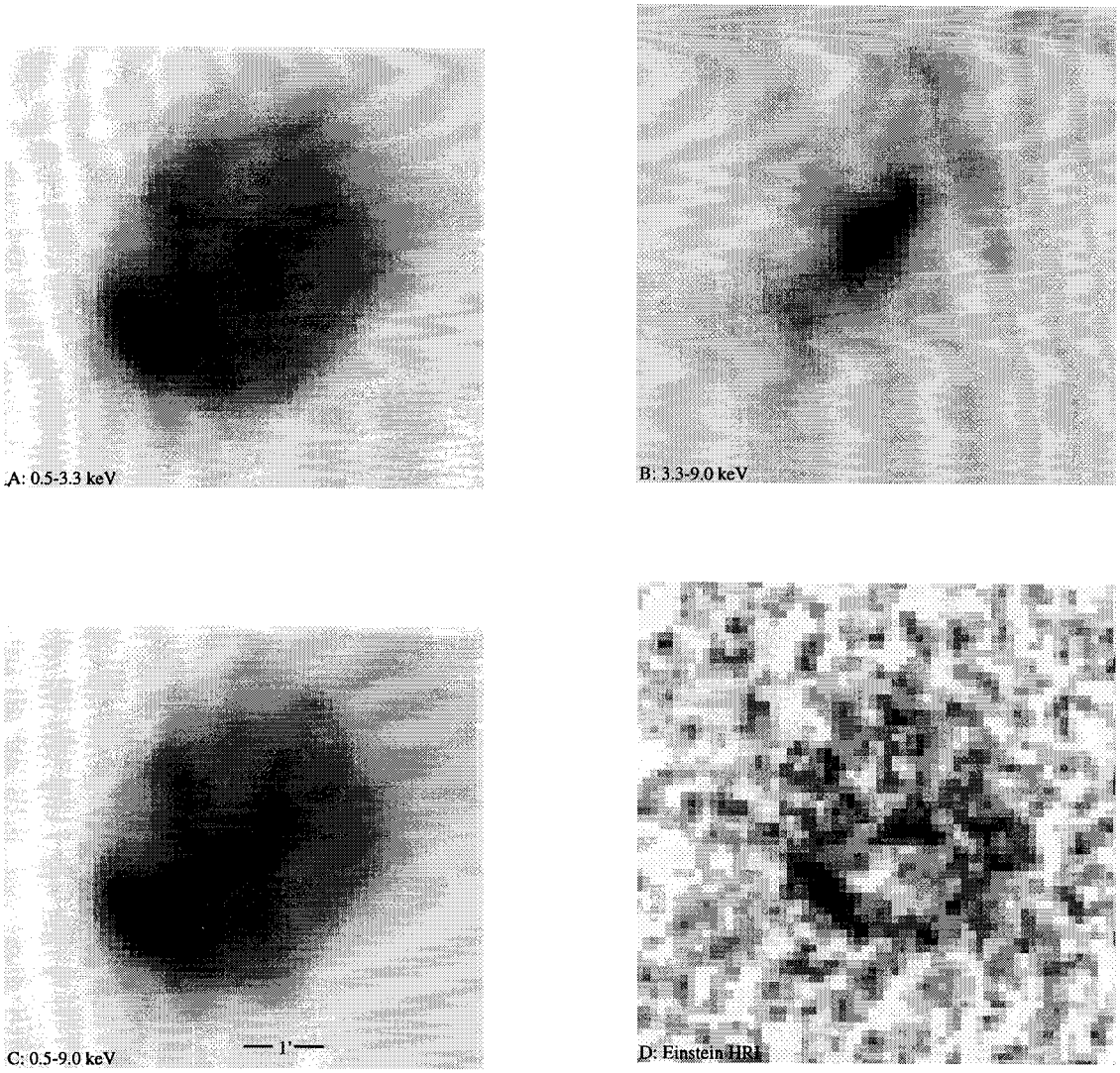

Figure 4.2: The figure shows G 11.2−0.3 in four X-ray bands in the adjacent panels. Panels A and B are the top panels; C and D are the bottom panels. The ASCA PSF is 3′ and all ASCA images are deconvolved using Lucy's algorithm (Lucy 1974). (A) Shows the remnant in the soft band limited between 0.5 – 3.3 keV. The brightest feature is the South-East rim of the shell. (B) Shows the hard ASCA band between 3.3 – 9.0 keV. The shell has disappeared and the hard emission is clearly concentrated towards the center of the remnant. We suggest this to be non-thermal emission from a plerionic nebula (C) Shows G 11.2−0.3 in the 0.5 – 9.0 keV ASCA band which includes both the strong thermal emission

from the shock and the non-thermal central component (D) Shows the EINSTEIN HRI image in the 0.5 – 4.0 keV band (see Becker et al. 1985) retrieved from cdrom. The raw image was convolved with a Gaussian (7×7 pixels^2 FWHM, pixel size is $2''$). The HRI resolution is $3''$. The central component and the shell emission are seen clearly (Panels A,B and C are displayed with the same grey scale intensity; however Panel B pixels have been made hotter by a factor of two; Panel D scale is matched closely to the other panels). The remnant is $\sim 4.4'$ across.

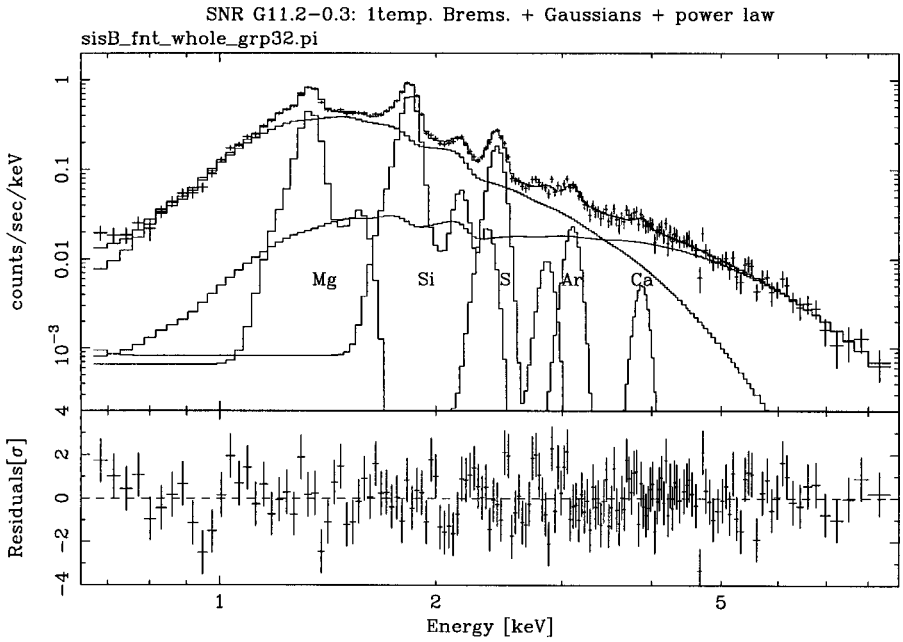

Figure 4.3: Result of spectral fitting of G 11.2−0.3: bremsstrahlung + power-law + gaussian fits for spectral lines. The upper panel represents a background subtracted pulse height spectrum of the supernova remnant in the entire region ($r \lesssim 2.4'$) and the best model function consisting of a single temperature bremsstrahlung, power-law and gaussians for the model. SIS-0 and SIS-1 data are summed after gain corrections. Crosses represent the actual data and the histogram represents the model. The three spectral components are also displayed

individually. Residuals are shown in the lower panel with 1σ error bars. Reduced χ^2 of 1.14 for 134 d.o.f. is obtained in this trial. In the energy band below about 3.3 keV, the thermal component (bremsstrahlung+gaussians) dominates, whereas the non-thermal component is dominant in the harder band. Relative line center energy is fixed in the analysis.

4.2.3 – DISCUSSION

Both the X-ray and radio images of G 11.2−0.3 show circular boundaries at a radial distance of $R_s \approx 3.3 d_5$ pc, where the source distance is $5 d_5$ kpc. The size of the X-ray plerion is $\sim 1 d_5$ pc. A lower limit to the remnant age can be obtained by postulating free expansion at a velocity of 10^4 kms^{-1}, a typical maximum velocity seen in spectra of Type II and Type Ib supernovae to be $t > 330 d_5$ yr. An approximate upper bound on the age $\sim$ 2000 yr is obtained by non-equilibrium ionization modeling of the spectrum (see Section 4.2.2; Aoki 1995). From here on we assume the remnant age to be $\sim$ 1600 yr, consistent with the supernova event of AD 386.

Since most of the thermal component is due to the shocked ISM of temperature 0.73 keV, we compute a shock speed $v_s = (16kT/3\mu m_p)^{1/2} \sim 800$ km s^{-1}. This assumes ion and electron temperature equilibrium behind the shock ($\mu = 0.6$ for cosmic abundances). Inefficient electron heating would result in a larger shock velocity i.e. $v_s \gtrsim 800$ km s^{-1}. From the Sedov solution, $R_s = 2.5 v_s t$ and therefore $R_s \gtrsim 3.1$ pc and $d \gtrsim 4.8$ kpc. (Both these values would be further reduced if the remnant has not yet fully attained Sedov phase).

From spectral fitting (section 2) we estimate the total unabsorbed X-ray luminosity of the SNR to be $L_X \sim 1 \times 10^{36} d_5^2$ erg s^{-1} in the 0.6−10 keV band and $L_H \sim 4.0 \times 10^{34} d_5^2$ erg s^{-1} in the hard 3.3−10 keV band, of which 90% is from the central hard source. In the soft 0.6−3.3 keV band however only 2% of the X-ray energy is emitted by the central source. We estimate the shell emission to be $L_S \sim 10^{36} d_5^2$ erg s^{-1}. The instantaneous power radiated from a shell is

$L_s(t) = (16\pi/3)R_s^3(t)n_o^2\Lambda(T)$, where n_o is the mean ambient particle density and $\Lambda(T) = 1.0 \times 10^{-22}T_6^{-0.7} + 2.3 \times 10^{-24}T_6^{0.5}$ erg cm^3 s^{-1} is the cooling function (McCray 1987). Here T_6 is the post shock temperature in units of 10^6 K. With our estimates of radius and the shell luminosity L_S, we derive an $n_o \sim 1.5d_5^{-0.5}$ cm^{-3}. The Sedov relation $R(t) = 13$ pc $(E_{51}/n_o)^{0.2}t_4^{0.4}$, where E_{51} is the energy of the explosion in units of 10^{51} erg and t_4 is the age in units of 10^4 yr, yields $E_{51} \sim 0.2d_5^{4.5}$. Since typical supernova energies do not exceed a few times E_{51}, the distance is constrained to be $d_5 \lesssim 2$.

We now consider the mechanisms for the hard emission from the remnant core. In a Sedov blast wave, the interior region is hotter (because they are shocked when the blast wave is faster) and has lower density (because the interim is isobaric). Most of the X-ray emission however is produced by the outer shell (of thickness $R_s/12$) which contains almost all the swept up matter. Thus the emission from the hotter interior is faint. Using the Sedov interior approximations for temperature and density as a function of radius (Cox & Franco 1982), and an emissivity $\propto n^2T^{0.5}$ per unit volume, we estimate the contribution of the interior of $0.5R_s$ to be $<<$ 1%. In G 11.2−0.3, the interior 1′ radius accounts for about $\sim$ 2% of all photons and 90% of all hard photons leading us to believe that there must be a central object powering this emission.

We begin with the two possible (but unlikely) explanations of the central object in G 11.2−0.3 i) Thermal emission from the surface of a hot young neutron star and ii) A Population-I X-ray binary containing an accreting black-hole or a neutron star. Firstly, we consider the above hypotheses unlikely because the central source is not point like, but appears extended in the EINSTEIN HRI observations (Becker et al. 1985). Secondly, our minimum age calculations, lead to a relatively cool NS surface temperature of $\sim 1\times10^6$ K (Page and Applegate 1992). This is inconsistent with the hardness and luminosity of the central source. We rule out the binary hypothesis from the absence of variability of the source on timescales of a few minutes to a few hours (section 4.2.2). Accreting black-holes have large amplitude variability absent in our source. On the other hand

wind accreting neutron stars are consistent with the sub-Eddington luminosity estimated from the G 11.2−0.3 core. However, many are X-ray pulsars and show aperiodic variability on timescales of hours to years.

The most plausible explanation is that the core emission represents non-thermal nebular emission powered by a pulsar, analogous to the X-ray nebulae seen in the youngest three pulsars known – the Crab, PSR 0540−69 in the LMC, PSR 1509−58 in the galactic remnant MSH 15−52. However all of these pulsars have X-ray pulse fraction of $\sim$ 20% modulating the steady emission from the nebula. Our failure to detect pulsations is therefore surprising, although it is possible that the parameters of the pulsar lie outside our search range. The more likely possibility is that the pulsar may not be beamed in our direction. We use the empirical relation by Seward and Wang (1983) to constrain the energetics of the pulsar. They deduce an empirical relation

$$\log L_X = 1.39 \log \dot{E} - 16.6$$

where L_X is the luminosity of the pulsar and its plerion in the EINSTEIN band and $\dot{E}$ is its spin-down luminosity. Using a central luminosity of $4.9 \times 10^{34} d_5^2$ erg s^{-1} for G 11.2−0.3 translated to the EINSTEIN band (0.5 to 4 keV) we derive an $\dot{E}$ for the pulsar of $10^{36.9} d_5^{1.44}$ erg s^{-1}which is lower than that of the three youngest pulsars.

Plerions are expanding bubbles of relativistic particles and magnetic fields powered by a central pulsar. A full dynamical treatment of these objects in time, incorporating particle energy losses yields a luminosity and characteristic spectrum (Reynolds & Chevalier 1984). Evolutionary effects chiefly synchrotron and adiabatic losses shape the spectrum. For a 1600 yr old pulsar as expected in G 11.2−0.3, which should have spun down far below its birth period, the spectrum should appear as having two break frequencies ; one due to synchrotron burnoff ν_b and a second break at lower frequency ν_p ascribed to be due to pulsar aging. The radio to X-ray spectrum therefore has three segments with spectral indices

α, β and $\alpha + 0.5$ where $\alpha \lesssim \beta < \alpha + 0.5$. The above scenario implicitly assumes a single injected particle spectrum $N(E) \propto E^{-s}$, where $s = 2\alpha + 1$, to explain the radio to X-ray spectrum. At least in one case, the Crab, this picture seems to be oversimplified (Kennel & Coroniti 1984).

In the Crab the spectral break is $\nu_b \approx 10^4$ GHz with a spectral change of 0.5. However reported breaks in spectra of other filled center remnants, some the same age and others older than the Crab are at frequencies between $\approx$ 10 to 100 GHz (Reich, Fürst & Sofue 1984, Morsi & Reich 1987, Salter et al. 1989). For example 3C58 has a break of 0.6 near 50 GHz. It is similar to Crab in both distance and age but has twice the diameter and is much fainter at all wavelengths (Green 1986). It pointed out by Green and Scheuer (1992) it is possibly very significant that the Crab has a central pulsar, but not 3C58 or G21.9-0.9 or G74.9+1.2 for which various groups have found evidence for low spectral break frequencies. We derive a similar low $\nu_b \lesssim 32$ GHz for G 11.2−0.3.

We discuss the radio to X-ray spectrum of the core of G 11.2−0.3. From our NEI fits the X-ray spectrum at 5 keV is $S_\nu \approx 1\mu\text{Jy}(\nu/2.5 \times 10^{18}\ \text{Hz})^{-0.8}$. The 32 GHz radio flux of the core is inferred to be $\gtrsim 0.8$ Jy, alongwith a total SNR flux of 4 Jy (Morsi & Reich 1987). The 32 GHz measurement is consistent with the X-ray spectrum when it is extrapolated backward (Fig. 4.4). A further backward extrapolation to 1 GHz shows an expected flux of 32 Jy whereas measured flux at 1 GHz for G 11.2−0.3 is $\sim$ 22 Jy with a major contribution due to the shell. It simply follows that ν_b is possibly somewhere between 1 and 32 GHz and the lower break $\nu_p < \nu_b$ must lie at an even lower value. Note however that the X-ray energy index plays heavily in determining ν_b. Our NEI model fit for the energy index of 0.8 is highly uncertain (refer to section 2). Admittedly, an index > 0.8 allowed by the fits would result in $\nu_b > 32$ GHz. Even a Crablike $\nu_b \sim 10^{13}$ could be accommodated by a three segment fit, avoiding the need to invoke the anomalously low ν_b derived above. We however favor an energy index $\alpha + 0.5$ of 0.8 because on all accounts it seems $\alpha \lesssim 0.3$. Although no direct estimates of the plerionic flux at radio frequencies exist (except at 32 GHz) as it is faint, earlier

maps at 20 cm and 6 cm (Green et al. 1988, Downes et al. 1984, Becker et al. 1985) are consistent with a flat average radio spectrum of the plerion out to 32 GHz, $\alpha \lesssim 0.3$.

Figure 4.4: The figure on the next page shows the spectrum of the Crab and its pulsar over the range 10^7 to 10^{24} Hz. The inferred spectrum of the core of G 11.2−0.3 and and that of 3C58 are also displayed with flux scaled to the Crab distance of 2 kpc. The break frequency $\nu_b \lesssim 32$ GHz for G 11.2−0.3 is similar to $\nu_b \sim 50$ GHz for 3C58, much lower than that observed for the Crab. The radio point for the G 11.2−0.3 plerion is from the 32 GHz observations from Morsi & Reich (1987). The $\sim$ 1 GHz point from observations of Green et al. 1988 corresponds to flux from the entire remnant. The 3C58 spectrum is adapted from Green & Scheuer (1992). The spectrum of the Crab and its pulsar are adapted from: Manchester & Taylor, "Pulsars" 1977, W.H. Freeman & Company.

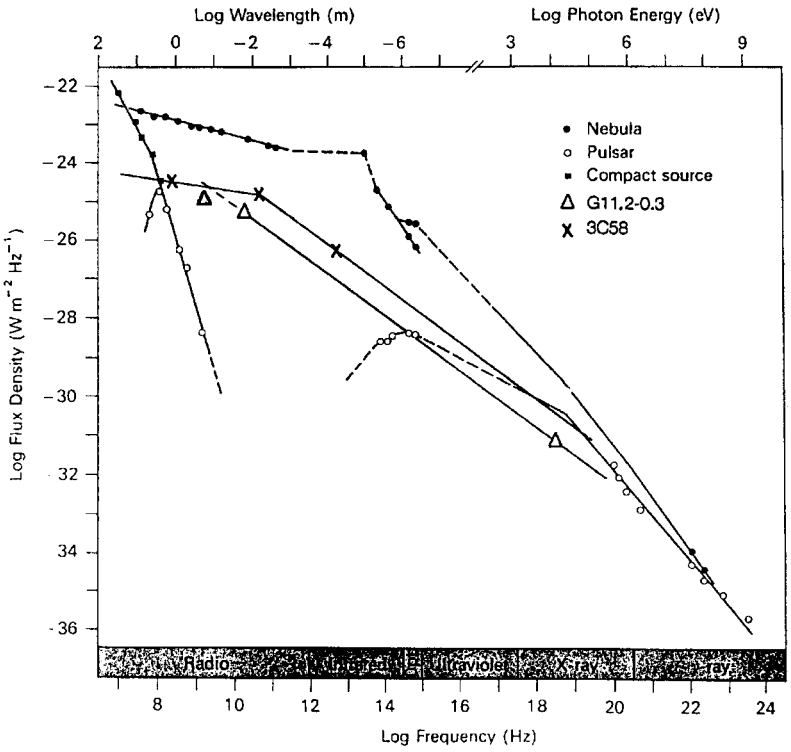
Log Wavelength (m)
Log Photon Energy (eV)
2
0
−2
−4
−6
3
6
9
−22
−24
−26
−28
−30
32
34
36
Log Flux Density (W m^{-2} Hz^{-1})
Nebula
Pulsar
Compact source
G11.2-0.3
3C58
Radio
Infrared
Ultraviolet
X-ray
γ-ray
8
10
12
14
16
18
20
22
24
Log Frequency (Hz)

A plausible way to explain a low break ν_b is to invoke an anomalously high plerion magnetic field, B. Equating the dynamic age to the synchrotron cooling age we get the relation, $\nu_b \approx 4 \times 10^{23} B^{-3} \tau^{-2}$, with $\tau \sim 1600$ yr and $\nu_b \lesssim 32$ GHz from which we infer a large magnetic field $B \gtrsim 2 \times 10^{-3}$ G, a factor of 10 higher than the Crab. The total field energy implied over the plerion volume is disturbingly large $\gtrsim 2 \times 10^{49}$ erg, where we assume the smallest plerion size to be ~ 1 pc. The plerion luminosity on the other hand ($L \approx 4\pi d_5^2 \int_{32GHz}^{10keV} S_\nu \, d\nu \sim 3 \times 10^{35}$ erg s^{-1}) is a factor $\sim 10^{-3}$ lower than that implied by equipartition. At this point we cannot explain how a pulsar can transport such a large fraction of its spindown energy ($\sim 4 \times 10^{50}$ erg for an initial period of 10 ms) in magnetic fields. In the Crab for example most of the spindown luminosity is thought to be in the pair plasma. Nevertheless, we stress again that the inferred B is subject to uncertainties in the spectra and although the above interpretation is highly interesting, it is not conclusive. Future radio measurements at higher frequencies out to mm wavelengths could be used to fill the gaps in the spectrum better constraining its shape and location of the breaks.

In conclusion, we point out that it is disturbing that it has taken twenty years of effort to correctly classify G 11.2−0.3 as a combination remnant. Its case highlights the difficulty in associating a plerionic component within one of the youngest Galactic SNR in spite the fact that the youngest SNR should harbor the brightest plerions. Shells with central non-thermal emission i.e. the classical combination morphology observationally upholds one the the basic tenets in stellar astrophysics: that neutron stars/pulsars are born in supernova events. So far the observational evidence for this remains meager. Of the $\sim$ 300 known Galactic remnants, only a dozen are confirmed to be associated with pulsars. Another $\sim$ 20 SNR show indirect evidence for an embedded pulsar via a plerionic component, with the above two sets having a small overlap. This is a small fraction, considering that 80% of all supernova events are thought to be of the types (II and Ib) that leave behind a neutron star. This is perhaps because the classification of remnants is not yet complete. Weaker plerions emerge as emitters at high radio frequencies

due to flatter spectra ($\alpha \sim 0.1$) and at hard X-rays ($\sim$ 10 keV). The contaminating influence of shell falls rapidly ($\alpha \sim 0.6$) at higher ν_R and is thermal ($\sim$ 1 keV) at X-rays. High resolution high frequency radio astronomy is only now coming of age, and broadband X-ray imaging with fine spectral capability has been available only with the launch of ASCA.

REFERENCES

Aoki, T. 1995, PhD Thesis, Gakushuin University

Becker, R. H., Markert, T., & Donahue, M. 1985, ApJ, 296, 461

Clark, D. H. & Stephenson, F. R. 1977, in The Historical Supernovae (Oxford: Pergamon)

Cox, D. P. & Franco, J. 1982, ApJ, 251, 687

Downes, A. 1984, MNRAS, 210, 845

Draine, B. T. & McKee, C. F. 1993, ARA&A, 31, 373

Green, D. A. 1986, MNRAS, 218, 533

Green, D. A., Gull, S. F., Tan, S. M. & Simon, A. J. B. 1988, MNRAS, 231, 735

Green, D. A. & Scheuer, 1992, MNRAS, 258, 833

Kennel, C. F. & Coroniti, F. V. 1984, ApJ, 283, 710

Lucy, L. B. 1974, AJ 79, 745

Masai, K. 1994, J. Quan. Spec., 51, 211

McCray, R. 1987 in Spectroscopy of Astrophysical Plasmas, Eds. A. Dalgarno & D. Layzer, Cambridge Univ. Press, 255

Morsi, H. W. & Reich, W. 1987, A&ASS, 71, 189

Page, D. & Applegate, J. H. 1992, ApJ, 394, L17

Radhakrishnan, V., Goss, W. M., Murray, J. D. & Brooks, J. W. 1972, ApJS, 24, 49

Reich, W., Fürst, E. & Sofue, Y. 1984, A&A, 133, L4

Reynolds & Chevalier 1984, ApJ, 278, 630

Reynolds, S. P., Lyutikov, M., Blandford, R. D. & Seward, F. D. 1994, MNRAS, 271, L1

Salter, C. J., Reynolds, S. P., Hogg, D. E., Payne, J. M. & Rhodes, P. J. 1989, ApJ, 338, 171

Seward, F. D. & Wang, Z. R. 1988, ApJ, 332, 199

Smith, A. 1988, in Supernova Remnants and the Interstellar Medium, Eds. R. S. Roger and T. L. Landecker, Cambridge Univ. Press, 117

Tanaka, Y., Inoue, H. & Holt, S. S. 1994, PASJ, 46(3), L37

4.3 THE CENTRAL SOURCE IN SNR PKS 1209–51/52

ABSTRACT: We present a $\sim$ 20 ks Advanced Satellite for Cosmology and Astrophysics (ASCA) observations of the intriguing X-ray source 1E 1207.4−5209. The source is situated centrally in PKS 1209− 51/52, one of the original barrel-shaped supernova remnants. For 1E 1207.4−5209 we derive a steep power-law spectrum of photon index 3.7 and an absorbing column density of $N_H = 2.1 \times 10^{21}$ cm^{-2}. Based on our results the source is unlikely to be a chance superposition of a background extragalactic object. Most likely, it is either an old weak plerion or more intriguingly a source similar to the anomalous X-ray pulsars. However, we find no evidence for the X-rays to be pulsed

4.3.1 – INTRODUCTION

PKS 1209−52 (also G 296.5+10.0) is a nearby (1-2 kpc), large diameter (81-arcmin) supernova remnant prominent both at radio and X-ray wavelengths (eg. Green 1991). The morphology consists of a shell but with a striking asymmetry (e.g. Storey et al. 1992), the origin of which has been a matter of much debate and discussion (Roger et al. 1988, Storey et al. 1992, Milne & Jones 1994).

EINSTEIN IPC observations revealed a compact source, 1E 1207.4−5209, intriguingly close to the center of the SNR. A 4000 s HRI image which collected 110 photons did not resolve the source. Given the small number of photons a meaningful search for pulsations could not be carried out (Seward 1989). Matsui et al. (1988) adopting $N_H = 3 \times 10^{21}$ cm^{-2} (obtained from HEAO A1 data) and concluding that the object could be fit with a thermal blackbody with kT = 0.13 keV. The IPC observations of the X-ray emission emanating from the SNR shock could be satisfactorily fit to Sedov solution with an ambient density of 0.08 cm^{-3}, and $E_{51} = 0.12$ (explosion energy in units of the usual 10^{51} erg) and an age of $t \sim 10^4$ yr. A distance of 2 kpc was assumed.

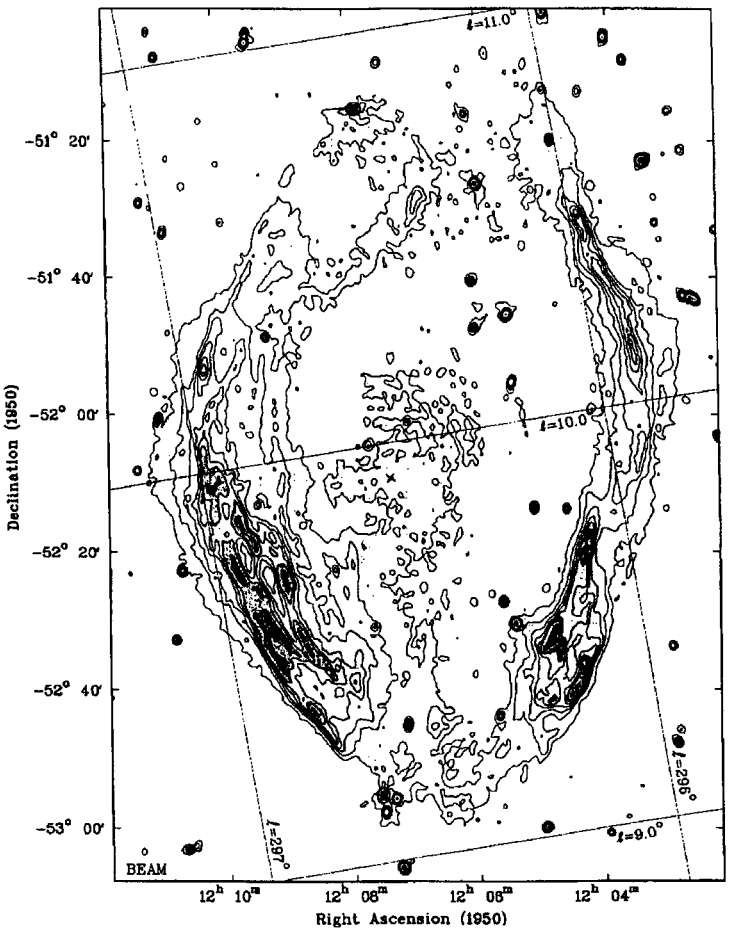

Figure 4.5: An 843 GHz map of PKS 1209−51/52 (or G 296.5+10.0) from combined Parkes and Molonglo observations by Roger et al. (1988). Contours are at the level of 6 mJy beam^{-1} and range from 4 to 52 mJy beam^{-1}. The synthesized half power beam is 44″ × 56″. The "x", 6 arcmin southeast of the map center,

marks the position of the compact X-ray source 1E 1207.4−5209. The faint diffuse emission around the position of the X-ray source could be plerionic. This figure is electronically scanned version of the published map in the Astrophysical Journal (Fig. 5 in Roger et al. 1988).

EXOSAT observations with the LE telescope and an imaging detector (PSD) were conducted by Kellett et al. (1987). They confirmed the point source and obtained somewhat different Sedov parameters: $n_o = 0.25$ cm^{-3}, $E_{51} = 0.375$ and $t \sim 10^4$ yr; a distance of 1.5 kpc was assumed. Thus both observations infer an old age for the SNR, $\gtrsim 10^4$ yr.

An X-ray flux L_X (0.15 - 4.5 keV) $= 2 \times 10^{-12}$ erg cm^{-2} s^{-1} has been deduced for 1E 1207.4−5209 (Matsui et al. 1988). Owing to the faintness of the source, the emission model is not very well constrained. A black body of $T \sim 10^6$ K, thermal bremsstrahlung ($kT = 0.35$ keV) and a power-law (photon index $\Gamma = 4.6$; where $F_\nu \propto \nu^{-\Gamma}$) are equally possible.

Optical observations for possible counterparts in and near the the HRI error box show that the X-ray source is indeed very peculiar: no plausible candidate counterpart has been identified implying $f_X/f_{opt} \gtrsim 10^3$ (Bignami et al. 1992). The N_H deduced from EXOSAT observations and the high Galactic latitude rule out large foreground and background extinction. We can safely conclude that 1E 1207.4−5209 is one of the following:

1. A peculiar extragalactic source. If so, the large f_X/f_{opt} is unprecedented. BL Lacs with $f_X/f_{opt} \sim 10$ have the highest such ratio; in fact in the entire EMSS the highest ratio is 50 (Stocke et al. 1991).

2. An isolated neutron star. Neutron stars such as Vela and Geminga have $f_X/f_{opt} \sim 10^3$. In support of this hypothesis, we note that 1E 1207.4−5209 appears to have a faint radio nebula surrounding it (Fig 4.5), which we identify as a plerion powered by a putative pulsar. Parenthetically we note that this connection seems to have been missed in the literature.

In regard to hypothesis 2, we are not perturbed that sensitive pulsar searches (Manchester et al. 1985) have failed to find a radio pulsar. It is well known that pulsar emission, at radio wavelengths is highly beamed and we expect a good fraction of pulsars to be undetectable for this reason. Also we have not seriously entertained the possibility of a cooling neutron star for two reasons: as yet there has not been a single convincing case for a cooling neutron star (i.e. non-magnetospheric origin) and the detection of a probable radio plerion around 1E 1207.4-5209 would strongly suggests that the X-rays are magnetospheric in origin (see Section 4.2.3).

From the above discussion it is clear that further progress requires the establishment of an X-ray spectrum of this source, which is the main focus of this effort. In our model, the relativistic wind from the pulsar is shocked and then fills up a non-thermal emitting region, a plerion, whose mean pressure is about equal to the thermal pressure of the Sedov shell. These is indeed observed around the Vela pulsar which has a 3 arcmin nebula, surrounded by a 1° shell, the plerion. We identify the 15 arcmin radio nebula surrounding 1E 1207.4-5209 as the plerion. In Vela, the plerion and the shock region respectively radiate $10^{-3}\dot{E}$ and $10^{-4}\dot{E}$ in the 0.1-4.0 keV band; here $\dot{E}$ is the pulsar spin-down luminosity.

In this section, we present the results of an ASCA observation of 1E 1207.4-5209 designed to infer the presence of a young pulsar within the confines of the SNR.

4.3.2 – OBSERVATIONS AND RESULTS

1E 1207.4-5209 was observed with the X-ray satellite ASCA on 1994 July 1, 16:52 UT through July 2, 10:00 UT, achieving $\sim$ 20 ks of net exposure with both the Solid State Imaging Spectrometer (SIS) and the Gas Scintillation Imaging Spectrometer (GIS). Brief descriptions of these instruments are given in § 4.2.2 (also see Tanaka et al. 1994 for instrumental aspects). Observations were made in the pulse-height (PH) mode for the GIS and 2 CCD bright mode for the SIS

respectively. X-ray photons of about 0.33±0.03 counts s^{-1} in the 0.6 - 10.0 keV range were detected by each SIS detector and of 0.36±0.04 counts s^{-1} by each GIS detector.

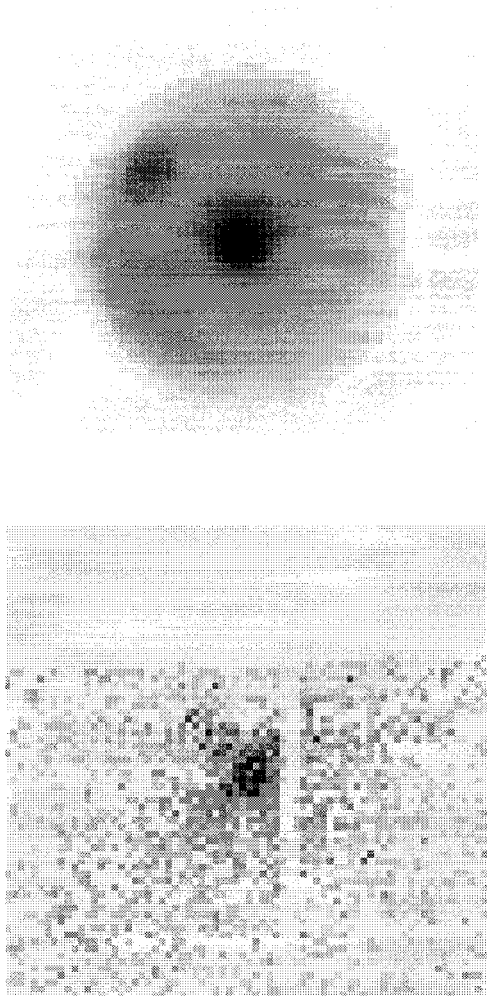

Figure 4.6: This figure shows ASCA GIS (top) and SIS (bottom) images of 1E 1207−5209 in the 0.5-2.0 keV band. The source is consistent with being a point source in both images. SIS pixel size is 6.4″ and the GIS pixel size is approximately 59″.

Figure 4.6 shows SIS and GIS images of 1E 1207.4-5209 in the energy band of 0.6-2.0 keV (soft X-rays). Both instruments show that the source is consistent with being point-like, like previous X-ray observations have indicated (EINSTEIN

HRI observations; Seward 1989). The point spread function (PSF) of the SIS detectors is $3'$ but sources $1'$ apart can be resolved because the PSF has a sharp core (Tanaka et al. 1994). The source is not detected in the hard band (2.0-10.0 keV) by either instrument. The obtained celestial position of the peak of X-ray emission is $\alpha_{(1950)} = 12^h07^m32.1^s$, $\delta_{(1950)} = -52^o09'55''$ with an error radius of $1'$. This position coincides with the faint diffuse structure visible in the the 843 GHz MOST radio map by Roger et al. 1988.

For both GIS and SIS spectral analysis, photons were selected from within a box of size $\sim 4'$ enclosing the source. Background photons were subtracted using the ASCA background files which are event lists from blank sky observations made at high Galactic latitudes. Best spectral fits for both SIS and GIS detectors for 1E 1207.4-5209 are obtained for a very steep power-law spectrum of a photon index Γ of 3.8 ± 0.27 and an absorbing column density of $N_H = 2.1 \pm 0.8 \times 10^{21}$ cm^{-2}. The obtained model is then used to compute the total flux density of $F_X \approx 1.9 \times 10^{-12}$ erg cm^{-2} s^{-1}. The total X-ray luminosity in the observed band is therefore $L_X \sim 8.6 \times 10^{32} d_2^2$, where the distance is $2d_2$ kpc. Neither blackbody nor thermal bremsstrahlung models are fit well to the almost featureless spectrum of the source seen rapidly cutting off at approximately 2 keV in the ASCA band (Figure 4.7).

The GIS light curves were binned with the satellite orbital period ($\sim$ 96 min) to remove the effect of the observing window. The data were also binned on shorter timescales of 10 minutes. In each case the obtained light curves are χ^2 tested against a constant model of the mean count rate and are consistent with being constant. We conclude that there is no significant variation in the central hard source on timescales varying from a few minutes to a few hours. This count rate obtained is consistent with that of previous X-ray observations of the source.

A time series of GIS photons were constructed with the following criterion: photons [0.5-2 keV] from the entire GIS and were selected so as to have enough

photons to do a meaningful FFT search. All photon times of arrival were translated to the barycentric frame.

The barycentered data were then binned with time steps of 0.488 ms and 7.8 ms into two separate time series. The barycentering and binning procedure was then tested on a series of test data of the Crab pulsar, PSR 0540−69 and PSR 1509−58. The time series data is Fourier transformed and interesting periodicities are harmonically summed and later folded at the period of interest. The predicted periods and pulse fractions of the test pulsars from known parameters such as the period and the period derivative were verified to the precision of our frequency resolution. The Fourier analysis for 1E 1207.4−5209 showed no obvious peak in the range 1 msec to several seconds. An acceleration search was performed, in which the time-series was re-sampled in accordance with a test acceleration which simulates pulsar spin-down. The searched $\dot{p}/p$ range was 0 - 9.9×10^{-13} s s^{-1}, where the upper value corresponds to the inferred age of the supernova remnant of 20,000 yr.

In an alternative search for coherent pulsations, all photons from a $4'$ region around the source were selected and barycentered. We then searched for periods in the X-ray data by folding the photon arrival times using a range of trial periods. The χ^2 statistic was used as a measure of whether a particular folded distribution is significantly different from a uniform distribution:

$$\text{Reduced } \chi^2 = \frac{1}{N-1}\sum_{i=1}^{N}\frac{(x_i-\bar{x})^2}{\sigma_i^2}$$

where N is the number of phase bins ($N = 16$ bins for this search), x_i is the counting flux of i-th folded bin, σ_i is the standard deviation of x_i, and $\bar{x}$ is the averaged counting flux. The stepping of trial period, ΔP, is carefully selected to be small enough so that $\Delta P = \frac{P^2}{m\,T_S}$, where P is the trial period and T_S is the time span of whole dataset and m is a number greater than 1 ($m = 4$). Periods ranging from 100 msec to 400 sec were examined, however, no significant signal was discovered in the periodogram.

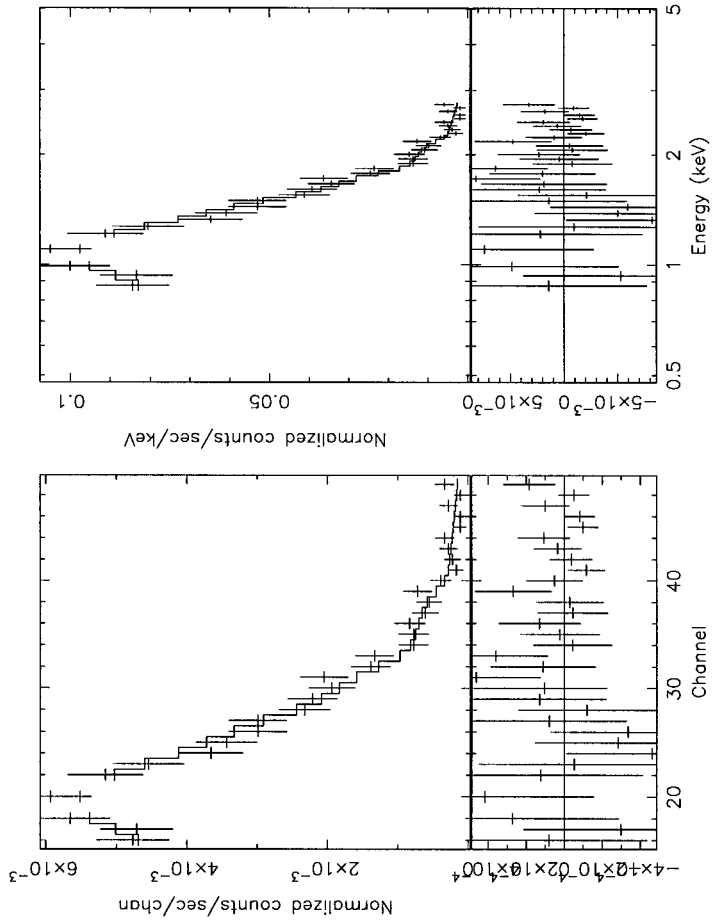

Figure 4.7: Displayed are two plots of the 1E 1207−5209 spectrum with separate abscissa: i) ASCA SIS energy channel number and ii) energy in keV. The spectra are fit to photons selected from a region surrounding the X-ray source from which the background has been subtracted. The best obtained fits are shown: a steep power-law of photon index of 3.8 ± 0.27 with an intermediate absorbing column density of hydrogen of $N_H = 2.1 \pm 0.8 \times 10^{21}$ cm^{-2}.

4.3.3 – DISCUSSION

From spectral fitting to the data we advocate two possible models for the source 1E 1207−5209:

1. *A old plerion powered by a middle aged pulsar ($\tau \sim 2 \times 10^4$ yr).* The power-law fit to the data seems to suggest a non-thermal or plerionic origin to the radiation. The photon index is steep compared to those inferred for other plerionic SNR which typically lie in the range 1.4 to 2.1 for young plerions (Aoki 1995). The steep photon index of 1E 1207−5209 immediately suggests that this is not a typical plerion. At this point we have no empirical confirmation as to whether the plerion photon index steepens with increasing age. However it is expected that the photon index would steepen if the central pulsar stops the production of high energy particles which radiate bulk synchrotron emission in the X-ray regime (Reynolds & Chevalier 1984). This heightened steepening of the spectral slope is therefore due to two effects. Gradual decline in the production of very high energy particles in the pulsar magnetosphere and the rapid synchrotron burnoff of such particles.

2. *Exotic Source similar to the Anomalous X-ray Pulsars.* A steep power-law spectrum of slope similar to the one observed in 1E 1207.4−5209 is also observed in the 7-s pulsar 1E 2259+586. However, along with a power-law component 1E 2259+586 also displays a softer black-body component ($kT = 0.1$ keV) which is thought to arise from the neutron star surface. The power-law emission in this case is thought to arise at least in part from a surrounding nebula. Just as 1E 1207.4−5209 is associated with PKS 1209−52, 1E 2259+586 lies in the core of the supernova remnant G109.1−1.0 or CTB 109 (Gregory & Fahlman 1980) strongly suggesting a connection between the two. Deep radio searches have not revealed a counterpart (Coe et al. 1994). There has so far been no confirmation of an optical counterpart just as in 1E 1207−5209 (Coe & Jones 1992). G109.1−1.0 has an estimated age of 10^4 yr and a distance between 3.6-4.7 kpc.

Although the hypothesis that 1E 2259+586 is a binary system has been strongly favored, we have yet to detect any direct evidence for an optical companion and there is no Doppler modulation of the X-ray pulses. In an alternative conjecture the neutron star could be accreting from a nearby molecular cloud (Corbet et al. 1995), circumstellar debris, an accretion disk from a tidally disrupted companion or the remnant of a common envelope phase (van Paradijs et al. 1995). Finally there is a suggestion that this source could be a "magnetar". Thompson & Duncan (1993) have proposed a model for soft γ-ray repeaters (see chapter 3) which involves neutron stars with very large magnetic fields for which the name "Magnetars" has been used (evidence of glitches in 2259+586 see Usov 1994). They apply the magnetar model to 1E 2259+586 and derive a magnetic field of $\sim 0.7 \times 10^{14}$ G. Their interpretation is motivated by the growing numbers of known anomalous X-ray pulsars (there are five known to date), all associated with SNR or diffuse thermal emission. The magnetar model invokes large magnetic fields to explain the perplexingly slow rotation of these pulsars while still residing in young SNR. Here the X-ray emission is powered by decaying crustal magnetic fields rather that spindown or accretion. It also predicts composite black-body and non-thermal emission for such sources which has now been observed in broad-band X-ray spectroscopy of 1E 2259+586 (Corbet et al. 1995).

REFERENCES

Aoki, T. 1995, PhD Thesis, Gakushuin University

Bignami, G. F., Caraveo, P. A. & Mereghetti, S. 1992, 389, L67

Coe, M. J. & Jones, L. R. 1992, MNRAS, 259, 191

Coe, M. J., Jones, L. R. & Lehto, H. 1994, MNRAS, 270, 178

Corbet, R. H. D., Smale, A. P., Ozaki, M., Koyama, K. & Iwasawa, K. 1995, ApJ, 443, 786

Green, D. A. 1991, PASP 103, 209

Gregory, P. C. & Fahlman, G. G. 1980, Nature, 287, 805

Kellett, B. J. et al. 1987, MNRAS, 225, 189

Manchester, R. N., D'Amico, N. & Tuohy, I. R. 1985, MNRAS, 212, 975

Matsui, Y., Long, K. S. & Tuohy, I. R. 1988, in Supernova Remnants and the Interstellar Medium, Eds. R. S. Roger & T. L. Landecker (Cambridge University Press), 157

Milne, D. K. & Haynes, R. F. 1994, MNRAS, 270, 106

Reynolds, S. P. & Chevalier 1984, ApJ , 278, 630

Roger, R. S., Milne, D. K., Kesteven, M. J., Wellington, K. J. & Haynes, R. F. 1986, ApJ, 332, 940

Seward, F. D. 1989, Space Sci. Rev., 49, 385

Stocke, J. T. et al. 1991, ApJ SS, 76, 813

Storey, M. C., Staveley-Smith, L., Manchester, R. N. & Kesteven, M. J. 1992, A&A, 265, 752

Tanaka, Y., Inoue, H. & Holt, S. S. 1994, PASJ, 46(3), L37

Thompson, C. & Duncan, R. C. 1992, in Compton Gamma Ray Observatory, ed. M. Friedlander et al. (New York: AIP), 1085

van Paradijs, J., Taam, R. E. & van den Heuvel, E. P. J. 1995, ApJ, 447, L41

Usov, V. V. 1994, ApJ, 427, 984

CHAPTER 5: BINARY PULSARS

5.1 OVERVIEW

5.1.1 – PULSARS BOUND TO MASSIVE COMPANIONS

This chapter describes two sensitive searches for binary radio pulsars in the direction of massive main-sequence (MMS) stars. The objects in question are disjoint from the set of recycled binary pulsars or the millisecond pulsars that orbit low mass stars. Millisecond pulsars are old neutron stars that undergo resurrection after the compact star accretes angular momentum laden material from its companion (see Phinney & Kulkarni 1994).

Pulsar timing over the years has established that the "garden variety" radio pulsar population is largely single (Taylor et al. 1993). This is decidedly surprising, as binarity is predominant in massive stars (Abt 1983). Evolution of binaries is theoretically well understood (Verbunt 1993; Bhattacharya & van den Heuvel 1991). Together these dictate that a certain small, but significant fraction of radio pulsars should possess massive main sequence companions (Lipunov et al. 1994; Lipunov & Prokharov 1984). Nevertheless, scores of neutron stars orbiting massive stars have been observed as luminous, accretion-driven X-ray pulsars (the massive X-ray binaries (MXRB); but not as radio pulsar main sequence companion systems.

Massive X-ray binaries occur in a wide orbital period range. In MXRBs with orbital periods $P_{orb} \lesssim 10$ d, X-rays are generated as the NS accretes from a

circumstellar disk formed as the companion overflows its Roche lobe (Bhattacharya & van den Heuvel 1991). Neutron stars accreting from a stellar wind are observed as X-ray sources orbiting early type supergiants and Be-stars, typically with larger orbital separations, $P_{orb} \lesssim 100$ d. In this case the companions are deep inside their Roche lobe.

Neutron stars can populate even wider orbits with massive companions, in which case they would be quiescent in X-rays. This idea is bolstered by mounting evidence that nascent NS are imparted large recoil velocities in asymmetric supernovae (Lyne & Lorimer 1994; Frail et al. 1994). With a substantial kick, the newborn neutron star could either completely escape the gravitational potential of its companion, or settle into a wide eccentric orbit around it. In orbits of $P_{orb} \gtrsim 10^3$ d, the accretion rate from a radially weakening wind is small to the extent that an orbiting NS may avoid accretion and be visible as a radio pulsar for longer time-span, perhaps for as long as the main sequence lifetime of the companion ($\sim 10^7$ yr).

5.1.1.1 – Discoveries of Two Interesting Binary Pulsars

Until recently, Pulsar-MMS binaries were the "missing link" in the evolutionary chain for massive stars. Recent discoveries of two binary pulsars have bridged this gap. From cumulative findings of all pulse searches in the past, population statistics suggest that a meager 1 in 500 pulsars have massive companions (Camilo 1995). The fractional abundance of binary pulsars may be larger, however, such systems could be elusive because severe selection effects could govern their observability (Illarionov & Sunyaev 1975; Korlinov & Lipunov 1984ab). If radio pulsar - main sequence star binaries occur as often as the Be X-ray binaries then only the "tip of the iceberg" of a vast hidden population of such binaries has thus far been observed (van den Heuvel & Rappaport (1987) rationalize in context of Be X-ray binaries).

The binary pulsar PSR B1259−63 system was discovered at Parkes in a survey of the Galactic plane at 1.5 GHz (Johnston et al. 1992a). The pulsar was later shown to be in a highly eccentric 3.5 yr orbit around a 10th mag Be star SS 2883 (Johnston et al. 1992b). The pulsar period is relatively short at 47.7 ms, and the measured period derivative implies a pulsar characteristic age $\tau_c = P/2\dot{P} \approx 3.3 \times 10^5$ yr and a surface magnetic field strength $B \approx 3.3 \times 10^{11}$ G. Optical observations indicate that the companion star is of the spectral type B2e, with an inferred mass close to 10 $M_\odot$ and a radius $R_* \sim 6R_\odot$ (Johnston et al. 1994). The mass estimate implies an orbital inclination $i \sim 35^o$ for this binary. The orbital eccentricity is very high, $e \approx 0.87$, and for $\sin i \sim 0.5$ the pulsar can approach within $\sim 25R_\star$ of the companion star at periastron, possibly passing through the Be circumstellar disk (Manchester et al. 1995; see also section 5.1.3). The first observed periastron passage showed that the pulsar was eclipsed at radio frequencies of 1.5 GHz (Johnston et al. 1992b), almost certainly due to free-free absorption and multi-path scattering. Effects of the companion's wind have been discussed extensively in the literature (see Kochanek 1993, Manchester et al. 1995) and probably play an important role in shrouding such pulsars from astronomers.

Kaspi et al. (1994) have described a second such system containing the pulsar PSR B0042−73, first discovered in a systematic survey of the Magellanic Clouds for radio pulsars (McConnell et al. 1991). This is the only known pulsar in the Small Magellanic Cloud. The pulsar orbits a 16th mag B1V star (Bell et al. 1995). In this case, the B-star shows no emission line activity. Lower limits to its mass loss rates ($\dot{M}_w < 10^{-11}\ M_\odot \mathrm{yr}^{-1}$) have been set (Kaspi, Tauris & Manchester 1996) with multifrequency timing observations of the pulsar near periastron and apastron. Pulsar timing shows that PSR B0042−73 has spin period of 0.93 s in an eccentric ($e \approx 0.81$), $P_{orb} \approx 51.17$ d orbit around the B-star. Timing measurements, have revealed interesting Newtonian orbital effects. The B star is probably spinning very rapidly and spin induced quadrupole contributions to its gravitational field influence advance (or regression) of periastron and precession of the binary orbital plane (Lai et al. 1995).

5.1.2 – MASSIVE BINARY EVOLUTION

Knowledge of the frequency of occurrence of binaries with two massive components and their orbital period distribution is necessary in order to quantify birthrate estimates for binary pulsars. These former are, however, poorly understood. Current ideas suggest that binarity in massive stars is probably a rule rather than an exception. Most searches for spectroscopic doubles to O and B stars concur on binary fractions $f_b \sim 0.4$ (Garmany et al. 1980, Abt & Levy 1976 & 1978). This is in spite of the fact that such searches remain incomplete due to the presence of large amplitude velocity perturbations in the atmospheres of early type stars ($\sim$ 30 km s^{-1} in O stars and $\sim$ 20 km s^{-1} in B stars; see Abt 1983). Observational studies of nearby binaries have generally found that the distribution of orbital periods is consistent with a flat distribution in $\log P$ for orbital periods between a few days and several thousand days (Popova, Tutukov and Yungelson 1982; Abt 1983). For massive stars, this distribution may be bimodal with intermediate orbits (between 10^3 and 10^4 d) being underpopulated. The short period bifurcation binaries have mass ratios close to unity, while longer period capture companions to massive stars obey the Salpeter mass function (Abt 1983).

The sheer abundance of binaries in nature means that an understanding of their evolution is important to our understanding of stellar evolutionary processes as a whole. In massive pairs, the simplest form of evolution proceeds in a 'conservative' way, i.e., total mass and total angular momentum of the system are conserved during mass transfer. As the primary evolves off the main sequence, it expands and may fill its Roche lobe transferring mass to the secondary. Stars can, in the process, lose all of their hydrogen rich envelopes and become He stars which are potential candidates of the Type Ibc supernovae. Three cases of mass transfer can occur (cases A, B & C; Kippenhahn & Weigert 1967). In case A, mass transfer occurs during the hydrogen burning phase of the primary; in case B, after core H burning and before He ignition; and in case C, during the core He burning (Figure 5.1). Details of the latter two cases may depend on whether

the primary has a radiative or a convective envelope during mass transfer. If the envelope is convective, dynamically unstable mass loss may result and a common envelope phase may ensue (Verbunt 1993).

If the primary star goes supernova, there is higher likelihood for the newborn neutron star to remain bound when the pre-supernova orbital separation is less than a few weeks. To most effectively avoid disruption at the time of the supernova, the Keplerian velocity of the pre-supernova star must not be much smaller than the average supernova imparted kick velocity. Therefore, binaries in which mass transfer occurs during the course of evolution, are more likely to result in neutron stars with bound orbits (also if the primary has lost mass, the supernova ejects less matter (Blaauw 1961)). Mass transfer ensures that a binary orbit shrinks to form a close pair as the more massive primary donates matter to the system secondary.

Podsiadlowski et al. (1992) have modeled the evolution of close binaries that have primaries ranging between 8 $M_{\odot}$and 20 $M_{\odot}$. They find that approximately one in three such stars would undergo close binary evolution, with mostly case B or case C mass transfer (see Figure 5.1). In their simulations, the authors trace pre-supernova evolution of mass tracks in order to predict the ratios of various types of supernovae. Computing a priori evolutionary tracks is difficult because, as previously discussed, statistical data on such binaries is incomplete, and major phases of evolution are theoretically incompletely understood and difficult to model. The numerical simulations conclude that perhaps a fraction $f \sim 0.15$ to 0.25 of all supernovae must be the result of explosions of massive primaries. This fraction can be used to estimate birthrates of neutron stars in binary systems as is demonstrated in § 5.1.2.

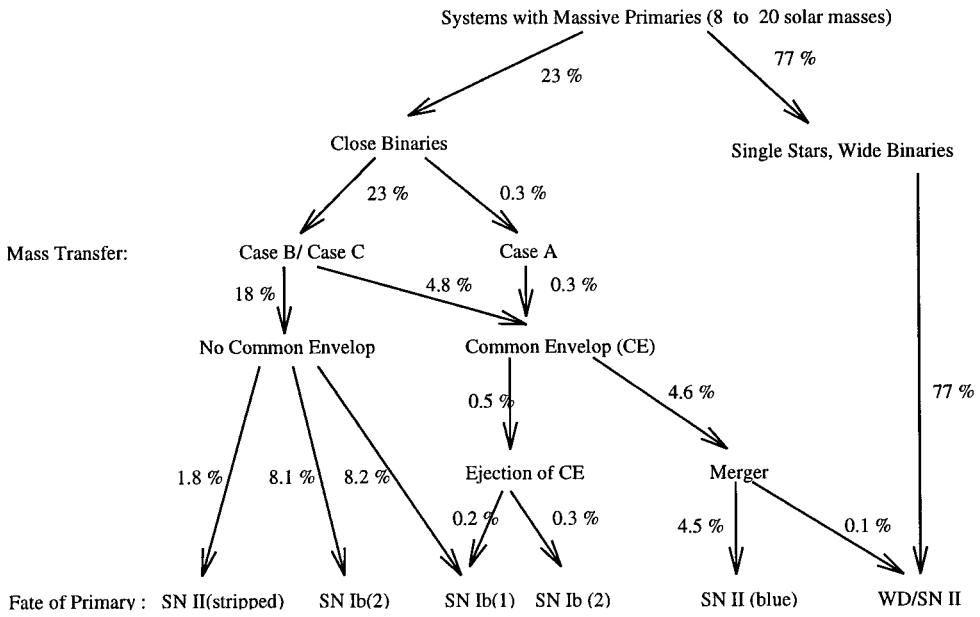

Figure 5.1: Summary of evolutionary scenarios for systems containing massive primaries with masses between 8 $M_\odot$ and 20 $M_\odot$ (simplified). The percentages give the (theoretical) probabilities that a system with a primary in the chosen mass range passes through a particular evolutionary channel. (The probabilities are based on Monte-Carlo simulations and are only very approximate; Figure adapted from Podsiadlowski et al. (1992)).

5.1.3 – EXPECTED NUMBERS OF BINARY NEUTRON STARS

Rough estimates of the rate of formation of neutron star and main sequence star (NS-MMS) binaries in the Galaxy can be made. The Galactic rate of non-Type Ia supernovae (Types Ib and Ic are most probably related to binary evolution), the progenitors of young neutron stars and a predominant fraction $\sim$ 80 % of all supernovae (van den Bergh & Tammann 1991), is about $R_{SNe} \sim 0.01e$ yr^{-1}, where e is a multiplicative factor embodying the uncertainty in this number and is of order unity.

Based on findings of binarity studies, as discussed previously, we assume that a fraction $f_b \sim 0.2$ of these SNe are due to primaries in massive binaries, although this number may be higher (Podsiadlowski et al. 1992). A majority of these are Case B mass transfer systems where the primary transfers mass, fattens its companion, and explodes as a He-star if the core mass $\gtrsim 2.2\ M_\odot$. If the supernova were symmetric, the system would remain bound, as more than half the system mass is in the secondary. However, with the newly revised estimates of pulsar kick velocities of $v_k \sim 450$ km s^{-1} (Lyne & Lorimer 1994) bound systems are less likely to occur. Brandt and Podsiadlowski (1995) estimate this number to be close to a fraction $f_k \sim 0.3$ with survival occurring predominantly in systems with the heaviest secondaries and close pre-supernova orbits $P_{orb} \lesssim 100$ d. The birthrate of isolated neutron stars/pulsars is, therefore, $R_{INS} \approx R_{SNe}(1 - f_k f_b) \sim 0.01e$ yr^{-1}; and for binary neutron stars/pulsars it is $R_{BNS} \approx R_{SNe} f_k f_b \sim 0.0005e$ yr^{-1}. As the secondary lifetimes are typically 10^7 yr, there must be about ~ 5000 neutron star - main sequence star systems in the Galaxy at any time. This estimate is in accordance with the demographics of Be X-ray binaries (Rappaport & van den Heuvel 1982) which are estimated to number $\sim 10^3 - 10^4$, from simple extrapolation of their local density to the entire Galaxy.

Our interests lie in neutron stars that are detectable as radio pulsars. Assume the lifetime of a radio pulsar in a binary to be $\tau_{BP} \sim \eta \tau_{IP}$, where τ_{IP} is the isolated pulsar lifespan $\sim 10^7$ yr and $\eta \leq 1$ is a survivability factor for a binary

pulsar. Binary pulsars spindown is steered by a combination of electro-magnetic and accretion torques (see appendix B) until pulsar action eventually ceases. Isolated pulsars undergo only electromagnetic spindown. The expected binary pulsar to isolated pulsar ratio in the Galaxy is simply

$$N_{BP}/N_{IP} \approx \eta R_{BNS}/R_{INS} \sim 0.05\eta. \tag{5.1}$$

From past pulsar surveys, the empirically determined ratio is ~ 0.003, or an order of magnitude lower (if $\eta \sim 1$) than expected from simple birthrate estimates. Reconciliation of these two numbers suggests that accretion torques may be important in decreasing the lifetime of a binary pulsar.

We must recognize, however, significant but inestimable contributions towards η from other selection effects as follows:

A. Radio pulsar surveys are traditionally performed at meter wavelengths because pulsars have steep radio spectra. However, detrimental effects to the propagation of meter-wave radiation from a putative binary pulsar, due to the companion stellar wind, could modify the spectrum at lower frequencies. Unless the pulsar is young and very luminous so as to disrupt coherent structure of the stellar wind, it is likely to remain invisible inside the companion's free-free photosphere (see appendix A). For instance, PSR B1259−63 was originally discovered at 1.5 GHz in the Parkes survey (Johnston et al. 1992a) and displays an anomalously inverted spectral index making it a factor of ten fainter at $\sim$ 400 MHz.

B. There must exist a distance effect as well. Isolated pulsars diffuse to occupy the local Galaxy with a filling factor close to unity due to large random space motions. On the other hand, binary pulsars possess smaller random motions $\lesssim 100$ km s^{-1}, shorter lifespans and must lie in the vicinity of their original birth sites, the OB associations. OB clusters are clumped near the spiral arms and therefore, on the average, the distances to binary pulsars must be greater than towards isolated pulsars. On the average, the electron column

density ($\int n_e dl$ or dispersion measure) can also be much higher towards OB associations as the line-of-sight traverses HII regions and an ISM that is constantly shocked and ionized by supernova remnants (Frail et al.1993).

These selection effects can drastically reduce the number of pulsars observed in non-directed searches. Therefore a careful, more sensitive targeted search towards massive stars carries justification.

5.1.4 – CHOICE OF TARGET STARS

A search for radio pulsar companions to massive stars should involve a judicious choice of target stars. The Be stars are intriguing targets to search as they show signs of a history of mass transfer. These emission line stars, which are 20% of all B stars (Cote & van Kerkwijk 1993) show strong Hα emission features along with a prominent far-IR excess (Sletteback & Snow 1987). Both the Hα and IR excesses are thought to originate from a circumstellar envelope. Moreover, these stars are rather rapid rotators ($v \sin i > 100$ km s^{-1}), with some stars rotating near equatorial breakup angular speeds (Underhill 1966). The so-called Be mechanism causes a strong rotationally driven wind which shows strongly aspherical symmetry and is confined to the equatorial plane of the star. In fact, observations of Be stars suggest that rapid rotation is a key ingredient in explaining the diverse phenomena observed in such stars. There are various possibilities for their formation (Pols et al. 1991 and refs. therein):

A) They could be born spinning rapidly and the Be phase could occur at any point during the main sequence lifetime of the star.

B) They could occur at the time of the spin-up phase when the star contracts following the exhaustion of the core hydrogen (Shild & Romanishin 1979), but the relatively large fraction of Be stars finds this hard to account for.

C) Finally, they could be post-mass-transfer systems. A system composed of a Be star and a He star could be formed at the end of case B mass transfer

in intermediate mass binaries. Calculations of mass and angular momentum transfer show that it would be rather hard to avoid spinning up B star to the observed rotation rates. In this case Be stars should have evolved companions.

Systems that are definitely post-mass-transfer are the Be/X-ray binaries, of which about 30 are known. In these systems the orbiting neutron star accretes matter from the dense stellar wind, thereby generating X-rays with luminosities in the range of $10^{34} - 10^{38}$ erg s^{-1}. The orbital periods are in the range $\sim$ 10 d to a few 100 d and the Be stars are of the earlier spectral type (B2 and earlier).

Numerical experiments of the Be star population show (Pols et al. 1991, Zwart 1995) that only the most massive Be (earlier than B2V) stars should possess neutron star companions. Neutron star - Be binaries should number $\sim$ 10% of the earliest Be stars. These models indicate a dramatic decrease of neutron star companions around later type Be stars (i.e., binaries that originally have primaries $> 10\ M_{\odot}$and $q < 0.4$). This is supported by the study of Be X-ray binaries, where the optically determined companions are of the spectral class B2 and earlier (Bradt & McClintock 1983).

5.2 TWO SEARCHES FOR PULSARS AROUND EARLY TYPE MASSIVE STARS

ABSTRACT: We describe two sensitive targeted surveys to search for pulsars in binary systems with massive, main sequence companions. A pulse search survey was undertaken at the Arecibo 305-m radio telescope at frequencies of 430 MHz and 1.4 GHz. A continuum mapping radio search was done at the VLA at 1.4 GHz. No new pulsars were discovered, and no radio sources were found associated with the target stars to impressive limits. We provide a background for motivation, discuss the sensitivities achieved in the searches and the implications of our results.

5.2.1 – INTRODUCTION

A newborn neutron star in a binary system will first be visible as a radio pulsar before electromagnetic and accretion torques stop the pulsar process; whereafter its emission is accretion powered. So far, two radio pulsar-main sequence star binaries have been discovered. The pulsar PSR B1259−63 is such a double and is shown to be a 48 ms pulsar in a highly eccentric 3.3 yr orbit around the Be star SS 2883 (Johnston et al. 1992b). Kaspi et al. (1994) have described a second such system containing the pulsar B0042−73 ($P \approx 0.93$ s) orbiting a B1V star in the Small Magellanic Cloud. Both pulsars have been discovered in general surveys that were not targeted towards any binary systems or massive stars.

These systems are widely recognized member of a period lasting up to $\sim 10^7$ yr in the evolution of a massive binary, starting at the point of the first supernova in the system and terminating as the secondary leaves the main sequence. As the primary evolves off the main-sequence, it expands to fill its Roche lobe, thereby transferring mass to be secondary. In the process stars can lose all of their hydrogen rich envelopes and become He stars, progenitors of the Type Ib supernovae. If the resulting supernova is symmetric, the system remains bound because a majority of the system mass is now in the companion star (Verbunt 1993). However, large

asymmetries in supernova explosions, leading to a kicked neutron star, can unbind the binary even if less than half the system mass is lost in the explosion (Brandt & Podsiadlowski 1995). If a bound system results, then the most common observed daughter systems are the Be/X-ray binaries (van den Heuvel & Rappaport 1987).

For Be/X-ray binaries, the progenitor is usually an intermediate mass system, e.g., with component masses of the order of 10-15 $M_\odot$. Conservative mass transfer ensures that the orbits of such systems widen considerably before the core collapse of the initially more massive star, such that the orbital period in such stars is expected to be at least a few weeks, as is indeed observed. If nascent neutron stars do indeed receive kicks, then even wider orbit systems with extreme eccentricities can result, provided the system does not become unbound. The supernova itself is preceded by two stages of mass transfer (Habets 1986). The first stage ends after the primary has transferred its H envelope to the secondary thereby becoming a He star. The reason for the second stage is that He stars $\gtrsim 3.5\ M_\odot$ also evolve into giants. He cores $\gtrsim 2\ M_\odot$ would undergo core collapse and create neutron stars. This requires the Be/X-ray systems evolve from primaries with initial masses greater than 8 $M_\odot$. None of the optical stars in Be/X-ray binaries has a spectral type earlier than B0V, corresponding to a mass of about 12 $M_\odot$; one expects Be/X-ray binaries to originate from systems with initial primaries in the range 8-15 $M_\odot$(assuming conservative evolution and an average initial mass ratio of 0.5)(van den Heuvel & Rappaport 1987). This corresponds to an initial spectral type of the range B3-4V to B0V.

The Be/X-ray binaries are the most abundant group of massive X-ray binaries in the Galaxy, with a total inferred numbers between 10^3 and 10^4 (Rappaport & van den Heuvel 1982). These estimates are made from extrapolation of the local density of these systems to the whole Galaxy. Bailes (1989) invokes a large Galactic population of wide separation binaries (like the Be systems) to explain the magnetic field velocity correlation (v-B) observed in radio pulsars. In this picture, the binary disrupts at the time of the second supernova. The older pulsar, which has undergone some magnetic field decay due to accretion, is now released

with a velocity $\sim v_{orb}$, whereas the newborn pulsar escapes with higher velocity $\sim v_{kick}$. Some pulsar population studies also find evidence for significant binary injection of pulsars into the isolated field population (Deshpande et al. 1995). These pulsars have weaker magnetic fields, presumably because of an accretion history and cluster around the spin-up line for pulsars in the $P - \dot{P}$ diagram.

We describe two sensitive searches for binary radio pulsars with massive main sequence companions. As previously mentioned, the two systems discovered to date were found in non-pointed searches. We have devised a more careful search strategy in the hope that general non-pointed searches are less sensitive towards discovering binary pulsars. The discovery of PSR B1259−63 at a higher search frequency (1.5 GHz) and its invisibility at traditional search frequencies ($\lambda \sim 1$ m) is one such cue. The motivation for discovering other such pulsars is two-fold: i) Such systems are inherently interesting as physics laboratories. Through pulsar timing one can study orbital dynamics, stellar structure, stellar winds and even accretion physics. ii) To obtain complete population statistics of binary pulsars. Combined with results of other such surveys (see §5.2.3) covering more than 700 massive stars, such a study is feasible.

The largest fraction of target stars are the Be-stars. There is evidence that these stars are the product of a phase of mass transfer in massive binaries and are likely to have degenerate companions.

5.2.2 – OBSERVATIONS

We detail the observations, data reduction procedures and sensitivities of our two radio searches.

5.2.2.1 – Arecibo Pulse Search Survey

We have carried out a search for pulsed radio emission towards 134 optically visible massive stars with the Arecibo 305-m Radio Telescope in Puerto Rico. The target stars were situated at low galactic latitudes and within 3 kpc of the sun.

Telescope coverage further limited the sample to lie within declinations of 18 ± 20 deg. The survey employed the use of dual circular polarization 430 MHz and 1.4 GHz feeds, using cryogenically cooled receivers mounted at the telescope foci. The 430 MHz line feed is centered at a frequency of 428.5 MHz with a total 3 dB bandwidth (BW) of 10.2 MHz and with a half power field of view of 10 arcmin; the total sky observed with this feed was ~ 3 deg^2). The 1.4 GHz system was centered at 1.480 GHz, with a bandwidth of 40 MHz and a field of view of 3 arcmin; the total sky observed was ~ 0.25 deg^2). The Arecibo autocorrelation spectrometer (AAS) (NAIC 1989), with a sampling rate of ~ 2 kHz. It was configured as a 2x128 channel system for our purposes, resulting in a channel BW of 78.125 kHz at 430 MHz and 312 kHz at 1400 MHz. The autocorrelator is divided into four 2.5 MHz banks (at 430 MHz), each of which is fed into a 32 lag, three level correlator. Correlator integration and hardware specifications result in an effective sampling time of 506.625 μs (τ_s). The autocorrelation functions for two polarizations along with additional 12 bit total power counters were blocked into records and written to magnetic tape by the control computer. Integration time at both frequencies was $\tau_{int} \sim 20$ min.

The data were reduced at Caltech using our standard pulsar reduction package PSRPACK installed and running on a local network of several Suns and one HP workstation. For a full description of the programs that are part of PSRPACK, refer to Deich (1996). For each pointing, raw autocorrelation samples, recorded by the AAS every τ_s for a total integration τ_{int} onto tape, were loaded onto a chosen computer. Each autocorrelation is Fourier transformed to reconstruct the instantaneous observing band at 128 adjacent frequency channels. The dynamic power spectrum (or filter bank time-stream) thus realized for each pointing is then dedispersed at a chosen set of trial dispersion measures ($DM = \int n_e dl$; the electron column density along the line of sight to the pulsar usually expressed in cm^{-3} pc). This operation includes applying a linear frequency dependent shift in time, appropriate for a chosen dispersion measure, and then collapsing the dynamic spectrum in frequency space. The dedispersed stream is then Fourier transformed and the

resulting power spectrum is searched for significant periodicities (above a certain threshold criterion; we choose 8 σ). All hits are harmonically folded to accumulate the total power in the periodic signal, and the resulting list of hits is sorted by signal to noise ratio. Finally, the dedispersed stream is folded at the best periods to form a signal profile, which is inspected by eye for pulsar-like signatures. Radio frequency interference (RFI), a real problem at these frequencies (more so at 430 MHz), is excised in both time and frequency domain. The zero DM time-stream is inspected for outlier (5 σ) events. Low level spurious periodicities are removed by narrow width frequency domain filtering. A list of spurious frequencies has been accumulated for Arecibo Observatory, and is inspected and updated for each observation. Sporadic interference is usually due to military radar, lightening or other forms of local interference. Data were deemed to be RFI corrupted if zero DM trial reductions could not be rid of spurious signals via either time-based or frequency-based techniques.

The standard expression for sensitivity is given by (Ray et al. 1995)

$$S_{min} \approx K\left[\frac{T_{rec} + T_{sky}(l,b) + T_{sp}(ZA)}{G(N_p B \tau_{int})^{1/2}}\right]\sqrt{\frac{w_{eff}}{P - w_{eff}}} \tag{5.2}$$

where factor $K \sim 12$ is empirically determined from measurements of known pulsars and corresponds to a detection threshold of $\sim 8\sigma$. T_{rec}, $T_{sky}(l,b)$ and $T_{sp}(ZA)$ are the receiver temperature, sky temperature and the effective spillover temperature (function of zenith angle, ZA) respectively. G is the forward gain of the telescope in K Jy^{-1} (18 and 8 K Jy^{-1} for the 430 MHz and 1.4 GHz systems respectively), $N_p = 2$ is the number of polarizations, and B is the feed bandwidth. The remaining factor gives the pulse duty cycle dependence, with P being the intrinsic pulsar period, w_{eff} the effective width of its pulse with intrinsic w, sampling and dispersion broadening and given as

$$w_{eff} = [w^2 + \beta^2 \tau_s^2 + \tau_{DM}^2]^{1/2}. \tag{5.3}$$

Dispersion broadening within a filter channel is expressed as

$$\tau_{DM} \approx 8.3\ \mu\text{s}\ \frac{\Delta\nu DM}{\nu^3}, \tag{5.4}$$

where $\Delta\nu$ is the frequency channel width in MHz and ν is the observing frequency in GHz. Sensitivities at the two observing frequencies are depicted in figures 5.2 and 5.3.

The estimated sensitivity thresholds this survey are near 200 μJy at 430 MHz and 100 μJy at 1.4 GHz. At the 3 kpc distance to the furthest observed star the survey should have detected a radio pulsar with period $P \gtrsim 30$ ms with a flux of $S_{0.4} \sim 1.8$ mJy-kpc^2. At 1.4 GHz, the flux limit is $S_{1.4} \sim 1$ mJy-kpc^2. These limits are reasonably constraining as most pulsars have luminosities well above these limits; the mean luminosity for pulsars at 400 MHz is ~ 100 mJy-kpc^2.

5.2.2.2 – VLA continuum survey

We describe radio observations of 86 Be stars (luminosity class III, IV, V) chosen from the Wackerling catalog (Wackerling 1970) with visual magnitudes $m_v \lesssim 9$. All stars were observed at L-Band (20-cm) with the VLA in its widest configuration (the A-array) at an angular resolution of $\sim 1.3''$. The observations were bunched into three separate epochs between October 10, 1992 and October 23, 1992. Two separate IF bands, each measuring both hands of circular polarization and each with an observing bandwidth of 50 MHz, were used at 1465 and 1515 MHz. The target stars were observed in the snapshot mode, with effective integration time on each star being in the range of seven to ten minutes. The large two dimensional structure of the VLA allows for adequate u-v coverage during such snapshot observations to search for point-like emission, free from spurious source confusion for the widest array configurations. Target observations were interspersed (every 20 to 30 min) with observations of standard VLA phase calibrator sources. This is a necessary step during observations in the A-array, as ionospheric gain variations across the VLA arms become important on such timescales. Subsequent calibration and reduction of the data was done with the AIPS data reduction package.

Wide field images approximating the primary beamsize ($\sim 30'$) of all the scans were first generated to determine the location and intensity of the brightest sources in the field. Source models of these were then used to CLEAN $1'$ maps around the position of the target star. Large sidelobe structure in the synthesized beam in the snapshot mode can be a potential source for confusion throughout the images. The average thermal noise level in the images was ~ 180 μJy beam^{-1}.

The objectives of the VLA search were twofold:

i) An active pulsar associated with the target star and beamed favorably would be detected as a continuum point source. An advantage of a continuum search is that sensitivity is not degraded as a result of propagation effects such as dispersion and multi-path scattering. These can wash out the temporal structure in pulsed signal, making a pulsed search relatively insensitive.

ii) Detection of possible non-thermal continuum emission generated at the interaction surface of the pulsar wind and the companion star wind (see for example, Kulkarni et al. 1992) was a second goal. Shock acceleration of particles in strongly interacting winds can be a potential source of strong synchrotron emission which is radiated isotropically, unlike the pulsed emission, which is beamed.

We observed at 1.5 GHz as a compromise between the steep spectral dependence of the pulsed emission and possible free-free absorption in the companion wind. A higher frequency would allow us to probe deeper into such a free-free photosphere. Such a photosphere will also radiate thermally with $S_\nu \propto \nu^{0.6}$ (Panagia & Felli 1975). Non-thermal emission from internal shocks in winds are seen in the early type O stars, Wolf-Rayet stars and the magnetic giants (Bp) (Beiging et al. 1989), but such emission should not effect our sample of mostly late OV and BV stars.

No radio sources were discovered within $2''$ of the cataloged B1950 positions of the target stars (Wackerling 1970). A search circle of $2''$ corresponds to a transverse speed of $250 d_1 t_{20}^{-1}$ km s^{-1}, where distance is in $1 d_1$ kpc and time is in

$20t_{20}$ yr. The search circle well accounts for possible proper motion of the target stars during the last twenty years. The 3σ limits on point source emission in the maps are ~ 0.5 mJy, translating to a source luminosity $L_R \sim 8 \times 10^{26} d_1^2$ erg s^{-1}.

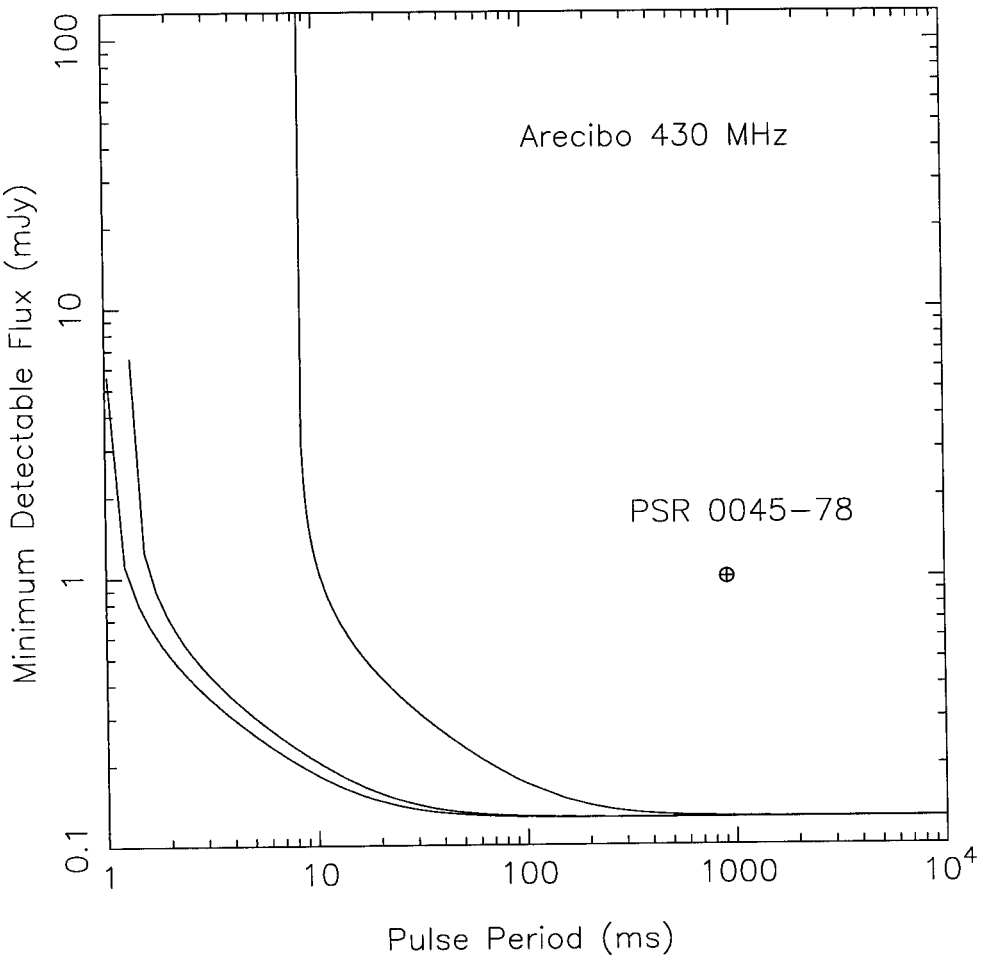

Figure 5.2: This figure shows the sensitivity plot for the Arecibo Observatory search at 430 MHz. The curves denote sensitivity at dispersion measures (DM) of 10, 10^2 and 10^3; with sensitivity decreasing as dispersion measure increases. PSR 0045−78, the binary pulsar in the Small Magellanic Cloud, is shown for comparison.

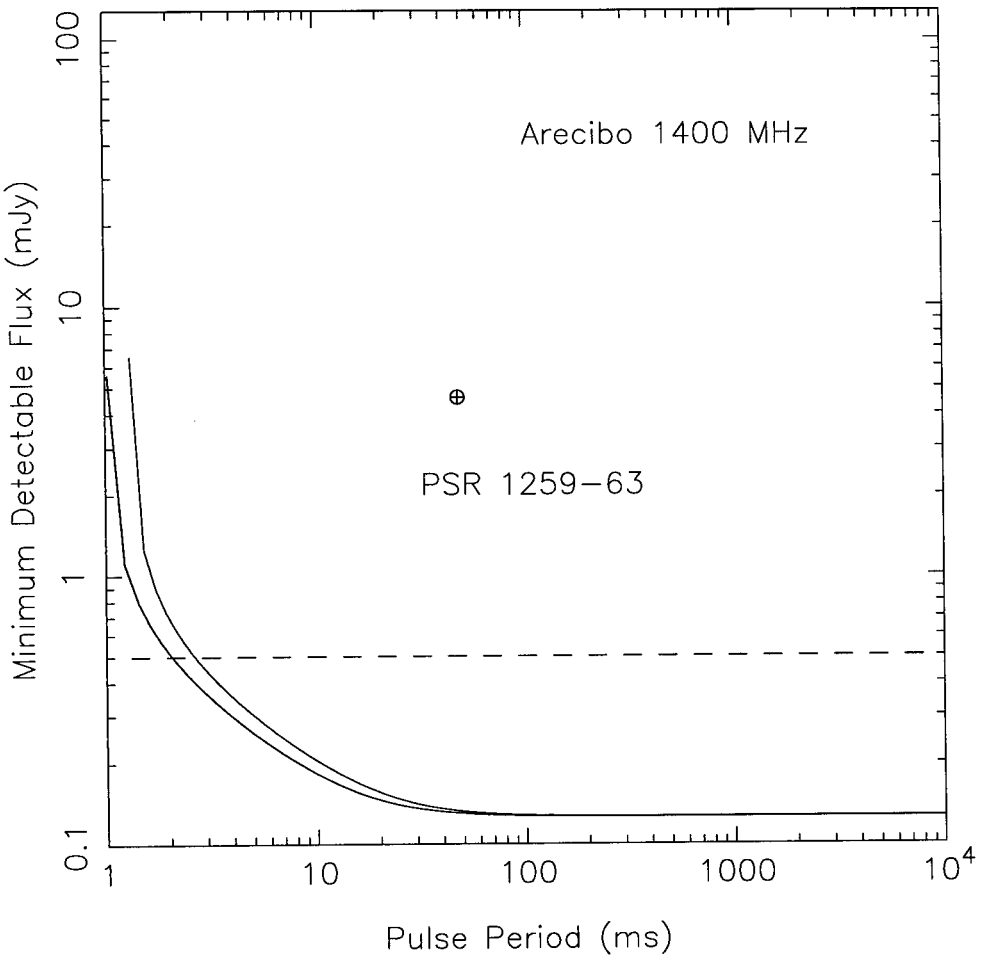

Figure 5.3: This figure shows the sensitivity curves for the Arecibo Observatory search at 1400 MHz. The individual curves denote sensitivity to pulsars at dispersion measures (DM) of 10, 10^2 and 10^3; with sensitivity decreasing with increasing dispersion measure. Curves at dispersion measures of 10 and 100 are indistinguishable on the plot. The binary pulsar PSR 1259−63 is shown for comparison. The horizontal dashed line denotes the period and dispersion independent sensitivity of the VLA survey.

5.2.3 – DISCUSSION

We have found no pulsars orbiting ~ 240 massive stars for which good quality data has been collected at either telescope. There are also no continuum point sources associated with the Be-stars observed at the VLA to a 0.5 mJy limit. Since neither the pulsar luminosity function (and fractional beaming) nor the local environments of massive stars are well quantified, it is hard to interpret the non-detection in a precise manner. Our claim is that these searches were most sensitive towards pulsars that populate wide eccentric orbits ($P_{orb} > 100$ d) around the target stars for two principal reasons. First, within $P_{orb} < 100$ d, the pulsar may have a significantly decreased radio lifetime (less than a few million years, the typical lifetimes of the observed stars) than is set by simple dipole spindown (Appendix B). This conjecture is supported by the existence of numerous Be/X-ray binaries in this orbital period range (Bhattacharya & van den Heuvel 1991). Second, outside such an orbital range the wind plasma of the companion is likely to become optically thin to propagation of low frequency radio waves (Appendix A). In addition, there should also be little influence of the wind on the pulse structure of the putative pulsar's emission (Appendix A). The chances of having missed a wide orbit pulsar due to shrouding near periastron are small as only a small time fraction of the orbital duration is spent there. The putative pulsars targeted in this search would be between $\sim 10^6$ to 10^7 yr old, i.e., close to the average age of the stars in our sample. Older pulsars, such as these, are unlikely to couple to and disrupt the structure of the stellar wind, $\dot{M}v_\infty^2 > \eta L_p$, where η is the hydrodynamical coupling factor, and shine through from any orbital separation. Presumably, $\eta < 10^{-3}$ if the wind is to maintain a coherent structure from studies of the PSR 1259−63/SS 2883 system (Kochanek 1993).

Using distances and sensitivity thresholds (Figs 5.2 and 5.3) for each target star, we plot an upper-limit luminosity function for both the Arecibo and VLA samples (Fig 5.4). Estimates were made for stars that did not have listed distances in the Bright Star Catalogue. With knowledge of the stellar spectral type, the

color excess E_{B-V} for each star provided estimates for the visual extinction $A_V = 3E_{B-V}$ towards that star. Distances are from relation $5 \log d = V - M_V + 5.0 - A_V$, where d is the distance in pc and M_V is the absolute visual magnitude. Note that in the histogram of figure 5.4, a possible pulsar around a star in luminosity bin $L_{R,i}$ actually lies anywhere to the left of that bin. A luminosity function of known pulsars in plotted in figure 5.5.

The non-detection leads to a limit on the number of pulsars orbiting the Arecibo stellar sample. Assume $\hat{p}$, an unknown, to be the probability that each of the observed stars has a radio pulsar companion detectable to us. Then the chance of "m" detections in a search of "N" stars is a binomial distribution, with the probability that there are no detections being $P(\hat{p}) = (1 - \hat{p})^N$. A 2σ or 95% confidence limit on $\hat{p}$ is then set by $\int_0^{\hat{p}_u} P(\hat{p}) d\hat{p} = 0.96$, implying $\hat{p}_u = 0.026$ or 2.6%.

Sensitivity threshold curves displayed in figure 5.7 demonstrate that the Arecibo search was sensitive to practically all pulsars younger than $\sim 10^7$ yr (Be star lifespans) lying within three kilo-parsec. This threshold-line nearly traces the death-line for radio pulsars. As a result, adopting a pulsar beaming fraction of $\sim$ 30 %, (Sayer, Nice & Kaspi 1996) we conclude that the number of target stars in the Arecibo sample that could have orbiting radio pulsar companions is $\lesssim$ 8%.

Since the upper-end of the VLA luminosity thresholds (Fig 5.4) overlap with the lower-end of the luminosity range of known pulsars (Fig 5.5) we employ a separate scheme to put upper limits on the number of pulsar companions. The probability for a star which occupies luminosity bin $L_{R,i}$, to have a radio pulsar companion is deduced by calculating the cumulative probability $\int_0^{L_{R,i-1}} \phi(l) dl$, where $\phi(l)$ is the normalized observed luminosity function for known pulsars (Fig 5.5). The probabilities $\hat{p}$ thus determined for all VLA stars to have radio pulsar companions are binned in figure 5.7. We estimate $< \hat{p} > \approx$ 7%. Using a beaming fraction as above, we conclude that the number of target VLA stars that could have orbiting radio pulsar companions is $\lesssim$ 25 %.

Other targeted searches of this type are: 1) Survey of $\sim$ 400 southern massive stars at Parkes by the Caltech, Sydney University, CSIRO (Aus.) and Univ. of Manchester groups (results are unpublished). A fraction 50% of the surveyed stars were main sequence Be-stars. 2) A VLA 1.4 GHz survey of 44 nearby OB runaway stars by Philip et al. (1996). The authors find that less than 20% OB runaways may have pulsar companions, however, the supernova ejection model for OB runaway stars is not ruled out. 3) An NRAO 140-ft telescope search towards 40 OB runaway stars by Sayer et al. 1996. Their non-detection places a limit such that at most $25 - 50\%$ OB-runaway stars have pulsar companions.

These sensitive searches for radio pulsars around main sequence stars, show that pulsar-MMS star systems are rare. It seems likely and can probably be addressed via simulations, that kicks only in a narrow selective range would lead to bound pulsars in wide enough orbits so that they are visible as radio pulsars. As a result, not many such systems would exist.

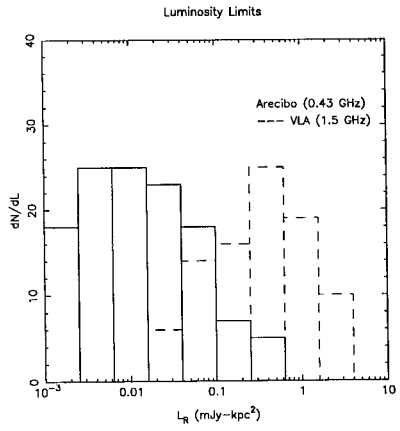

Figure 5.4: Histogram of luminosity upper limits for all stars in a Arecibo and VLA samples in mJy kpc^2 at 0.43 and 1.5 GHz respectively. The Arecibo search is sensitive enough that all known pulsars would have been detected at either 0.43 or 1.5 GHz. According to figure 5.5, the VLA search would have missed some pulsars.

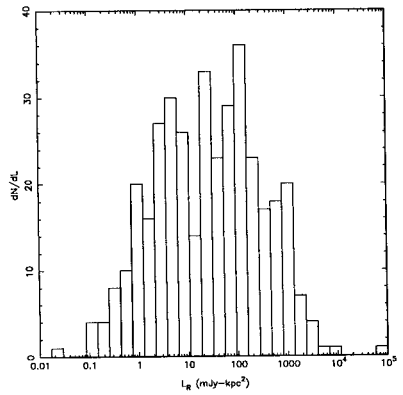

Figure 5.5: Histogram displaying the 1.4 GHz luminosities of $\sim$ 400 known pulsars.

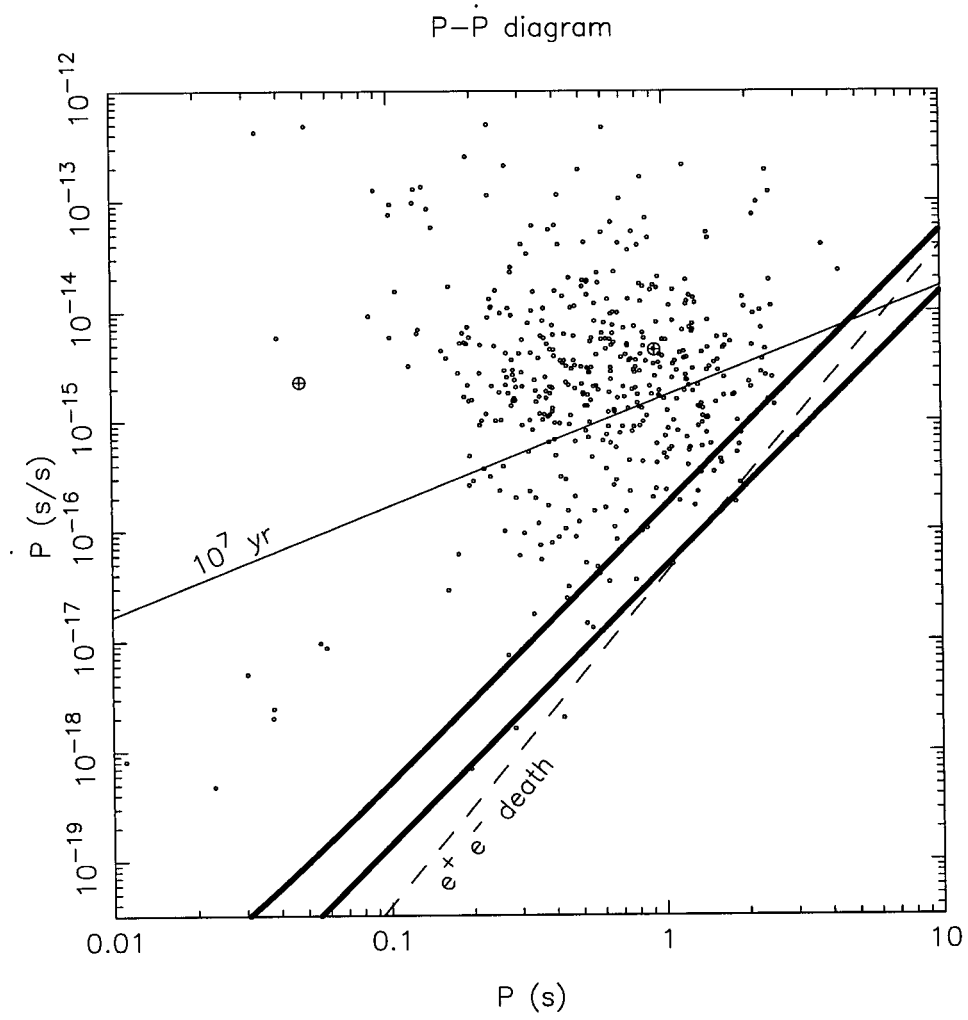

Figure 5.6: Standard $P - \dot{P}$ diagram for Galactic and Magellanic cloud radio pulsars. Small points represent individual pulsars. The solid line shows the characteristic age $\tau_c = P/2\dot{P} \sim 10^7$ yr. All pulsars with massive main sequence companions must lie to the upper left of this ten million year line. The dashed line represents the standard pulsar death line, below which a pulsar cannot initiate pair cascades and will not be radio luminous. The lower thickened line indicates the sensitivity of the Arecibo search assuming a standard pulsar luminosity function and a distance of 3 kpc to the pulsar (distance to furthest stars in the search).

The upper thickened line represents a sensitivity trace for the Very Large Array search to a continuum source. Circles with crosses represent the two known binary pulsars PSR B 1259−63 and PSR J 0045−78.

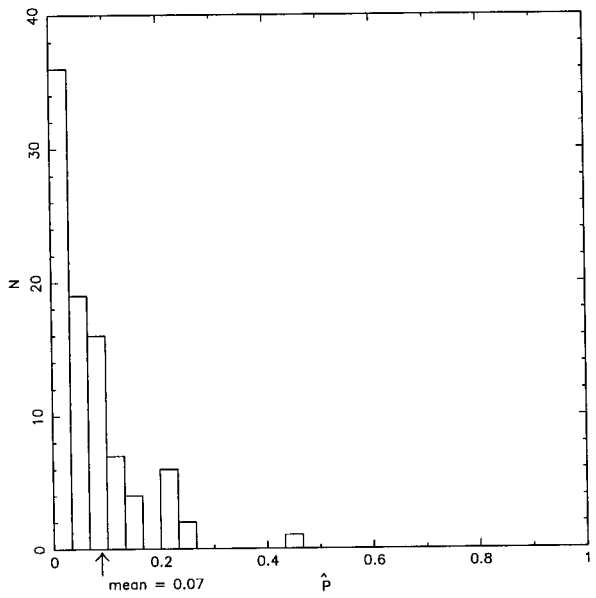

Figure 5.7: Probability of missing a pulsar in the VLA search is histogrammed for each target star.

REFERENCES

Abt, H. A. 1983, ARA&A, 21, 343

Abt, H. A. & Levy S. G. 1976, ApJSS, 30, 278

Abt, H. A. & Levy S. G. 1978, ApJSS, 36, 241

Bailes, M. 1989, ApJ, 342, 917

Beiging, J. H., Abbott, D. C. & Churchwell, E. B. 1989, ApJ, 340, 518

Bell, J. F., Bessell, M. S., Stappers, B. W., Bailes, M. & Kaspi, V. M. 1995, ApJ, 447, L117

Bhattacharya, D. & van den Heuvel, E. P. J. 1991, Phys Report, 203, 1

Blaauw, A. 1961, Bull. Astron. Inst. Neth., 15, 265

Bradt, H. V. D. & McClintock, J. E. 1983, ARA&A, 21, 13

Brandt, N. & Podsiadlowski, P. 1995, MNRAS, 274, 461

Camilo, F. 1995, PhD Thesis, Princeton Univ.

Campana, S., Stella, L., Mereghetti, S. & Colpi, M. 1995, A&A, 297, 385

Cote, J. & van Kerkwijk, M. H. 1993, A&A, 274, 870

Deich, W. T. S. 1996, Ph. D. Thesis, California Institute of Technology, to be submitted

Frail, D. A., Kulkarni, S. R. & Vasisht, G. 1993, Nature, 365, 136

Frail, D. A., Goss, W. M. & Whiteoak, J. B. Z. 1994, ApJ, 437, 781

Garmany, C. D., Conti, P. S., & Massey, P. 1980, ApJ, 242, 1063

Habets, G. M. H. J. 1986, A&A, 165, 95

Illarionov, A. F. & Sunyaev, R. A. 1975, A&A, 39, 185

Johnston, S., Lyne, A. G., Manchester, R. N., Kniffen, D. A., D' Amico, N., Lim, J. & Ashworth, M. 1992, MNRAS, 255, 401

Johnston, S., Manchester, R. N., Lyne, A. G., Bailes, M., Kaspi, V. M. & Qiao, G. J. 1992, ApJ, 387, L37

Johnston, S., Manchester, R. N., Lyne, A. G., Nicastro, L. & Spyromilio, J. 1994, MNRAS, 268, 430

Kaspi, V. M., Johnston, S., Bell, J. F., Manchester, R. N., Bailes, M., Bessel, M., Lyne, A. G. & D' Amico, N. 1994, ApJ, 423, L43

Kaspi, V. M., Tauris, T. M. & Manchester, R. N. 1996, ApJ, 459, 717

Kennel, C. F. & Coroniti, F. V. 1984, ApJ, 283, 694

King, A. & Cominsky, L. 1994, ApJ, 442, 910

Kippenhahn, R. & Wiegert, A. 1967, Z. Astrophys., 65, 251

Kochanek, C. S. 1993, ApJ, 261, 453

Korlinov, V. G. & Lipunov, V. M. 1984, AZh, 60, 284

Korlinov, V. G. & Lipunov, V. M. 1984, AZh, 60, 574

Kulkarni, S. R., Vogel, S. N., Wang, Z. & Wood, D. O. S. 1992, Nature, 360, 139

Lai, D., Bildsten, L. & Kaspi, V. M. 1995, ApJ, 452, 819

Lipunov, V. M., Nazin, S. N., Osminkin, E. Y. & Prokhorov, M. E. 1994, A&A, 282, 61

Lipunov, V. M. & Prokharov, M. E. 1984, Astro Sp Sc, 98, 221

Lyne, A. G. & Lorimer, D. R. 1994, Nature, 369, 127

Manchester, R. N., Johnston, S., Lyne, A. G., D' Amico, N., Bailes, M. & Nicastro, L. 1995, ApJ, 445, L137

McConnell, D., McCulloch, P. M., Hamilton, P. A., Ables, J. G., Hall, P. J., Jacka, C. E. & Hunt, A. J. 1991, MNRAS, 249, 654

Packet W. 1981, A&A, 102, 17

Panagia, N. & Felli, M. 1975, A&A, 39, 1

Philip, C., Evans, C. R., Leonard, P. J. T. & Frail, D. A. 1996, AJ, 111, 1220

Phinney, E. S. & Kulkarni, S. R. 1994, ARA&A, 32, 591

Podsiadlowski, P., Joss, P. C., Hsu, J. J. L. 1992, ApJ, 391, 246

Pols, O. R., Cote, J., Waters, L. B. F. M. & Heise, J. 1991, A&A, 241, 419

Popova, E. I., Tutukov, A. V. & Yungelson, L. R. 1982, Sov. Astr. L., 8, 160

Rappaport, S. & van den Heuvel, E. P. J. 1982, IAU Symposium No. 98, "Be Stars", eds. M. Jasheck & H. G. Groth, Reidel, Dordrecht, 327

Ray, P. S. et al. 1995, ApJ, 443, 265

Sayer, R. W., Nice, D. & Kaspi, V. M. 1996, ApJ, accepted.

Sletteback, A. & Snow, T. P. (eds.) 1987, "Physics of Be Stars", Cambridge Univ. Press, 557 pp.

Schild, R. E. & Romanishin, W. 1976, ApJ, 204, 493

Stella, L., Campana, S., Colpi, M., Mereghetti, S. & Tavani, M. 1994, ApJ, 423, L47

Taylor, J. H., Manchester, R. N. & Lyne A. G. 1993, ApJSS, 88, 529

Tavani, M., Arons, J. & Kaspi, V. M. 1994, ApJ, 433, L37

Underhill, A. B. 1966, "The Early Type Stars", Reidel Publ. Comp., Dordrecht

van den Bergh, S. & Tammann, G. A. 1991, ARAA, 29, 363

van den Heuvel, E. P. J. & Rappaport, S. A. 1987, IAUC 92, in the "Physics of Be Stars", eds. A. Sletteback & T. D. Snow, Cambridge University Press

Verbunt, F.1993, ARAA, 31, 1993

Wackerling, L. R. 1970, Mem. Roy. Astr. Soc., 73, 153

Waters, L. B. F. M., Taylor, A. R., van den Heuvel, E. P. J., Habets, G. H. M. J. & Persi, P. 1988, A&A, 198, 200

Zwart, S. F. P. 1995, A&A, 296, 691

5.2.4 – APPENDIX A

Plasma in the NS companion's stellar wind will affect the propagation of pulsar emission (Illarionov & Sunyaev 1975) due to absorption, multipath scattering and dispersion of the pulsed signal. Massive stars have radiationally driven winds with mass loss rates $\dot{M}$ typically of order $10^{-8}\dot{M}_8\ M_\odot \mathrm{yr}^{-1}$. The wind is kept ionized at $T_e \sim 5 \times 10^3$ K by the background stellar radiation field. For Be stars, it is proper to assume two separate components for the wind; a rotationally driven dense equatorial outflow, with $\Omega \sim \pi$, with low terminal speeds, $v_\infty \sim 500$ km s^{-1}, and a tenuous high latitude flow with $v_\infty \sim 2000$ km s^{-1}. Mass loss rates estimated in the equatorial flow are ~ 50 times larger than those inferred in the polar flow, with typical total $\dot{M}_8 \sim 0.1 - 1\ M_\odot$ yr^{-1} (Waters et al. 1988). Let us assume that the stellar wind is diffuse, with no significant clumping.

The free-free optical depth to radiation generated a distance a from the mass losing star is $\tau_{ff} = \int_a^\infty \alpha_{ff}(r)dr$ or

$$\tau_{ff} \approx 1.15 T_4^{-3/2} \nu_{1.4}^{-2} \dot{M}_8^2 v_{\infty;3}^{-2} a^{-3} \qquad (A.1)$$

where α_{ff}, the free-free absorption coefficient is approximated as

$$\alpha_{ff} \approx 0.018 T_e^{-3/2} n_e n_p \nu^{-2} g_{ff}\ \mathrm{cm}^{-1} \qquad (A.2)$$

where T_e is the electron temperature, $n_p = n_e$ the plasma density assuming hydrogen, ν the frequency and $g_{ff} \sim 1$ is the quantum mechanical Gaunt factor. The wind temperature is $10^4 T_4$ K and the wind's terminal speed is in units of $10^3 v_{\infty;3}$ km s^{-1}. A mass losing star therefore possesses a free-free photosphere of radius

$$R_\nu \approx 5.4 \times 10^{12}\ \mathrm{cm}\ T_e^{-1/2} \dot{M}_8^{2/3} v_{\infty;3}^{-2/3} \nu_{1.4}^{-2/3}. \qquad (A.3)$$

Notice the $\nu^{-2/3}$ dependence of the photospheric size on the observing frequency.

Assuming a $10 M_\odot$ star, a companion radio pulsar with orbital period less than

$$P_{orb} \lesssim 72\ \mathrm{days}\ (M/10\ M_\odot)^{-1/2} (a/1\ \mathrm{AU})^{1/2} \qquad (A.4)$$

may not be observable, unless the pulsar is strong enough to be able to disrupt the coherent structure of the stellar wind (Kochanek 1993).

The intrinsic dispersion measure contribution of the ionized stellar wind is computed to be

$$DM \approx 1 \text{ cm}^{-3} \text{ pc } (\frac{\dot{M}}{10^{-8} M_{\odot}\text{yr}^{-1}})(\frac{v_{\infty}}{10^{8} \text{ cm s}^{-1}})^{-1}(\frac{a}{1 \text{ AU}})^{-1} \qquad (A.5)$$

and is small compared with typical contributions to DM from the ISM.

5.2.5 – APPENDIX B

Interaction with the companion stellar wind can extract spin angular momentum from a binary pulsar, thus effectively reducing its lifetime. In binaries with $P_{orb} < 10^2$ d the effect can be pronounced, quickly spinning the pulsar down to beyond its death line. The result is the formation of a Be X-ray binary. In wider eccentric orbits, there can be epochs (such as at periastron passage or episodic mass ejections from the Be star) where the enhanced wind can overwhelm the pulsar wind as the pulsar enters the propeller phase (Illarionov & Sunyaev 1975; Campana et al. 1995; Stella et al. 1994). As the pulsar moves away from its companion, accretion may halt and radio pulsar activity can set in again.

A pulsar wind of luminosity L_p creates a standoff shock against the stellar wind at a distance r_s. If r_s is greater than $r_g = 2GM_n/v_{rel}^2$, r_g is the Bondi-Hoyle radius (M_n is the mass of the neutron star and v_{rel} is the relative speed between the pulsar and the stellar wind), electromagnetic spindown is dominant.

The condition for r_s to be greater than r_g is easily computed. The shock forms when pressure balance in the two media is achieved; therefore,

$$\frac{f\dot{M}v_{\infty}}{(d-r_s)^2} \approx \frac{L_p}{r_s^2 c} \qquad (B.1)$$

where $\dot{M}v_{\infty}$ is the wind thrust, d the orbital separation, f the wind focusing factor ~ 4 (Waters et al. 1988). Then $r_s > r_g$ implies

$$L_p \approx 4\pi^2 I \frac{\dot{P}}{P^3} > \frac{f\dot{M}v_{\infty}c}{(\frac{d}{r_g}-1)^2}. \qquad (B.2)$$

When the pulsar radiation barrier is overcome as a consequence of spindown or as a consequence of locally enhanced stellar wind density or speed, matter overwhelms the pulsar and it may enter the propeller regime. Inside the accretion radius, the pressure of the pulsar wind has the weaker radial dependence (r^{-2} for pulsar wind pressure as opposed to $\propto r^{-5/2}$ for spherical free fall). Matter flows into the light cylinder, quenching the pulsar mechanism until it is slowly dominated by the magnetic field pressure $\propto r^{-6}$ at the Alfv/'en radius

$$r_m \approx 1.8 \times 10^8 \mu_{30}^{4/7} M_{1.4}^{-1/7} \dot{M}_8^{-2/7} \text{ cm}. \qquad (B.3)$$

The pulsar cannot accrete because it is well to the left of its spin-up line, or in other words, the rigid magnetosphere at r_m is super-Keplerian (Stella et al. 1994, King & Cominsky 1994). For decreasing accretion rates the magnetospheric boundary will expand, and eventually r_m becomes larger than the light cylinder radius at which point the radio pulsar mechanism resumes. Work is done at the expense of rotational energy of the neutron star. Energy is reduced by a minimum amount that is needed to eject the accreted matter to infinity from the accretion boundary,

$$\delta E \approx 4\pi^2 I \frac{\delta p}{p^3}. \qquad (B.4)$$

In a steady state, there is infall of matter towards the neutron star at a rate $\dot{M}_p$. The propeller expels gas relentlessly, thereby establishing equilibrium. We assume that the pulsar is immersed in the stellar wind at a constant distance d from the companion and is spinning with a rate P. The mass capture rate is $\Omega d^2 \dot{M}_p \approx \pi r_g^2 \dot{M}$, where $\dot{M}_p$ is the rate at which the NS captures mass, Ω is the wind opening solid angle and $\dot{M}$ is the stellar wind loss. Using eqns. B.3 and B.4, and assuming that the rigid magnetosphere expels matter at velocity $(2\pi/P)r_m$, doing work at a rate $4\pi^2 \dot{M}_p P^{-2} r_m^2$, a timescale for rotational energy release solely due to propeller action is

$$\tau_p \sim 10^7 \text{ yr } \mu_{30}^{-8/7} \left(\frac{M_{ns}}{1.4\ M_\odot}\right)^{-4/7} \left(\frac{\dot{M}_w}{10^{-8}\ M_\odot \text{yr}^{-1}}\right)^{-3/7} \left(\frac{v_\infty}{500 \text{ kms}^{-1}}\right)^{12/7} \left(\frac{d}{1 \text{ AU}}\right)^{6/7}. \qquad (B.5)$$

Notice that τ_p is independent of P and is hence not coupled to other spindown mechanisms such as electromagnetic spindown. It critically depends on v_∞, a quantity constant to within factors of a few. In reality, a pulsar in a highly eccentric orbit will spend only a fraction of time in the propeller phase (near periastron) and, therefore, its propeller spindown age is increased further by a factor $\sim P_{orb}/t$ where t is the time spent in the propeller mode for every orbit. Timing observations of PSR B1259−63, a pulsar in a highly eccentric orbit around a Be star, show compelling evidence for propeller torque spindown with $\tau_p \sim 5\times10^8$ yr (Manchester et al. 1995).

We conclude that the propeller regime is effective in suppressing the lifetime of a binary pulsar if it is in a sufficiently close orbit around a Be star $P_{orb} < 10^2 d$. Beyond this orbital range, a neutron star can be radio luminous for as long as the main sequence stay of the companion.

5.2.6 – APPENDIX C

The possibility of detecting non-thermal radio emission from the shocked pulsar wind at r_s (see Appendix B) in our VLA continuum data is discussed. A bow-shock (Kennel & Coroniti 1984) resulting from the interaction of a pulsar wind with the ram pressure of the companion wind can be observed as a synchrotron source.

We use a simple prescription for the Be wind with a terminal velocity ~ 500 km s^{-1} as in Appendix B. From eqn. B.1 we derive a shock radius r_s, under the condition $L_p << \pi \dot{M} v_\infty c$, as

$$r_s \approx 10^{12.7}\ \mathrm{cm}\ (\frac{d}{10^{14}\ \mathrm{cm}})(\frac{\dot{M}}{10^{-8}\ M_\odot \mathrm{yr}^{-1}})^{-1/2}(\frac{v_\infty}{500\ \mathrm{km\ s}^{-1}})^{-1/2}(\frac{L_p}{10^{34}\ \mathrm{erg\ s}^{-1}})^{1/2} \qquad (C.1)$$

for a typical pulsar in a wide eccentric orbit with a Be star (an orbit coplanar with the Be disk wind).

Assume a pulsar wind composed mainly of pairs and magnetic fields with σ being the ratio of the Poynting flux to the particle energy flux. Hydrodynamic modeling of the Crab nebula shows that in-order to create a strong standoff shock th Crab pulsar wind is likely to be dominated by particle flux with $\sigma \lesssim 0.01$ (Kennel & Coroniti 1984). The upstream field B at r_s is

$$B(r_s) = [\sigma(1+\sigma)]^{1/2}(L_p/r_s^2 c)^{1/2}$$

and deduced to be

$$B(r_s) \approx 0.05 \text{ G } (\frac{\dot{M}}{10^{-8}\ M_\odot \text{yr}^{-1}})^{1/2}(\frac{v_\infty}{500 \text{ km s}^{-1}})^{1/2}(\frac{d}{10^{14} \text{ cm}})^{-1}. \qquad (C.2)$$

Behind the shock-front, the field settles down to $B \approx 3B(r_s)$.

Accord the pair plasma a simple power-law prescription in Lorentz factors γ with $N(\gamma)d\gamma = K\gamma^{-s}d\gamma$ particles s^{-1} being injected downstream of the shock. At the shock, the spindown luminosity carried in pairs upstream of the shock is converted to random motion of the pairs in the range $\gamma_{min} \approx 1$ to $\gamma_{max} \approx eBr_s/m_e c^2 \sim 10^8$ where γ_{max}, corresponds to the particles with gyro-radii equivalent to the pulsar shock radius, r_s. Synchrotron emission from very hot particles is likely to be the reason that PSR B1259−63 has been detected by ASCA and GRO (Grove et al. 1995).

Equating the energy in pairs to the total spindown luminosity of the pulsar

$$L_p \approx m_e c^2 \int_{m_e c^2}^{\gamma_{max}} K\gamma\gamma^{-s}d\gamma \Rightarrow K \approx (2-s)L_p\gamma^{s-2}/m_e c^2. \qquad (C.3)$$

Pairs with Lorentz factor γ radiate at a critical frequency of $\nu \approx \gamma^2 eB/m_e c$. Particles radiating within a small range of frequencies have $d\gamma \sim (m_e c/\gamma eB)d\nu$. Each particle radiates for a duration of a flow time $\tau_f \sim kr_s/(c/3)$ where $k \gtrsim 1$ and $\tau_f \sim 10^3 k$ s. The radiative times for radio emitting particles $\tau_r \gg \tau_f$ so we regard their flow as adiabatic (Tavani et al. 1994).

Using the above derived expressions, we estimate the total energy radiated from the shock region at the frequency of interest ($\nu \approx 1.5$ GHz). The total luminosity L in a bandwidth $d\nu$ centered around frequency ν is given as

$$L \approx N(\gamma) d\gamma \tau_f P(\gamma) \qquad (C.4)$$

where $P(\gamma)$ is the power radiated by a single particle at γ. It can be shown that

$$L \approx [\frac{(2-s)L_p \gamma_{max}^{s-2} \gamma^{-s}}{m_e c^2}] [\frac{2\pi}{3} \frac{m_e c}{\gamma e B} d\nu] [\frac{k r_s}{c/3}] [\frac{4}{3} \sigma_T c \beta^2 \gamma^2 \frac{B^2}{8\pi}] \qquad (C.5)$$

where relevant expressions for the four terms of eqn. C.4 are substituted within the parentheses. After making the relevant numerical substitutions, we obtain $L \sim 4 \times 10^{30} k$ erg s^{-1} which translates into a 1.5 GHz flux density of 10 mJy ($k \sim 1$) at a distance of a kilo-parsec. Radio emission at this level may have been observed from the PSR B1259−63 system. A radio source ($\sim$ 50 mJy at 20-cm) much brighter than that attributable to the pulsed emission, has been observed in this system at the time of periastron passage (Melatos, private communication).

We have detected no continuum sources associated with our VLA sample of stars to a detection threshold of 0.5 mJy.

Tables 5.1 & 5.2: These tables are a compendium of target stars observed at Arecibo Observatory and the VLA, for which good quality data were collected. Stellar identifications are given whenever possible, along with positions, spectral types and apparent visual magnitudes. All positions are in 1950 coordinates. Identifications are HD (Henry Draper Catalogue) numbers and where possible, the other common names of the stars are listed. Sometimes the primary beam contained more than one star. In those cases, we include the spectral types of the extra stars. Details of these stars are obtainable with a SIMBAD coordinate search on the main star. One known pulsar was rediscoverd in the dataset of star HD 220318.

TABLE 5.1: Target Stars at Arecibo

Source	RA (B1950) (h m s)	Dec (B1950) (° ′ ″)	Sp	V
829	00:10:14.0	37:24:56	B2V	6.6
3322	00:33:41.0	26:58:46	B8IIIpHgMn:	6.5
7019	01:08:21.0	37:27:30	B7III	5.8
14951	02:22:07.9	10:23:05	B7IV	5.5
18552	02:57:01.2	37:56:00	B8Vne	6.2
19374	03:04:36.2	17:41:18	B1.5V	6.1
20756	03:18:20.1	20:58:04	B5IV	5.3
22780	03:37:52.1	37:25:11	B7Vne	5.5
22951	03:39:11.8	33:48:21	B0.5V	2
23016	03:39:25.5	19:32:29	B9Vne	1
23302	03:41:54.0	23:57:25	B6IIIe	3.7
Mel 22 980	03:43:21.1	23:47:36	B6IVe	4.2
23625	03:44:41.7	33:27:47	B2.5V	6.6
23630	03:44:30.3	23:57:04	B7IIIe	2.9
23862	03:46:12.3	23:59:05	B8Vpe	5.0
24534	03:52:14.9	30:54:00	O9.5ep	6.4
24912	03:55:42.7	35:38:56	O7e	4.0
26398	04:08:11.9	16:31:04	B8e	7.1
26912	04:12:48.9	08:46:05	B3IV	4.3
27777	04:21:14.1	34:00:57	B8V	5.7
28867	04:30:39.0	17:54:44	B9IVn	6.3
30122	04:42:41.0	23:32:15	B5III	6.4
31293	04:52:34.2	30:28:20	A0ep	7.1
32039	04:57:54.7	03:32:32	B9Vn	7.0
32991	05:04:55.8	21:38:24	B2Ve	1
33647	05:09:06.9	00:27:17	B9Vn	6.7
34078	05:12:59.7	34:15:25	O9.5Ve:	5.9
35439	05:22:08.9	01:48:07	B1Vpe	4.9
36267 (2)	05:28:06.3	05:54:39	B5V,B7V,B5IV	4.2
36408 (1)	05:29:20.4	17:01:15	B7IIIe,B7IV	5.4
36576	05:30:35.6	18:30:23	B2IV-Ve	5.72
36822 (1)	05:32:04.3	09:27:26	B0III,B2IV-V	6.4
36861 (4)	05:32:22.8	09:54:08	O8e,O8III,B0.5V	3.4
			B9,B9V	3.4
6862	05:32:23.0	09:54:11	B0.5V	5.6
7202	05:34:39.1	21:06:48	B4IIIpe	3.0
7269	05:35:25.1	30:27:52	B9.5V+F9III	5.4

TABLE 5.1: Target Stars at Arecibo (Contd.)

Source	RA (B1950) (h m s)	Dec (B1950) (° ′ ″)	Sp	V
37438	05:36:38.1	25:52:14	B3IV	5.2
37490	05:36:32.5	04:05:40	B3IIIe	4.6
37967	05:40:17.1	23:10:55	B2.5Ve	6.2
38010	05:40:33.4	25:25:05	B1Vpe	6.8
39286	05:49:25.5	19:51:25	B8III+G2IIIe	6.0
42035 (1)	06:06:03.2	08:40:44	B9V,B9	6.5
43112	06:12:18.2	13:52:03	B1V,Be	5.9
43285	06:12:59.2	06:05:00	B6Ve	6.1
43819	06:16:07.2	17:20:46	B9IIIpSiCr:	6.3
44766	06:21:40.7	29:44:07	B8IIIn	6.7
45314	06:24:24.3	14:55:14	O9pe	6.6
45542	06:25:59.4	20:14:42	B6IIIe	4.1
45910	06:27:52.4	05:54:06	B2IIIpeShell	6.7
45995 (1)	06:28:22.4	11:17:12	B2V:nne, B9IVe	6.0
46150 (7)	06:29:15.9	04:58:48	O6fVe	6.7
395	06:36:23.8	28:18:32	B7III	W
47839 (6)	06:38:13.3	09:56:36	O7Ve...	4.6
48099 (1)	06:39:18.0	06:23:38	O6e+O6e	5.9
48434	06:41:00.2	03:59:00	B0III	5.9
50083	06:49:06.1	05:08:43	B2Ve	6.9
58050	07:21:36.5	15:36:57	B2Ve	6.4
58715	07:24:26.1	08:23:27	B8Ve	2.9
60848	07:34:13.3	17:01:01	O8Vpe	6.8
66552	08:01:51.7	18:59:04	B9V	6.2
74393	08:41:21.9	04:30:58	B9.5III-IV	6.4
80613	09:18:29.6	15:35:03	A1V	6.5
102509	11:45:23.9	20:29:48	A7V+G5III-IV	4.6
129956	14:42:56.9	00:55:37	B9.5V	-
130109	14:43:42.6	02:06:07	A0V	3.7
138749	15:30:54.5	31:31:35	B6Vnne	4.1
143454	15:57:24.4	26:03:39	sdBe+gM3+Q	9.9
149121	16:30:07.8	05:37:34	B9.5III	5.6
154441	17:02:30.5	19:40:00	B9.5V	6.2
164284	17:57:47.0	04:22:11	B2Ve	4.6
164447	17:58:17.5	19:30:23	B8Vne	6.5
165174	18:02:05.6	01:54:54	B0IIIn	b

TABLE 5.1: Target Stars at Arecibo (Contd.)

Source	RA (B1950) (h m s)	Dec (B1950) (° ′ ″)	Sp	V
166014	18:05:35.3	28:45:16	B9.5V	3.8
168797	18:19:00.9	05:24:40	B3Ve	6.1
168957	18:19:25.0	25:01:53	B3Ve	7.0
170111 (1)	18:24:40.0	26:25:05	B3V,B2V	6.5
171301	18:30:55.0	30:30:56	B8IV	4
171406	18:31:28.7	30:51:11	B4Ve	6.6
171780	18:33:24.9	34:24:58	B5Vne	6.1
173087	18:40:19.7	34:41:48	B5V	
173370	18:42:18.3	02:00:26	B9V	5.0
174638	18:48:13.8	33:18:12	B7Ve+A8p	3.4
174853	18:49:44.2	13:54:14	B8Vnn	6.1
175869	18:54:45.5	02:28:04	B9IIIep:Hg:	5.6
176301	18:56:34.4	19:43:29	B7III-IV	6.5
177109	18:59:57.2	33:32:53	B5IV	6.4
177648	19:02:32.3	23:15:11	B2Ve	7.2
179343	19:09:32.3	02:32:16	B9eShell	6.9
180968	19:15:36.5	22:56:02	B0.5IV	5.4
181182	19:16:37.0	19:31:04	B8III+K:	6.2
181409	19:17:11.3	33:17:44	B2IVe	6.6
182618	19:22:21.7	27:59:19	B5V	6.5
183261	19:25:42.9	20:08:40	B3II/IIIe,B5V	6.9
183362	19:25:50.9	37:50:17	B3Ve	6.3
183656	19:28:02.9	03:20:19	A0eShell	6.1
183914	19:28:44.1	27:51:32	B8Ve	5.2
184279	19:31:07.2	03:39:07	B0.5IVe	6.9
185037	19:34:00.3	36:49:56	B8Vne	6.0
186568 (1)	19:41:58.2	34:02:29	B8II,B8	6.2
187399	19:46:41.5	29:16:33	B8IIIeShell	7.0
187567	19:47:51.8	07:46:29	B2.5Ve	6.5
187811	19:48:54.8	22:28:53	B2.5Ve	4.9
188260	19:51:20.0	23:56:54	B9.5III	4.6
189432	19:56:46.0	37:58:07	B5IV	6.3
189687	19:58:05.0	36:54:17	B3IVe	5.2
190429 (2)	20:01:37.2	35:52:58	O9.5IVe,O5e,Oe+	6.6
191610	20:07:34.0	36:41:30	B2.5Ve	4.9
192044	20:09:54.7	26:19:41	B7Ve	5.9

TABLE 5.1: Target Stars at Arecibo (Contd.)

Source	RA (B1950) (h m s)	Dec (B1950) (° ′ ″)	Sp	V
192685	20:13:08.6	25:26:17	B3V	4.8
193237	20:15:56.4	37:52:35	B2pe	4.8
193911	20:19:54.2	24:17:07	B8IIIne	5.5
194335	20:21:52.0	37:18:50	B2Vne	5.9
195325	20:27:54.2	10:43:38	A1eShell	5
197419	20:40:24.4	35:16:33	B2IV-Ve	6.6
198183 (2)	20:45:27.4	36:18:21	B5Ve,B4V,B7V	4.5
202904	21:15:51.5	34:41:10	B2Vne	4.4
203699	21:21:11.9	13:50:06	B2.5IVne	6.8
204403	21:25:18.8	36:53:55	B3V	5.3
208057	21:50:47.0	25:41:21	B3Ve	5.1
209008	21:57:37.9	06:28:36	B3III	6.0
212076	22:19:03.2	11:57:10	B2IV-Ve	5.0
212571	22:22:43.3	01:07:23	B1Ve	4.7
212883	22:24:32.2	37:11:19	B2Ve	6.5
217891	23:01:19.8	03:33:00	B6Ve	4.5
220318 + PSR	23:20:10.8	20:33:14	B9.5V	6.2
224544	23:56:15.8	32:06:12	B6IVe	6.5

TABLE 5.2: Target Stars at the VLA

Source	RA (B1950) (h m s)	Dec (B1950) (° ′ ″)	Sp	V
148184	16:24:07.3	-18:20:40	B2Vne	4.6
164284	17:57:17.1	04:22:11	B2Ve	4.8
168797	18:19:01.0	05:24:41	B3Ve	6.1
173219	18:41:51.4	-07:09:46	B1Vnpe	7.8
174513	18:48:27.0	-07:51:32	B1Vnpe	8.9
174705	18:49:29.3	-11:41:37	B2Vne	8.3
187350	19:46:58.5	-01:13:39	B1Vne	8.7
187567	19:47:51.9	07:46:30	B2.5IVe	6.5
187811	19:48:54.8	22:28:54	B2.5Ve	4.9
187811	19:48:54.8	22:28:54	B2.5Ve	4.9
228041	20:08:04.8	35:20:52	B0.5Ve	9.0
228104	20:08:45.4	35:43:31	B1IVpe	8.8
193009	20:14:49.5	32:13:29	B1Vnnpe	7.2
190944	20:03:52.3	46:31:41	B1.5Vne	8.8
197419	20:40:24.6	35:16:34	B2IV-Ve	6.7
198512	20:47:06.9	53:43:12	B1Vnnpe	8.3
198931	20:50:23.8	44:14:44	B1Vnne	8.7
AG+49 1900	21:59:44.1	49:55:35	Be	8.9
BD+53 2790	22:08:35.8	54:29:24	O9.5IIIe	
13867	02:13:18.5	9:35:18	B0.5Vp	7.5
237056	02:58:49.7	57:24:60	B0.5Vp	8.3
19243	03:04:47.7	62:11:36	B1Ve	6.7
21212	03:24:25.2	62:19:12	B2Ve	8.1
22298	03:34:09.9	55:00:27	B2Vne	7.7
25348	04:00:29.9	53:11:32	B1Vnnpe	8.3
24560	03:52:49.9	44:47:33	B1.5Vne	8.1
25940 (MX PER)	04:05:01.3	47:34:52	B3Ve	4.0
33152	05:06:33.7	36:56:31	B1Ve	8.1
33461	05:08:43.7	41:09:20	B2Vnne	7.8

TABLE 5.2: Target Stars at the VLA (Contd.)

Source	RA (B1950) (h m s)	Dec (B1950) (° ′ ″)	Sp	V
33604	05:09:44.4	40:08:06	B2Vpe	7.3
34921	05:19:10.7	37:37:44	B0IVpe	7.5
242257	05:14:26.9	34:01:48	BQ*	10.3
35345	05:22:23.8	35:36:14	B1Vpe	8.4
35347	05:22:06.6	29:34:16	B1Ve	8.9
32343(11 CAM)	04:59:13.4	23:57:29	B1Ve	5.2
29441	04:35:53.6	08:04:37	B2.5Vne	7.6
30076(56 ERI)	04:41:41.0	-08:35:44	B2Ve	5.9
28497	04:26:47.5	-13:09:26	B	5.6
35439(25 ORI)	05:22:09.0	01:48:08	B1Vpe	4.9
36576(120 TAU)	05:30:35.7	18:30:23	BIV-Ve	5.6
245770	05:35:48.0	26:17:18	09.7IIe	9.4
37318	05:35:48.2	28:25:58	B1Vne	8.4
245493	05:34:32.5	33:56:18	B2Vpe	8.6
BD+37 1292	05:39:24.7	37:57:40	B3Vpe	9.1
37657	05:38:44.0	43:02:10	B3Vne	7.1
40978	06:00:54.0	46:35:18	B3Ve	7.3
249695	05:55:22.7	30:12:13	B1Vnnp	9.0
249179	05:52:44.4	28:46:43	B5ne	9.2
248753	05:50:25.2	25:43:57	B1Vnee	8.4
38010	05:40:33.6	25:25:05	B1Vpe	6.8
37967	05:40:17.2	23:10:57	B2.5Ve	6.2
38191	05:41:56.3	21:26:26	B1Vne	8.7
44674	06:20:58.5	25:26:40	B1Vne	8.5
44637	06:20:33.0	15:07:43	B2Vpe	8.0
42908	06:10:58.2	08:43:39	B2Ve	8.2
47359	06:35:45.5	04:55:33	B0.5Vpe	8.8
45901	06:27:40.6	02:52:59	B2Ve	8.8
41335	06:01:47.6	-06:42:19	B2Vne	5.2
46380	06:30:18.2	-07:28:15	B2Vne	8.0
47761	06:37:33.2	-04:39:06	B2Vpe	8.6
49787	06:47:28.0	-05:27:16	B1Vpe	7.5
49977	06:48:09.1	-14:03:14	B1.5Vn	8.0
53367	07:02:03.6	-10:22:44	B0IVe	7.0
50696	06:51:48.2	00:14:45	B1Vnne	8.9
50083	06:49:06.2	05:08:44	B2Ve	6.9
50868	06:52:33.7	05:29:56	B2Vne	7.9
58050	07:21:36.6	15:36:57	B2Ve	6.3

TABLE 5.2: Target Stars at the VLA (Contd.)

Source	RA (B1950) (h m s)	Dec (B1950) (° ′ ″)	Sp	V
65079	07:54:27.2	03:05:08	B2Vne	8.3
65875	07:58:13.2	-02:44:35	B2.5Ve	8.0
55606	07:11:02.6	-01:59:28	B1Vne	9.1
54464	07:06:18.7	-03:58:36	B2Vpe	8.3
57386	07:18:18.5	-08:19:35	B1.5Vn	8.0
58343	07:22:24.5	-16:06:06	B2Vne	5.3
59094	07:25:35.1	-15:59:28	B2Vne	8.4
62532	07:41:31.0	-17:49:32	B3Vnne	8.4
56139(o CMA)	07:12:46.9	-26:41:05	B2Ve	3.8
203467(A CEP)	21:18:20.0	64:39:34	B3IVe	5.1
204116	21:22:57.3	55:09:02	B1Ve	8.0
206773	21:40:50.3	57:30:25	B0Vpe	6.9
235793	22:17:10.6	51:52:09	B1Vnne	9.1
212044	22:18:24.9	51:36:33	B1Vnnp	7.0
211835	22:16:56.0	45:33:04	B3Ve	8.5
204722	21:27:21.0	44:07:07	B2Vnne	7.6
BD +43 3913	21:23:09.7	44:14:08	B1.5Vnn	8.9
205618	21:33:33.2	29:31:17	B2Vne	8.1
208057(16PEG)	21:50:47.1	25:41:21	B3Ve	5.0
203699	21:21:12.1	13:50:07	B2.5IVne	6.9
212076(31PEG)	22:19:03.3	11:57:10	B2Ve	5.0
212571(πAQR)	22:22:43.4	01:07:23	B1Ve	4.7
216200(14LAC)	22:48:06.2	41:41:18	B3IVe	5.9
BD+53 2964	22:41:19.9	53:48:33	B2IVnnp	9.2
220116	23:18:19.5	58:00:13	B0.5Vpe	6.7
223501	23:47:25.6	61:56:10	B0.5Vpe	7.9
225096	00:00:52.6	55:16:21	B2IVne	7.9
2789	00:29:08.0	66:53:08	B3Vne	8.2
11606	01:52:15.7	59:01:44	B2Vne	7.0
AG+57 295	02:18:17.4	57:09:31	B1Vpe	9.1

APPENDIX 1: THE FFB HARDWARE MANUAL

This appendix contains a description of the Flexible Filter Bank (FFB) hardware. Aspects of pulsar observing, signal flow through the FFB and simple, but complete descriptions of the separate modules are provided in chapter 2 of this thesis. Presented here, is a more detailed functional and hardware-level description of the various modules, and the circuit boards comprising these modules. Chapter 2 and the appendix, together, make a complete document. The appendix is sub-divided into the following sections:

A.1 **The FFB at WSRT:** This section is an overview of the specifications and capabilities of the FFB at Westerbork Observatory. We explain how the FFB is used in conjunction with the telescope as a pulsar back-end, list important future hardware developments that WSRT personnel wish to implement and key scientific projects that are currently being undertaken.

A.2 **The FFB Computer:** We discuss the FORCE CPU-30 as part of the FFB. Its functions as master of the FFB VMEbus are described. Some important features of the computer are listed.

A.3 **The IF-Subsystem:** Dual polarization IFs are the input signals into the FFB. Two step downconversion of these inputs is required, before the observing band can be channeled in the filter-boards. The IF-subsystem is a heterodyne system that accomplishes these downconversions. Its components

are an IF-chassis, an 80 MHz Reference Box, four splitter-boards, four LO-splitter-boards and eight mixer-boards. Two local-oscillator (LO) and mixer stages are used in the two-step demodulation (IF to sub-IF and then sub-IF to baseband). The first stage LOs (master LOs) and mixers are in the IF-chassis. The second stage LOs (slave LOs) are digitally synthesized on the LO-board (since the LO-board resides in the VME cage, we defer discussion of this circuit board to the VME subsection) and are mixed with the sub-IFs in the mixer-boards.

A.4 **The VME Subsystem:** These are printed circuit boards that are mounted in the VME cage. Within the VME subsystem are eight filter-boards, the master control-board, the LO-board and the buffer-board. The filter-boards use the baseband outputs from the mixer-boards to construct the 32 dual-polarization filter bank channels and then sample the channel voltage. The master control-board triggers and controls the sampling rate. The buffer-board acts as in intermediate buffer for the sampled data before it is written to mass storage media. The LO-board is used for generation of slave local-oscillators (used in the IF-subsystem).

The contents of this appendix are better grasped with a good feel for the signal flow in the FFB (see Chapter 2). To visualize how various modules are tied together, refer to FFB functional block diagrams as in figure A.1 or figure 2.3. Block diagrams of the subsystems and of individual printed circuit-boards (pcbs) are also provided. Circuit schematics for all major circuit-boards follow at the end (pp. 256). Throughout the appendix, we restrict ourselves to signal characteristics and signal flow, and do not become too involved in the performance characteristics of individual parts. For actual specifications on parts and components, refer to the manufacturer's data sheets. Names of parts and their manufacturers are provided wherever necessary. For common components (such as operational amplifiers and digital logic), names of manufacturers are not included.

A.1 THE FLEXIBLE FILTER BANK AT WSRT

A.1.1 – Overview

The Westerbork Synthesis Radio Telescope (WSRT) has recently been fitted with the Flexible Filter Bank for pulsar observations. This back-end is a filter bank with 32 channels, for both receiver polarizations. For each observing frequency and each pulsar (with a known dispersion measure) an optimal bandwidth and signal smoothing can be chosen. This is attained with adjustable channel bandwidths that are digitally tunable between 6.25 kHz and 2.8 MHz. The time constant of the integration which follows detection can be digitally set at values between 50 ms and 25 μs. A functional block diagram of the WSRT FFB is in figure A.1 (pp. 192). The machine rests in a single large crate displayed in figure A.3 (pp. 194). The crate carries a hybrid 6U/9U VME cage which houses the VME subsystem.

A.1.2 – The Filter Bank

The back-end was constructed at the Caltech Radio Astronomy Laboratory and also at Owens Valley Radio Observatory (OVRO). It was installed at WSRT by Lodie Voûte and Hans Weggemans of Westerbork. The software, originally written at Caltech was adapted and extended by Will Deich of NFRA. It has been fully operational since the end of August 1995.

For detecting pulsars the signals of all 14 Westerbork dishes are phased up and split into 8 frequency bands for both polarizations. Each band is mixed with four (computer controlled) slave-oscillator signals and disseminated into 64 digitally tunable filters. Then the signals are detected and the dc-components are removed. After smoothing they are 2-bit sampled and stored on disk or tape. The smoothing filter and the sampling interval again are computer controlled and are set in such a way that the signal is sampled almost at Nyquist rate.

The fan beam of the Westerbork array has 9 – 11 major fans, each 30″ $\times$ $\sim$ 1° (at 1420 MHz). As a result of the beam-shape, it is very hard to

do untargeted searches for pulsars. However, with the use of the imaging and polarization capabilities of the telescope and the timing capabilities of this back-end, efficient targeted searches are possible.

Table A.1: Parameters of the Westerbork Flexible Filterbank Backend

Number of Channels	32 (future: 8000)
Number of polarizations	2 (future: 4)
Bandwidth per channel	3.25 kHz... 200kHz in steps
	0.35 MHz... 2.8 MHz in steps
Smoothing filter	24 Hz ... 50 kHz in steps
Sampling interval	51.2, 102.4, 204.7 μs ...
DC time removal	2... 100 s (in steps)

A.1.3 – Key Projects

At this moment the following scientific projects are planned:

i. Pulsar searches towards steep spectrum sources discovered in the Westerbork Northern Sky Survey (WENSS at P-band) and the VLA Faint Images of the Radio Sky (FIRST at L-band).

ii. Pulsar searches towards highly polarized objects in the WENSS.

iii. Pulsar searches towards a few globular clusters.

iv. Pulsar searches towards radio sources near possible supernova remnants in the WENSS.

v. Timing of a few northern sky millisecond pulsars.

vi. Investigation of giant pulses.

A.1.4 – Future

For the future, the following hardware enhancements of the machine are planned:

i. Implementation of a faster workstation: maximum sampling rate: 2.5 MHz.

ii. Detection of all 4 Stokes parameters.

iii. Extension of the number of channels to 8000.

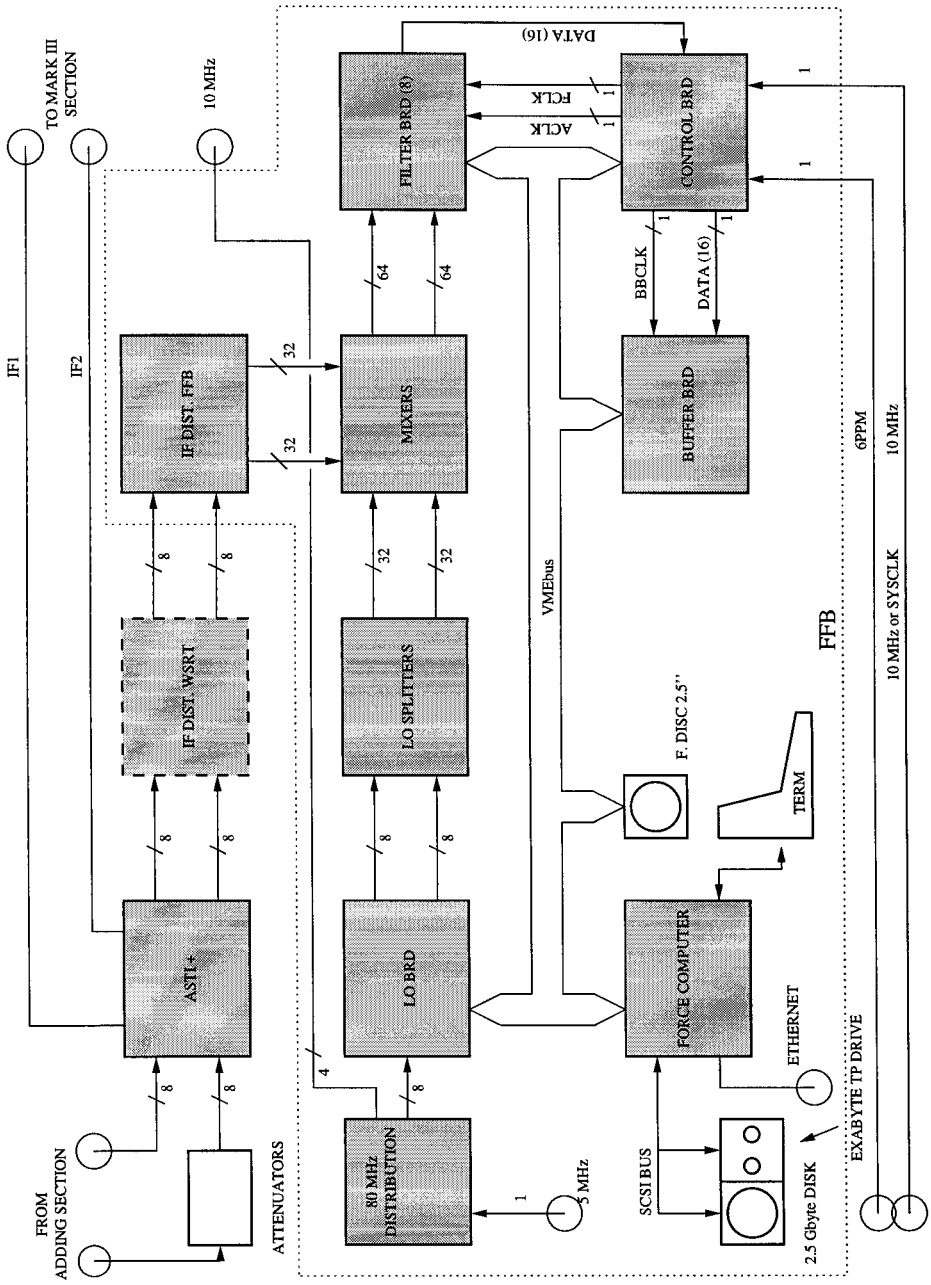

FIG A.1: FFB FUNCTIONAL BLOCK DIAGRAM (WSRT)

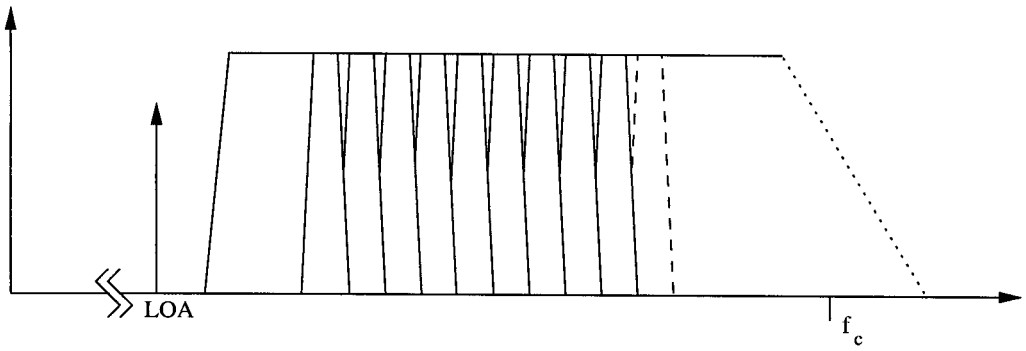

Fig A.2 Panel 1: We depict the telescope IF (SSB) and 8 frequencies where channels are to be constructed. Only one master oscillator is shown. Four oscillators are used to construct 32 channels. This is the IF->Sub-IF down conversion (in the IF-Chassis).

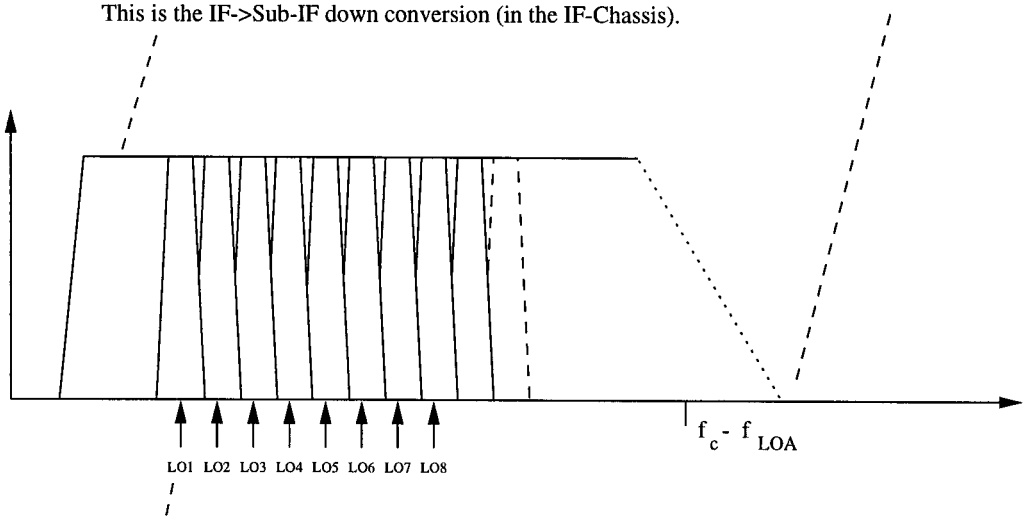

Panel 2: Each of 4 Sub-IFs (one depicted) is mixed with 8 slave oscillators to create 8 baseband signals. 4 Sub-IFs give 32 baseband signals, all centered at different frequencies within the observing band. Second stage mixing is complex (sine/cosine LOs).

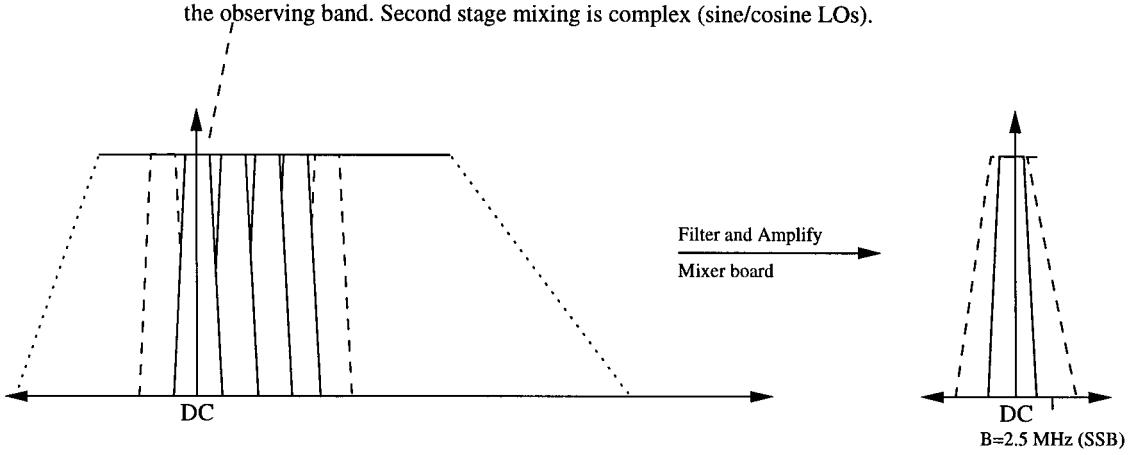

Panel 3: The result of mixing the Sub-IF with LO1 is depicted. Channel 1 is now centered at baseband. The baseband signal is filtered for rejection of higher frequencies and amplified. The output bandwidth is 2.5 MHz (SSB). The 8 complex baseband signals are now fed into the filter boards.

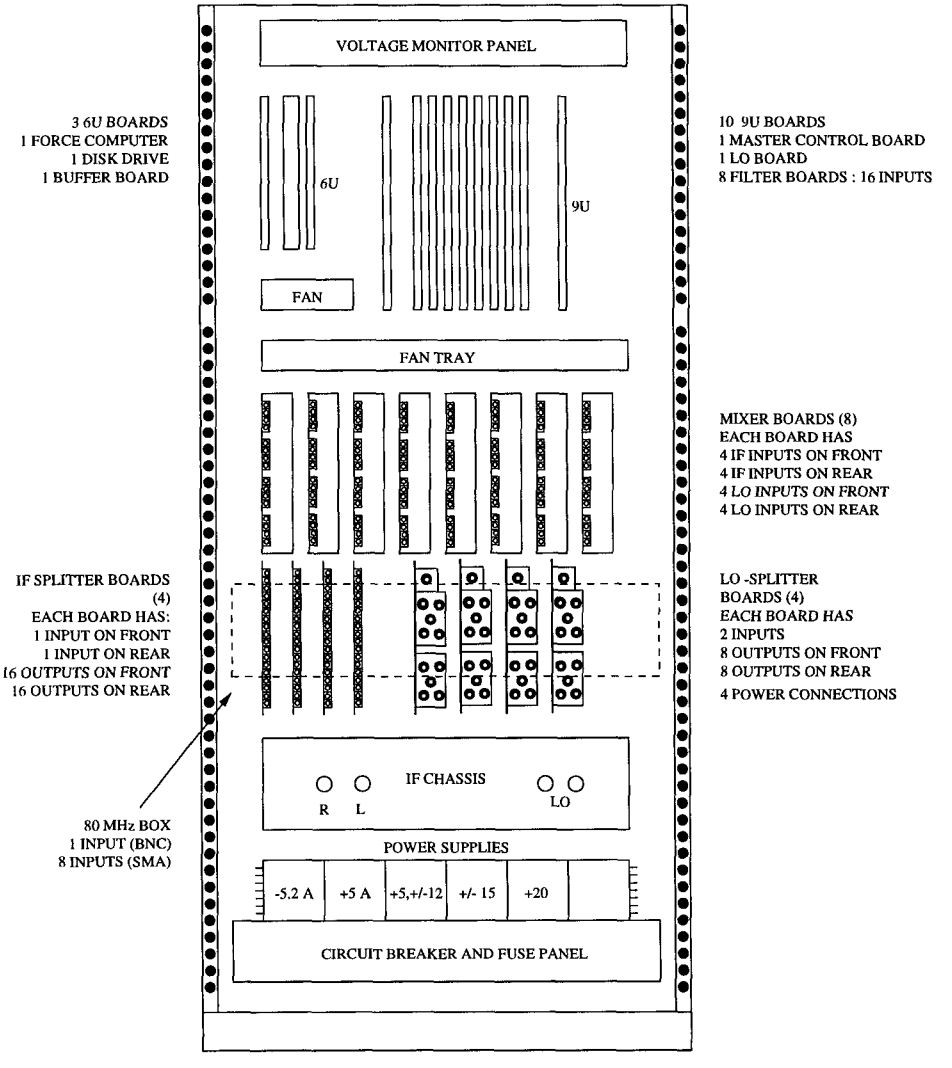

FIG A.3: THE FFB CRATE

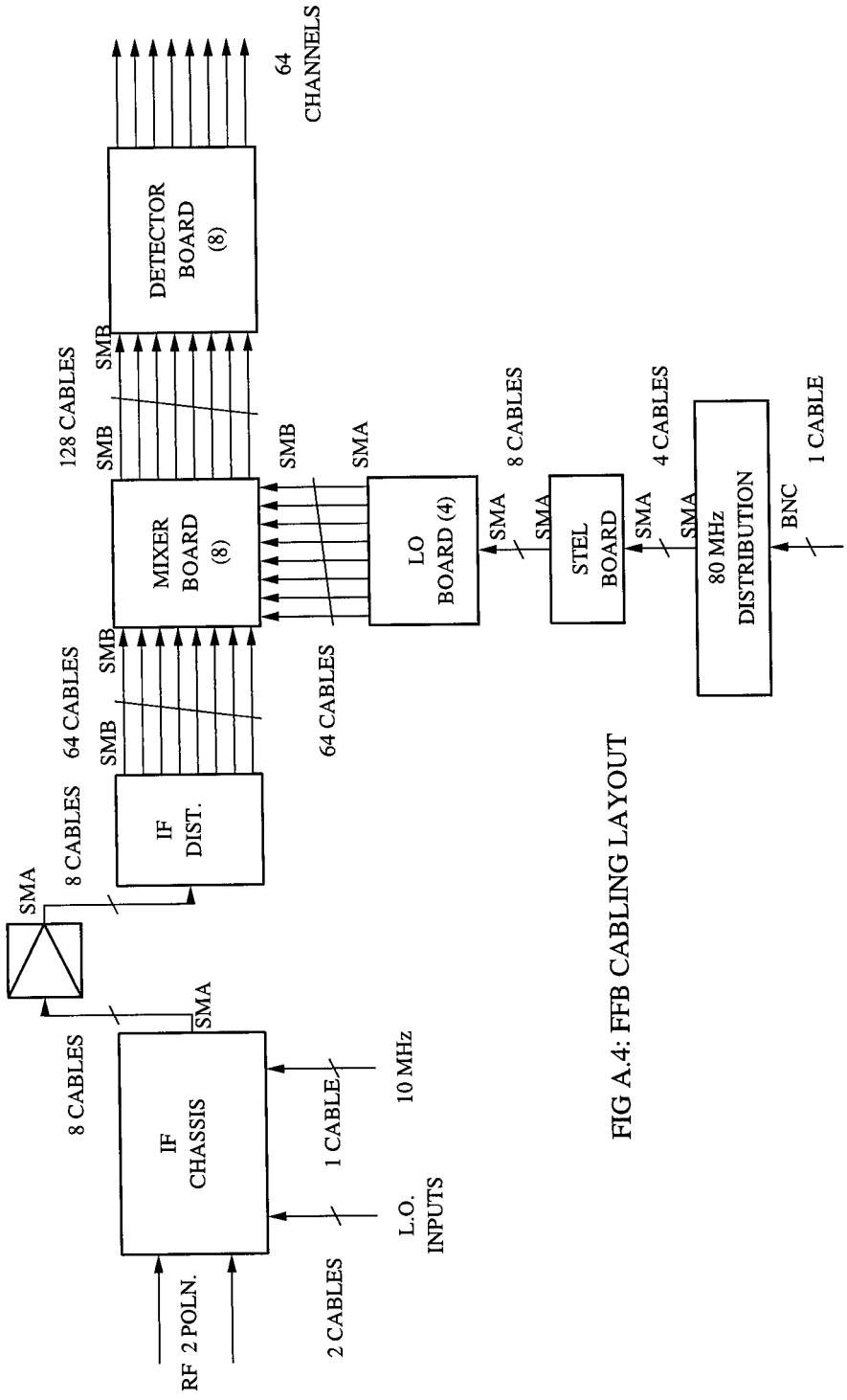

FIG A.4: FFB CABLING LAYOUT

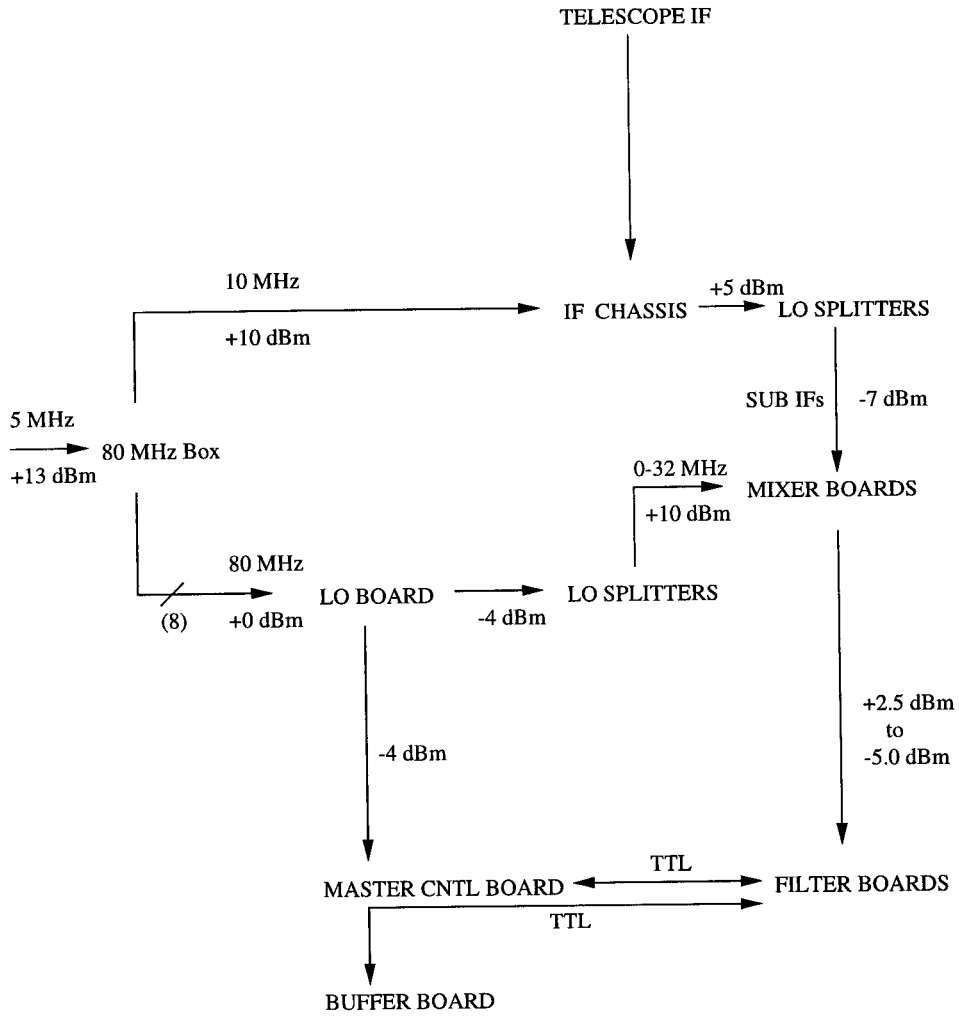

FIG A.5: FFB SIGNAL LEVEL DIAGRAM

A.2 THE FFB COMPUTER

The FFB computer is a VME based FORCE CPU-30 (6U card) running OS-9, a real-time multi-tasking operating system. User level interaction with the computer, is either through a conversation terminal, such as a VT-220, via a RS-232 port, or over the network with the help of a local-area-network port mounted on the computer front panel. Computer-to-slave board communication is over the VMEbus. Each slave board, situated on the bus, carries simple VME interface circuitry (see VMEbus section) for read/write operations. In the FFB, only the computer can become bus master.

The main uses of the computer, are in configuration of the FFB and the accumulation of sampled channel data. To "configure", is to set up the system to behave according to the user's wishes, i.e., to have desired sky-frequencies, desired channel-widths and sampling rates for a variety of pulsar observations. Configuring consists in programming the VMEbus peripheral memory locations on the slave boards (see list of peripheral memory addresses on page 213). This operation is not time consuming and the observing set-up can be changed every so often without losing much observing time. Data accumulation, requires the computer to read sampled data that is clocked into buffer-board memories, followed by asynchronous writing to mass storage media such as hard-disk or tape. To accomplish these tasks, a host of debugging and data-taking software (originally written by P. S. Ray and D. Kornreich at Caltech and documented in the "FFB Software Manual"; extended by W. T. S. Deich of NFRA) is available.

Configuring the FFB us a multi-step process. It requires resetting and initialization of all the slave boards. For this, the data-taking program reads a set of FFB parameters from a configuration file (see FFB Software Manual) which resides on the system-disk. Using these parameters, it first sets-up the slave local-oscillator frequencies on the LO-board, thereby configuring the IF-system. Second, a control-word is written on the buffer-board registers to decide the read and write

modes of its two memories (16-bit mode is used in the FFB). Third, required filter-types, filter-widths and suitable signal levels are set on all filter-boards. Finally, all FFB clock frequencies are programmed on the control-board. Thereafter, the computer issues a "data-taking" command to this board which triggers the sampling hardware.

All sampled data is buffered into the buffer-board memories. As soon as one-of-two memories is full, it interrupts the computer. The computer responds by rapid DMA transfer of the buffered data to hard disk. For a short while, a DMA controller takes over as bus master and the computer relinquishes control. This process will continue, switching from one memory to the other, until data-taking is stopped.

Given below is a list of important hardware features of the computer. For detailed information, refer to FORCE CPU-30 manuals, provided by the FORCE corporation.

A.2.1 – Features of the FORCE CPU-30 Board

1. 68030 CPU with a 16 MHz clock frequency.
2. 68882 Floating point co-processor with 16 MHz clock frequency.
3. 32-bit high speed DMA controller for data transfers to/from the shared RAM and/or to/from the VMEbus memory. 32 byte internal FIFO for burst DMA.
4. Four M-byte of shared DRAM with byte parity supporting the 68030 burst fill mode.
5. The DRAM is accessible from the VME side via the Gate Array (FGA-002).
6. Four serial I/O interfaces built with two Dual Universal Serial Communications Controllers. One channel is RS-232 and 3 channels are RS-232/RS-422/RS-485 compatible.
7. Four system EPROM devices providing up to 4 M-byte capacity using a 32 bit data path.

8. One boot EPROM for local booting and initialization of the FGA-002 array.
9. Up to 512 k-bytes of local SRAM (battery back-up on board)/EEPROM using one 28/32 pin socket (JEDEC standard).
10. Real time clock with calendar and battery backup.
11. SCSI interface with 2.0/4.0 MHz data transfer rate using the on board DMA controller.
12. Floppy disk interface (SA 460 compatible) for connection of 3, 3.5, 5.25 inch drives.
13. LAN controller for connection to Ethernet/Cheapernet.
14. Two 24-bit timers with 5-bit prescaler.
15. One 8-bit timer with software programmable clock.
16. All local I/O devices are able to interrupt CPU on a software programmable level.
17. Bus ERROR handling fully under software control via different timeout counters for local and VMEbus accesses.
18. Full 32-bit VMEbus master/slave interface supporting the following data transfer types:
19. Master: A32, A24, A16: D32, D16, D8 Slave : A32: D32, D16, D8 ADO, UAT and RMW cycles are also supported.
20. Single level VMEbus arbiter.
21. SYSCLK (system clock) driver.
22. VMEbus interrupt handler.
23. Two independent Message broadcast channels for simultaneous access of up to 20 CPU boards installed in one rack.
24. Support level for ACFAIL and SYSFAIL via software programmable IRQ levels.

25. Timeout master if the board does not receive bus master-ship.

26. VMEPROM, the real time monitor with file manager and Real Time Kernel (PDOS compatible) is installed on each board version.

A.3 THE IF-SUBSYSTEM

This section covers the modules of the FFB IF-subsystem. Its modules are an 80 MHz Reference box, which generates the FFB reference-signals of 80 MHz and 10 MHz; an IF-chassis for the first downconversion in the system, from telescope IF to sub-IF; splitter-boards for distribution of the sub-IFs; LO-splitters-boards for the distribution of the slave local-oscillators and finally, mixer-boards for the second downconversion from sub-IF to baseband signals after mixing with the slave LOs. IF signal processing, in this subsystem, eventually leads to 32 dual-poln. complex baseband signals (128 baseband signals) which are routed into eight filter-boards (part of VME subsystem) for channel filtering. A block diagram depicting the IF-subsystem, its modules and their interaction is in Fig A.7. Its overall single-side-band function is illustrated in Fig A.2 (pp. 193).

The overall importance of the IF-subsystem is easily understood. It acts as a go-between the telescope-IF system, usually band-limited and centered at a high IF frequency, and the 128 lowpass filters which eventually form 32-channels. As previously mentioned, the IF subsystem performs a two-step demodulation of the IF (IF(dp) $\Rightarrow$ sub-IF(4dp) $\Rightarrow$ baseband signals(32dpc); "dp" represents dual-polarization and "c" is complex). The first downconversion and image rejection is in the IF-chassis using a set of master-oscillators† tuned near the telescope-IF. The telescope-IF is downconverted to four sub-IFs which are each split eight ways and routed into mixer-boards for the second downconversion to baseband signals. For this, each sub-IF is mixed with eight slave LOs, filtered and amplified. Nominal baseband signals are 2.5 MHz (SSB) wide with $V_{rms} \approx 0.3$ V.

† This is only one possible IF scheme originally employed at OVRO. Other schemes can be used as well. For instance the WSRT FFB uses a separate IF scheme.

A.3.1 THE 80 MHz REFERENCE BOX

Inputs:	5 MHz at +13 dBm
Outputs:	80 MHz (8) at +0 dBm
	10 MHz at +10 dBm

A.3.1.1 – Function

The FFB requires a phase-stable 80 MHz reference signal, that is locked to the observatory maser, in order to run numerically controlled oscillators (NCOs) that in turn generate local-oscillators and the FFB sampling clock. For this purpose, an 80 MHz synthesizer box is mounted on the back of the crate (see Fig A.8 pp. 209). The reference is phase locked to an observatory 5 MHz (input level +13 dBm) clock (see Fig A.7 pp. 208). This 5 MHz is fed into a MITEQ phase-lock oscillator which outputs a stable phase 80 MHz with a harmonic rejection of −35 dB. Output power from the MITEQ is typically at +14 dBm and signal side-lobes are further reduced by the sharp bandpass filtering with a SBP-70. The 80 MHz is then split 8-ways, and these eight outputs are available via SMA connectors mounted on the rear of the 80 MHz Reference Box. All eight outputs are channeled into each of eight NCOs on the LO-board.

The 5 MHz clock is simultaneously fed into a frequency doubler, a MK-3BR, to create a stable 10 MHz clock, which in turn is used to phase-lock the master-oscillators in the IF-chassis (see Fig A.8 pp. 209 and Fig A.9 pp. 210).

A.3.2 THE IF-CHASSIS

Inputs:	Telescope IFs dual-poln.
Outputs:	Sub-IFs (4) dual-poln. at -3 dBm

A.3.2.1 – Function

As stated, the first stage downconversion is in the IF-chassis. Therefore, this is the only observatory specific module in the FFB and its construction is slave to

the IF center-frequency and bandwidth. The block diagram of an IF-chassis built expressly for the 600 MHz receiver on the OVRO 40-m telescope, and used during the initial assembly and testing of the FFB, is shown in figure A.9 (pp. 210).

The chassis incorporates four local-oscillators and eight mixers. Two oscillators are in-built synthesizers and two are externally fed, for example, with waveform generators. Four separate sections of the observing band, each with a single-sideband bandwidth of 50 MHz centered at dc, are downconverted and filtered for image rejection. The four sub-IF outputs (both polarizations L and R) are directly fed into either the splitter-boards of the IF-distribution module, or alternatively first channeled into a set of power amplifiers for signal boosting, if required. The amplifiers used for this purpose, are mounted on a flat panel located at back of the FFB crate. These are Mini-Circuits ZFL-500LNs, that have input bandwidth 0.1-500 MHz and and a gain 24 dBm (minimum). The maximum amplifier output power is +5 dBm.

A.3.3 SPLITTER BOARDS

Inputs (per board):	Sub-IFs (2) at -3 to -1 dBm
Outputs (per board):	Sub-IFs (16) at -13 dBm

A.3.3.1 – Function

The sub-IFs from the IF-chassis are routed to a set of four splitter-boards. Each splitter-board makes multiple copies of the sub-IFs. There are two inputs on each board, and a maximum of 16 copies of each input are possible (all connectors are SMB) with a total attenuation of 12.2 dB. The operation is performed via a 2-way and an 8-way split in succession. The input is band-limited to 0.01-400 MHz and a maximum amplitude of +7 dBm. No special attempt has been made to preserve similar path lengths for the signal traces, as the shortest input wavelengths are of order ten meters (30 MHz).

In the FFB, four splitter-boards are employed to produce, 4 sub-IFs $\times$ 2 poln.$\times$ 8 copies = 64 output sub-IFs. A further 2 way split takes place on the mixer-board, thereby, generating 128 sub-IFs. This are required for further down-conversion to 32 channels $\times$ 2 poln. $\times$ 2 (sine/cosine) = 128 baseband inputs for the filter-boards.

A.3.4 THE LO-SPLITTERS

Inputs (per board):	Slave LOs (2) at +0 dBm
Outputs (per board):	Slave LOs (8) sine/cosine at +10 dBm

A.3.4.1 – Function

The FFB filter-boards accept 128 baseband inputs. These are at 32 separate sky-frequencies with two complex inputs of two polarizations. We employ a two stage LO conversion: A set of 4 primary LOs (in the IF-chassis) converts 4 selected sky frequencies to base-band, and then, a set of 8 secondary LOs further mix the signal down to 32 (4×8) baseband sky-frequencies. The primary LOs are housed in the IF-chassis (see Fig A.9 pp. 210). The eight slave LOs (1..8) are generated by the LO-board (Figs A.7 pp. 208 and A.19 pp. 254). The eight pure tones from the LO-board are phase shifted (for sine and cosine LOs), split and adjusted to a +10 dBm level before they can be used for mixing.

In each of four LO-splitter-boards (see Fig A.10 pp. 211), the pure tone input is first amplified by a +23 dB gain using an IF-amplifier (ANZAC AM-110). It is important to verify that the inputs are amplitude limited so that the AM-110 does not operate near its 1-dB compression point. The amplifier output is fed into an ANZAC JH-6-4 quadrature hybrid to produce a sine and cosine local-oscillator. Each sine/cosine LO is reproduced four ways (to +10 dBm) and directed into the mixer-boards.

A.3.5 THE MIXER BOARD

Inputs (per board):	Sub-IFs (8) at -13 dBm
	Slave LOs (8) at +10 dBm
Outputs (per board):	Baseband Signals (16) at -1 dBm

A.3.5.1 – Function

Mixer-boards are used for the second stage downconversion (sub-IF(4dp) $\Rightarrow$ baseband signals(32dpc)). Figure A.11 shows a block diagram of a mixer-board. Each board has four identical sections. The inputs are sub-IFs and slave LOs, and the outputs are baseband signals. Two piggy-back boards carrying baseband amplifiers, are mounted on each mixer-board but are not depicted in Fig A.11.

Each mixer-board section is sub-divided to do the following functions:

A.3.5.2 – Power Splitting

Four independent 3 dB power-splitters are employed to make two images each of two sub-IFs and two LOs. The splitting are Mini-Circuits PSC 2-1s. The PSC2-1 is a 2-way-0° splitter capable of operation in the range $0.1 - 400$ MHz, with a typical insertion loss of about 3.3 dB. The maximum phase unbalance is about 4°. The input LO power is near +10 dBm, as a 3 dB split results in the recommended operating LO power of +7 dBm. The sub-IF power may vary, but has a maximum allowed value of +4 dBm at the mixer-board inputs.

A.3.5.3 – Second Downconversion

Each of the two slave LOs is mixed with each of two input sub-IFs in one of four mixer-board sections (see Fig A.11 pp. 212). Each mixing operation uses the four-quadrant, double-balanced mixer SBL-1-1 (Mini-Circuits). The SBL-1-1 mixes in the LO range 0.1-400 MHz (in FFB max. LO is $\approx$ 32 MHz) with an LO power of +7 dBm. Sub-IF power is up-to +1 dBm. Typical midband conversion loss is about 5-6 dB. Good isolation (40 dB) between the various signals is provided

on the SBL-1-1 (refer to specifications on the SBL-1-1 in the Mini-Circuits product guide).

A.3.5.4 – Low Pass Filter PLP-5

The mixer outputs are lowpass filtered to reject extraneous frequencies using a Mini Circuits PLP-5 passive filter, with a 3 dB cutoff at 5 MHz. The filtered outputs are routed to one of two piggy-back boards for amplification.

A.3.5.5 – Baseband Amplification

The filter boards require baseband voltage levels of $\sim 0.3V$ (rms), and therefore amplification is necessary immediately after mixing. The amplifiers are carried on two piggy-back cards that are mounted on the solder-side of each mixer-board. Each piggy-back board carries eight amplifiers. Two supply lines of +15 V and −15 V and a return ground are run into the piggy-back cards. The MAX-450, a CMOS video signal amplifier is implemented in a gain configuration of $G = 100$, without any external compensation circuitry. The gain-bandwidth product of this device allows a small signal bandwidth of 2.5 MHz in this gain configuration. All amplifier outputs are ac-coupled with 0.1 μF capacitors.

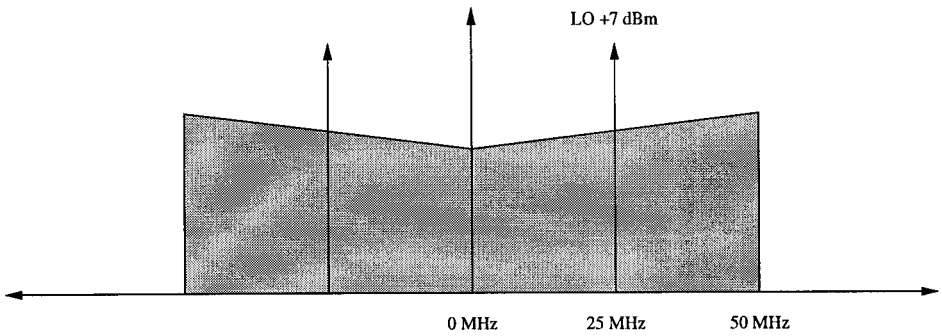

1. Signal inputs to SBL-1-1: IF 0-50 MHz, LO @ +7 dBm

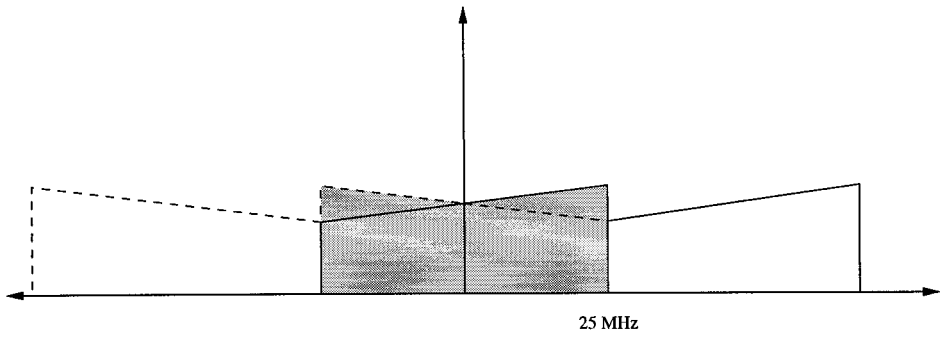

2. Signal output from SBL-1-1 mixer

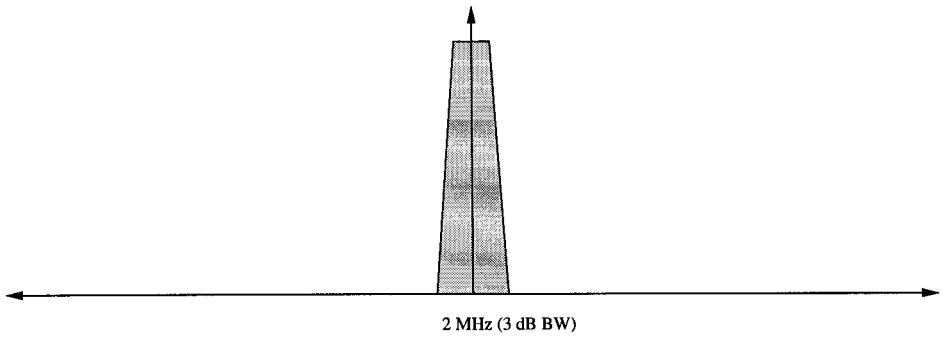

3. After image rejection filtering (PLP-5) and ampification

FIG A.6: STAGE TWO DOWNCONVERSION

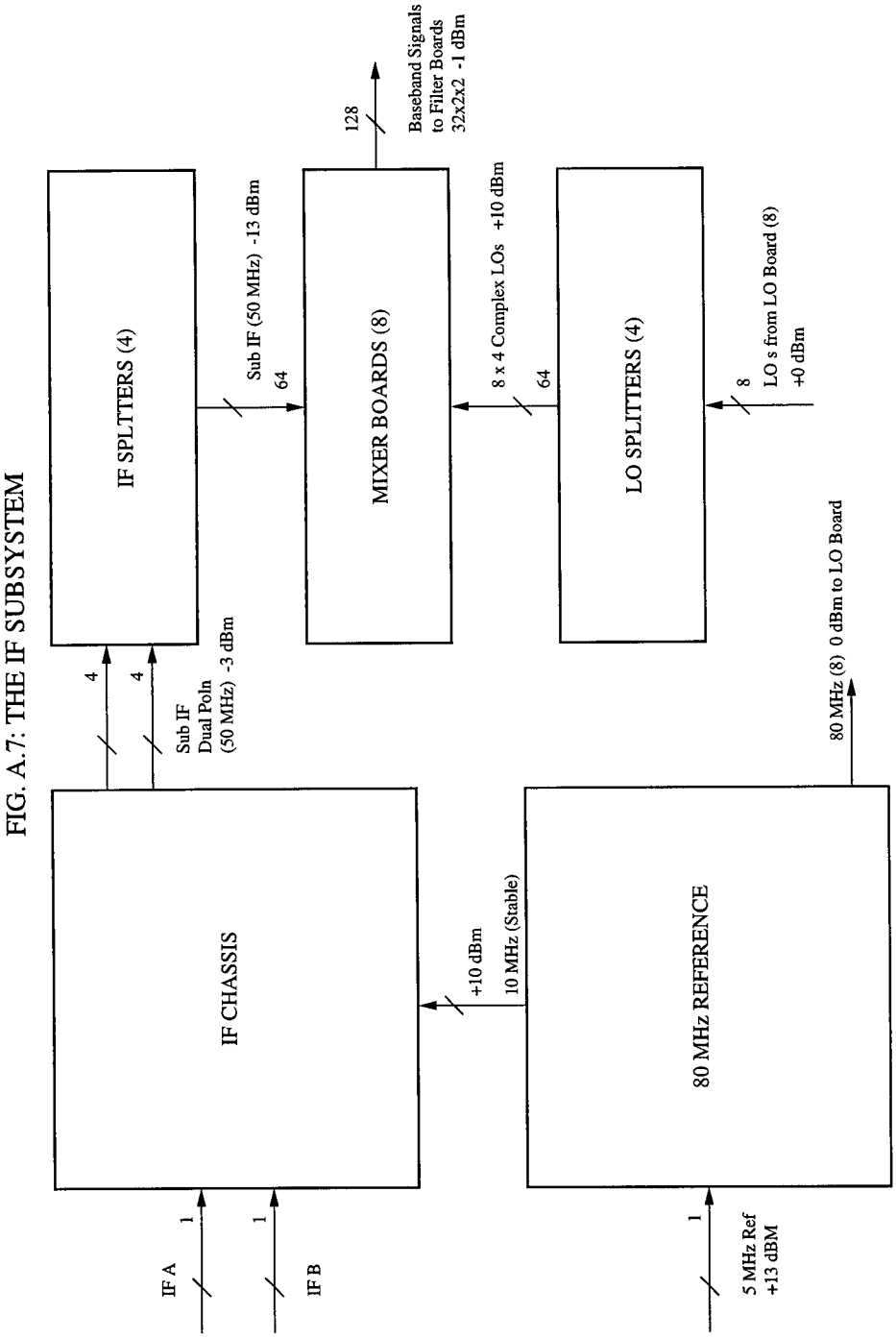

FIG. A.7: THE IF SUBSYSTEM

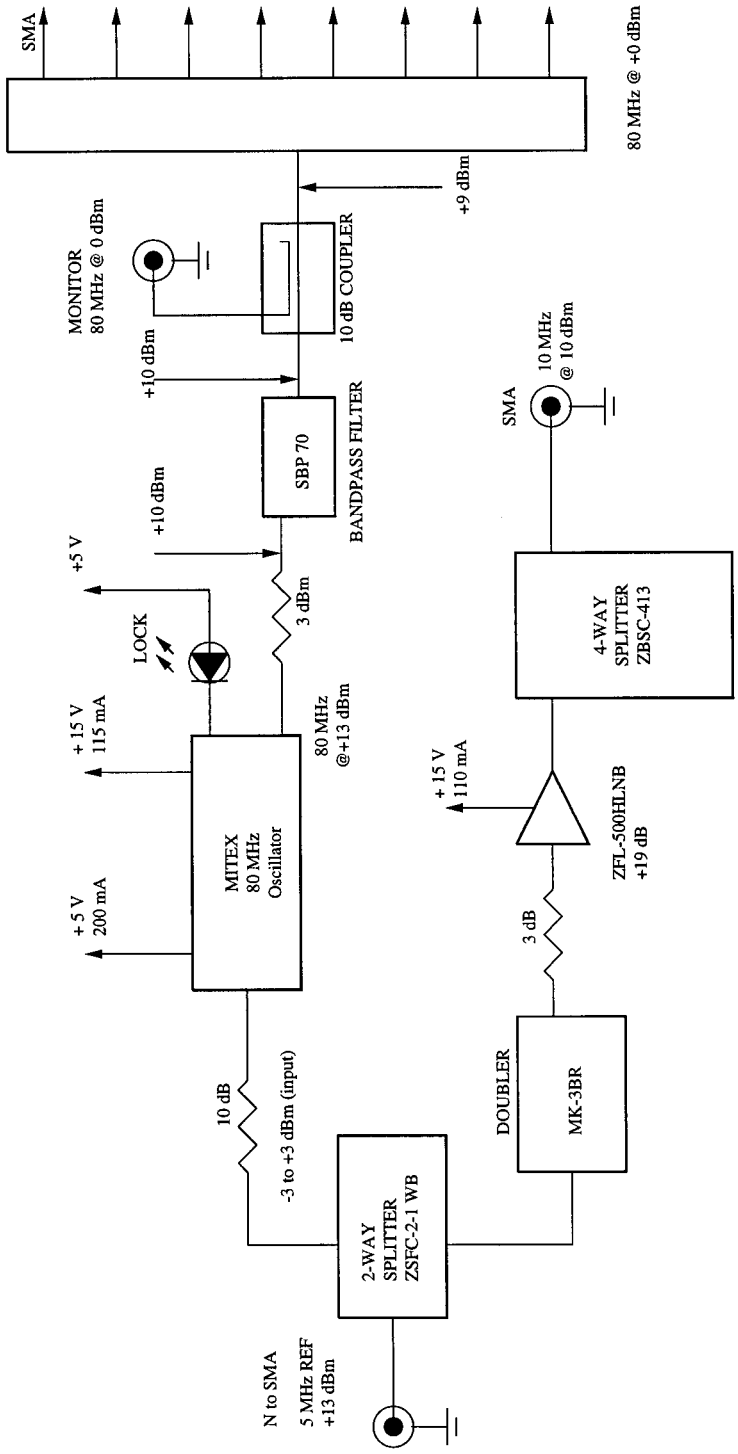

FIG A.8: 80 MHz REFERENCE BOX

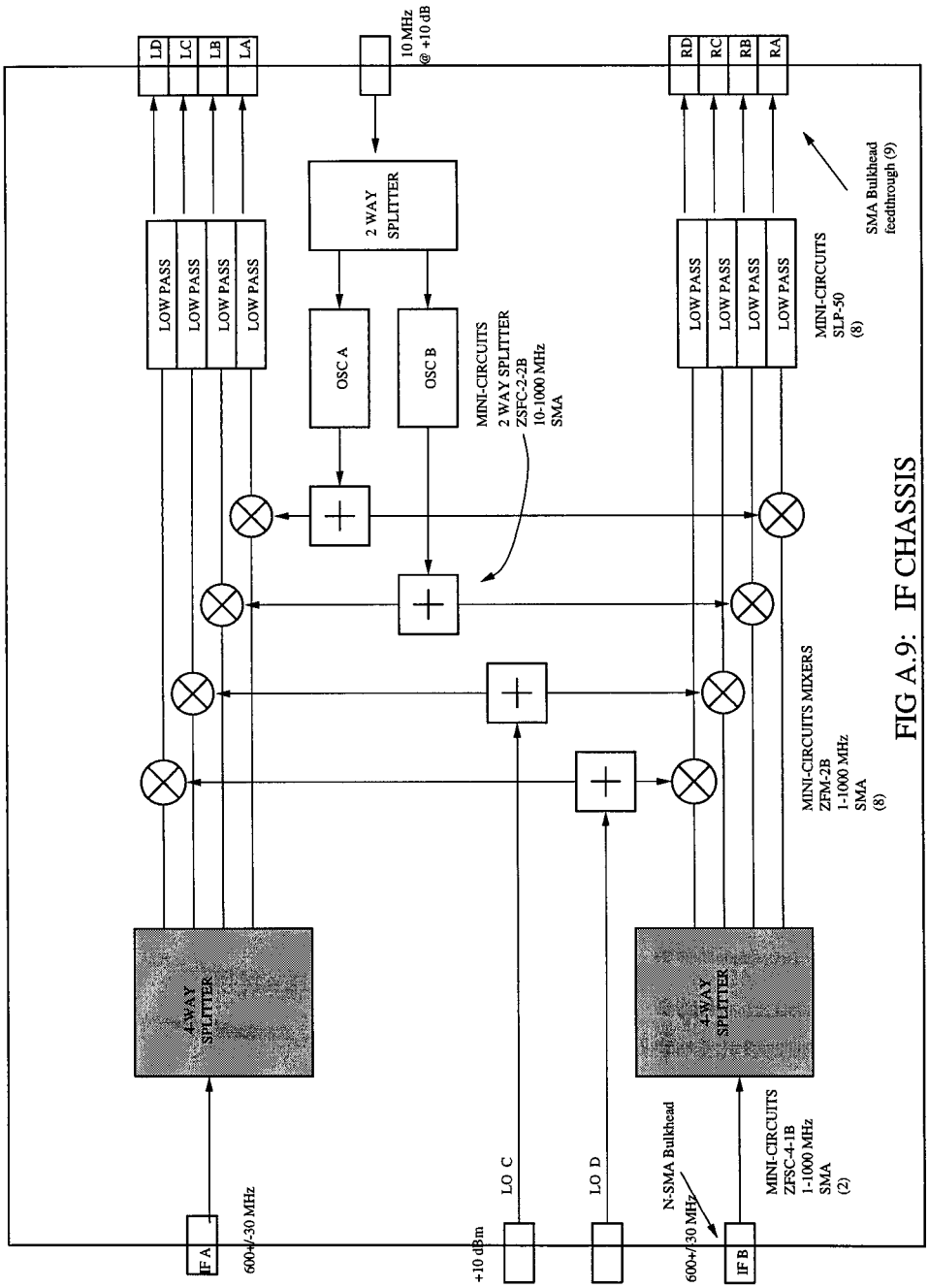

FIG A.9: IF CHASSIS

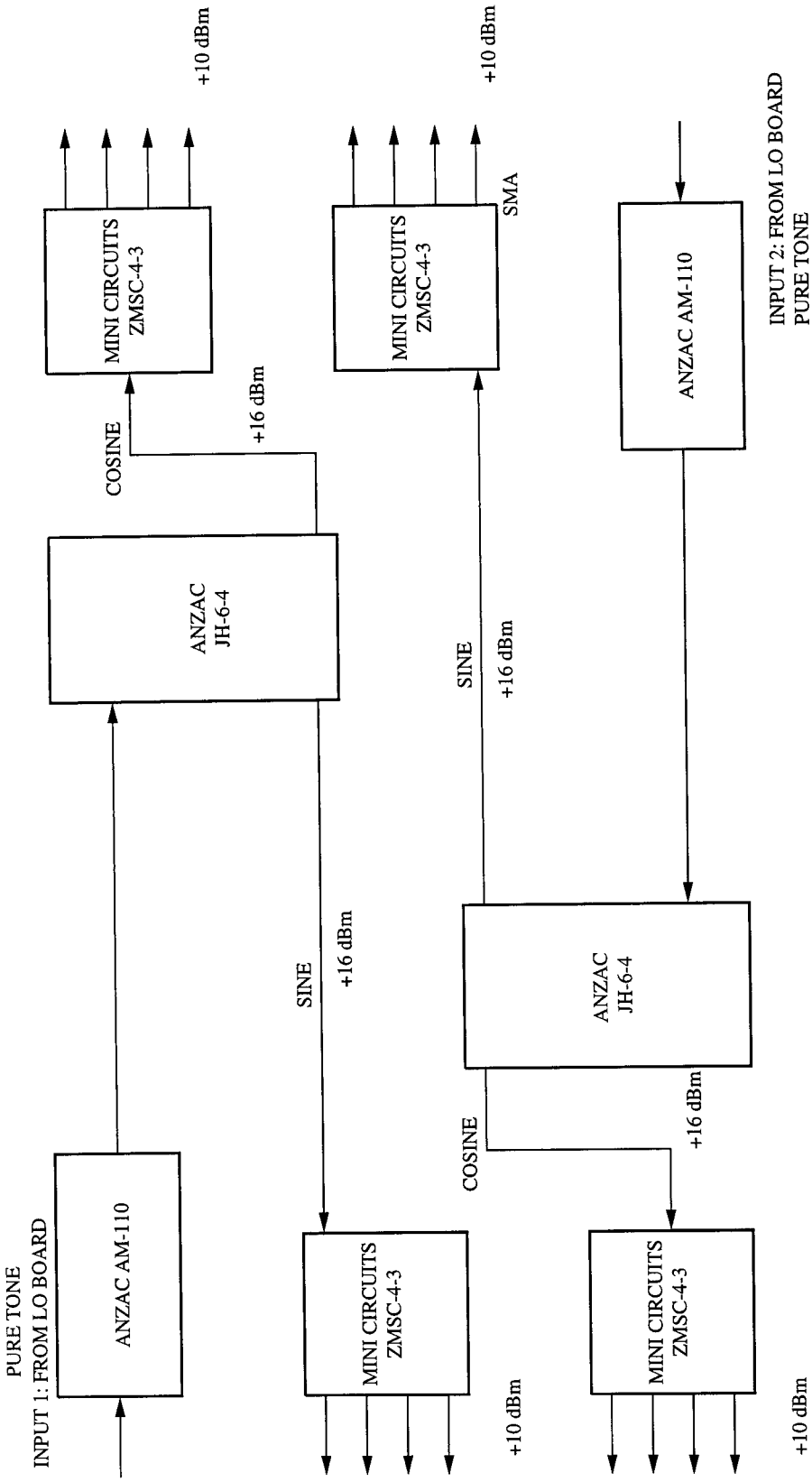

FIG A.10: LO SPLITTER BOARD

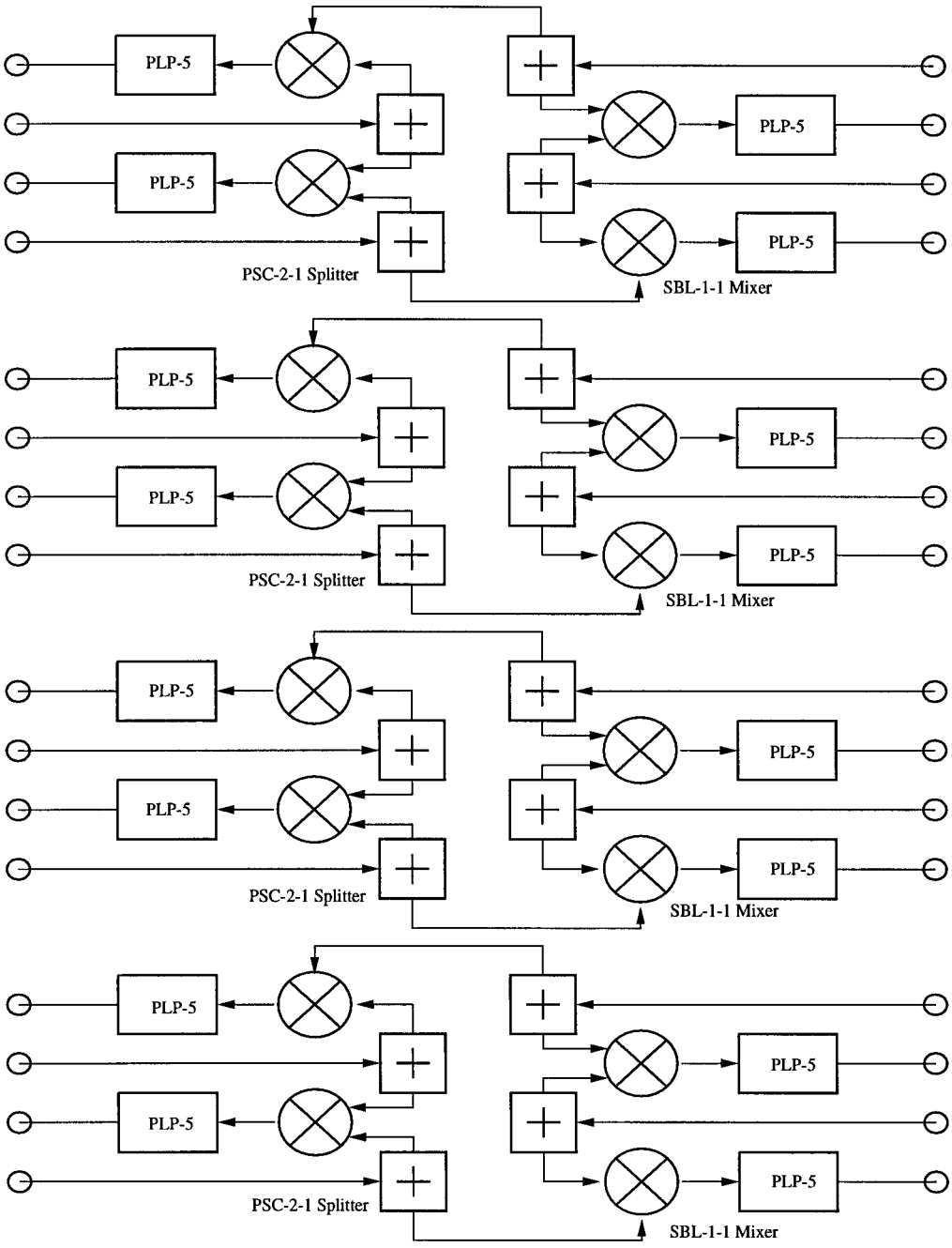

FIG A.11: MIXER BOARD

A.4 THE VME SUBSYSTEM

This module has eight filter-boards, the master control-board, the buffer-board and the local-oscillator board (Fig A.20 pp. 255). The 32 dual-polarization complex baseband voltages from the IF-subsystem are fed into the filter-boards, where they are filtered, detected, smoothed and sampled. The sampled data from each filter-board is pipelined via the master control-board into either of two resident memories on the buffer-board. When either buffer-board memory is full, it is asynchronously read by the computer and data is transferred to mass storage devices.

These are the main functions of the VME subsystem. They are described in greater detail as part of descriptions of the various boards that follow.

A.4.1 THE FILTER BOARDS

Inputs:	Baseband signals (16) at -1 dBm
	Audio-filter clock (ACLK) TTL
	Smoothing filter clock (FCLK) TTL
Outputs:	Digitized channel data (2-bytes/sample)

A.4.1.1 – Function

The filter-board is the heart of the Flexible Filter Bank. It is cleanly subdivided into separate functional modules with unique functions. Each board has eight identical frequency channels which form the analog section of the board. All eight filter-boards are used to configure a dual-polarization 32-channel system. A

digital section on each board is used for manipulation of parameters of the analog section, for sampling the channel data and for data I/O. A standard VMEbus interface is used to address all resident peripheral memory and data registers, whereas, a user-defined P2 VMEbus interface is used for communication of sampled data to the master control-board (see Fig A.16 pp. 251).

The filter-board front panel accepts eight complex baseband signals through SMB connectors. Each channel, therefore, takes one complex pair of inputs that are lowpass filtered to a pre-selected filter setting, detected, smoothed and sampled (see Fig A.14 pp. 249). The detected and smoothed voltage in each channel is sampled with two bits of resolution, and transparently latched for readout by the data-acquisition system. The complex, undetected signals in each channel, if so desired, are available as outputs through 16 straight SMB connectors that are mounted on the component side of the board (see schematics). As an example, the undetected signal (electric field) could be digitized by fast ADC cards and recorded in a direct-baseband processor (Chapter 2, see Fig 2.5).

Each channel is conveniently divided into functionally separate modules. We list them below and, thereafter, describe each in greater detail.

1. Channel Filter Module (complex signal)
2. Detectors (complex signal)
3. Additive Post-Detection Amplifier
4. Smoothing Filter
5. Post-Smoothing Variable Gain Amplifier
6. Sampling Circuit

A.4.1.2 – Description of the Channel Filter Module

Each filter module accepts a sine and cosine baseband input via front panel SMB connecters (see Fig A.14 pp. 238). The inputs have an impedance of

$\Re(Z_{in}) = 4.0$ kΩ looking into the board. Each baseband input is lowpass filtered by either of two active filters placed in parallel and appropriately selected by means of an analog switch (Precision Monolithics SW-201). A computer controlled software signal called VIDEO (or AUDIO = VIDEO\ ) selects the appropriate filter. The two lowpass filters are dubbed Video-filter and Audio-filter. These names are mnemonics for the range of programmable cutoffs (3 dB points). In all, the two filters allow bandpass cutoff frequencies, f_c, spanning four decades in frequency space (see Fig A.12 pp. 218).

The filter covering higher frequencies (part no. Silicon Systems SSI 32F8131-CL; 16 lead SOL package) is a programmable lowpass video filter with 0.14 MHz $\lesssim f_c \lesssim$ 1.5 MHz in single-side-band (SSB) mode. It is implemented in the so-called "normal" mode in which its time-differentiated lowpass outputs are disconnected. The chip has two programmable numbers, the CUTOFF and BOOST, which are controlled by two on-chip 7-bit current digital-to-analog converters. The CUTOFF programs the filter anywhere in the above mentioned range. BOOST magnitude equalization is programmable from 0 to 10 dB. The magnitude equalization, measured in dB, is the amount of high frequency peaking at the cutoff frequency relative to the original -3 dB point. For example, when a boost of 10 dB is applied, the magnitude of the response peaks up 7 dB above the DC gain. Since BOOST is implemented as two zeroes on the real axis (on the complex filter response plane) with opposing signs, the flat group delay characteristic of the filter is not affected by the boost programming.

The cutoff frequency is determined by the following equation

$$\text{SSI 32F8131 } f_c \text{ kHz } = 10.81 \times \text{F-Code} + 37.$$

where F-Code $\in 12 \ldots 127$ in integer steps.

The magnitude equalization is also controlled via an on-chip 7-bit DAC and is determined by the equation

$$\text{SSI 32F8131 Boost (dB)} = 20 \times \log[0.01703 \times \text{S-Code} + 1]$$

where S-Code $\in 0 \ldots 127$ in integer steps.

All inputs and outputs of the 32F8131 are ac-coupled. This is necessary since all input and output pins on this IC are pulled to $V_{cc}/2$. The outputs are referenced back to board ground (AGND) with an electronic transformer (a differential amplifier of gain 3.3) mounted on small piggy-back boards. Originally, magnetic transformers MCL T1-6T's were used. However, it was realized that the magnetic cores in the transformers were causing significant low-frequency attenuation and hence the transformers were discarded.

The filter covering lower frequency ranges is a clock sweep-able, switched-capacitor, Cauer lowpass filter (8-pole response) (also called the Audio-filter; Linear Technologies LTC 1064-4; 14 pin DIP). Used with external compensation, the filter gives a passband ripple of ± 0.1 dB and a stop-band attenuation of 80 dB at $2f_c$. An external TTL clock (ACLK) sets f_c to be $f_c = f_{ACLK}/50$. Cutoffs of 80-100 kHz can be achieved. The filter displays low harmonic distortion as long as input voltage levels are less than $3V$ (rms). This is not a problem in the FFB, as front panel inputs are typically around $0.3V$ (rms).

The input signal to the Audio-filter is first filtered and amplified by the Video-filter, usually configured to its smallest cutoff of 150 kHz. This is to ensure that inputs to the Audio-filter are band-limited to much less than the 2.5 MHz bandwidth of the baseband signals. This sidesteps an irritating characteristic of switched-capacitor filters. In addition to generating a relatively flat response from $-f_c$ to $+f_c$, they also respond to aliasing sidebands centered at $f = 10^2(2n+1)f_c$, where n is an integer. Any substantial signal in this sidebands would be aliased back into the main-band of the filter. It must, therefore, be ensured that the input signal is band-limited to approximately 200 kHz. This requirement sets a lower limit on of an single-side-band of ~ 3 kHz for this filter.

Since the LTC 1064-4 is a CMOS analog device, it has a tendency to acquire "latch-up" state. In order to avoid latch-up from occurring when the power supplies are switched on and transient states occur — two 1N 5817 Schottky diodes

(one on each positive and negative supply) have been added to the analog power receptacles on the filter-board.

A large voltage drop $\propto \sqrt{(b_{out}/b_{in})}$ occurs when this filter is used. The input signal which is about 2 MHz wide now drops to < 100 kHz in total bandwidth. In order to recover acceptable voltage levels, a post-filter gain stage of amplitude-gain of 10 has been provided.

In order to isolate the two filter sections in each channel we use monolithic analog bipolar JFET switches (pno. SW-201). The IC contains four separate SPST JFET switches and associated control circuitry. The control circuit of this device acts to keep the "ON" resistance typically at the 150 Ω (200 Ω at max) over an analog range of -5 to $+5$ V, varying only by about 10 Ω over this entire input voltage range. In the "OFF" condition the switch leakage current will be less than 1 nA at 25^o C and for $V_{in} - V_{out} = 4$ V. These characteristics ensure good input to output isolation. The "OFF" state isolation however decreases markedly with increasing frequency due to a parasitic drain-to-source capacitance of the FET switch. Thus at a frequency of 1.0 MHz the "off" state isolation will be -50 dB with a load resistance of about 680 Ω. This corresponds to a drain-to-source capacitance of about 0.7 pF. We employ use of a single SW-201 for proper isolation of the two filters (see Fig A.15 pp. 250). When the Video-filter is operational, the Audio-filter must be untuned by cutting off ACLK. This help remove ground plane noise that is generated by ACLK switching. On the other hand, when the Audio-filter is used, the Video-filter must be programmed to its minimum cutoff-frequency.

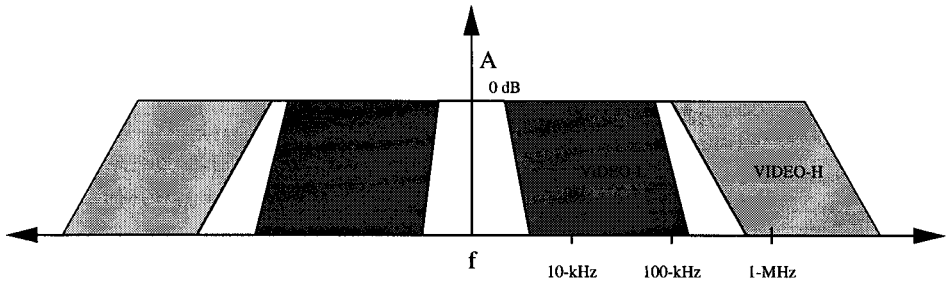

FIG. A.12: FILTER-CUTOFF REGIME
frequency vs. amplitude

A.4.1.3 – Detection

Power detection follows lowpass filtering, and is accomplished with a broad-band multiplier chip (part no. Burr Brown MPY600) set up in squaring mode with a voltage response of $V_o \approx 1/2V_{in}^2$. Input bandwidths of up to 2.5 MHz (SSB) are squared within acceptable errors. Therefore multiplication of the filtered signal is well within the capacity of the MPY600.

In a four-quadrant voltage multiplier with the operation $V_o = \kappa.V_x.V_y$ where κ is in units of V^{-1}. An ideal multiplier with a scale factor κ of 0.5 V^{-1} will have an actual output given by

$$V_o = \frac{(V_x + V_{osx})(V_y + V_{osy})}{(2V)(1+\epsilon)} + V_{os} + (\text{non-linear terms in } V_x^n.V_y^n)$$

The Burr Brown MPY 600 has provision for trimming and nulling so that the various error terms can be reduced down to a range of 0.1%. In the squaring application, the important index of accuracy is the squaring-mode accuracy for which inputs V_x and V_y are tied together (look up numbers in the data sheet). This is the maximum deviation of the output from an ideal best fit parabola, usually expressed as a percentage of the full-scale output voltage. For the MPY 600, 3-dB multiplication output bandwidths of up to 4.8 MHz are available.

Typical multiplication errors for the (X,Y) inputs for -1 V $< X <$ 1 V and -2 V $< Y <$ 2 V are about 15 mV, and increase to 25 mV for -2V $< X <$ 2 V. The

gain errors are typically within a percent. The chip is operated off recommended power levels of $\pm 5V$. Since the output levels are limited to ± 2 V, larger supply voltage is not required for a full voltage output swing and furthermore power dissipation in the circuit is considerably reduced. No offset trimming is used, however, an ac-coupler is provided soon after the multiplication stage (see FB schematics). The gain of the output internal op-amp has not been increased to preserve bandwidth of the multiplication. It is important that the input to the multiplier does not increase beyond the $1V$ rms level. In the DC-multiplication mode, used in the variable-gain-amplifier (see section A.4.1.6), limit inputs to the terminals X to within $\pm 1V$ and Y to $\pm 2V$.

A.4.1.4 – Summing Amplifier

After detection the sine and cosine powers are added to construct a detected double sideband signal. A summing amplifier circuit, built with op-amp LM 318N, is used for this purpose and has a voltage response of $V_o = -3.3(V_1 + V_2)$. The input impedance with respect to the two input voltages V_1 and V_2 is about 1 k-ohm each. Two voltage followers LM 310 are used to buffer the inputs of the adder.

The LM 318 operational amplifier is used "everywhere" on the filter-board. A reasonable understanding of the LM 318 characteristics will enhance the technical person's ability to debug the circuit board if necessary. Please refer to LM 318 data sheets (for example the National Semiconductors Linear Devices Databook). The LM 318 series is a high precision high speed operational amplifier used for application in high bandwidth and high slew rate. It has a typical small signal bandwidth of 15 MHz and a guaranteed slew rate of $50\text{V}/\mu\text{s}$. On the filter-board, the LM 318 is used as inverting amplifier and differential amplifier.

A.4.1.5 – The Smoothing Filter

The detected and added channel voltage carries total power information. Pulsars have periods that range between a few seconds to about a millisecond.

Since they have small duty cycles, higher harmonics carry frequency information up to 10 kHz or higher. The detected and added signal has a single side bandwidth of up to $2f_c$, i.e., up to 3 MHz and must therefore be averaged to timescales of interest. We use signal averaging to increase the signal-to-noise ratio with the help of a smoothing filter.

The smaller the smoothing time constant, the larger is the signal sampling rate (Nyquist rate). There has to be a compromise between smoothing and fast data collection. For instance, a 10 kHz smoothing constant sampled at a Nyquist rate of 20 kHz will generate sampled data from the FFB at the rate of 320 kb s^{-1} or about one G-byte hr^{-1}. Amassing such formidable amounts of data is only occasionally necessary and smoothing time constants can be reduced when observing slower pulsars by programming the clock FCLK appropriately. Hardware limits to smoothing constants are dictated by the maximum filter cutoff of the smoothing filter of $f_c \sim 50$ kHz, implying a maximum sampling rate of 10 μs.

The smoothing filter is implemented as a cascade of three low-pass filters in succession. The first stage is a simple RC time-constant of 1.6 μs. The second stage is an 8 pole lowpass switched capacitor filter (same as the Audio-filter IC). The cutoff f_c, is controlled by a T^2L clock (FCLK) at $f_{FCLK} = 50 \times f_c$. The first stage simply limits the inputs to the smoothing filter to 100 kHz in order to prevent aliasing-back of frequencies at integer multiples of f_{FCLK}, into the main filter-passband. The third stage consisting of another RC-filter (1.6 μs), is used for elimination of FCLK feed-through into the filtered output. Although the IC carries in-built isolation, FCLK feed-through is still substantial, making the third stage necessary. Substantial bandwidth and therefore voltage attenuation occurs during smoothing and therefore, a variable gain stage follows. Remember that the characteristics of the smoothed signal can be assumed Gaussian.

A.4.1.6 – Amplification of the Channel Signal

The bandwidth losses incurred during the filtering stages result in equivalent voltage losses. Therefore, amplification is a must after the smoothing operation and before the signal is sampled. Due to the tunability of the filters, the loss in voltage levels and be large and variable. They can also depend on channel-to-channel variations and roll-off of the receiver band and system response. The variable gain amplifier used at this stage is made up of two inverting operational amplifiers with a total voltage gain of 22. The amplifiers are separated by a multiplier (MPY 600), which multiplies with a variable gain k such that the total gain is $22k$. The dc-gain k can be varied between zero and one and is generated by a programmable octal digital-to-analog converter. Each of the eight DACs on a single Analog Devices 7228 IC controls k on one of eight channels. This variable gain can be used to eliminate channel-to-channel variations in voltage levels.

A.4.1.7 – Sampling the Smoothed Signal

The smoothed signal in each channel is sampled with 2-bits of resolution. The sampling circuitry displayed in figure A.12 employs a scheme involving comparison of the analog voltage with three steady dc-voltage levels. These are analog ground, and positive and negative programmable dc thresholds. The fast LM 311 (2 MHz bandwidth) is used as comparator. The pull-up resistor at the open-collector output the LM 311 assures rapid state switching between TTL levels. Note that the signal is pseudo-digital after the comparator stage. Comparison with ground (AGND) results in the sign-bit which is one or zero depending on the signal polarity. The magnitude-bit is determined by logical exclusive OR operation on the combined outputs of the threshold comparators. The smoothed analog input to the comparator is usually normally distributed if the smoothing constant is much larger than the channel bandwidth. Therefore, if the thresholds voltages are suitably set at the 1σ level, using the programmable thresholds, we expect hits in the four levels to be roughly in the ratio 1:2:2:1.

The 2-bytes of data produced for every sample by all eight channels on a board, are transparently latched and buffered so that they now see the user defined lines A1-16 on the P2 backplane. As soon as the board is addressed, the data are transferred onto the VME-buslines and then via the control-board, are transparently buffered to the buffer-board.

A.4.1.8 – Noise in the Filter Boards

In any system, unwanted and extraneous signals will interfere with the desired signal (from the telescope) and will set a lower limit to the strength of the desired signal that can reliably and accurately be received and understood. The interfering "noise", when of a random nature is extremely hard to deal with and eliminate. Interfering signals that have a well defined or fixed nature, such as spurious leakage of the mains modulation frequency (60 Hz) can be eliminated with special signal processing techniques either in the hardware itself or more easily so later in the software. Although there are techniques for noise reduction it can never really be eliminated. Such signal processing for noise reduction typically involve system trade-offs. An example of such a trade-off is the reduction of the system bandwidth. In the filter-boards, therefore, we need to maintain a certain signal to noise ratio for proper detection of the signals. The initial signal to noise ratio S_i/N_i is undergoes degradation in a lumped series of M stages as

$$(SNR)_M = \frac{S_i}{(N_i + N_1) + (N_2/G_1) + (N_3/G_1G_2) + ... + (N_M/G_1G_2...G_{M-1})}$$

The *sensitivity* of a system is a measure of the ability of the system to detect or receiver weak signals. It is usually described as the minimum acceptable SNR that can reliably be used to detect the presence of a signal. In each channel, in the filter bank, the noise levels on the lines have been measured empirically. In the absence of any signal and with a filter BW of about 1 MHz the measured noise in the system is about $V_{rms} \sim 20$ mV. To obtain a signal-to-noise ratio of about 10, the pre-sampled signal should have and rms voltage of about 200 mV. The

required front panel input levels, at 1 MHz channel bandwidth, is about 300 mV RMS.

A.4.1.9 – The Digital Section

The filter-board digital section consists of a VMEbus interface, the sampling circuitry, and peripheral memory for control of various analog functions (see Fig A.17 pp. 252). There is only one way communication with the CPU, i.e., the board generates no hardware interrupts and cannot be bus master. The digital section manages software control of the following:

1. Video-filter cutoff frequency: The cutoff f_c for this filter is controlled by serial programming of a 7-bit number into an internal current DAC on the SSI 32F8131. Refer to data sheets or section 2 for details on the control word. The three control signals are serial data in (SDI), serial data enable (SDE) and serial clock (SCLK).

2. Video-filter boost: The boost is set by a 7-bit control word programmed onto a second DAC on the SSI 32F8131. The serial interface described in section A.4.1.2 is used (see Fig A.15 pp. 250) for boost programming as well.

3. Audio-filter cutoff: f_c for Audio-filter (the switched capacitor filter LTC 1064-4) is set at the frequency of ACLK divided by fifty. ACLK frequency is set by reprogramming the STEL 1173A on the master control-board. ACLK is distributed to all filter-boards on the VMEbus trace P2:A30. Once on the filter-board, ACLK is immediately daisy-chain buffered on a fast 10-bit buffer (or bus driver) 74ALS29827 which produces eight copies of ACLK. Each copy is input to each of two Audio-filters on a single filter-board channel.

4. Smoothing filter cutoff: Same as above. The cutoff clock is the master control-board clock FCLK and transmitted to filter-boards via J2:A32.

5. Variable Gain control: The variable-gain-amplifier control is accomplished by loading a constant number for each channel of an 8-bit octal DAC. Output voltage is 2.5(VAR/255) V, where VAR is the programmed variable. The

Octal DAC is an Analog Devices AD 7228 referenced to a stable 2.5 V from a REF-43GP. Each filter-board has four REF-43GP chips. The AD 7228 contains 8-bit voltage mode digital to analog converters, with output buffer amplifiers and interface logic on a single monolithic chip. Three address-lines and 8-wide data-lines are used for programming the AD 7228 (see Fig A.17 pp. 252). The single-chip, octal-DACs were used to allow a dramatic reduction in board space requirements.

6. Threshold generation: Sampling thresholds are generated by a pair of octal multiplier DACs (Analog Devices DAC 8840). One DAC 8840 produces all positive thresholds and the other all negative ones. The DACs are referenced to stable 2.5 V from REF-43GP. Internally the DAC 8840 contains eight voltage output CMOS digital to analog converters, each with separate reference inputs (all tied together for this application). Each DAC has its own DAC register which holds the output state. At the start of the observation, the required output state can be stored in each DAC via software control. The four quadrant multiplying capability is used for signal inversion to generate the negative thresholds. Each output is fully buffered by the DAC 8840's internal amplifier. In this application, the DAC drives a high impedance load, so we do not worry about the internal circuitry overloading itself. We do not worry about digital feed-through as we are dealing with just a simple DC operation for the DAC 8840. The DAC has 3 address and 8 data lines. $V_{out} = (\mathrm{TH}/128 - 1) \times 2.5$ V. TH is a number ranging between 0 and 255.

A.4.1.10 – Power Requirements

The filter-board uses both analog and digital power supplies. These are +5 V_{DD} (digital), +5 V_{CC} (analog) and -5.2 V_{EE} (analog). Return paths are through a digital ground (DGND) and an analog ground (AGND). All analog power and grounds are run into the board through the user defined J3 VME connector (see VMEbus layout Table). The digital power enters the board through dedicated VMEbus power lines with V_{DD} on J1:A32,B32,C32 and J2:B1,B32 and DGND on

J1:A9,A11,A15, A17,A19,B20,C9 and J2:B2,B31. All power and grounds planes are placed on internal pcb layers and are wire mesh planes or thick trace conductors. All analog power entry points are capacitively coupled with 10-50 μF electrolytic capacitor. All power points on individual chips are bypassed with 0.1μF ceramics. The V_{CC} and V_{EE} are also Zener (1N 5817) protected against turn-on transients. These are required to protect the sensitive CMOS LTC 1064-4 analog filters from going into "latch-up" state.

The total power consumption for a single filter-board in steady operation is nearly 35 W. All eight filter boards are responsible for a major fraction of total power consumption of the machine estimated at 600 W.

+5 V digital	0.8 A	4 W
+5 V analog	4.0 A	20 W
-5.2 V analog	2.0 A	10 W

A.4.2 THE MASTER CONTROL BOARD

A.4.2.1 – Function

The master control-board triggers and oversees sampling of the filter-board signals (see Fig A.18 pp. 253). The sampled data is transferred along the VMEbus to the control-board, which redirects this data to either of two buffer-board memories along with data strobes which clock the buffer-board and make the data valid. In addition, the control-board generates three TTL clocks, including the sampling clock, that are used by the filter-boards. The clocks are generated using a reference clock, that is routed in from the LO-board. At present, the control-board is on wire-wrap 9U VME Eurocard; in order to facilitate future adaptations such as expansion of the timing circuitry. It should eventually be moved to printed circuit board as it has five high frequency clocks on board. Ground plane and signal isolation are degraded on the wire-wrap board by clocks of frequency as low as 10 MHz.

A.4.2.2 – Synthesis of Control Clocks

The control-board generates three clocks that are distributed to the filter-boards via the VME-backplane. These clocks are made by independent direct digital synthesis NCOs STEL 1173As which are capable of up to 25 MHz of square-wave operation. A 32-bit number is loaded onto each NCO via an 8-line parallel interface and this number determines the output frequency w.r.t. the reference clock frequency (MASTERCLK). It is absolutely vital to remember, that the STEL be used only in the 2^n mode, i.e., the 32-bit number should be a power of two. This ensures that the DDS table counting in the STEL 1173A does not cause slippage, which tends to produce spurious, high level harmonics. To make any output frequency possible, we employ a trick which makes the reference variable, while still using the STEL 1173As in 2^n mode. The variable reference is available from the LO-board STEL 1378A mothercards. The variable analog reference (MASTERCLK) is generated by a STEL 1378A on the LO-board and is frontally fed into the control-board. A zero-crossing comparator circuit is used for analog to TTL conversion with an upper frequency limit of 30 MHz. The three secondary clocks are:

1. Sampling Clock (SCLK) – This clock controls runs the sampling of the filter-boards. At the rising edge of each SCLK, a state machine inside a custom PAL is triggered to generate a series of addresses in burst mode (burst mode means that time for each circulation of addresses is much less than the period of SCLK itself). Addresses 0 through 7 are generated sequentially for the eight filter-boards. These addresses are latched transparently onto user defined VMEbus lines P2: C1,C2,C3. The filter-board of the corresponding address responds by latching sampled data on the VMEbus. Maximum useful SCLK is 100 kHz.

2. Audio Clock (ACLK) – ACLK determines the lowpass cutoff frequency for the Audio-filters on the filter-board. Its frequency is set to be fifty times the demanded cutoff frequency. ACLK is distributed to all filter-boards via a

user defined J2 VMEbus line. The maximum useful frequency of ACLK is 5.0 MHz.

3. Smoothing Clock (FCLK) – The FCLK controls the cutoff for the Audio-filter on the filter-boards. The FCLK frequency is set to be fifty times the required smoothing frequency. FCLK is transfered to all filter-boards via a user-defined J2 VMEbus line. The maximum useful frequency is 2.5 MHz.

For greater details on programming and timing diagrams of the STEL 1173A, refer to Stanford Telecom data-sheets or the control-board circuit schematics.

A.4.2.3 – Sampling the Filter Boards

Addresses for filter-board sampling are generated on the control-board. A 3-bit address is put out on user-defined VME lines P2:C1,C2,C3, and the corresponding filter-board responds by transparently latching its 2-byte sample onto P2 data lines. Sampling addresses are hardwired by a DIP switch setting on each filter-board. Each 2-byte sample is then buffered on the control-board and transferred to the buffer-board with the help of a 40-pin ribbon cable (attached to the front panel) along with a DATA STROBE. All sampling is done is burst mode, i.e., eight filter-board addresses are generated in a burst sequence beginning with the rising edge of the sample clock and lasting 2 μs. The sample clock itself is valid for a duration much longer than 2 μs.

Sampling begins when the computer sends an arming (ARM) signal to the control-board at the beginning of data-taking. As soon as both ARM and SCLK are valid, a control state machine (on a PAL; U12) is triggered to generate eight filter-board addresses in sequence, along with a DATA STROBE for every address. After the address cycle is over, the state machine resets and waits for the next rising edge of the sample clock. The state machine is essentially a 3-bit counter, that is run off a 4 MHz clock (a divided down 16 MHz VME system clock). If the exact time of start up is important, as in timing applications, the sampling can

begin on the count of an external 10 second tick (6PPM), which is locked to some timing standard.

A.4.2.4 – Control Board Specifications

Control Board VME address		0xEF000000
Control Board Reset	-	0xEF000000
Control Board Armed	-	0xEF080000
Control Board S6PPM	-	0xEF100000
Write to SCLK	-	0xEF200000
Write to ACLK	-	0xEF280000
Write to FCLK	-	0xEF300000
Load Clocks	-	0xEF380000
Power Supplies		+5 V_{cc} digital
Power plane		Component side of brd.
Ground plane		Solder side of brd.
Reference Clock (TTL)		Max 30 MHz
Smoothing Clock (TTL)		Max $f_{MASCLK}/2$
Audio Clock (TTL)		Max $f_{MASCLK}/2$
Sampled Data In		J2 A[1...16]
Sampled Data Out		40 PRC [01...16]
Date Strobe		40 PRC [18]
Detector Address lines		J2 C[1...3]
Function Addresses		VME Addr[19...21]

A.4.3 THE BUFFER BOARD

The buffer-board was built by Jose′ Navarro at part of his thesis at Caltech. This description of the board is from Navarro's thesis (Jose′ Navarro 1994, PhD Thesis, California Inst. of Technology, Appendix D, pp. 94). The buffer-board is a 6U VMEbus board that can be used to read and buffer digital data into a VME

computer, or onto a hard disk or tape connected to the computer. The input data to the board consists of 8, 16 or 32 bits and a strobe, all TTL levels. The input data is automatically written into one of two large memories. When that memory becomes full, a VMEbus interrupt is issued to the computer and the new incoming data is routed to the other memory. The memory not being written to can be read by the VME computer, asynchronously with the incoming data.

A.4.3.1 – Front Panel Inputs

The input data can be 8, 16 or 32 bits wide, and requires a strobe or clock that indicates when the data bits must be sampled. All data bits as well as the strobe are TTL signals, and bits which corresponds to a HIGH TTL level will be read as 1's, and 0's otherwise.

The relative timing of the strobe with respect to the data is not important as long as it remains stable, since the strobe can be delayed on-board with respect to the data until the timing is correct. The exact delay that can be applied to the strobe is software selectable from 0 to 480 ns in units of 60 ns. Likewise, whether the rising or falling edge of the strobe must be used can be selected from the software.

The maximum sustained strobe rate is better than 1.5 μs, but it really depends more on the speed at which data can be read from the buffer-board and written to permanent storage. In burst mode, the separation between strobes can be as small as 200 ns, as long as the average strobe rate is larger than 1.5 μs. This is a hard limit and cannot be reduced to less than 200 ns without changing components in the buffer-board itself.

In the current printed circuit-board version of the Buffer Board there is a front panel 40-pin ribbon cable connector. This connector contains 16 pins for input and 1 for the strobe, as well as multiple grounds. This means the board can be used as is for 8 and 16-bit parallel input, but requires special provisions for 32-bit wide input.

A.4.3.2 – The VMEbus Output

Whether the input is 8, 16 or 32 bits wide, the Buffer Board is always read through the VMEbus in 32-bit words. This allows for a minimum number of transfers and least overhead on the computer end. In the case of 8- and 16-bit input, earlier data are written in the least significant part of the 32-bit word. Thus data in higher memory positions always correspond to later times.

The rate at which data can be read out of the board and into the VME computer depends mostly on the speed of the device it is to written to, say a hard disk or tape drive. For a 1 Gb type hard disk we have achieved sustained data rates of 1.5 Mb/s, although of course most transfers happen in bursts as the CPU takes care of its needs.

A.4.3.3 – Memory Switching

The size of each memory bank is always 256 kb, independent of the input bus width. As a result, an interrupt will always mean that 64 kwords are waiting to be read. The computer cannot choose which memory bank to read, it will automatically read the one that is not being written to. This means that if it cannot read the entire bank before the next interrupt arrives, the data not read will be lost. Therefore it is important to respond to interrupts quickly as is expected in a real-time system, or else data will be lost.

A.4.3.4 – Selftest Features

The Buffer Board has some built-in self-test features. The most important one is that the board is able to generate test data. The test data is generated as digital output on a ribbon cable, and a 40-pin ribbon cable loop can feed the test data into the board input. In this manner the entire input circuit of the board can be tested, and one can see whether the output data is read correctly and the interrupts received when they are expected.

The test data can be generated a word at a time, or a data word can be set and then a strobe rate chosen. The former method is preferred when data integrity is to be tested, the latter when interrupts are the issue.

For this test mode the input part of the board is completely unaware that test data is being read, since it comes from the outside just like read data. Another test mode is available, where the board can force force some of the input bits to 0's or 1's and thus test the memories without having to produce output test data. A loop-back ribbon cable (or a ribbon cable with real data) is still needed in order to produce an input strobe.

Needless to say, the digital test data produced by the Buffer Board can be used as digital data for any other purpose. With the current PCB, 16 bits and a strobe are generated. The timing of this strobe with respect to the data cannot be fiddled with, since that option exists at the input end alone.

Note: in self-test loop-back mode the board will try to generate an interrupt immediately after it sends a test word out, and sometimes this results in a missing interrupt. It is a problem with the interrupt timing and it can be fixed by modifying the VMEbus interface PALs.

A.4.3.5 – Internal Registers

The Buffer Board has a single 16-bit control register. This control register controls the input bus width, the strobe polarity and delay, and the test data. Here are the 16 bits:

Bits	Function	Values
1,0	input bus width	00= 8-bit, 01= 16-bit, 11= 32-bit
2	strobe polarity	0= rising edge, 1= falling edge
3	overwrite test mode	enables test data. 0= off, 1= on
7-4	on-board strobe delay	0000= none, 0001= 60ns, 0010= 120ns ... 1000= 480n s
11-8	output strobe period	0000= none, 0001= 1μs, 0010= 2μs ... 0101= 16μs
12	overwrite test data	value of data bits 0,1,8,9,16,17,24,25

13	overwrite test data	value of data bits 2,3,10,11,18,19,26,27
14	overwrite test data	value of data bits 4,5,12,13,20,21,28,29
15	overwrite test data	value of data bits 6,7,14,15,22,23,30,31

Note: it is important that in normal operation bit 3 be zero, or else some of the input data bits will be overwritten to 0's or 1's (depending on control register bits 15-12).

In addition to the control register, the Buffer Board has a 16-bit data register. In order to generate fake data, one must first write the data into the data register, then generate an output strobe. That strobe will clock the data into the input part of the board if a loop-back ribbon cable is connected.

A third register is available, which contains the 16-bit address where the next 32-bit input word will be written. Thus, this 16-bit value can be used as a counter that tells how much data has been written into the current input memory bank, and how much time there is before the next interrupt is issued. Note that the address counter could be in a transitional state when it is read from the CPU (since the two processes are asynchronous), and therefore you should either take its value with a grain of salt or read it several times for confirmation.

A.4.3.6 – Internal Functions

In order to read a word from the output memory bank into the computer, or set the control register, or write to the output register, one must access one of the board functions. They are listed here:

#	Data	Function	Description
0	none	board reset	resets internal counters to bank A and address 0
1	16-bit	write control register	writes a 16-bit word to the control register
2	16-bit	write data register	writes a 16-bit word to the data register
3	none	test clock	generates output strobe pulse
4	16-bit	read data	reads a 32-bit data word from memory

5	16-bit	read counter	reads the 16-bit address of the current input word

A.4.3.7 – CPU Control of the Buffer Board

Despite the fact that some of the data transfers over the VMEbus are only 16 bits wide, like the address counter reads, all data transfers over the VMEbus should be 32-bit wide. The current Buffer Board will respond to a bus read or write when the 8 most significant bits match those in a board PAL (for example, A31-24=0xEB). The rest of the address bits select the internal board function, while the data to be written or read will be transfered over the 32-bit VME data bus.

Here follows a description of the 32-bit address:

Bits	Description
31-24	selects the board. For example, 0xEB
23	confirms that a CPU read (board write) is being done. 0= CPU write, 1= CPU
22-21	selects one of four function chips. Always 00 on the Buffer Board
20-18	selects a function. 0=reset, 1=write control register, etc (see above)
17-02	16-bit address point to the 32-bit word to be read
01	ignored by the Buffer Board
00	is not part of the VMEbus

A.4.4 THE LOCAL OSCILLATOR BOARD

A.4.4.1 – Function

The local-oscillator (LO) board (see Fig A.19 pp. 254) generates a maximum of sixteen independent sinewaves. It uses eight dual-NCO STEL 1378A motherboards to generate these signals. The STEL 1378A is a complete Dual Direct Digital Frequency Synthesizer in a single dual inline package measuring $3.25 \times 1.6''$. A maximum of eight STEL-motherboards can be mounted on the LO-board along with support circuitry for programming the STELS. All LOs are

generated off the 80 MHz reference signal (REFCLK), that is synthesized in the 80 MHz Reference Box (see Fig A.8 pp. 199). In the FFB, four STELs are used to make eight LOs that can span the frequency range 10-32 MHz. One STEL is used as the secondary reference (MASCLK) which is routed to the control-board and synchronizes SCLK, ACLK and FCLK on the DDS STEL 1173A chips (see Fig A.18 pp. 253).

Before mixing, the eight LOs are routed into the four LO-splitter boards (see Figs A.4 and A.10; there are two inputs per LO-splitter). Each is amplified, split, quadrature phase shifted and split again to obtain four sine and cosine versions of the original signal. (This scheme is explained in greater detail in the section on the LO-splitter board in A.3.4.1).

The STEL 1378A carries 32-bit frequency resolution (19 milli-Hz @ 80 MHz), with

$$f_o = \frac{f_{ref} \times \Delta - \text{phase}}{2^{32}}$$

where f_o is the output frequency and f_{REF} is the frequency of the reference clock (REFCLK). $\Delta - \text{phase}$ is a 32-bit number that is stored in an internal register on the NCO and programmed (consult the STEL 1378A data sheets) by the CPU to generate the desired frequency.

The spectral purity of the NCO-DAC combination on-board the STEL 1378A, depends upon variables such as phase and amplitude quantization, ratio of reference clock to output frequency and the dynamic characteristics of the final DAC. STEL 1378A generates 13 bits of phase-resolution and 12 bits of amplitude resolution resulting in theoretical spurious levels that are at least 75 dB down from the main signal level. The highest frequency of operation that is half the reference clock. Spurious components are removed by lowpass filtering. As the output of NCO approaches $f_{ref}/2$, the image spur at $f_{ref} - f_o$ also approaches $f_{ref}/2$ from higher frequencies. If the desired frequency is very near $f_{ref}/2$, it is almost impossible to filter the spurious image spur. Therefore, the recommended operating range for LO-board is limited from 12 to 32 MHz.

A.4.4.2 – Reference Signal (REFCLK)

The reference clock has a maximum allowable frequency of $f_{REF} = 80$ MHz (-5 to +5 dBm) and is a sine-wave. The clock is capacitively coupled at the input of the motherboard and undergoes translation to ECL levels on board. The front panel input is SMA, and is directly routed via coaxial cable to the input pin of the motherboard, so as to limit spurious crosstalk. The eight inputs on the front panel are on connector numbers $3n + 3$, where $n = 0 \ldots 7$.

A.4.4.3 – STEL Outputs

The signals appearing on OUT1/2 pins of the STEL motherboards are the analog outputs of the NCO and digital-to-analog converter combination (Analog Devices AD-9721). The DACs have 10-bit resolution. The outputs are stepped sine-waves, where the number of steps in each cycle is equal to the ratio of the clock frequency to the output frequency. When this number is no an integer the steps will not repeat from one cycle to the next, but the fundamental component of the output will always be a sine-wave at the desired frequency. The outputs will have a DC offset of typically less than $0.5V$, which is ac-coupled with a time constant of 60 ms. The output power is (typically) -4 dBm for $f_{out} < 0.25 \times f_{REF}$.

A.4.4.4 – Filtering

Spurious sidebands in the STEL output are suppressed using a passive filter (pno. Mini-Circuits PLP-30). The filter lowpass response from DC-32 MHz (with less than one dB insertion loss) with a $f_{cutoff}(3dB) = 35$ MHz and a stop band > 20 dB of $47 - 61$ MHz Spur levels are limited by the dynamic linearity of the DAC. It is important to remember that when the output frequency exceeds 25% of the clock frequency, the second harmonic will be higher than the Nyquist frequency, 50% of the clock frequency. When this happens, the image of the harmonic at $f_{REF} - 2f_0$ becomes intrusive, since its frequency falls as the output

frequency rises, eventually crossing the fundamental output when its frequency crosses $f_{REF}/3$.

The filtered output is routed by coaxial cable to the front panel outputs with SMA bulkheads (nos. 3n+1 and 3n+2 where n = 0...7), for a total of sixteen outputs, of which 9 are used for the FFB in its present configuration.

A.4.4.5 – Digital Section and Power Supplies

The digital section is simple and primarily consists of address decoding circuitry used to program the STEL 1378A registers (see Fig A.19 pp. 254). The CPU programs the STELS to a desired frequency and phase-modulation (the latter is not used in the FFB application). See the STEL 1378A data sheets, FFB software manual and LO-board schematics for signal details and timing diagrams of the programming of the STEL 1378A. Attached to this document are the PAL files for the VME interface chips with reference designators U10, U11 and U14 (shift register). Connectors J1 and J2 interface with the VME address and data lines and the digital power is input to the board on standard +5 V VME lines. The +5 V analog, -5.2 V (analog & digital) and AGND connections are on the J3 connector.

A.4.4.6 – LO Board Specifications

Board dimensions:	Standard 9U VME
STEL 1378A mothercards:	5 cards numbered 0,1,2,3,7
LO-board VME address:	0xE1000000
Outputs:	9 pure tones
Output frequency range:	0-35 MHz
Advisable output frequency range:	12-32 MHz

Reference clock: 80 MHz at 0 dBm

Reference clock connectors are SMA bulkhead mounted on front panel nos. 3n+3 (n is number of the STEL)

Output connectors are SMA bulkhead mounted on front panel nos. 3n+1 and 3n+2. (n is number of the STEL)

A.4.4.7 – Errors in LO Board Layout

1. The ground inputs on the connector J3 are not connected to the ground plane on the board (An external wire on the solder side of the board makes a connection between J3 and U35(GND)).
2. The following inputs are not grounded: U7 (pins 18,19,20); U10 (pin 23); U11 (pins 9,10,13); (pins 13,9,10); U12, U13, U14 ,U15 & U16 (pins 1,19). All connection have been made via jumper wires on the solder side of the board.

A.4.5 THE VMEbus

The VMEbus is an industry standard for computers and digital boards that reside together in one crate or interconnected crates. It specifies the physical dimensions of the cage, the backplanes and connectors, as well as the signals and their electrical properties and timing. This appendix describes the VMEbus standard, as well as a simple slave interface that is used for the Flexible Filter Bank.

A.4.5.1 – The VMEbus System

The VMEbus is an industry standard for data exchange between boards in the same crate. It is housed on a backplane and defines a protocol for using it. The backplane specifications not only include physical dimensions, power supplies, slot separation, connectors and traces, but also the electrical properties of anything that connects to the backplane, the proper ways to request the bus, to respond to a request and to transfer data, and the timing of all electrical signals that have to do with the bus.

A.4.5.2 – The VMEbus Formats

The VMEbus comes in two sizes. The small VMEbus has a single backplane containing a 24-bit address bus, a 16-bit data bus and a series of control signals. There are actually 43 control signals on the VMEbus, besides the 24 address bits and 16 data bits. The extended VMEbus has the same 43 control signals, plus 32 address bits and 32 data bits. The extended VMEbus has a second backplane with an additional 8 bits of address and 16 bits of data. The extended VMEbus thus permits 32-bit data transfers over a 32-bit address space and is therefore faster and more versatile. In the FFB, the VME crate is A32:D32.

The pin layout of the J1/P1 and J2/P2 is shown in the tables in this section. P1 and P2 normally refer to the backplanes, while J1 and J2 refer to the connectors that plug into the backplanes. P1 is always the top backplane. The signals on

P1/P2 and J2/P2 connectors is shown in Tables 1 and 2. In triple-height crate used in the FFB there is a P3 backplane situated underneath P2, but this plane is entirely user-defined. One is free to use all 96 pins in each P3 connector for special purposes, as well as the 64 unused pins from the P2 backplane. In the FFB the P3 plane is used to transmit the analog power supplies +5 V, -5.2 V and the return analog ground (AGND).

Table A.2: Signal layout in the VMEbus P1 backplane. The signals that are active-low are marked with an asterisk. All control signals, address bits and data bits are high when undriven due to terminators on each end of the backplane. The power pin "+5 V STDBY" is sometimes used in crates that have a backup power supply, and provides alternative power to volatile memory in case of main power failure.

Pin #	Row A	Row B	Row C	Pin #
1	D00	BBSY*	D08	1
2	D01	BCLR*	D09	2
3	D02	ACFAIL*	D10	3
4	D03	BG0IN*	D11	4
5	D04	BG0OUT*	D12	5
6	D05	BG1IN*	D13	6
7	D06	BG1OUT*	D14	7
8	D07	BG2IN*	D15	8
9	GND	BG2OUT*	GND	9
10	SYSCLK	BG3IN*	SYSFAIL*	10
11	GND	BG3OUT*	BERR*	11
12	DS1*	BR0*	SYSRESET*	12
13	DS0*	BR1*	LWORD*	13
14	WRITE*	BR2*	AM5	14
15	GND	BR3*	A23	15

16	DTACK*	AM0	A22	16
17	GND	AM1	A21	17
18	AS*	AM2	A20	18
19	GND	AM3	A19	19
20	IACK*	GND	A18	20
21	IACKIN*	SERCLK	A17	21
22	IACKOUT*	SERDAT*	A16	22
23	AM4	GND	A15	23
24	A07	IRQ7*	A14	24
25	A06	IRQ6*	A13	25
26	A05	IRQ5*	A12	26
27	A04	IRQ4*	A11	27
28	A03	IRQ3*	A10	28
29	A02	IRQ2*	A09	29
30	A01	IRQ1*	A08	30
31	−12V	+5V STDBY	+12V	31
32	+5V	+5V	+5V	32

Pin #	**Row A**	**Row B**	**Row C**	**Pin #**

Table A.3: All control signals are in the P1 backplane. The P2 backplane has the address and data pins for the A32:D32 extension, as well as additional power and ground pins for the larger boards. Rows A and C are not used in the extension and are free for the user to define and use. For the same reason, however, the pins in rows A and C not only are not terminated in commercial backplanes, but they are not connected from slot to slot through the backplane. All signals in rows A and C are FFB defined and not in typewriter font.

Pin #	**Row A**	**Row B**	**Row C**	**Pin #**
1	SD1	+5V	FB1	1
2	SD2	GND	FB2	2
3	SD3	RESERVED	FB3	3

4	SD4	A24	FB4	4
5	SD5	A25	FB5	5
6	SD6	A26	FB6	6
7	SD7	A27	–	7
8	SD8	A28	–	8
9	SD9	A29	–	9
10	SD10	A30	–	10
11	SD11	A31	–	11
12	SD12	GND	–	12
13	SD13	+5V	–	13
14	SD14	D16	–	14
15	SD15	D17	–	15
16	SD16	D18	–	16
17	–	D19	–	17
18	–	D20	–	18
19	–	D21	–	19
20	–	D22	–	20
21	–	D23	–	21
22	–	GND	–	22
23	–	D24	–	23
24	–	D25	–	24
25	–	D26	–	25
26	–	D27	–	26
27	–	D28	–	27
28	–	D29	–	28
29	–	D30	–	29
30	ACLK	D31	–	30
31	–	GND	–	31
32	FCLK	+5V	–	32
Pin #	**Row A**	**Row B**	**Row C**	**Pin #**

A.4.5.3 – Termination

Most control signals are active-low, and terminators on each end of the backplane ensure that the undriven signals remain high. For address and data signals the termination is not absolutely necessary, since the board driving these lines drives them low or high as required. However, having the terminators gives the lines the proper impedance and reduces signal reflections and bouncing. For control signals, on the other hand, the terminators are always necessary. Signals like interrupt or bus requests could cause havoc if they were left floating.

Each signal is terminated with a 330 ohm resitor to +5 Volt and a 470 ohm resitor to GND, on each side of the backplane. The resulting undriven level is +2.94 V, which is TTL logic HIGH. Similar termination can be achieved with a 220 ohm/330 ohm resistor pair.

A.4.5.4 – Master and Slave Interfaces

A VMEbus read or write cycle is always initiated by a bus master. The board that responds to a read or write request is called a bus slave. In general there is just one master per VME cage, it resides in one slot (the leftmost slot), and it is a computer where the control programs run. The rest of the slots tend to be filled with slave boards that respond to requests from the computer, or master.

There are two ways for the other boards to initiate a bus cycle. They can either become bus master, or they can issue an interrupt request and wait for the computer to initiate a bus cycle in response to the interrupt request. Becoming a bus master gives the requesting board total control of the bus, but it also requires a more sophisticated hardware interface. Issuing interrupts is relatively simple, which makes a simple slave interface with interrupt capabilities pretty easy to implement. Such a slave interface will have most of the functionality needed in standard applications.

There exist commercial VMEbus interface chips for user developed boards. These usually consist of one or two large chips (PGA packages, 81-149 pins) and

their main function is to make the VMEbus transparent to a Motorola 68k bus. They are very convenient if the board being built is controlled by a 68k-type microprocessor, but if not, they are of no help whatsoever. Not only they are expensive and difficult to use, but they take a lot of real estate on the board and they have more power than is needed.

As a result we have developed our own VMEbus interface. It performs the minimal functions of a VMEbus slave, but can issue interrupts. All in all it fits in four small programmable logic arrays and is cheap and easy to use. The working of the VMEbus interface is easily understood by going through the logic equations in the VMEbus PAL files.

A.4.5.5 – Read and Write Cycles

All VMEbus read and write cycles are initiated by the bus master, usually a computer. The master first requests the bus and then initiates the bus cycle. "Requesting the bus" means nothing else but waiting until the bus is idle and then grabbing it. "Initiating the cycle" means putting an address on the address bus, driving the address strobes low, and waiting for a response from the slave board that is being addressed.

In the case of a write cycle, the master puts data on the data bus as well, and drives the data strobes. In a read cycle, it expects the responding slave to drive the data lines, but the master drives the data strobes itself because they convey information to the slave, such as the data bus width.

The terminology of read and write cycles is always from the point of view of the bus master. Thus, a write cycle always implies that the master drives both the address and the data buses, while a read cycle implies that the master drives the address bus but reads data from the slave, who must drive the data bus.

In either case, the master must wait until the slave acknowledges the transaction. This acknowledgment is given after the slave has put the data in the bus (in the case of a read cycle), or when it has read the data from the bus (in a write

cycle). If an acknowledgment does not come from any of the boards on the bus, a timeout will occur and the master will generate a bus error. This normally results in a program aborting in the master, or a software trap being executed if one has been set.

A.4.5.6 – Hardware Interrupts

Issuing an interrupt allows an otherwise passive board to ask for attention from the bus master. The bus master, normally a computer, responds to the interrupt request and performs the necessary actions. The actions depend on the application, but in general they involve reading data from the slave that issued the interrupt. Peripherals like keyboards issue an interrupt for every keystroke, in which case the computer stops what it is doing, reads the character code from the keyboard, and then returns to what it was doing.

Each interrupt is characterized by two numbers: the interrupt level and the interrupt vector number. The interrupt level (a number between 0 and 7) establishes the urgency of the interrupt with respect to other interrupts. A low level interrupt will be serviced only when no interrupts of equal or higher level are pending. On the other hand, a high level interrupt will preempt a low level interrupt. Only when the higher level interrupt has been serviced will the lower level interrupt continue to be serviced.

The interrupt vector number (a number between 0 and 255) tells the computer which software subroutine to execute in order to service the interrupt. The service routine for a keyboard interrupt might just read a character code from the keyboard, then exit. There can be one or more service routines linked to a vector number, as well as none at all. If there are no entries for a vector number in the interrupt vector table (each entry being a pointer to a service routine), then no action is taken. But at the same time, no error is generated since the only effect of the dummy interrupt was a small waste of time.

If several service routines are attached to a vector number, then each one of them is polled in turn until one of them acknowledges the interrupt. In case none of the routines claim the interrupt then no action is taken and that interrupt is declared serviced.

In the FFB, only the buffer-board issues interrupts. For more details, refer to the buffer-board section.

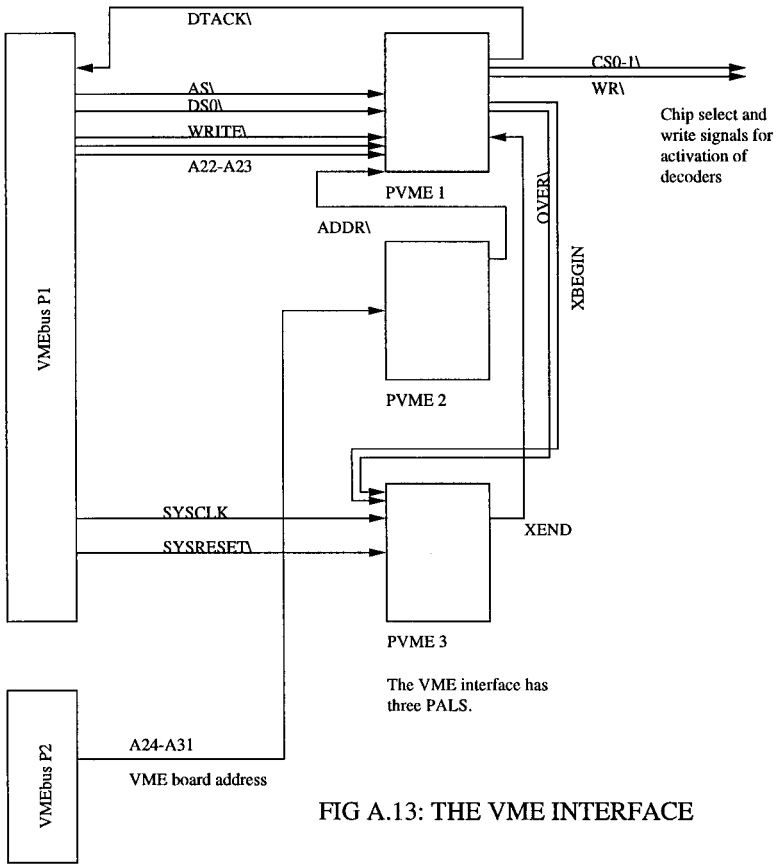

FIG A.13: THE VME INTERFACE

A.4.5 PERIPHERAL MEMORY VME ADDRESSES

Peripheral memory on any slave board is addressed by the computer by the bit-wise logical combination BOARD-ADDR.or.MEMORY-ADDR. Listed below are all memory locations in the FFB.

Master Control Board Locations

CNTL-BOARD	0xEF000000
CNTL-RESET	0x00000000
CNTL-ARM	0x00080000
CNTL-6PPM	0x00100000
CNTL-SCLK	0x00200000
CNTL-ACLK	0x00280000
CNTL-FCLK	0x00300000
CNTL-CLKLD	0x00380000

Buffer Board Locations

BUF-BOARD	0xEB000000
BUF-RESET	0x00000000
BUF-WR-CTRL	0x00040000
BUF-WR-DATA	0x00080000
BUF-TCLK	0x000C0000
BUF-RD-DATA	0x00900000
BUF-RD-CTR	0x00940000

Buffer Board Control Register

BUF-BITS-08	0x00000000
BUF-BITS-16	0x00000001
BUF-BITS-32	0x00000003
BUF-EDGE-UP	0x00000000
BUF-EDGE-DOWN	0x00000004

BUF-TEST-ON	0x00000008
BUF-DELAY-000	0x00000000
BUF-DELAY-060	0x00000000
BUF-DELAY-120	0x00000000
BUF-DELAY-180	0x00000000
BUF-DELAY-240	0x00000000
BUF-DELAY-300	0x00000000
BUF-DELAY-360	0x00000000
BUF-DELAY-420	0x00000000
BUF-DELAY-480	0x00000000
BUF-CLK-TCLK	0x00000000
BUF-CLK-01-MUS	0x00000100
BUF-CLK-02-MUS	0x00000200
BUF-CLK-04-MUS	0x00000300
BUF-CLK-08-MUS	0x00000400
BUF-CLK-16-MUS	0x00000500
BUF-T0-ON	0x00001000
BUF-T1-ON	0x00002000
BUF-T2-ON	0x00004000
BUF-T3-ON	0x00008000

Filter Board Locations

FILT-BOARDS	0xE[2...9]0000000
FILT-VAMP	0x000[0...7]00000
FILT-VIDEO	0x00180000
FILT-PTHDAC	0x00080000
FILT-PTHLTCH	0x00100000
FILT-NTHDAC	0x00300000
FILT-NTHLTCH	0x00380000
FILT-SDEN	0x00200000

FILT-SCLK	0x00280000

LO Board Locations

STEL-BOARD	0xE1000000
STEL-NOOL	0x00000010
STEL-NCO1	0x00000000
STEL-NCO1	0x00000040
STEL-PHREG0	0x00000000
STEL-PHREG1	0x00000004
STEL-PHREG2	0x00000008
STEL-PHREG3	0x0000000C
STEL-ARST	0x00000030
STEL-HOP	0x00002000

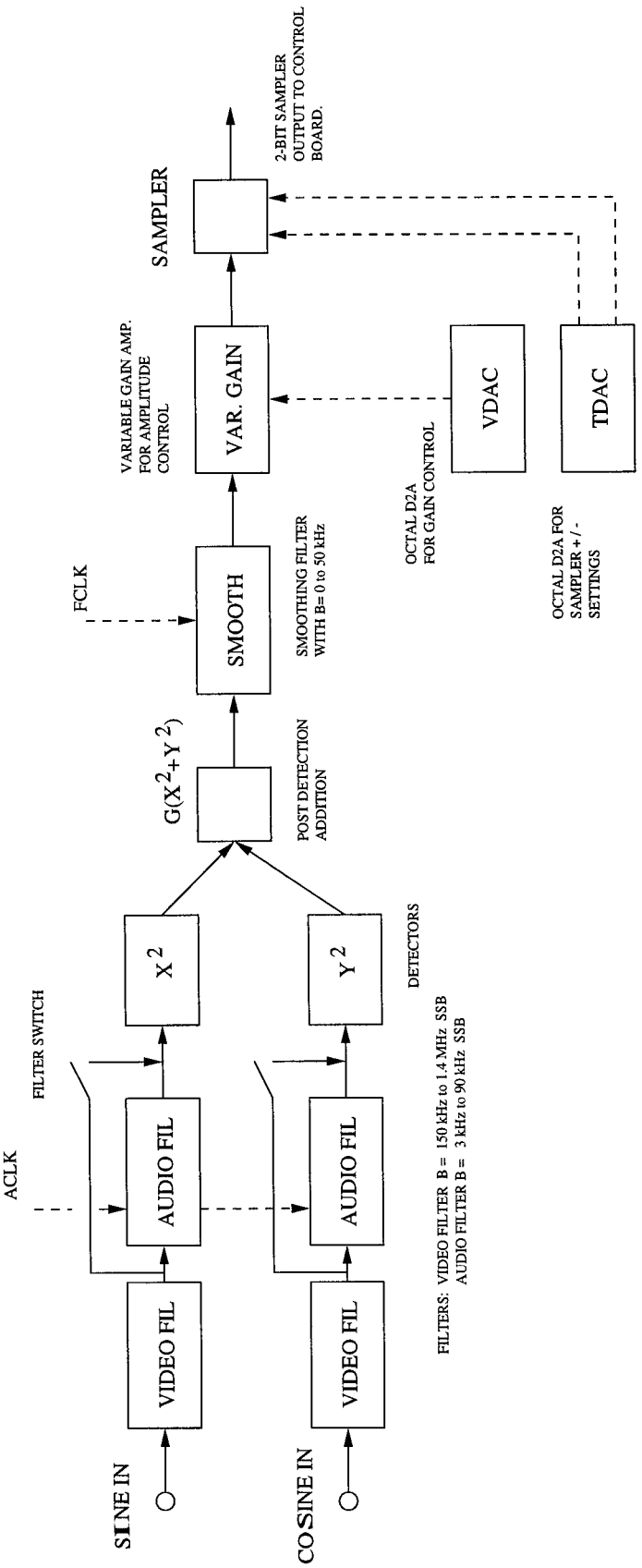

FIG A.14: SCHEMATIC OF A SINGLE FILTER BOARD CHANNEL

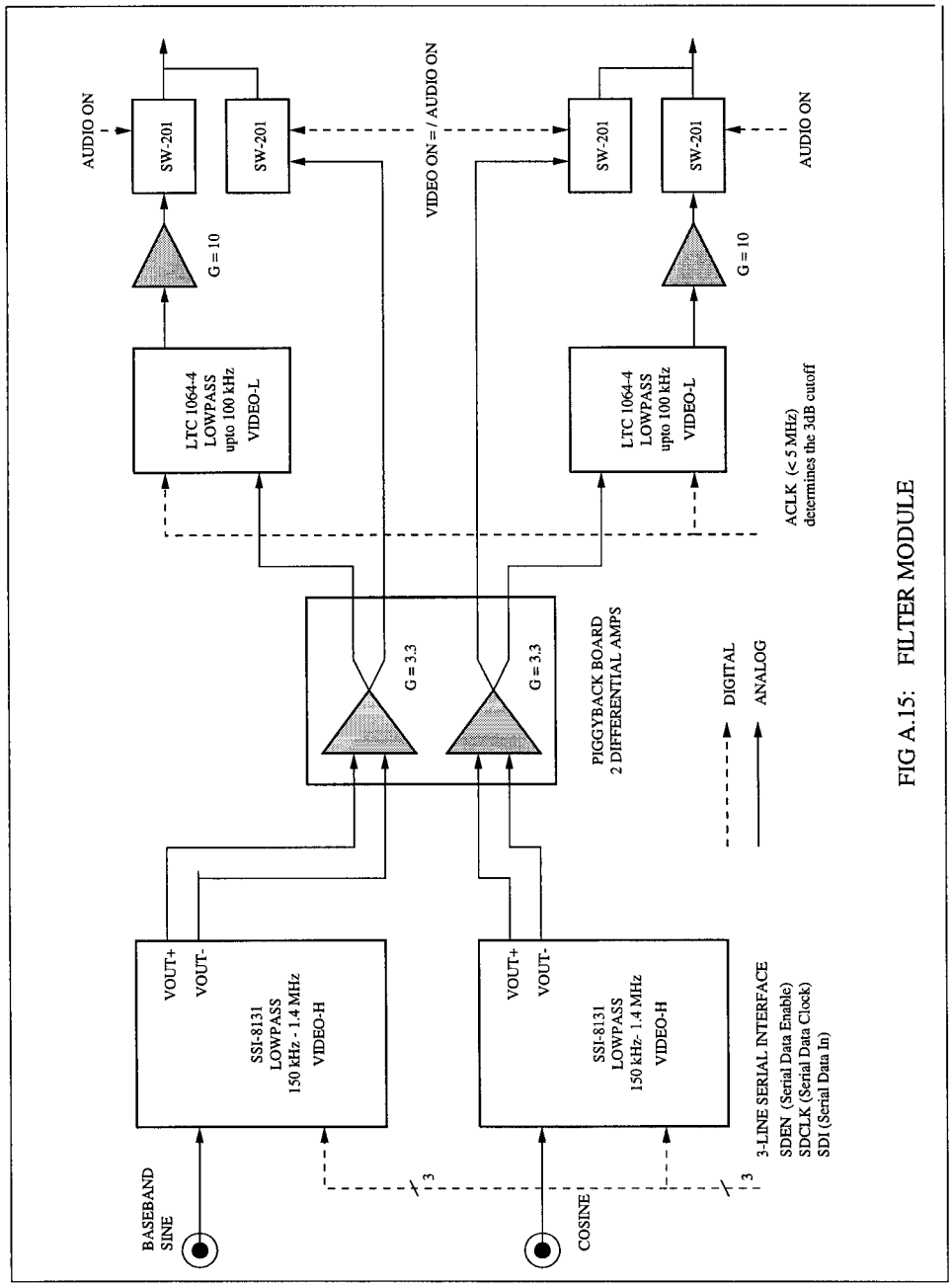

FIG A.15: FILTER MODULE

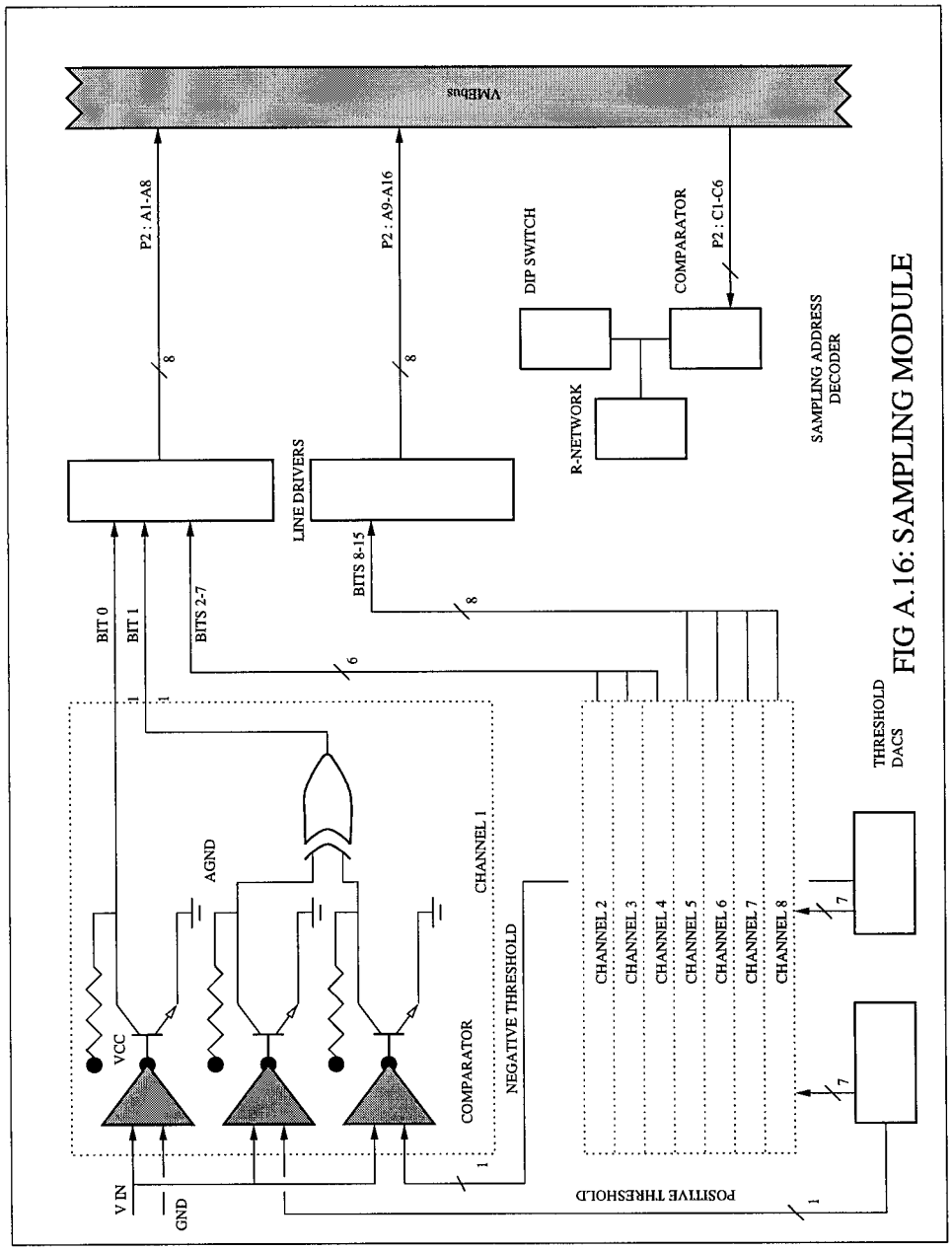

FIG A.16: SAMPLING MODULE

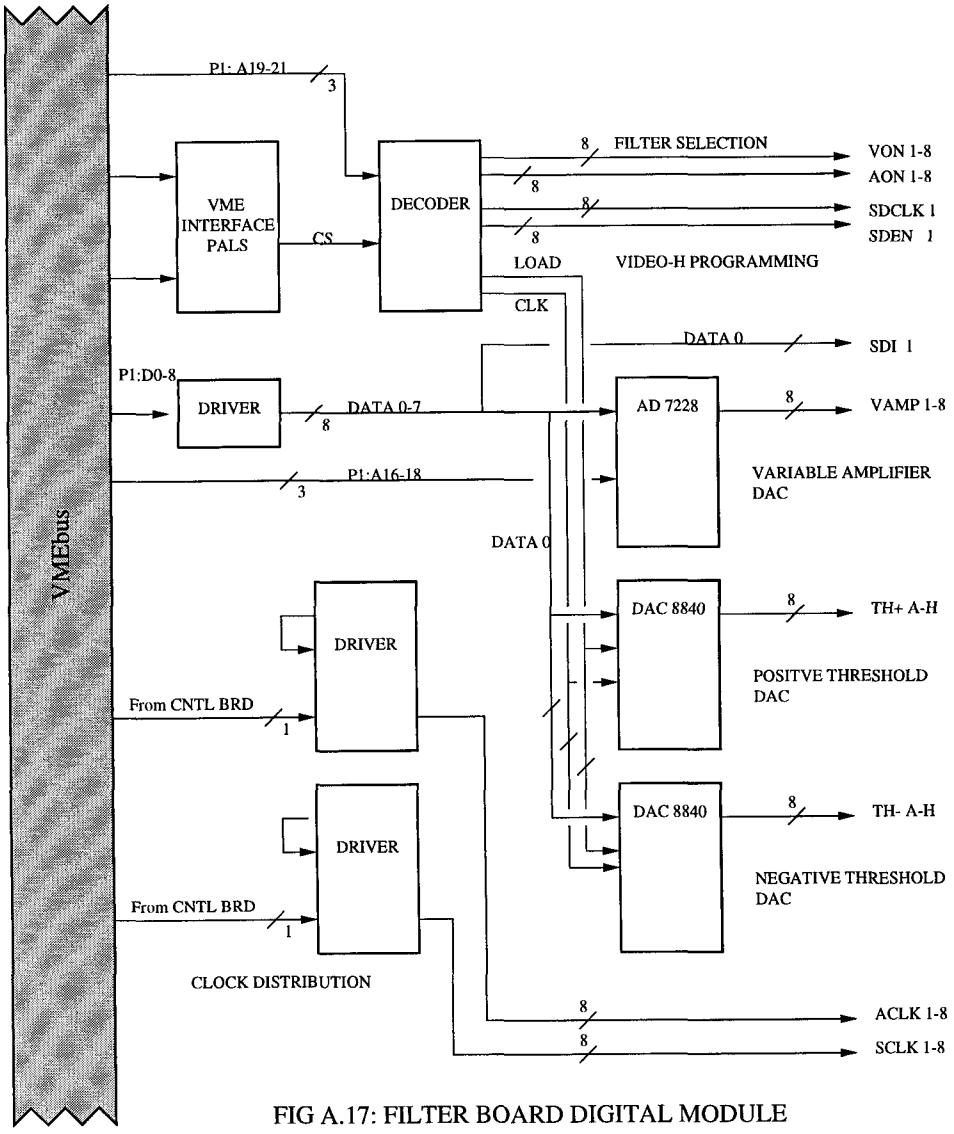

FIG A.17: FILTER BOARD DIGITAL MODULE

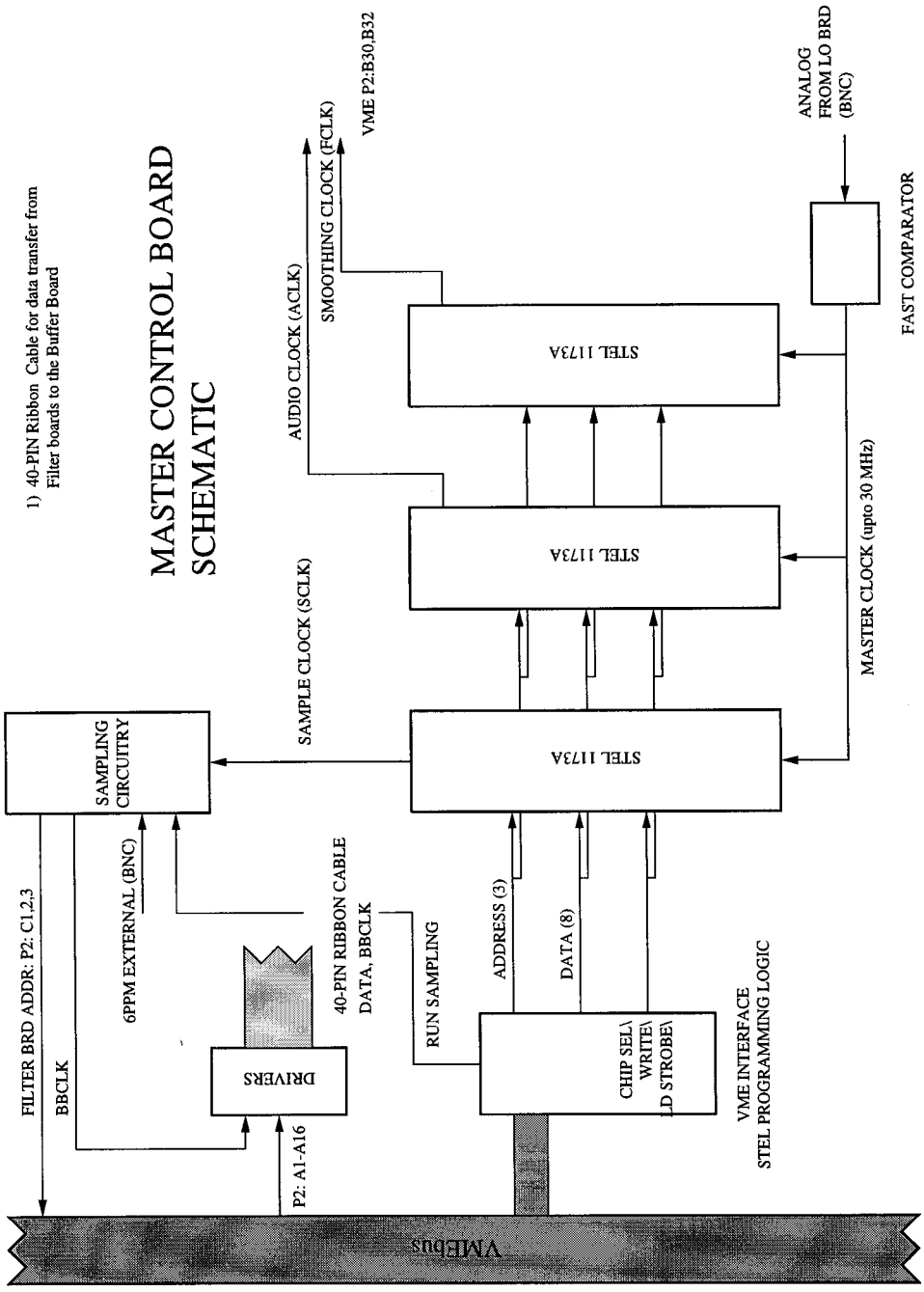
MASTER CONTROL BOARD
SCHEMATIC
1) 40-PIN Ribbon Cable for data transfer from
Filter boards to the Buffer Board
ANALOG
FROM LO BRD
(BNC)
VME P2:B30,B32
SMOOTHING CLOCK (FCLK)
AUDIO CLOCK (ACLK)
FAST COMPARATOR
STEL 1173A
STEL 1173A
STEL 1173A
MASTER CLOCK (upto 30 MHz)
SAMPLE CLOCK (SCLK)
SAMPLING
CIRCUITRY
FILTER BRD ADDR: P2: C1,2,3
BBCLK
6PPM EXTERNAL (BNC)
DRIVERS
40-PIN RIBBON CABLE
DATA, BBCLK
RUN SAMPLING
ADDRESS (3)
DATA (8)
CHIP SEL\
WRITE\
LD STROBE\
VME INTERFACE
STEL PROGRAMMING LOGIC
P2: A1-A16
VMEBUS

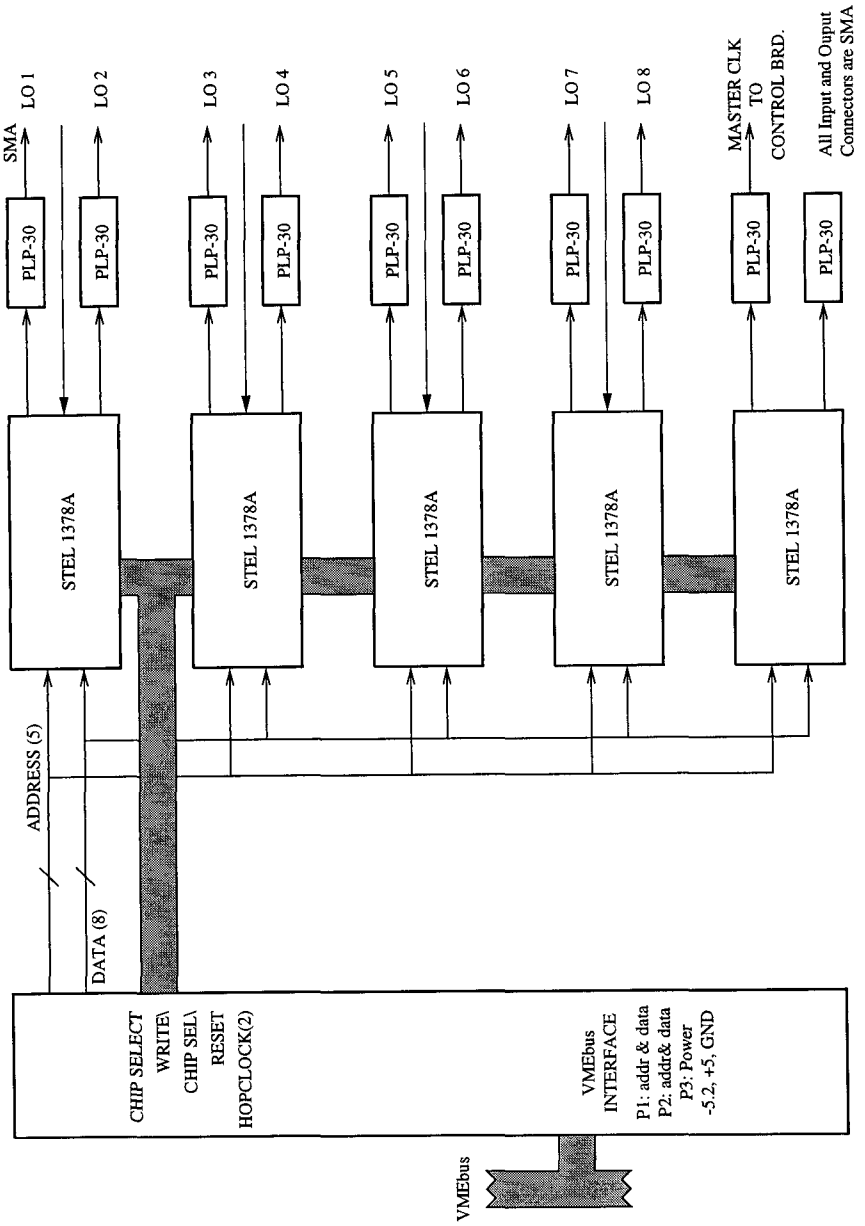

FIG A.19: LO-BOARD BLOCK DIAGRAM

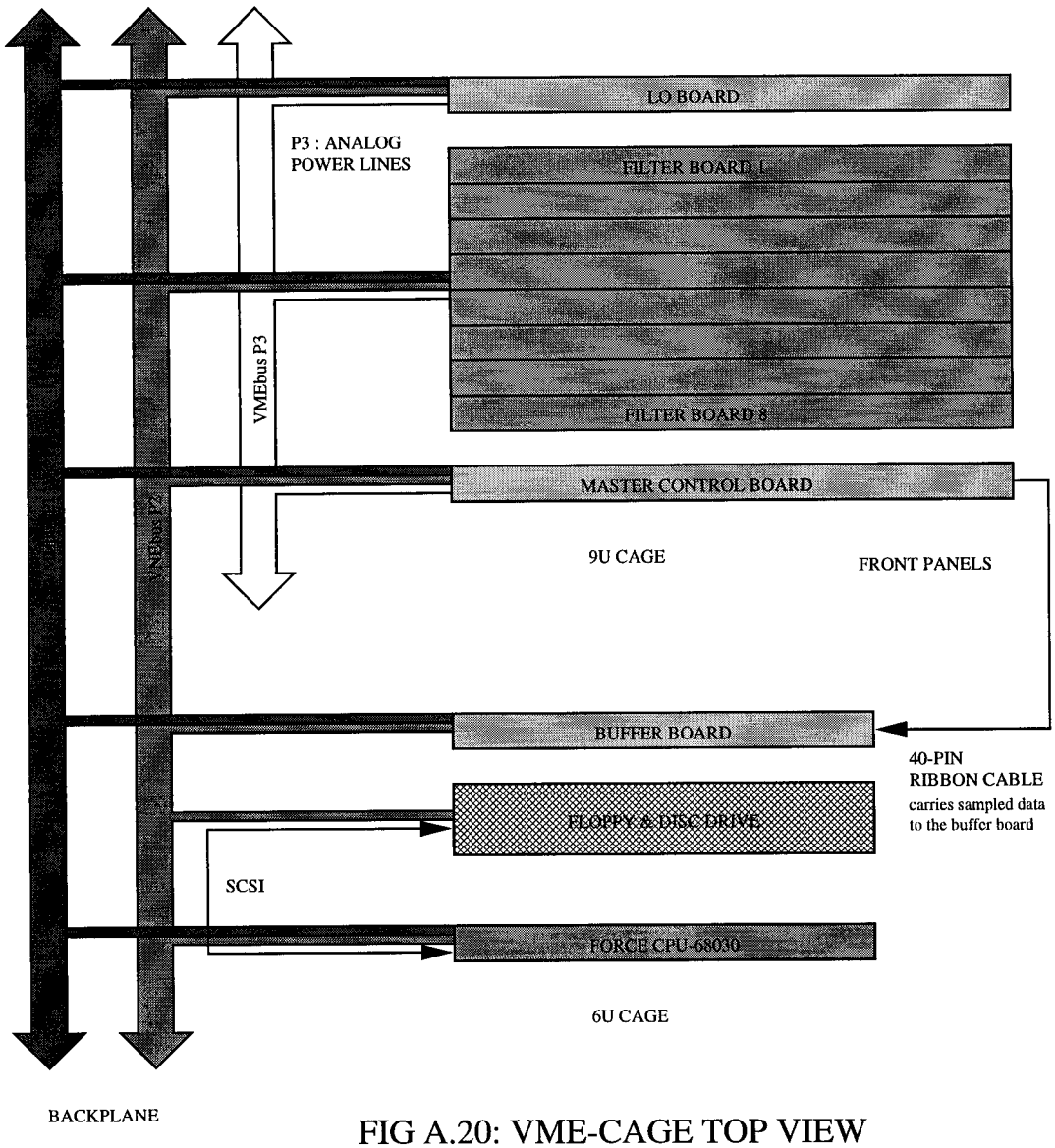

FIG A.20: VME-CAGE TOP VIEW

Top cross-section of the hybrid 6U/9U VME cage used in the FFB. The computer, system disk and buffer board occupy the 6U slots. A LO board, master control board and eight filter boards are in the 9U slots. VME backplanes P1 and P2 carry VME and user defined signals. VME backplane P3 carries analog powers and grounds to the 9U boards.

A.5 FFB CIRCUIT SCHEMATICS

1. Flexible Filter Bank Top Level
2. LO-Splitter Schematic
3. Filter-Board Top Level
4. Filter-Board Filter Module
5. Filter-Board Channel
6. Filter-Board Digital Section
7. Filter-Board Piggyback Board
8. Master-Control-Board
9. Buffer-Board VME Interface
10. Buffer-Board Schematics
11. Buffer-Board Schematics
12. Buffer-Board Schematics
13. LO-Board Schematic

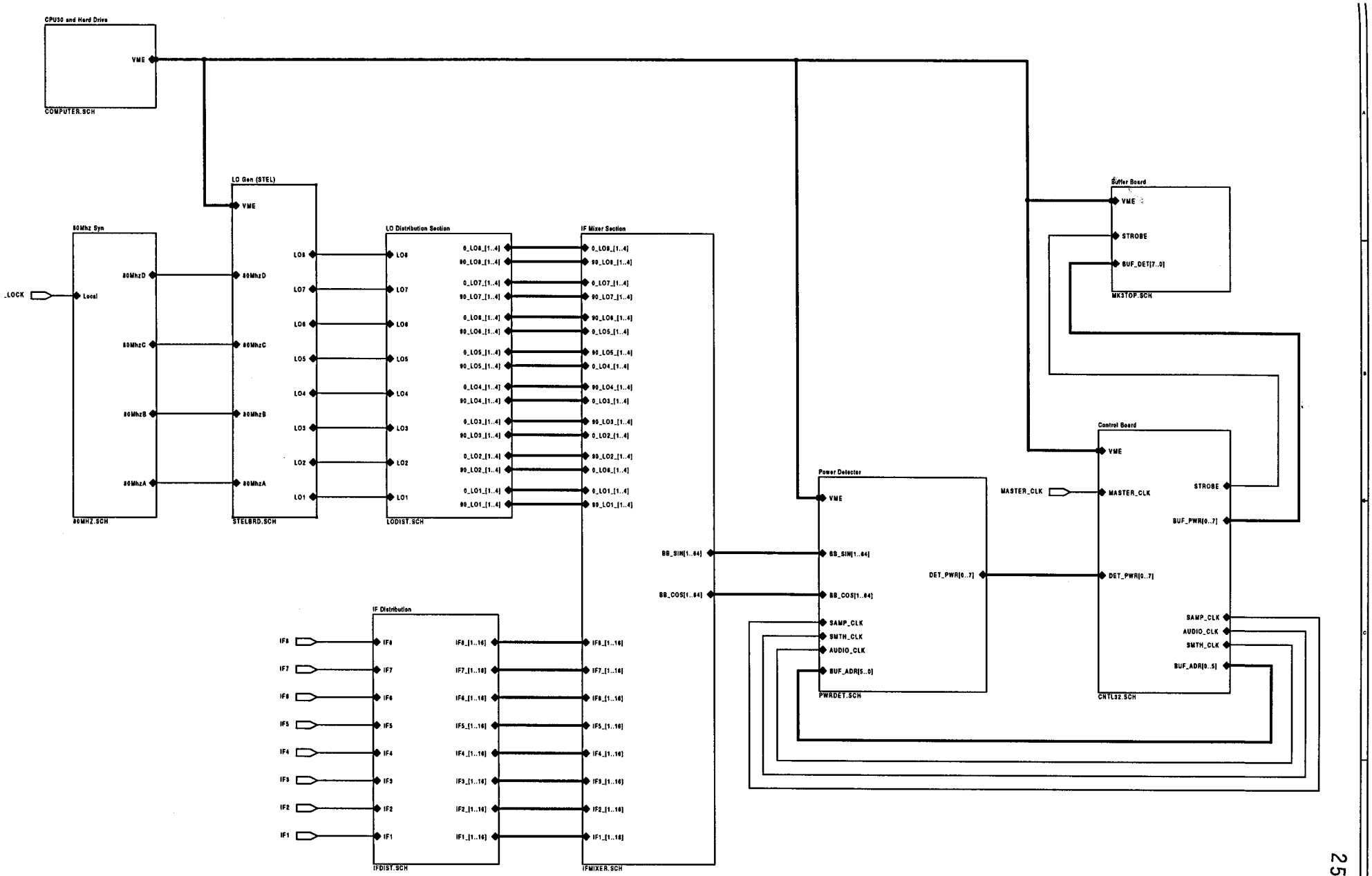

257

CALIFORNIA INSTITUTE OF TECHNOLOGY

1201 E. California Blvd,
Pasadena, California 91125

John K Yamasaki

Title: FLEXIBLE FILTER BANK TOP LEVEL

Size: C | Document Number: FFB94.SCH | Rev:

Date: Friday, May 10, 1996 | Sheet 0 of 0

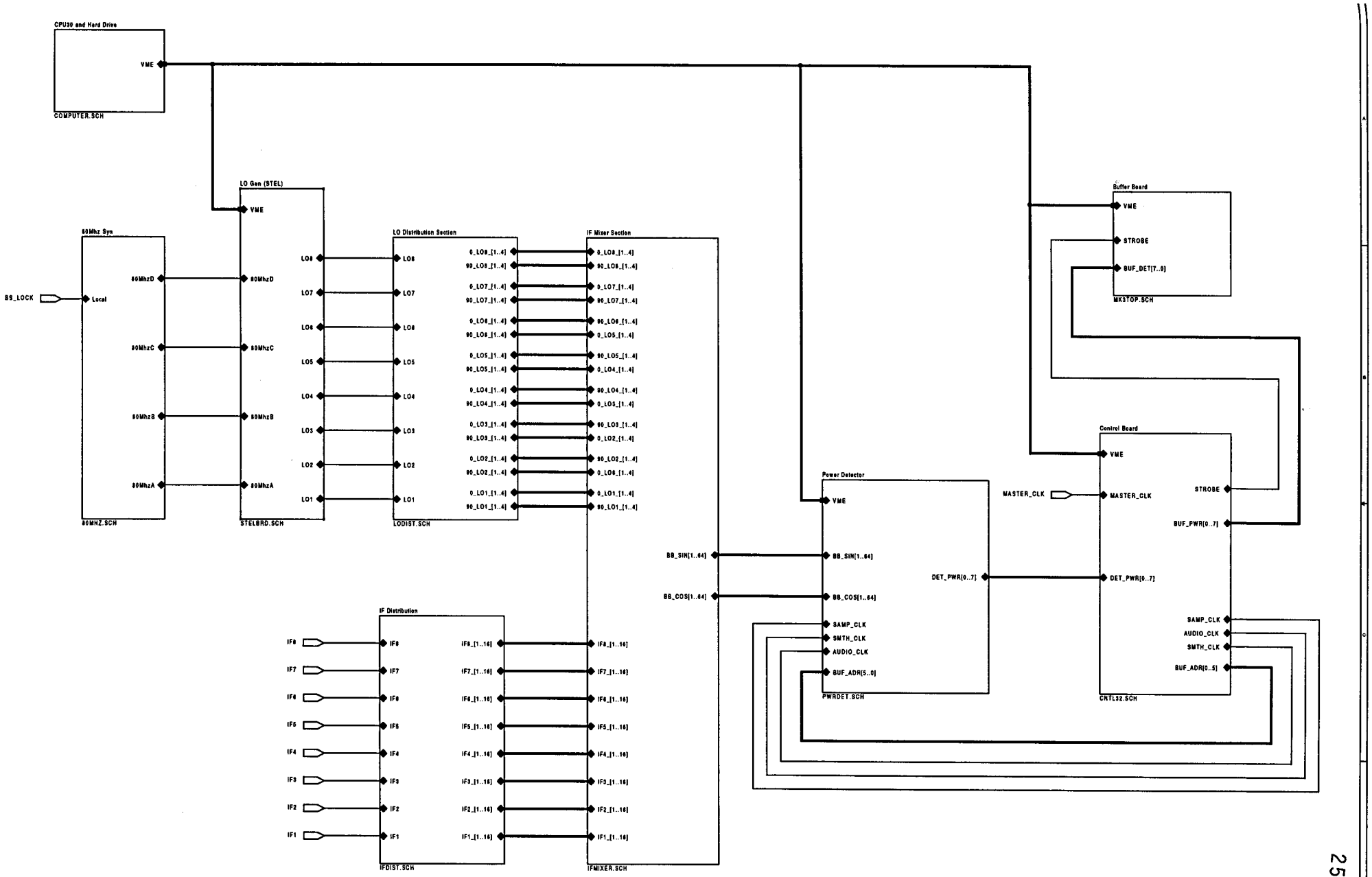

257

CALIFORNIA INSTITUTE OF TECHNOLOGY

1201 E. California Blvd,
Pasadena, California 91125

John K Yamasaki

Title: FLEXIBLE FILTER BANK TOP LEVEL

Size: C | Document Number: FFB94.SCH | Rev:

Date: Friday, May 10, 1996 | Sheet 0 of 0

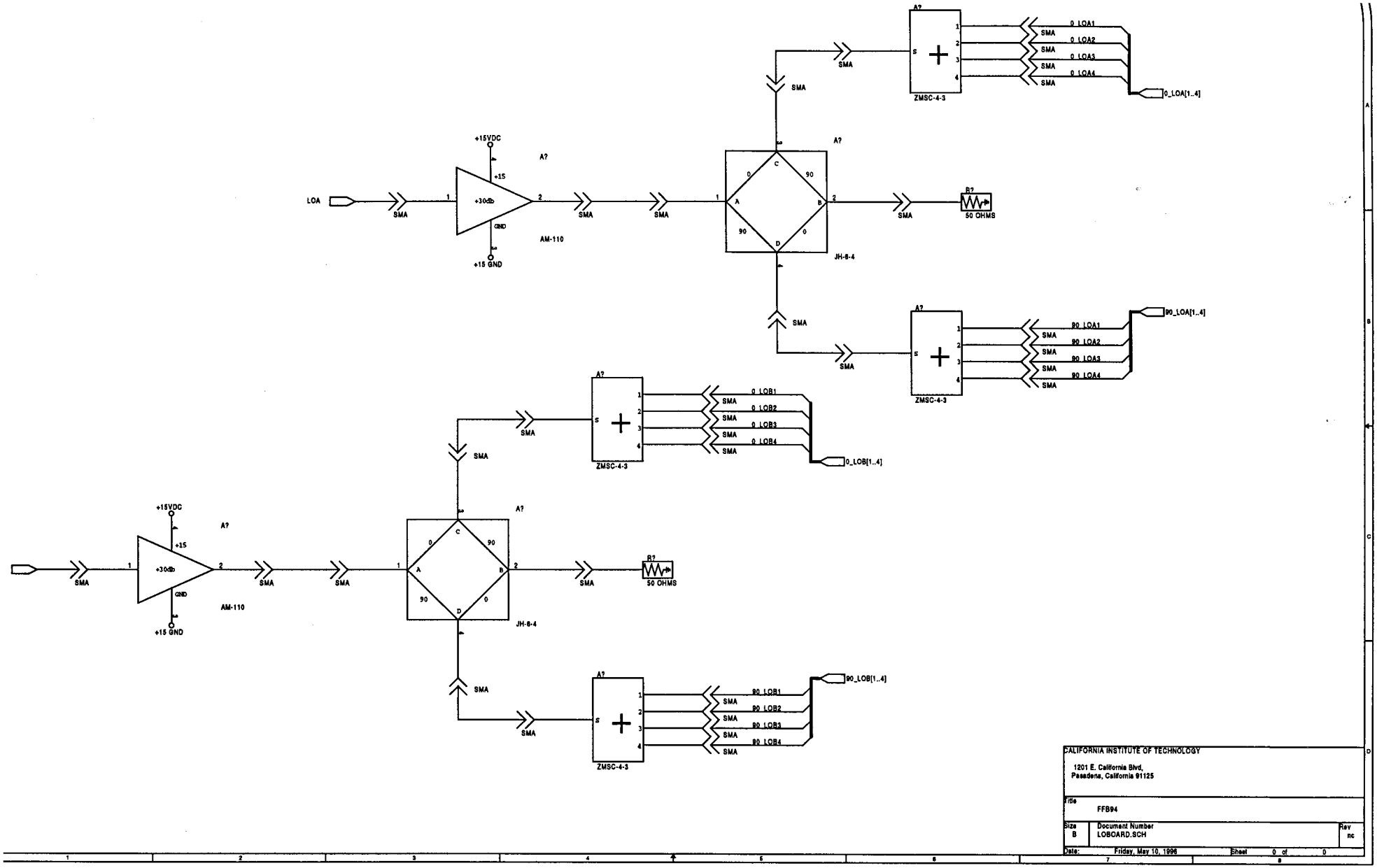
LOA
SMA
+15VDC
+15
+30db
GND
+15 GND
AM-110
A?
JH-8-4
50 OHMS
R?
ZMSC-4-3
0_LOA1
0_LOA2
0_LOA3
0_LOA4
0_LOA[1..4]
90_LOA1
90_LOA2
90_LOA3
90_LOA4
90_LOA[1..4]
0_LOB1
0_LOB2
0_LOB3
0_LOB4
0_LOB[1..4]
90_LOB1
90_LOB2
90_LOB3
90_LOB4
90_LOB[1..4]
CALIFORNIA INSTITUTE OF TECHNOLOGY
1201 E. California Blvd,
Pasadena, California 91125
Title
FFB94
Size
B
Document Number
LOBOARD.SCH
Rev
nc
Date:
Friday, May 10, 1996
Sheet
0 of
0

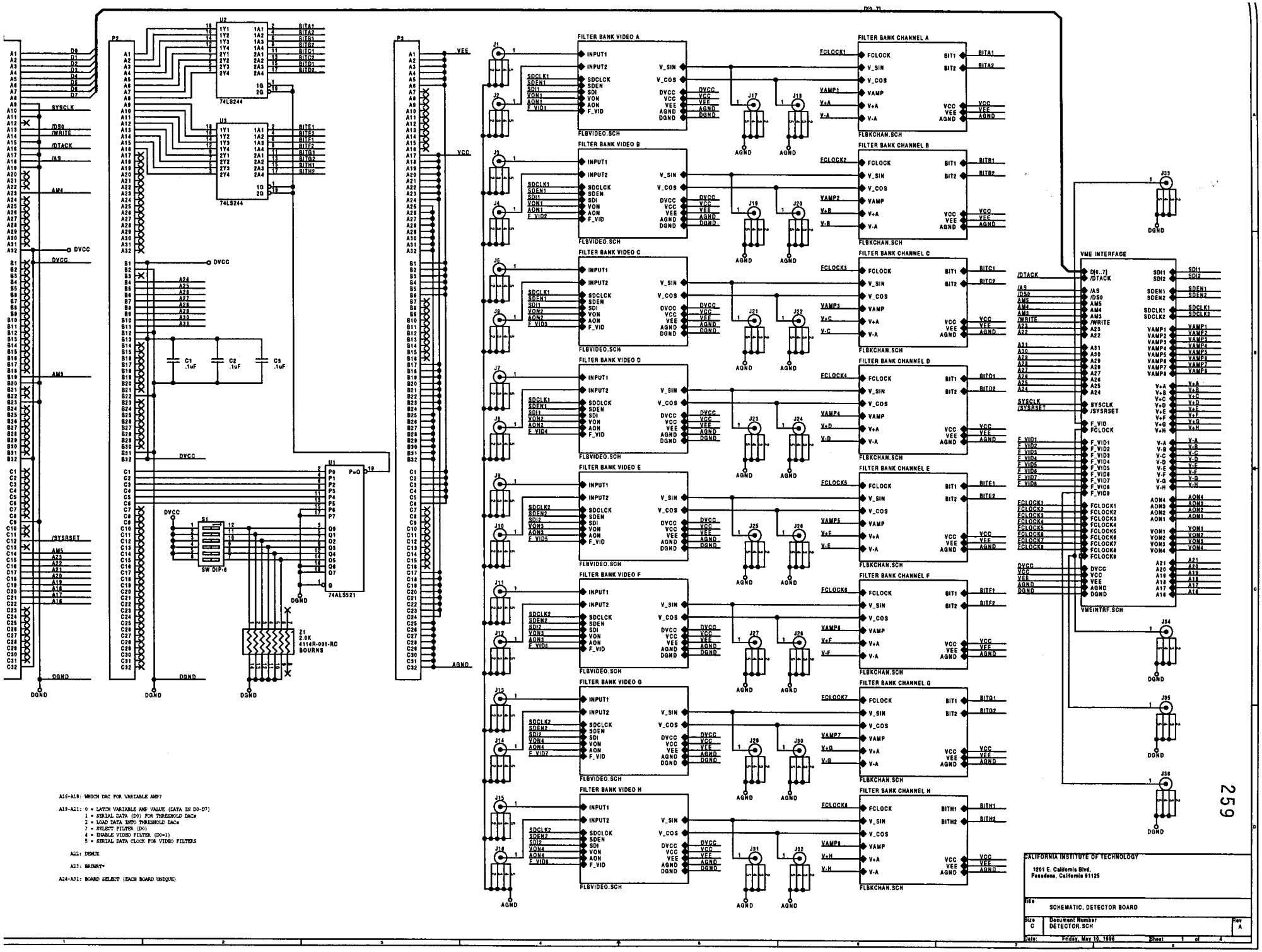
FILTER BANK VIDEO A
FILTER BANK VIDEO B
FILTER BANK VIDEO C
FILTER BANK VIDEO D
FILTER BANK VIDEO E
FILTER BANK VIDEO F
FILTER BANK VIDEO G
FILTER BANK VIDEO H
FLBVIDEO.SCH
FILTER BANK CHANNEL A
FILTER BANK CHANNEL B
FILTER BANK CHANNEL C
FILTER BANK CHANNEL D
FILTER BANK CHANNEL E
FILTER BANK CHANNEL F
FILTER BANK CHANNEL G
FILTER BANK CHANNEL H
FLBKCHAN.SCH
VME INTERFACE
VMEINTRF.SCH
74LS244
74ALS521
SW DIP-8
A16-A18: WHICH DAC FOR VARIABLE AMP?
A19-A21: 0 = LATCH VARIABLE AMP VALUE (DATA IN D0-D7)
1 = SERIAL DATA (D0) FOR THRESHOLD DACs
2 = LOAD DATA INTO THRESHOLD DACs
3 = SELECT FILTER (D0)
4 = ENABLE VIDEO FILTER (D0=1)
5 = SERIAL DATA CLOCK FOR VIDEO FILTERS
A22: DEMUX
A23: BRDWR*
A24-A31: BOARD SELECT (EACH BOARD UNIQUE)
CALIFORNIA INSTITUTE OF TECHNOLOGY
1201 E. California Blvd.
Pasadena, California 91125
SCHEMATIC, DETECTOR BOARD
Document Number DETECTOR.SCH
Friday, May 10, 1996

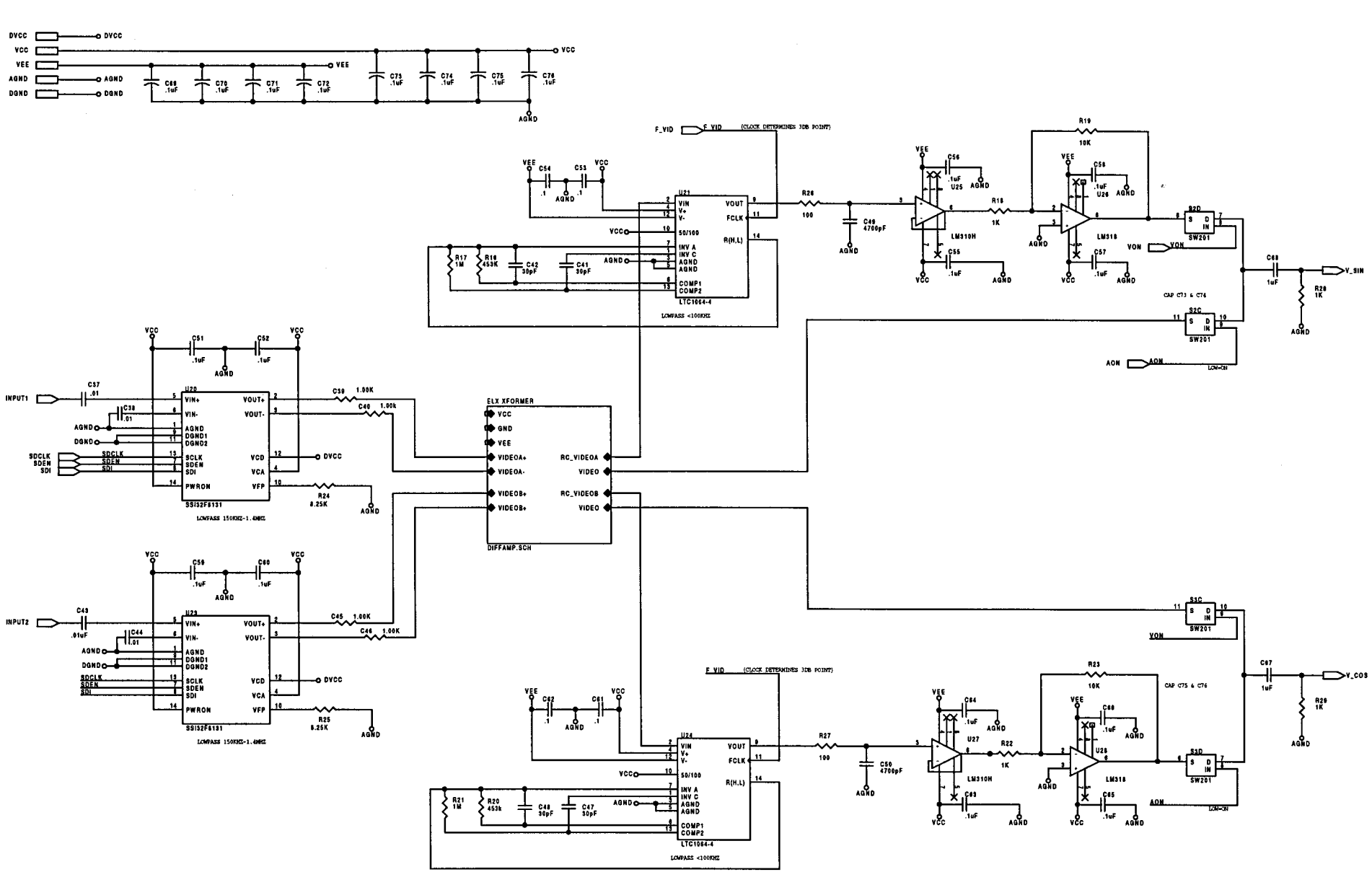

260

CALIFORNIA INSTITUTE OF TECHNOLOGY
1201 E. California Blvd,
Pasadena, California 91125

Title: SCHEMATIC, FILTER BANK VIDEO

Size: C | Document Number: FLBVIDEO | Rev: A

Date: Friday, May 10, 1996 | Sheet 3 of 4

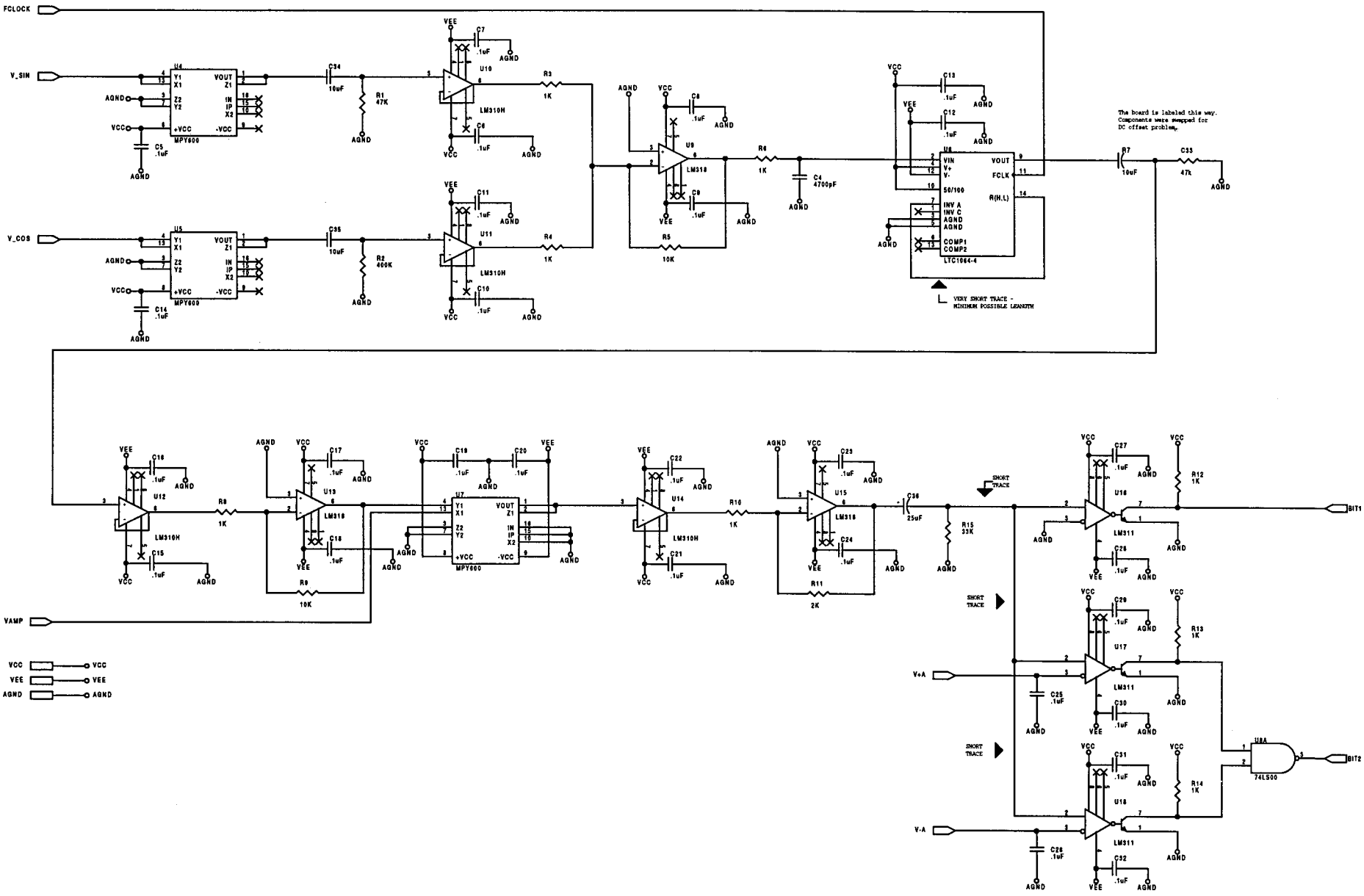

261

CALIFORNIA INSTITUTE OF TECHNOLOGY

1201 E. California Blvd.
Pasadena, California 91125

Title: SCHEMATIC, FILTER BANK CHANNEL

Size: C | Document Number: FLBKCHAN | Rev: A

Date: Friday, May 10, 1996 | Sheet 2 of 4

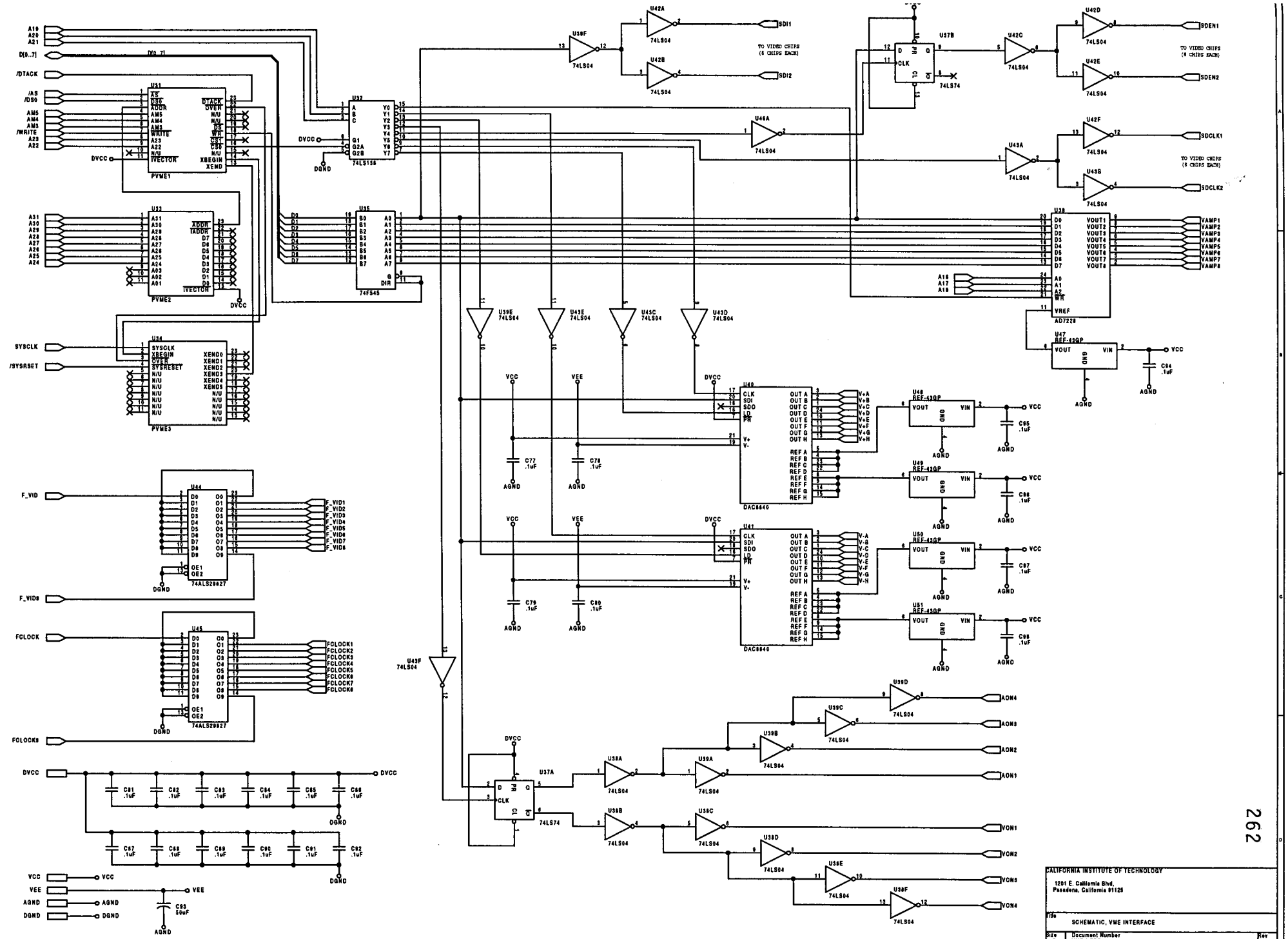

FITTER CLOCK SECTION (One per board)

CALIFORNIA INSTITUTE OF TECHNOLOGY
1201 E. California Blvd.
Pasadena, California 91125

Title: SCHEMATIC, VME INTERFACE

Size: C | Document Number: VMEINTRF | Rev:

Date: Friday, May 10, 1996 | Sheet 4 of 4

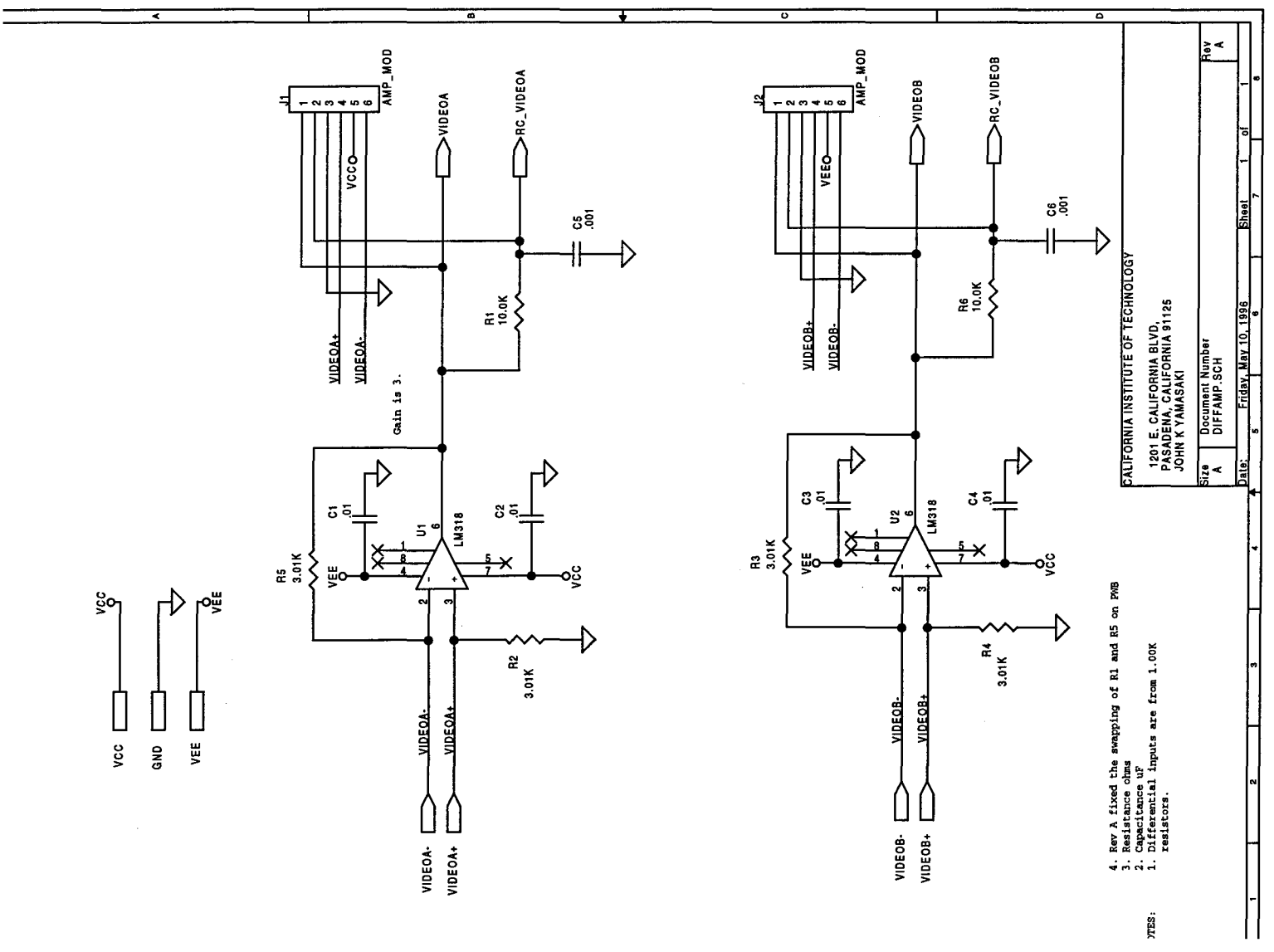
VCC
GND
VEE
VCC
VEE
J1
AMP_MOD
VCCO
VIDEOA
RC_VIDEOA
C5
.001
R1
10.0K
VIDEOA+
VIDEOA-
Gain is 3.
C1
.01
U1
LM318
C2
.01
R5
3.01K
VEE
VCC
R2
3.01K
VIDEOA-
VIDEOA+
J2
AMP_MOD
VEEO
VIDEOB
RC_VIDEOB
C6
.001
R6
10.0K
VIDEOB+
VIDEOB-
C3
.01
U2
LM318
C4
.01
R3
3.01K
R4
3.01K
VIDEOB-
VIDEOB+
CALIFORNIA INSTITUTE OF TECHNOLOGY
1201 E. CALIFORNIA BLVD,
PASADENA, CALIFORNIA 91125
JOHN K YAMASAKI
Size
A
Document Number
DIFFAMP.SCH
Rev
A
Date:
Friday, May 10, 1996
Sheet
1
of
1
NOTES:
1. Differential inputs are from 1.00K resistors.
2. Capacitance uF
3. Resistance ohms
4. Rev A fixed the swapping of R1 and R5 on PWB

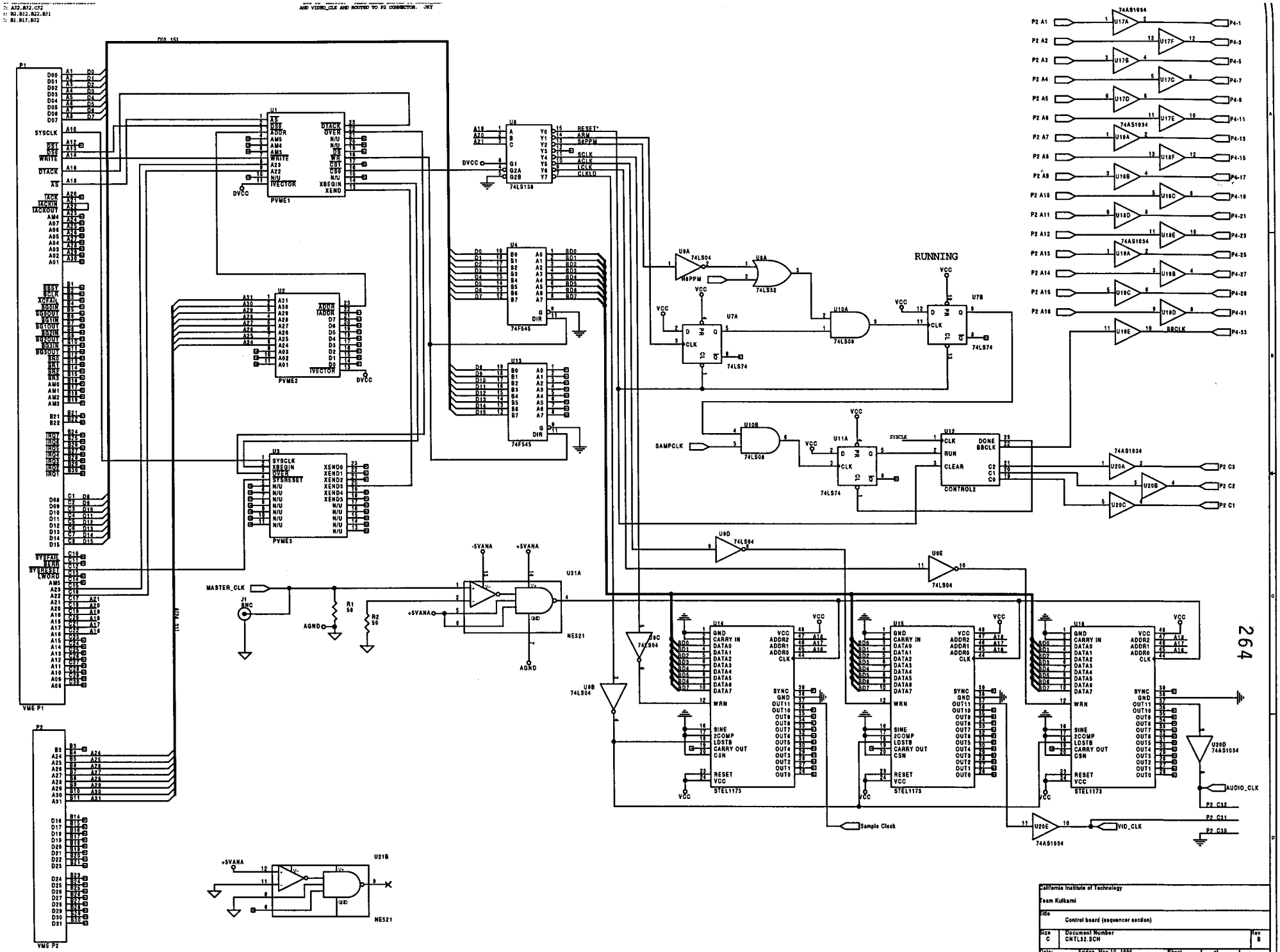
RUNNING
MASTER_CLK
SAMPCLK
Sample Clock
VID_CLK
AUDIO_CLK
California Institute of Technology
Team Kulkarni
Control board (sequencer section)
Document Number CNTL32.SCH
Friday, May 10, 1996
264

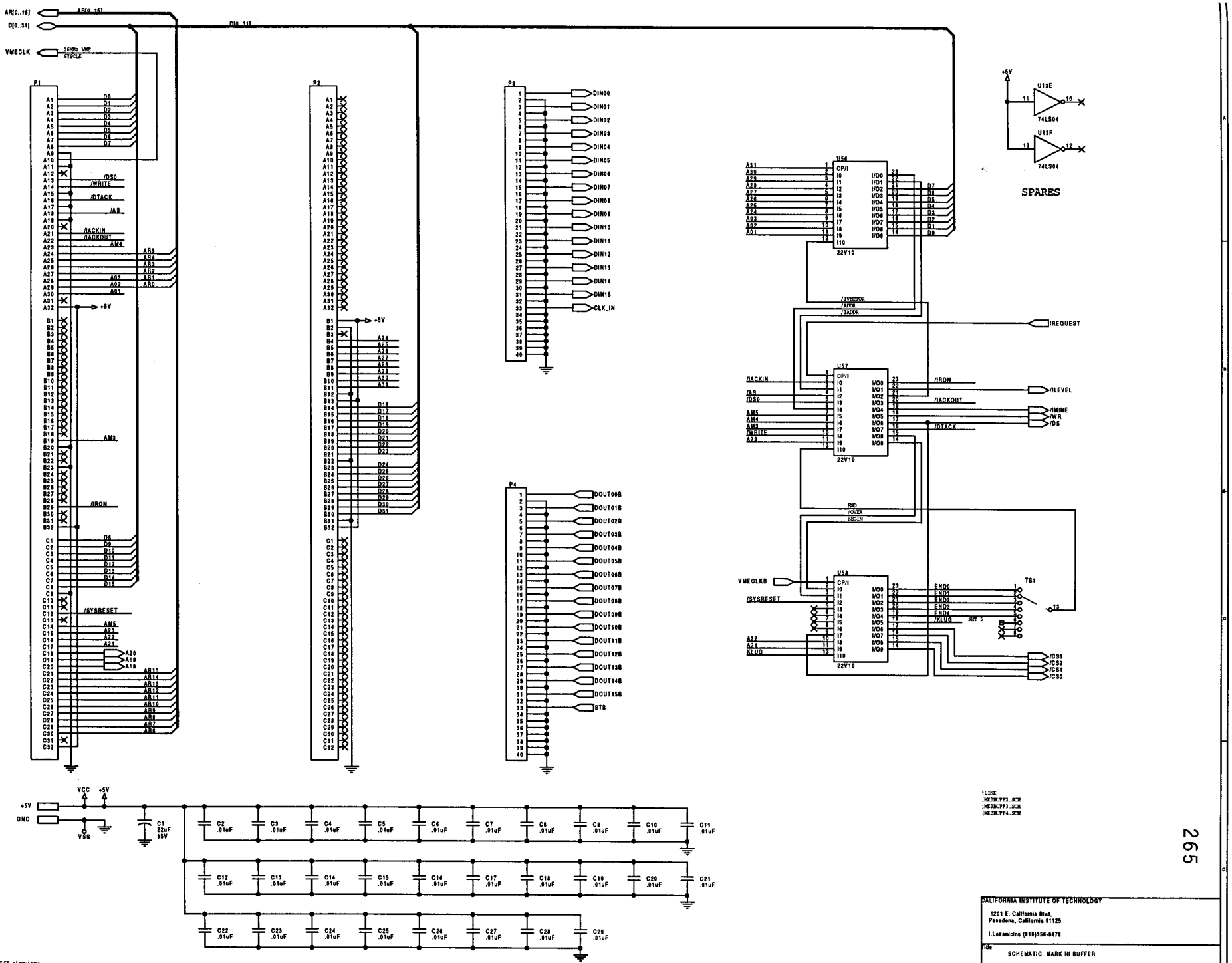

2. REV B: Added the VPULSE circuitry.
1. REV B: Incorporated the "KLUG" fix for the slipping of data words.

265

CALIFORNIA INSTITUTE OF TECHNOLOGY
1201 E. California Blvd,
Pasadena, California 91125
f.Lozenoins (818)356-8478

Title: SCHEMATIC, MARK III BUFFER

Size: C | Document Number: MK3BUFFR-01 | Rev: A

Date: Friday, May 10, 1996 | Sheet 2 of 5

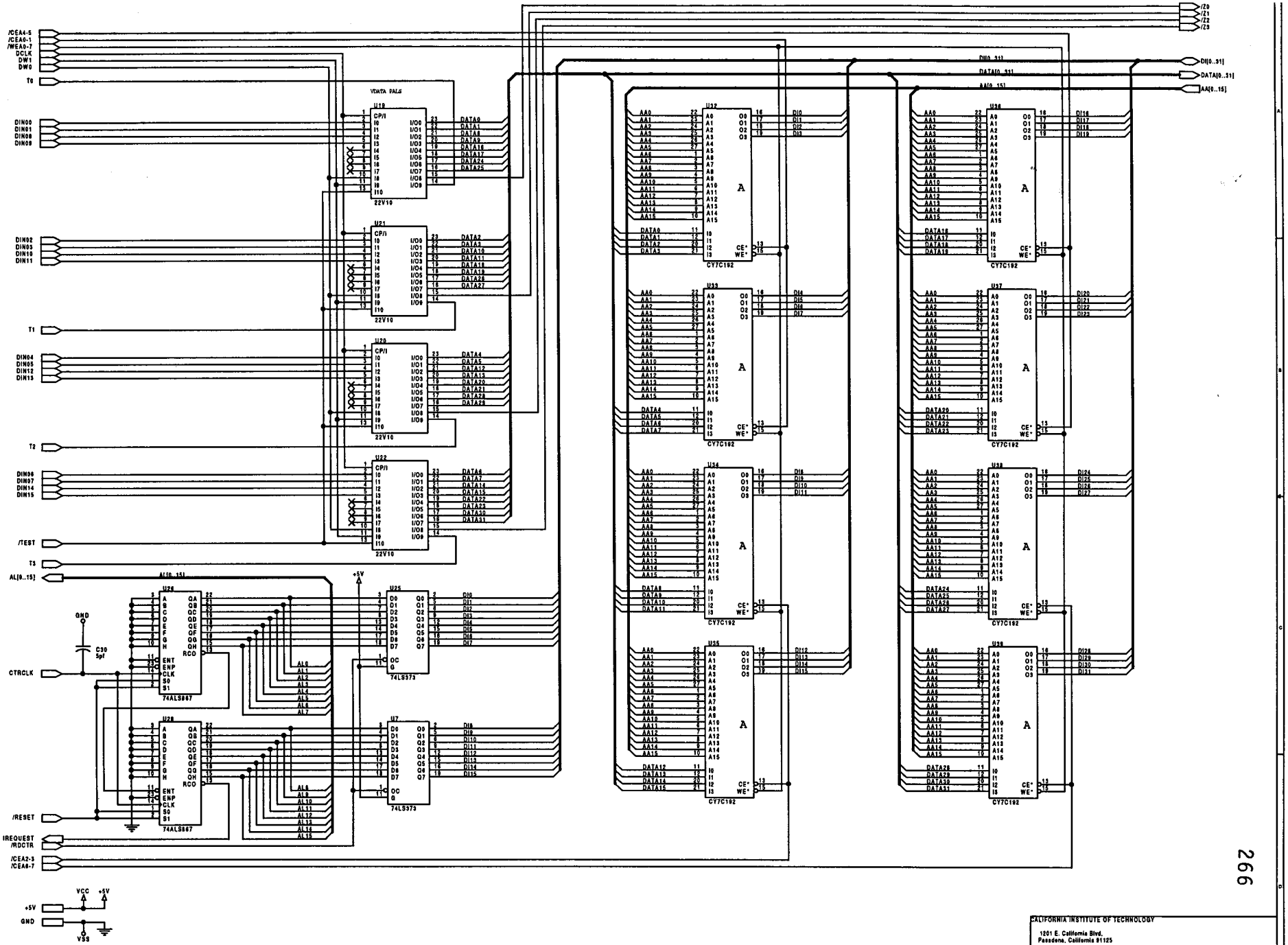

266

CALIFORNIA INSTITUTE OF TECHNOLOGY		
1201 E. California Blvd. Pasadena, California 91125 I.Lozenicins (818)356-6478		
Title: SCHEMATIC, MARK III BUFFER		
Size: C	Document Number: MK3BUFFR-02	Rev: A
Date: Friday, May 10, 1996	Sheet 3 of 5	

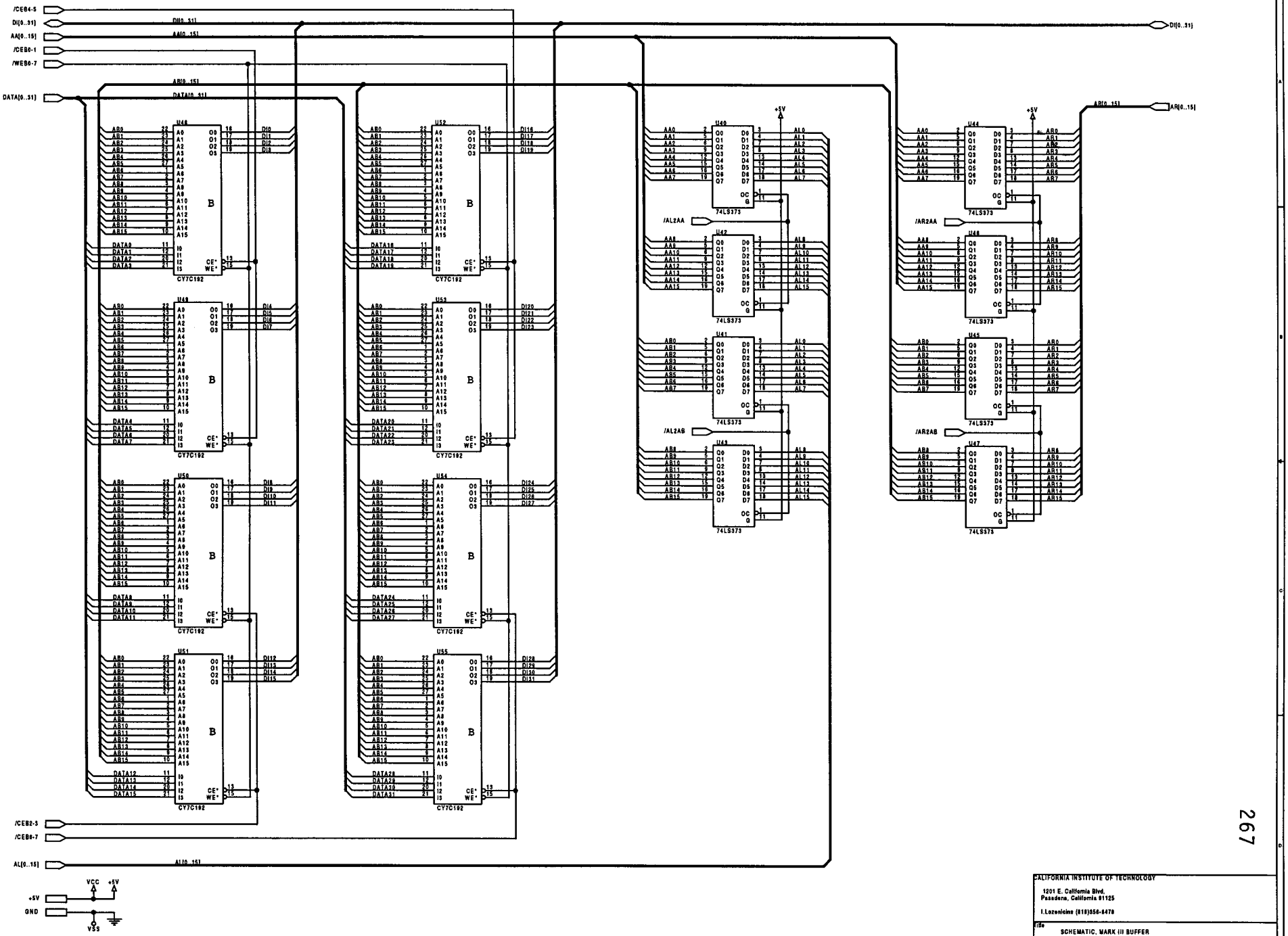

CALIFORNIA INSTITUTE OF TECHNOLOGY
1201 E. California Blvd.
Pasadena, California 91125
I.Lozenicins (818)356-6478

Title: SCHEMATIC, MARK III BUFFER

Size: C | Document Number: MK3BUFFR-03 | Rev: A

Date: Friday, May 10, 1996 | Sheet 4 of 5

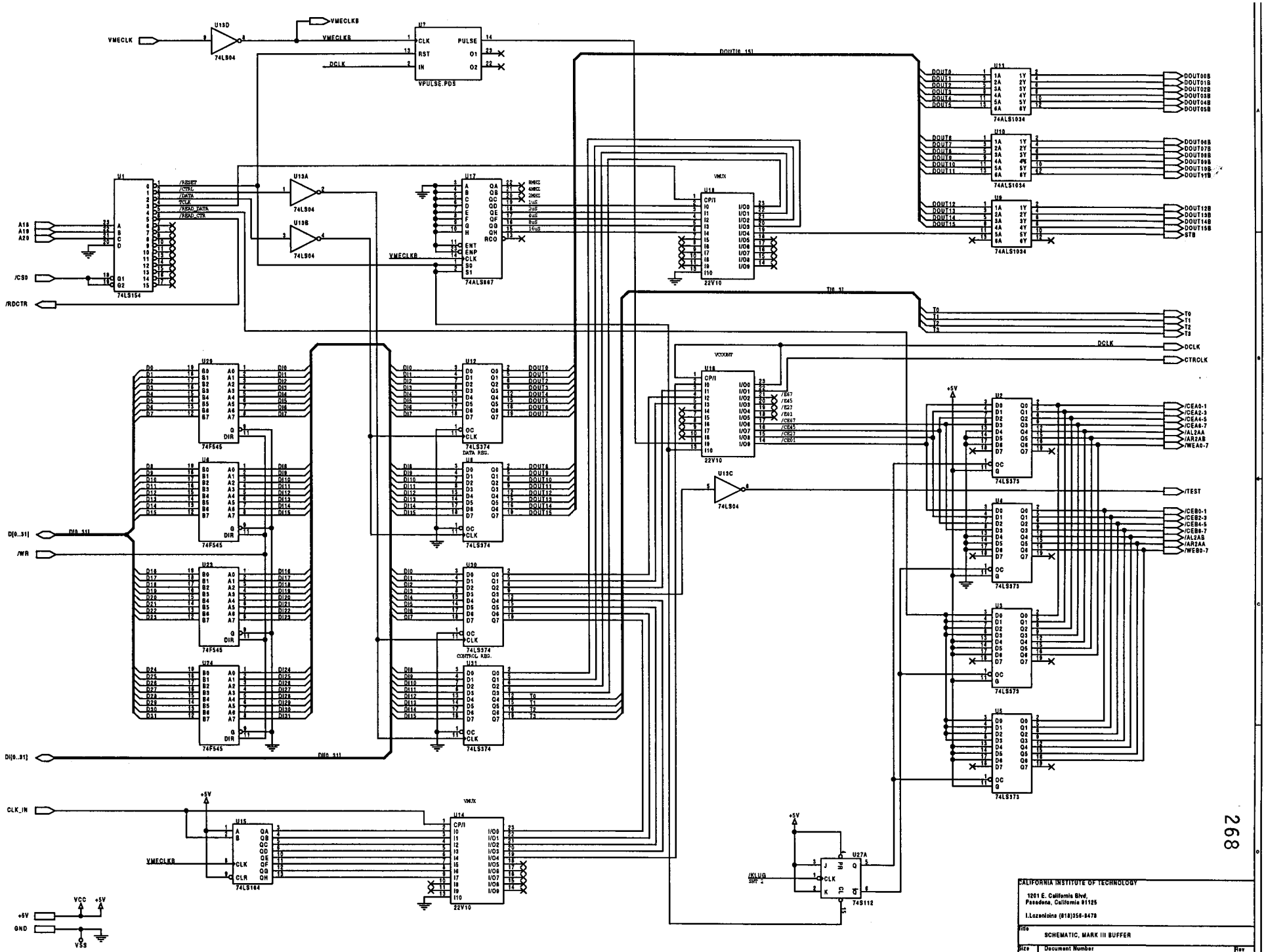

CALIFORNIA INSTITUTE OF TECHNOLOGY
1201 E. California Blvd.
Pasadena, California 91125
I.Lozenicine (818)356-8478

Title: SCHEMATIC, MARK III BUFFER

Size: C | Document Number: MK3BUFFR-04 | Rev: A

Date: Friday, May 10, 1996 | Sheet 5 of 5

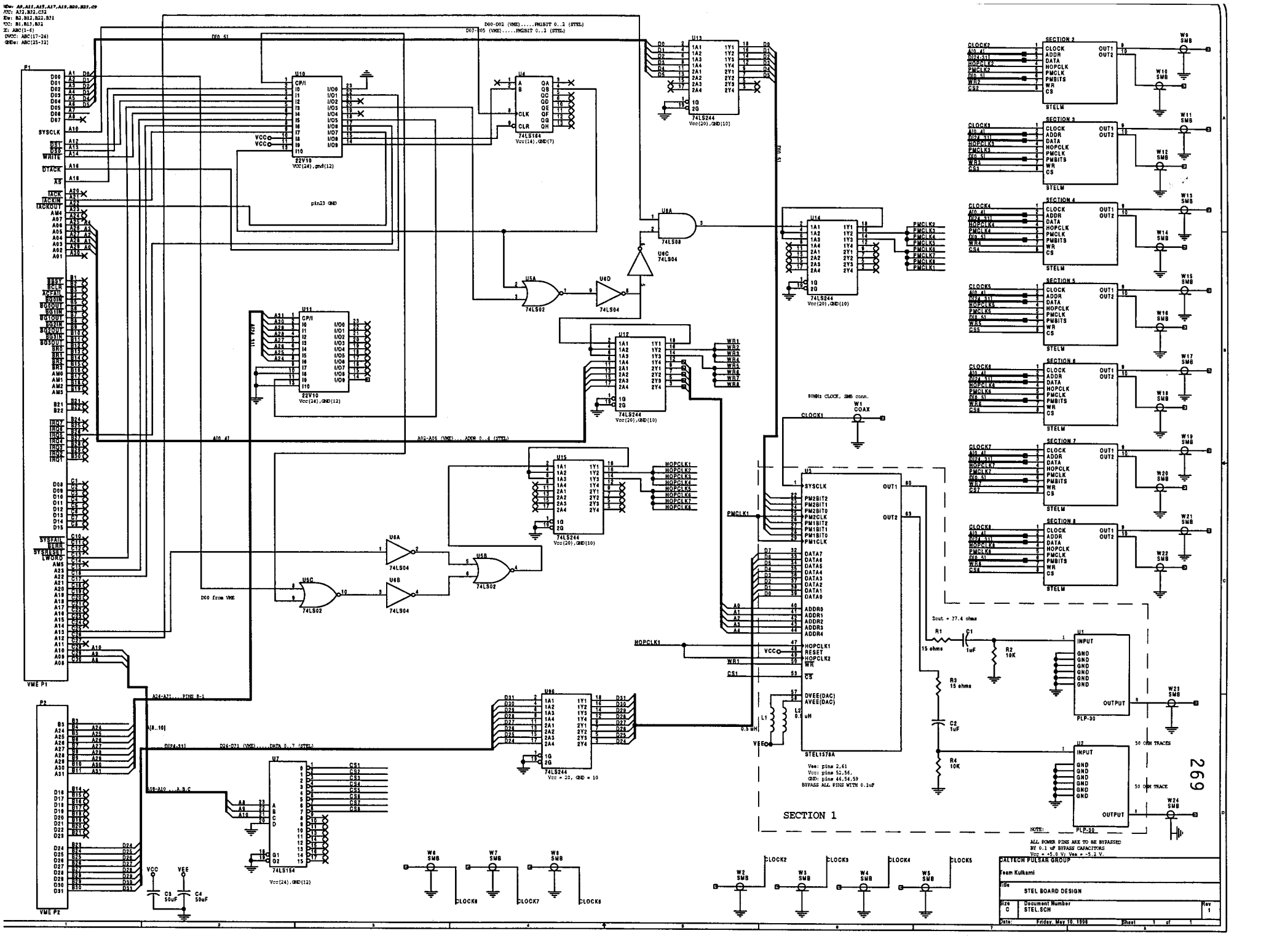
SECTION 1
SECTION 2
SECTION 3
SECTION 4
SECTION 5
SECTION 6
SECTION 7
SECTION 8
STEL1378A
STELM
PLP-30
VME P1
VME P2
50MHz CLOCK, SMB conn.
ALL POWER PINS ARE TO BE BYPASSED BY 0.1 uF BYPASS CAPACITORS
Vcc = +5.0 V; Vee = -5.2 V.
CALTECH PULSAR GROUP
Team Kulkarni
STEL BOARD DESIGN
Document Number STEL.SCH
Friday, May 10, 1996
269